

# KINETICS OF ROCK-WATER REACTIONS

by

Charles Owen Grigsby

B.S. in Geology  
New Mexico Institute of Mining and Technology  
(1973)

S.M. in Chemical Engineering  
Massachusetts Institute of Technology  
(1983)

SUBMITTED IN PARTIAL FULFILLMENT  
OF THE REQUIREMENTS  
FOR THE DEGREE OF

DOCTOR OF PHILOSOPHY

at the

MASSACHUSETTS INSTITUTE OF TECHNOLOGY

January 17, 1989

© Massachusetts Institute of Technology, 1989

Signature of Author \_\_\_\_\_  
Department of Chemical Engineering  
January, 1989

Certified by \_\_\_\_\_  
Dr. Jefferson W. Tester  
Thesis Supervisor

Accepted by \_\_\_\_\_  
Dr. Robert C. Armstrong, Chairman  
Departmental Committee on Graduate Students

# Kinetics of Rock-Water Reactions

by

Charles Owen Grigsby

Submitted to the Department of Chemical Engineering  
on January 17, 1989 in partial fulfillment  
of the requirements for the Degree of  
Doctor of Philosophy in Chemical Engineering.

## Abstract

Dissolution rates for aluminosilicate minerals typically show a "U"-shaped dependence of the rate on the solution pH - that is, the minimum rate is at some intermediate pH and the rate increases as the pH changes from this minimum. Previous attempts to explain the position of this minimum and the overall reaction order with respect to  $[H^+]$  were not based on realistic reaction mechanisms for hydrolysis of Si-O and Al-O bonds.

In this thesis, reaction mechanisms consisting of sets of elementary reactions were developed for the dissolution of quartz and albite (feldspar). Hydrolysis of Si-O and Al-O bonds is catalyzed by  $[H^+]$  at low pH and by  $[OH^-]$  at high pH. For quartz, the catalyzed hydrolysis is interpreted as following an  $S_N2$  reaction mechanism. The fractional order of the dissolution rate with respect to catalyst activity is shown to be a result of the stoichiometry of the elementary reactions. The pH dependence of the albite dissolution rate was shown to depend upon the aluminum concentration in solution.

For quartz, the minimum rate occurs at pH 3 which is close to the pH at the point of zero surface charge,  $pH_{pzc}$ . The minimum in the albite dissolution rate occurs at pH 6.5 which is about four pH units of the albite  $pH_{pzc}$ . However, this effect results from aluminum in tetrahedral coordination in the crystal structure reacting by  $S_N1$  as well as  $S_N2$  reaction mechanisms under acid-catalyzed conditions. When the effects of decreased rate due to the presence of aqueous aluminum ions and increased rate in the acid region due to  $S_N1$  reactions at aluminum sites in the crystal structure are eliminated, the dissolution rate versus pH curves for albite and quartz have exactly the same form.

Rate laws based on the comprehensive reaction mechanisms for quartz and albite dissolution show that the overall dissolution rate includes terms for reaction at several types of surface sites including sites at flat surfaces, "ledge" sites and "kink" sites. The relative contributions of each of these terms to the overall dissolution rate cannot be evaluated without knowledge of the relative concentrations of these types of sites.

Furthermore, this knowledge is required to evaluate kinetic parameters for elementary reactions.

To partially test some aspects of the proposed mechanisms and rate laws, quartz dissolution rates were measured experimentally at 25° C and at low pH using a packed bed reactor geometry. Natural quartz sand was prepared by tumbling with silicon carbide grit to remove surface irregularities, and ultrafine particles were removed by careful washing. Dissolution rates measured using this material were about two and one-half orders of magnitude faster than rates reported in the literature for crushed quartz. Examination of the surface of the sand by SEM reveals that the tumbling did not completely remove the etched surface of the as-received sand, so the relative concentration of ledge sites is higher in this material than it is for crushed quartz samples.

The experimental work verifies the pH dependence of the quartz dissolution rate at low pH and gives a reaction order with respect to  $[H^+]$  that is close to one-half as predicted by the stoichiometry of the elementary reactions. Furthermore, these experiments show the importance of sample preparation and characterization techniques for studies of dissolution rates.

The ideas presented in this thesis provide much of the necessary theoretical basis for further developments in geochemical kinetics. Major contributions include recognition of the catalytic role of  $[H^+]$  and  $[OH^-]$  in the hydrolysis of Si-O and Al-O bonds, the development of realistic reaction mechanisms for aluminosilicate dissolution reactions and of rate laws corresponding to those mechanisms that relate the bulk dissolution rate to the rates of elementary reactions, the interpretation of the albite dissolution rates in terms of the effects on the rate of aluminum in the crystal structure and in aqueous solution, and the recognition that kinetic parameters cannot be calculated without knowing the relative rates of the various parallel reaction pathways.

Thesis Supervisor: Dr. Jefferson W. Tester, Professor of Chemical Engineering



Jonathan Machen (1964-)

El arroyo de la sierra  
Me complacé mas que el mar.

José Martí  
(1853-1895)

## Table of Contents

Abstract	2
List of Figures	7
List of Tables	12
Nomenclature	14
<b>Chapter 1. Kinetics of Rock-Water Interactions - Overall Summary</b>	<b>18</b>
1.1 Introduction and Background.	18
1.2 Thesis Objectives and Organization.	20
1.3 Review of Geochemical Kinetics.	20
1.4 $\equiv\text{Si-O-Si}\equiv$ Bond Hydrolysis Mechanism.	27
1.5 Quartz Dissolution Mechanism and Rate Law.	31
1.6 $\equiv\text{Al-O-Si}\equiv$ Bond Hydrolysis Mechanism.	34
1.7 Albite Dissolution Mechanism and Rate Law.	36
1.8 Calculation of Kinetic Parameters.	39
1.9 Quartz Dissolution Rate Experiments.	42
1.10 Conclusions and Recommendations.	46
<b>Chapter 2. Geochemical Kinetics - A Review of the State-of-the-Art</b>	<b>49</b>
2.1 Introduction and Background.	49
2.2 Experimental Methodology.	55
2.3 Geochemical Rate Laws.	62
2.4 Quartz Dissolution Kinetics.	69
2.5 Feldspar Dissolution Kinetics.	74
<b>Chapter 3. Thesis Motivation and Objectives</b>	<b>80</b>
<b>Chapter 4. Mechanisms of Aluminosilicate Dissolution Reactions</b>	<b>83</b>
4.1 Acid- and Base-Catalyzed Hydrolysis of Epoxides: an Analog for Aluminosilicate Reaction Mechanisms.	85
4.2 Acid- and Base-Catalyzed Mechanisms for Aluminosilicate Hydrolysis.	91
4.2.1 $\equiv\text{Si-O-Si}\equiv$ Hydrolysis Mechanism.	96
4.2.2 $\equiv\text{Al-O-Si}\equiv$ Hydrolysis Mechanism.	99
4.2.3 Successive Reactions at a Specific Tetrahedral Atom.	101
4.3 Quartz Dissolution Mechanism.	103
4.4 Feldspar Dissolution Mechanism.	111

<b>Chapter 5. Rate Laws for Quartz and Albite Dissolution</b>	<b>113</b>
5.1 Rate Laws for Elementary Reactions in Solution.	114
5.2 Rate Expressions for the Quartz Dissolution Mechanism.	116
5.2.1 Comprehensive Rate Expression for Quartz Dissolution.	120
5.2.2 Graph of the Quartz Dissolution Mechanism.	123
5.3 Rate Expressions for Feldspar Dissolution Kinetics.	127
5.3.1 Effect of Dissolved Aluminum on the Feldspar Dissolution Rate.	128
5.3.2 The Effect of $S_N1$ versus $S_N2$ Mechanisms on the Rate of Feldspar Dissolution at Low pH.	130
 <b>Chapter 6. Experimental Tests of the Proposed Mechanisms and Rate Laws</b>	 <b>139</b>
6.1 Experiment Design.	140
6.2 Sample Preparation, Characterization and Chemical Analysis.	145
6.3 Reactor Design and Analysis.	148
6.4 Experimental Results.	161
6.4.1 Determination of the Residence Time Distribution for the Packed Bed Reactor.	161
6.4.2 Calculation of the Solution pH.	167
6.4.3 Quartz Dissolution Results.	174
6.4.4 Comparison with Previous Results.	178
 <b>Chapter 7. Discussion of the Theoretical and Experimental Results and         Recommendations for Future Work</b>	 <b>182</b>
7.1 Discussion of the Results.	182
7.2 Recommendations for Further Work.	188
 References	 192
 Appendices	 201
Appendix A. The Feldspar-Water System.	201
Appendix B. Analysis of Complex Reaction Systems	206
Appendix C. Bond Additivity Method for Estimating Thermochemical Properties of Aluminosilicate Minerals	212
Appendix D. Experimental Quartz Dissolution Rate Data	217
 Acknowledgements	 225
 Biographical Sketch	 228

## List of Figures

- Figure 1.1** 22  
Suggested mechanism of potassium feldspar dissolution in acid solutions (from Aagaard and Helgeson, 1982). The initial feldspar structure is shown in (a). Exchange of a hydronium ion for a potassium ion in (b), and addition of an "interstitial" hydronium ion in (c) form the "activated complex" in (d). This complex has the stoichiometry  $(\text{H}_3\text{O})\text{AlSi}_3\text{O}_8(\text{H}_3\text{O})^+$ . In (e), the "activated complex" is released to aqueous solution.
- Figure 1.2** 24  
Quartz dissolution rates as a function of pH from data reported in the literature. Because Kamiya, et al (1974) did not report specific surface areas for their quartz samples, the vertical position of this data set is arbitrarily chosen to match the data of other investigators. However, the positions of these data points relative to each other are fixed.
- Figure 1.3** 26  
Feldspar dissolution rates as a function of pH from data reported in the literature.
- Figure 1.4** 28  
Schematic acid- and base-catalyzed mechanisms for quartz dissolution.
- Figure 1.5** 29  
Mechanism of (a) an  $\text{S}_{\text{N}}2$  reaction showing the trigonal bipyramidal transition state and inversion of the  $\text{SiO}_4$  tetrahedron, and (b) a unimolecular ( $\text{S}_{\text{N}}1$ ) bond fission reaction with subsequent attack by a nucleophile (water molecule).
- Figure 1.6** 33  
Graph of the quartz dissolution mechanism. Each vertex or corner is a surface species and each directed line represents a reversible elementary reaction. Heavy lines are bi-directional reaction pathways. The arrows on the uni-directional reaction pathways point in the direction of the dissolution reaction.
- Figure 1.7** 35  
Rates of  $\text{S}_{\text{N}}1$  (solid line) and  $\text{S}_{\text{N}}2$  (dashed line) reaction pathways for the acid-catalyzed hydrolysis of albite at 25°C. Notice that the  $\text{S}_{\text{N}}2$  pathway intersects the base-catalyzed reaction at the  $\text{pH}_{\text{psc}}$  for albite (about pH 3).
- Figure 1.8** 37  
Effect of aluminum concentration in solution on the rate of feldspar dissolution (from Chou and Wollast, 1985).
- Figure 1.9** 37  
Albite dissolution rates (solid lines) and rates adjusted for the effect of dissolved aluminum (dashed lines). The dashed lines are consistent with reaction orders with respect to catalyst concentration of one-half.

- Figure 1.10** 44  
Comparison of the experimentally determined quartz dissolution rates (this study) with published quartz dissolution rates.
- Figure 1.11** 45  
SEM photographs of the surfaces of (a) tumbled quartz (Ottawa) sand and (b) crushed quartz. Notice the smooth surface and sharp edges on the crushed quartz compared to the relatively rough surface of the tumbled quartz.
- Figure 2.1** 50  
Activity diagram for the system  $K_2O-Al_2O_3-SiO_2-H_2O-HCl$  at 25°C, 1 bar and unit activity for  $H_2O$  (modified after Helgeson and Murphy, 1983). Helgeson and Murphy's (1983) calculated reaction path for microcline dissolution is shown as the dashed line. The solid lines are the boundaries of the mineral stability fields in equilibrium with the solution.
- Figure 2.2** 59  
Schematic fluidized bed reactor used by Chou and Wollast (1984, 1985) in their studies of feldspar dissolution.
- Figure 2.3** 60  
Schematic stirred flow cell reactor used by Holdren and Speyer (1985b, 1986) in their studies of feldspar dissolution.
- Figure 2.4** 61  
Schematic differential packed bed reactor used by Knauss and Wolery (1986, 1988) in studies of quartz and feldspar dissolution.
- Figure 2.5** 67  
Aagaard and Helgeson's (1982) mechanism of potassium feldspar dissolution in acid solutions. The initial feldspar structure is shown in (a). Exchange of a hydronium ion for a potassium ion (b), and addition of an interstitial hydronium ion (c) form the "activated complex" (d) which has the stoichiometry  $(H_3O)AlSi_3O_8(H_3O)^+$ . In (e), the "activated complex" is released to aqueous solution.
- Figure 2.6** 73  
(a) Thornton and Radke's (1988) mechanism of quartz dissolution and precipitation from aqueous solution. (b) representation of "primary", "secondary" and "tertiary" silicate groups at the quartz-water interface (from Thornton and Radke, 1988).
- Figure 2.7** 75  
Quartz dissolution rates as a function of pH from data reported in the literature. Because Kamiya, et al (1974) did not report specific surface areas for their quartz samples, the vertical position of this data set is arbitrarily chosen to match the data of other investigators. However, the positions of these data points relative to each other are fixed.
- Figure 2.8** 78  
Feldspar dissolution rates as a function of pH from data reported in the literature.



<b>Figure 4.1</b>	86
Hydrolysis rates of (a) Ethyl acetate (after Kirby, 1972) and (b) isobutylene oxide (after Long and Pritchard, 1956) as a function of pH at 25°C. At low pH, both reactions are catalyzed by H <sup>+</sup> , and at high pH, OH <sup>-</sup> catalyzes the reactions. Isobutylene oxide also reacts by a pH independent reaction at intermediate pH.	
<b>Figure 4.2</b>	88
(a) Acid- and (b) base-catalyzed mechanisms of epoxide hydrolysis (after Gould, 1959).	
<b>Figure 4.3</b>	93
Superposition of (a) the quartz dissolution rate data sets, and (b) the feldspar dissolution rate data sets. The rates for each data set (for example, the quartz dissolution rate data at 25°C) are offset by a constant value as discussed in Table 4.3.	
<b>Figure 4.4</b>	94
Comparison of (a) equation (4.2a) with the published quartz dissolution rate data, and (b) equation (4.2b) with feldspar dissolution rate data.	
<b>Figure 4.5</b>	97
Schematic acid- and base-catalyzed mechanisms for ≡Si-O-Si≡ bond hydrolysis.	
<b>Figure 4.6</b>	100
Mechanism of (a) an S <sub>N</sub> 2 reaction showing the trigonal bipyramidal transition state and inversion of the SiO <sub>4</sub> tetrahedron, and (b) a unimolecular (S <sub>N</sub> 1) bond fission reaction with subsequent attack by a nucleophile (water molecule).	
<b>Figure 4.7</b>	102
Reaction coordinate-energy diagram for successive reactions at a particular tetrahedral site. Each peak corresponds to the activated complex and each valley corresponds to a stable surface species as shown in the figure.	
<b>Figure 4.8</b>	110
Surface charge density as a function of pH and electrolyte concentration for an amorphous silica sol (from Bolt, 1957).	
<b>Figure 5.1</b>	124
Graph of the quartz dissolution mechanism. Each vertex is a surface species and each directed line represents one or more reversible elementary reactions from Table 5.2. The arrows point in the direction of the dissolution reaction. Complete cycles that include only two vertices (or bi-directional connections) are shown as heavy lines.	
<b>Figure 5.2</b>	127
Idealized quartz surface showing the relationship between Si <sub>3</sub> , Si <sub>2</sub> and Si <sub>1</sub> sites and bulk surface, ledge and kink sites.	
<b>Figure 5.3</b>	129
Effect of dissolved aluminum concentration of the rate of dissolution of feldspar (from Chou and Wollast, 1985).	

- Figure 5.4** 130  
Albite dissolution rates (solid lines) and rates adjusted for the effect of dissolved aluminum (dashed lines). The dashed lines are consistent with reaction orders with respect to catalyst concentration of one-half.
- Figure 5.5** 133  
Rates of  $S_N1$  (solid line) and  $S_N2$  (dashed line) reaction pathways for the acid-catalyzed hydrolysis of albite at 25°C. Notice that the  $S_N2$  pathway intersects the base-catalyzed reaction at the  $pH_{pzc}$  for albite (about pH 3).
- Figure 5.6** 134  
Comparison of feldspar dissolution rate data with the adjustments for aluminum concentration effects and the incorporation of both  $S_N1$  and  $S_N2$  reaction mechanisms.
- Figure 5.7** 135  
Comparison of the adjusted feldspar dissolution rates with quartz dissolution rate data.
- Figure 6.1** 141  
Schematic drawing of the experimental apparatus used in these experiments. The reaction vessel is a high-pressure filter that is constructed of teflon-coated stainless steel. All wetted parts in the system are polyethylene, teflon or teflon-coated except for the two valves which are stainless steel.
- Figure 6.2** 147  
SEM photographs of the quartz sand used in these experiments. (a) and (b) show the sand before any treatment to remove fine particles and surface roughness, (c) and (d) are after tumbling and fluidization to remove fines, and (e) and (f) are reacted sand. The magnification of (a), (c) and (e) is about 43.5 x, and the magnification of (b), (d) and (f) is about 2230 x.
- Figure 6.3** 154  
Schematic cross-section of a packed bed reactor. The performance equation for the reactor is derived by performing a material balance on the control volume shown in the figure.
- Figure 6.4** 159  
(a) Concentration profile and (b) dimensionless concentration profile in a packed bed reactor.
- Figure 6.5** 164  
Normalized Na-Fluorescein dye concentrations as a function of time for the packed bed tracer experiment. The concentrations are normalized automatically by setting the spectrophotometer to display the feed concentration as 1.000 and the background concentration as 0.000.
- Figure 6.6** 166  
Comparison of the tracer concentration data with the axial dispersion model for small extents of dispersion (equation (6.15)).
- Figure 6.7** 169  
Comparison of a portion of Meissner's (1980) family of curves of reduced mean ionic activity coefficient,  $\Gamma$ , with experimental values for the mean ionic activity coefficient for  $HNO_3$  at 25°C (from Conway, 1952; Harned and Owen, 1958; Dobos, 1975).

- Figure 6.8** 171  
 Comparison of the experimental values for the mean ionic activity coefficient for  $\text{HNO}_3$  (Conway, 1952; Harned and Owen, 1958; Dobos, 1975) with Meissner's (1980) and Pitzer's (1979) models for calculating activity coefficients.
- Figure 6.9** 171  
 Calculated pH versus ionic strength for Meissner's (1980) and for Pitzer's (1979) activity coefficient models.
- Figure 6.10** 173  
 Comparison of calculated pH values with experimentally measured values of pH for various  $\text{HNO}_3$  solutions.
- Figure 6.11** 176  
 Measured ( $\blacksquare$ ) and calculated (+) values for (a) silica concentration, (b) pH, and (c) flow rate for the quartz dissolution rate experiments in the packed bed reactor. Feed solutions are labeled on the graph. The major breaks shown at about days 1 and 5 are of several days duration each; the time axis for these graphs is compressed to show the important features of the experimental results.
- Figure 6.12** 177  
 Results of the quartz dissolution rate studies on Ottawa sand. The open squares are the rates calculated using equation (6.8), and the diamonds correspond to the rates calculated from equation (6.12). The solid diamonds were used in calculating the least squares line.
- Figure 6.13** 179  
 Results of the quartz dissolution rate experiments compared with published quartz dissolution rate data. Notice that the quartz dissolution rate increases with  $[\text{H}^+]$  at low pH. The rates from this study are considerably higher than expected based on the 25°C data shown in the Figure.
- Figure 6.14** 180  
 SEM photographs of (a) a grain of Ottawa sand from these experiments and (b) the crushed quartz used by Knauss and Wolery (1988). Fracture surfaces in (a) (at the arrow) and (b) are very smooth compared with the outside surface of the sand grain.

## List of Tables

<b>Table 1.1</b>	40
Activation energies and pre-exponential factors reported for quartz and feldspar dissolution.	
<b>Table 2.1</b>	56
Typical experimental conditions for quartz and feldspar dissolution studies reported by various investigators.	
<b>Table 4.1</b>	84
Activation energies and pre-exponential factors reported for quartz and feldspar dissolution.	
<b>Table 4.2</b>	90
Percentage of $^{18}\text{O}$ entering the epoxide at the primary carbon in Long and Pritchard's (1956) studies of epoxide hydrolysis mechanisms.	
<b>Table 4.3</b>	95
Regression of quartz and albite reaction rate data to find the reaction order with respect to $[\text{H}^+]$ for the quartz and albite dissolution reactions. The quartz data sets and offsets to the rate data used in the regression are: Knauss and Wolery (1988) 70°C, -2.7; Kamiya, et al. (1974) 60°C, -2.4; Kamiya, et al. (1974) 90°C, -2.9; all 25°C data, 0.0. For albite, the data sets are: Knauss and Wolery (1986) 70°C, -0.715; Chou and Wollast (1984, 1985) 25°C, 0.0.	
<b>Table 4.4</b>	104
Elementary reactions for the detailed quartz dissolution mechanism.	
<b>Table 4.5</b>	108
Elementary reactions which add to give the composite reaction (9) in Table 4.4. The coefficient of the elementary reaction gives the product distribution for reaction at an $\text{Si}_3\text{-O-Si}_4$ site.	
<b>Table 5.1</b>	117
Rate laws for the elementary reactions in Table 4.4.	
<b>Table 5.2</b>	121
Rate equations for the change in surface species concentrations with time for the acid-catalyzed $\text{S}_\text{N}2$ reactions given in Table 4.4. The $\mathfrak{R}_i$ are given in Table 5.1.	
<b>Table 6.1</b>	144
Summary of the results of the quartz dissolution rate experiments. The reported time is the time the sample changer advanced. Measured sample masses were corrected for evaporation applying an average evaporation rate over the time from sample collection to measurement of the sample mass. This correction for evaporation was then used to correct the flow rate and the $\text{HNO}_3$ and silica concentrations.	
<b>Table 6.2</b>	151
Characteristics of flow-through reactors reported in the literature.	

<b>Table 6.3</b>	165
Na-fluorescein concentrations from the dye tracer experiment. The elapsed time is the actual time that the automatic sampler advanced. The calculated time is figured for a constant flow rate of 0.22 ml/min.	
<b>Table 6.4</b>	173
Ionic strength and pH measured for various HNO <sub>3</sub> solutions. The ionic strength was determined by adding 5.0 ml of 0.1 N KOH to 1.0 ml of sample and then titrating with 0.1 N H <sub>2</sub> SO <sub>4</sub> .	
<b>Table 6.5</b>	175
Experimentally determined quartz saturation concentrations at low pH, steady-state outlet silica concentrations from the packed bed reactor, and calculated rates of quartz dissolution.	
<b>Table A.1</b>	202
Simplified Feldspar nomenclature (after Deere, et al., 1971). Pure component (or end-member) feldspar compositions, crystallographic classes and Si-Al ordering are described in part a. Part b describes the intermediate feldspar compositions and structures. For example, a high-temperature andesine has the high-albite structure, but a low-temperature andesine has exsolved at the microscopic level to a Na-rich phase having a low-albite structure and a Ca-rich phase with the low-anorthite structure.	
<b>Table A.2</b>	205
Secondary minerals (alteration products) in the feldspar-water system.	
<b>Table C.1</b>	214
Individual bond contributions to the enthalpy and entropy of formation for aluminosilicate minerals at 298 K and 1 bar pressure.	
<b>Table C.2</b>	215
Comparison of calculated and measured values of the enthalpy of formation from the elements. Measured values are from Robie, et al. (1979). Coordination numbers for the various minerals are from Smyth and Bish (1988).	
<b>Table D.1</b>	218
Experimental quartz dissolution rate data.	

## Nomenclature

a,b,c,d	stoichiometric coefficients
$a^*$	ratio of interfacial surface area to the fluid volume
$a_i$	activity of a species (equation (2.11))
$a_i, b_i, c_i$ $d_i, e_i, f_i$ $g_i, h_i$	undetermined multipliers
$\underline{a}, \underline{b}, \underline{c}$	concentration vectors
A	pre-exponential factor in the Arrhenius rate expression
$\Delta A$	chemical affinity for a reaction (equation (2.11))
C	concentration of a species in solution
d	diameter of a reactor
D	axial dispersion coefficient
Da	Damköhler number - $L^2 \kappa / (D C)$
$E_{act}$	activation energy (kJ/mol-K)
h	Planck's constant ( $6.626 \times 10^{-34}$ J/s)
$\Delta H^\ddagger$	activation enthalpy (kJ/mol)
I	ionic strength - $0.5 \sum m_i z_i^2$
k	rate constant for a reaction
$k_f, k_r$	rate constants for the forward and reverse reaction
$k_i, k_{-i}$	rate constants for the $i^{\text{th}}$ forward and reverse reaction
$\underline{k}$	rate constant vector
$k_B$	Boltzmann's constant ( $1.381 \times 10^{-23}$ J/K)
$K, K^{eq}$	equilibrium constant for a reaction

<u><b>K</b></u>	rate constant matrix
<b>L</b>	length of a reactor
<u><b>L</b></u>	stoichiometric coefficient matrix
$m_i$	molarity of species $i$
<u><b>M</b></u> , <u><b>M</b></u> *	variable matrices
$O^{18}$	isotope of oxygen
<b>Pe</b>	Peclet number ( $uL/D$ )
$pH_{pzc}$	pH at the point of zero surface charge
$q$	adjustable parameter in Meissner's (1980) activity coefficient model
$\dot{q}$	volumetric flow rate
<b>R</b>	ideal gas constant (8.314 J/mol K)
<b>r</b>	vector of surface reaction rates
<b>r</b>	rate of a reaction
$Si_L$	number of bridging oxygen atoms attached to a given silicon atom
$\Delta S^\ddagger$	activation entropy (J/mol K)
<b>s</b>	vector of surface species concentrations
<b>t</b>	time
<b>T</b>	absolute temperature (Kelvins)
<b>T</b>	general tetrahedrally coordinated atom (Chapter 4)
<b>u</b>	linear fluid velocity
<b>V</b>	fluid volume
<b>x</b>	length along the reactor
$z_+, z_-$	charge on a cation or anion

## Greek

$\gamma_i$	activity coefficient of species $i$
$\gamma_{\pm}$	mean ionic activity coefficient
$\Gamma$	reduced mean ionic activity coefficient
$\kappa_{ij}$	rate constant for an $S_N2$ reaction at an $Si_i-O-Al_j$ site
$\lambda_{ij}$	rate constant for an $S_N1$ reaction at an $Si_i-O-Al_j$ site
$\nu_n^i$	stoichiometric coefficient of species $n$ in reaction $i$
$\xi_i$	extent of reaction $i$ (equation (2.13))
$\xi$	dimensionless length along the reactor
$\sigma$	average stoichiometric number (equation (2.11))
$\tau$	mean residence time
$\tau_{ss}$	time required to reach steady-state
$\Psi$	dimensionless concentration
$\Omega$	ohms

## Superscripts

$\alpha, \beta, \pi, \rho$	reaction orders
sat	saturation
surf	surface



## Subscripts

ab	albite
Al	aluminum
eff	effective
in	inlet
out	outlet
qtz	quartz

## Special Characters or Symbols

{ }	concentration of a species
[ ]	activity of a species
[ ] <sup>‡</sup>	activated complex or transition state
≡	lateral ligands to a silicon or aluminum atom

## **Chapter 1**

### **Kinetics of Rock-Water Interactions - Overall Summary**

**1.1 Introduction and Background.** Chemical reactions between rocks and water are complex in that several solid phases and multiple reactions are coupled or in competition for reactants which are transported through a common liquid phase. The state of a complex reaction system - which phases are present and the amounts and compositions of those phases - is determined by the path of the reaction and the rate of progress along the reaction path rather than solely from thermodynamic equilibrium considerations. Previous attempts to model rates of rock-water reactions have largely assumed near-equilibrium conditions for most of the possible reactions in a system (Helgeson, 1968; Helgeson, et al., 1970; Helgeson, 1971; Helgeson and Murphy, 1983; Helgeson, et al., 1984). However, under the conditions encountered or expected in engineered systems such as man-made geothermal reservoirs and nuclear waste repositories, the assumption that most reactions are near equilibrium places an artificial constraint on a kinetic model of the reacting system reducing the set of highly coupled reactions to a few more or less independent reactions.

As evidenced by the increase in the number of articles published on geochemical kinetics, the importance of understanding rates of chemical reactions in geologic systems is growing. In addition to the general scientific interest in fundamental rock-water reaction kinetics, there are a number of practical applications where modeling coupled heat transfer, fluid flow, chemical reactions, and changes in rock

mechanical properties is essential. The most important and immediate applications of geochemical kinetics involve the storage of nuclear waste in underground repositories, but direct applications of this research can also be found in a number of related fields involving the environment (chemical waste migration, leaching of mine tailings, effects of acid rain), energy production (performance of man-made geothermal reservoirs, reinjection of flashed geothermal brines, *in-situ* coal gasification, *in-situ* oil shale retorting, acid stimulation of oil wells), mineral recovery (solution mining, ore leaching), and geology and geochemistry (ore deposition, hydrothermal alteration, chemical weathering).

A major factor that has limited the rate of development of geochemical kinetics is the lack of a suitable theoretical framework for guiding the experimental studies. Experimentally determined rates of quartz,  $\text{SiO}_2$ , and feldspar,  $(\text{Na,K})\text{AlSi}_3\text{O}_8$ , dissolution depend primarily on temperature and solution pH (Chou and Wollast 1984, 1985; Holdren and Speyer, 1985b; Knauss and Wolery, 1986, 1988). Aagaard and Helgeson (1982) developed rate equations to describe the dissolution rate of quartz, feldspar, and other aluminosilicate minerals, and kinetic parameters have been calculated by a number of researchers. However, these rate equations, activation energies and pre-exponential factors are not based on realistic mechanisms. By default, kinetic parameters are assigned to an overall global reaction which is treated as if it were an elementary reaction. Transition-state theory (Eyring, 1935; Glasstone, et al., 1941) has recently been employed (Rimstidt and Barnes, 1980; Lasaga, 1981, 1984; Aagaard and Helgeson, 1982) to describe reaction rates, but since the reaction

mechanisms are based on overall reactions, the applications of transition-state theory usually violate some basic assumptions of transition-state theory.

**1.2 Thesis Objectives and Organization.** The primary objectives of this thesis are (1) to develop detailed reaction mechanisms for specific geochemical reactions, (2) to derive rate laws corresponding to those reaction mechanisms, and (3) to evaluate the kinetic parameters in the derived rate laws. By accomplishing these objectives, other goals will also be met: (4) to provide a conceptual framework into which geochemical kinetics studies may be fit, and (5) discover what specific information is required for future developments.

The current state-of-the-art in geochemical kinetics is reviewed in Chapter 2 with particular emphasis placed on studies of quartz ( $\text{SiO}_2$ ) and albite (sodium feldspar -  $\text{NaAlSi}_3\text{O}_8$ ) dissolution kinetics. The thesis objectives are defined in Chapter 3. Reaction mechanisms for quartz and albite dissolution are proposed in Chapter 4, and the corresponding rate laws are derived in Chapter 5. Experimental studies designed to verify some of these predictions are presented in Chapter 6, and the results of these studies are discussed in Chapter 7 along with recommendations for further work.

**1.3 Review of Geochemical Kinetics.** Within the past twenty years there has been renewed interest in determining mineral solubility and reaction kinetics under a wide variety of reaction conditions. The increased interest in rates of mineral-water reactions has not, in general, been accompanied by adequate understanding of chemical

kinetics. Only within the past five years has the geochemical community abandoned the "parabolic" (rate =  $k t^{1/2}$ ) rate laws (Helgeson, 1971; Grandstaff, 1977; White and Classen, 1979; Lahann and Robertson, 1980; Lin and Clemency, 1981) in favor of transition-state theory.

Unfortunately, transition-state theory is being adopted without certain essential concepts. In particular, the concept of an elementary reaction (as opposed to an overall reaction) is absent in papers which employ transition-state theory (see, for example Rimstidt and Barnes, 1980; Aagaard and Helgeson, 1982). It is not unusual to find researchers defining an improbable species based on the stoichiometry of an overall reaction as the "activated complex". For example, the reaction mechanism cited by Rimstidt and Barnes (1984) for quartz dissolution is given by the stoichiometry of the overall reaction:



Even though it has the appropriate form of an elementary reaction, equation (1.1) does not give any details of the molecular processes that occur during the reaction. Furthermore,  $[\text{SiO}_2 \cdot 2\text{H}_2\text{O}]^*$  is a pseudospecies, not a real (albeit shortlived) entity.

Aagaard and Helgeson (1982) describe feldspar dissolution as the breakdown of certain pH dependent, activated complexes at the feldspar surface: at low pH (less than 2.9), the "activated complex" is given by  $(\text{H}_3\text{O})\text{AlSi}_3\text{O}_8(\text{H}_3\text{O})^+$ ; at intermediate pH

(from 2.9 to 8) -  $(\text{H}_3\text{O})\text{AlSi}_3\text{O}_8(\text{H}_3\text{O})^n$  ; and at high pH (greater than 8) -  $[(\text{K},\text{Na})\text{Al}(\text{OH})_n\text{Si}_3\text{O}_8]^{-n}$ , where n is an empirically determined parameter. According to their mechanism, the rate-limiting step at low pH is the release of an H-feldspar complex, eg.  $[(\text{H}_3\text{O})\text{AlSi}_3\text{O}_8(\text{H}_3\text{O})]^+$ , from the feldspar structure by the simultaneous rupture of five Si-O (or Al-O) bonds as shown in Figure 1.1 (from Aagaard and Helgeson, 1982). However, the release of an entire formula unit of feldspar to solution from the mineral surface due to the simultaneous breaking of five widely separated Si-O or Al-O bonds is inconsistent with the accepted concept of a transition state.

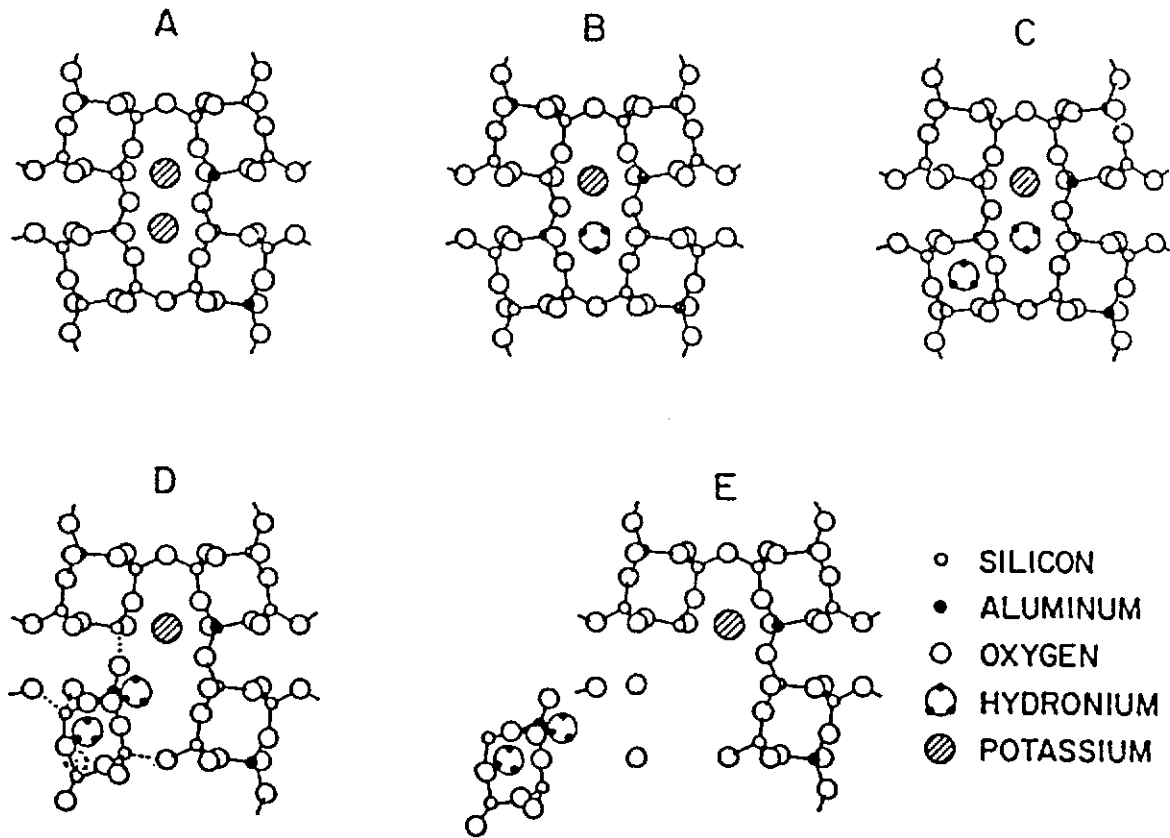


**Figure 1.1** Suggested mechanism of potassium feldspar dissolution in acid solutions (from Aagaard and Helgeson, 1982). The initial feldspar structure is shown in (a). Exchange of a hydronium ion for a potassium ion in (b), and addition of an "interstitial" hydronium ion in (c) form the "activated complex" in (d). This complex has the stoichiometry  $(\text{H}_3\text{O})\text{AlSi}_3\text{O}_8(\text{H}_3\text{O})^+$ . In (e), the "activated complex" is released to aqueous solution.

Quartz and feldspar are two of the most common minerals at the earth's surface, and although both minerals have been extensively studied, less is actually known about the reaction kinetics of these minerals in aqueous environments than is commonly assumed. For example, while it has been known for some time that the quartz dissolution rate depends upon the solution pH (Iler, 1979), the details of this pH dependence have yet to be fully established. Knauss and Wolery (1988) found that the quartz dissolution rate appears to be essentially independent of pH within the scatter of the data in the pH range from 1 to 6; above a pH of 6, the dissolution rate increases linearly with pH. On the other hand, Kamiya, et al (1974) found the quartz dissolution rate increases with decreasing pH below a pH of about 2, and Thornton and Radke (1988) did not observe a pH dependence for the quartz dissolution rate in the pH range from 11 to 12.

Experimentally determined quartz dissolution rates reported by various investigators are presented as a function of pH in Figure 1.2. With the exception of Kamiya, et al (1974) all investigators report the quartz dissolution rate in terms of the number of moles dissolved per second per  $\text{cm}^2$  of mineral surface area determined by BET gas adsorption isotherms. Kamiya, et al (1974) did not measure the BET surface area of their samples, but from their data, we can calculate rates in units of moles per second per gram of quartz. If the sample preparation techniques were consistent for their experiments, then the specific surface area of their samples would be approximately constant from experiment to experiment. The calculated rates based on the data presented by Kamiya, et al. (1974) were multiplied by an arbitrary constant to

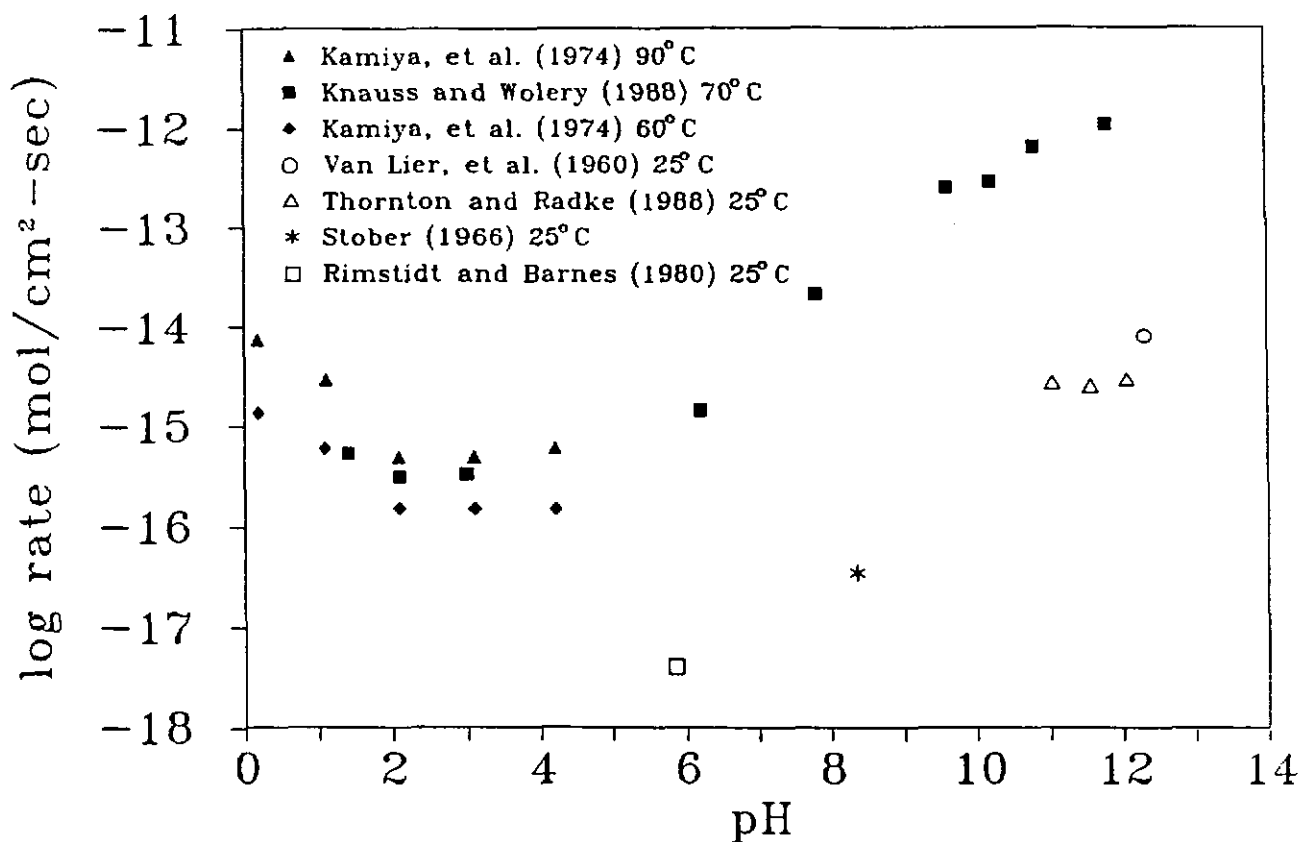
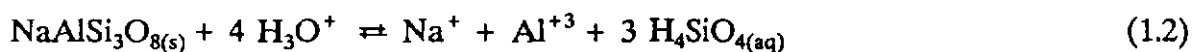


**Figure 1.2** Quartz dissolution rates as a function of pH from data reported in the literature. Because Kamiya, et al (1974) did not report specific surface areas for their quartz samples, the vertical position of this data set is arbitrarily chosen to match the data of other investigators. However, the positions of these data points relative to each other are fixed.

adjust the vertical position of these rates on the graph in Figure 1.1. Although there is considerable uncertainty in the vertical position of these data, the relative rates within the data set show that the dissolution rate depends upon  $[H^+]^{1/2}$  at very low pH.

In contrast with quartz dissolution, the transient stage of feldspar dissolution appears to be an incongruent process (reaction products do not appear in solution in ratios which correspond to the feldspar stoichiometry), but steady-state dissolution appears to approach congruent behavior (Chou and Wollast, 1984, 1985; Knauss and Wolery, 1986). The overall reaction for feldspar dissolution is:





Covering of the mineral surface by either a leached residuum or by the precipitation of reaction products from solution was offered as an explanation for both the incongruent nature of the reaction and for the observed "parabolic" kinetics in the early stages of a dissolution experiment. Because of the dependence of the rate on  $t^{1/2}$ , "parabolic" kinetics was attributed to diffusion limitations within a hypothesized surface layer (Wollast, 1967; Helgeson, 1971, 1972; Paces, 1973; Busenberg and Clemency, 1976; White and Classen, 1979; Chou and Wollast, 1984, 1985).

This "leached-layer/armoring precipitate" hypothesis has largely been abandoned for a number of reasons. Examination of reacted feldspar surfaces using x-ray photoelectron spectroscopy showed no evidence for a leached layer (Petrovic, et al., 1976; Berner, 1978). The apparent parabolic kinetics could be attributed to rapid dissolution of ultrafine particles produced during sample preparation (Holdren and Berner, 1979; Grandstaff, 1980; Petrovic, 1981a,b). Finally, activation energies considerably in excess of 15 to 20 kJ/mole (4 to 5 kcal/mole) indicate surface reaction rather than diffusion control (Berner, 1978), and the apparent activation energy for feldspar dissolution is about 83 kJ/mole (20 kcal/mole) (Helgeson, et al., 1984).

Experimentally determined albite dissolution rates are shown as a function of pH in Figure 1.3. In this figure, the rate of dissolution (moles of feldspar/cm<sup>2</sup>-s) is a minimum at a pH of 7, and the rate increases linearly with pH at both lower and

higher values of the pH. For feldspar dissolution, the apparent reaction order with respect to  $[H^+]$  or  $[OH^-]$  is about one-third.

Lasaga (1984) suggested that the fractional order dependence of the rate of aluminosilicate mineral dissolution on pH is due to the presence of several types of surface sites having different adsorption and reaction energies. He also suggested that the minimum in the rate versus pH curve might be related to the pH at the point of zero surface charge,  $pH_{pzc}$ , and that the "U-shaped" nature of the rate versus pH curve

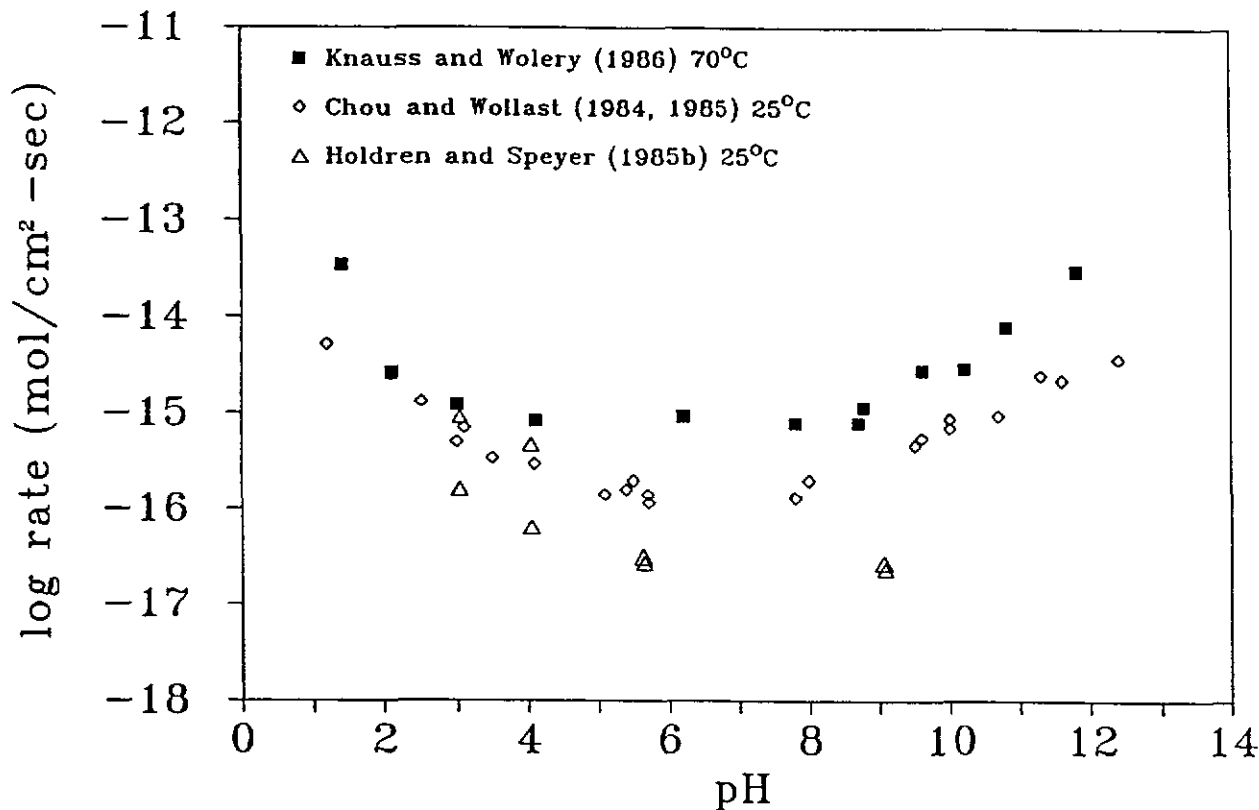


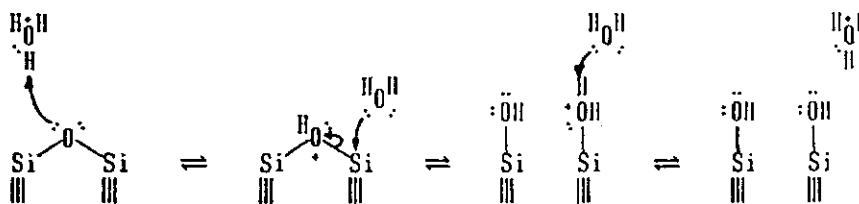
Figure 1.3 Feldspar dissolution rates as a function of pH from data reported in the literature.

is due to the amphoteric nature of aluminum in solution. However, this last explanation does not account for the shape of the quartz dissolution rate curve, and the  $\text{pH}_{\text{pzc}}$  for albite is about 2 to 3 (Stumm and Morgan, 1979) rather than at a pH of about 7 as seen in Figure 1.3.

**1.4  $\equiv\text{Si-O-Si}\equiv$  Bond Hydrolysis Mechanism.** Another explanation for the fractional order dependence of the quartz and albite dissolution rates comes from careful examination of the dissolution process. Quartz and albite dissolution rates depend on solution pH in a way that is qualitatively similar to ester and epoxide hydrolysis rates, but instead of hydrolyzing C-O bonds, quartz and albite dissolution involve hydrolysis of Si-O and Al-O bonds. By analogy with the epoxide hydrolysis mechanisms, I propose that  $\equiv\text{Si-O-Si}\equiv$  bonds are hydrolyzed via acid- and base-catalyzed mechanisms as shown in Figure 1.4. (note: the " $\equiv$ " indicates three single-bonded ligands attached to the silicon or aluminum.)

For the acid-catalyzed mechanism, the first step is the protonation of a bridging oxygen (that is, an oxygen that "bridges" two silicon atoms as opposed to a terminal oxygen or hydroxyl). This protonated oxygen is the leaving group and water is the attacking nucleophile in a bimolecular nucleophilic substitution ( $\text{S}_{\text{N}}2$ ) reaction. The catalyst is regenerated in a subsequent reaction. Under basic conditions, the reaction proceeds without the initial protonation step. Hydroxide ion is a stronger nucleophile than water (see, for example, Fessenden and Fessenden, 1982), so even at low hydroxide concentrations, the reaction proceeds with hydroxide ion as the nucleophile.

*Acid-Catalyzed Mechanism*



*Base-Catalyzed Mechanism*

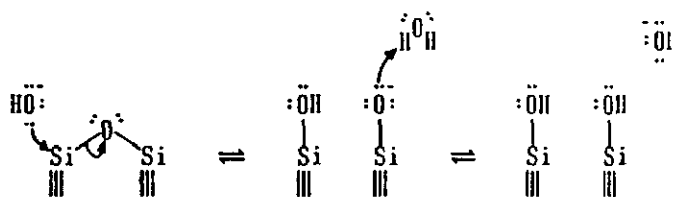


**Figure 1.4** Schematic acid- and base-catalyzed mechanisms for quartz dissolution.

For the  $S_N2$  reaction, the transition state involves a temporary change in electron orbital hybridization of a silicon atom from  $sp^3$  to  $sp^2$  and back to  $sp^3$  (Figure 1.5a). To change the hybridization of a silicate tetrahedron requires a considerable amount of energy - especially when the lateral ligands (those oxygens not involved in breaking or making bonds) are bound into the crystal structure. A silicate tetrahedron which has only one bridging oxygen (the reaction site) will have a "looser" transition state than one which has two or three bridging oxygens because lateral hydroxyls are more free to move than lateral oxygens that are bound into the crystal structure. A "loose" transition state implies a larger pre-exponential factor in the Arrhenius expression for the rate constant, and therefore a faster reaction rate (Benson, 1976). Thus, the rate of hydrolysis of an  $\equiv\text{Si-O-Si}\equiv$  bond depends on the next-nearest neighbor ligands.

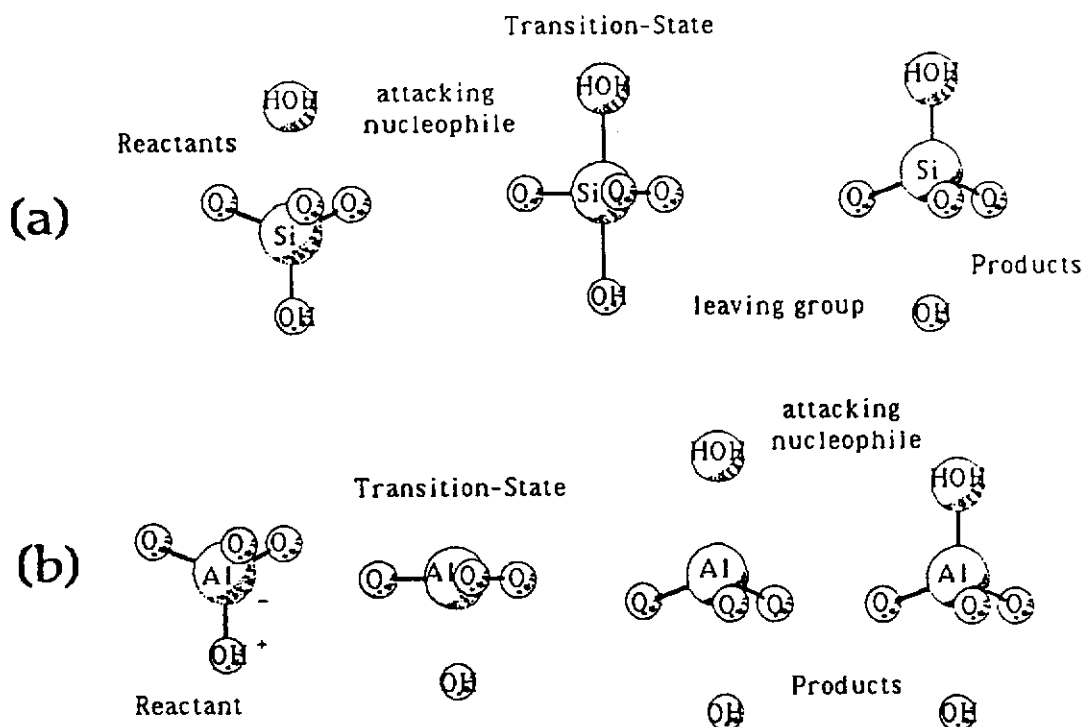
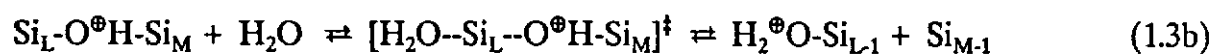
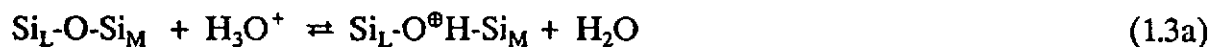


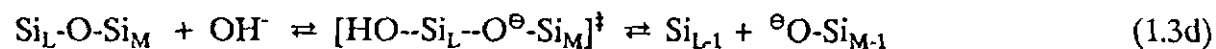
**Figure 1.5** Mechanism of (a) an S<sub>N</sub>2 reaction showing the trigonal bipyramidal transition state and inversion of the SiO<sub>4</sub> tetrahedron, and (b) a unimolecular (S<sub>N</sub>1) bond fission reaction with subsequent attack by a nucleophile (water molecule).

If Si<sub>L</sub> represents a silicon with L bridging oxygens, then there are eight possible combinations of Si<sub>L</sub>-O-Si<sub>M</sub> groups: Si<sub>3</sub>-O-Si<sub>4</sub>, Si<sub>3</sub>-O-Si<sub>3</sub>, Si<sub>2</sub>-O-Si<sub>3</sub>, Si<sub>1</sub>-O-Si<sub>3</sub>, Si<sub>2</sub>-O-Si<sub>4</sub>, Si<sub>2</sub>-O-Si<sub>2</sub>, Si<sub>1</sub>-O-Si<sub>2</sub>, and Si<sub>1</sub>-O-Si<sub>4</sub> (Note: Si<sub>4</sub>-O-Si<sub>4</sub> is an interior bond, not a surface moiety, and Si<sub>1</sub>-O-Si<sub>1</sub> is a dimer of silicic acid in solution.) Acid- and base-catalyzed reactions at any given Si<sub>L</sub>-O-Si<sub>M</sub> site (with L < M) involve the following elementary steps:

acid-catalyzed reactions



base-catalyzed reactions



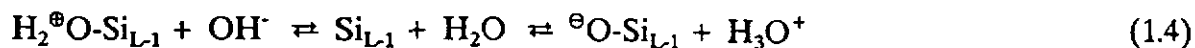
In these equations, the transition states are indicated by [ ]<sup>‡</sup>, and the dashed bonds show the axis of the reaction coordinate. Formal charges on a given oxygen atom are shown by ⊕ and ⊖. The terminology introduced here for silicon atoms, ie. Si<sub>x</sub> where the "X" tracks the number of bridging oxygens attached to a given silicon, also accounts for the number of hydroxides attached to the silicon (4 - X). The apparent "loss" of an OH in equations (1.3b) and (1.3d) is due to the fact that hydroxyls are automatically incorporated in the definition of Si<sub>x</sub>. In both the acid- and the base-catalyzed mechanisms, the nucleophile is shown attacking the Si which has more hydroxyls (Si<sub>L</sub>) because the rate is faster for the "looser" transition state.

The explanation for the quartz dissolution rate being approximately one-half order in catalyst concentration is apparent from the stoichiometry of the elementary reactions: one catalyst molecule is involved in a reaction that results in two product Si's being formed. On a per product Si basis, the reaction is one-half order in catalyst concentration.

A subset of these reactions describes the electrical interactions between the solid surface and the solution. For example, consider the modified versions of equations (1.3c) and (1.3e):



or,



At low pH, the surface has a net positive charge; at high pH, the surface charge is negative; and at some intermediate pH, the surface has no net charge. This last condition is the point of zero surface charge or  $\text{pH}_{\text{pzc}}$ . The measured  $\text{pH}_{\text{pzc}}$  for quartz and albite are in the pH 1.5 to 3.5 range (Iler, 1979; Stumm and Morgan, 1981), and the minimum rate for quartz dissolution corresponds closely to the  $\text{pH}_{\text{pzc}}$ .

**1.5 Quartz Dissolution Mechanism and Rate Law.** The interrelationships in a large set of reactions such as the set of elementary reactions for quartz dissolution mechanism are complex. Thus, the reaction network is often easier to visualize when presented in graphical form. A graph of the acid-catalyzed quartz dissolution mechanism is shown in Figure 1.6. In this figure, the "corners" (or "vertices") are labeled as the various  $\equiv\text{Si-O-Si}\equiv$  moieties, and the "edges" (or lines) connecting the vertices correspond to elementary chemical reactions. Each line is directed from the reactant to one of the possible products of the reaction.

At the top and bottom of the graph in Figure 1.6 are the bulk crystal species,  $\text{Si}_4$ , and aqueous silica,  $\text{Si}_0$ . Aqueous silica is produced by reactions at  $\text{Si}_1\text{-O-Si}_4$ ,

Si<sub>1</sub>-O-Si<sub>3</sub>, and Si<sub>1</sub>-O-Si<sub>2</sub> sites, while reaction at Si<sub>3</sub>-O-Si<sub>4</sub>, Si<sub>2</sub>-O-Si<sub>4</sub>, and Si<sub>1</sub>-O-Si<sub>4</sub> sites brings material from the bulk crystal to the surface. At steady-state, the rate at which crystalline material arrives at the surface equals the rate of production of aqueous silica. This overall rate of dissolution,  $\mathfrak{R}_{\text{qtz}}$ , is given by:

$$\mathfrak{R}_{\text{qtz}} = k_{34} [\text{Si}_3\text{-OH}^+\text{-Si}_4][\text{H}_2\text{O}] + k_{24} [\text{Si}_2\text{-OH}^+\text{-Si}_4][\text{H}_2\text{O}] + k_{14} [\text{Si}_1\text{-OH}^+\text{-Si}_4][\text{H}_2\text{O}]$$

(rate at which Si reaches the surface) (1.5a)

$$= k_{14} [\text{Si}_1\text{-OH}^+\text{-Si}_4][\text{H}_2\text{O}] + k_{13} [\text{Si}_1\text{-OH}^+\text{-Si}_3][\text{H}_2\text{O}] + k_{12} [\text{Si}_1\text{-OH}^+\text{-Si}_2][\text{H}_2\text{O}]$$

(rate at which silica enters the solution) (1.5b)

where  $k_{LM}$  is the rate constant corresponding to the reaction at Si<sub>L</sub>-OH<sup>+</sup>-Si<sub>M</sub> and  $\mathfrak{R}_{\text{qtz}}$  is the bulk rate of quartz dissolution.

According to equation (1.5a), the rate of quartz dissolution is the sum of the rates of three reactions. The relative contribution of each reaction to the bulk rate depends upon the surface concentrations of the key reactive species - Si<sub>3</sub>-O-Si<sub>4</sub>, Si<sub>2</sub>-O-Si<sub>4</sub> and Si<sub>1</sub>-O-Si<sub>4</sub> - as well as on the magnitudes of the rate constants. Smooth mineral surfaces should be covered mostly by Si<sub>3</sub>-O-Si<sub>4</sub>, but at edges, ledges and dislocations, Si<sub>2</sub>-O-Si<sub>4</sub> and Si<sub>1</sub>-O-Si<sub>4</sub> should predominate. The experimental material used in most experiments is crushed to fine particle sizes, sieved and then washed to remove ultrafine particles. Crushed samples typically have smooth cleavage surfaces bounded by sharp edges.



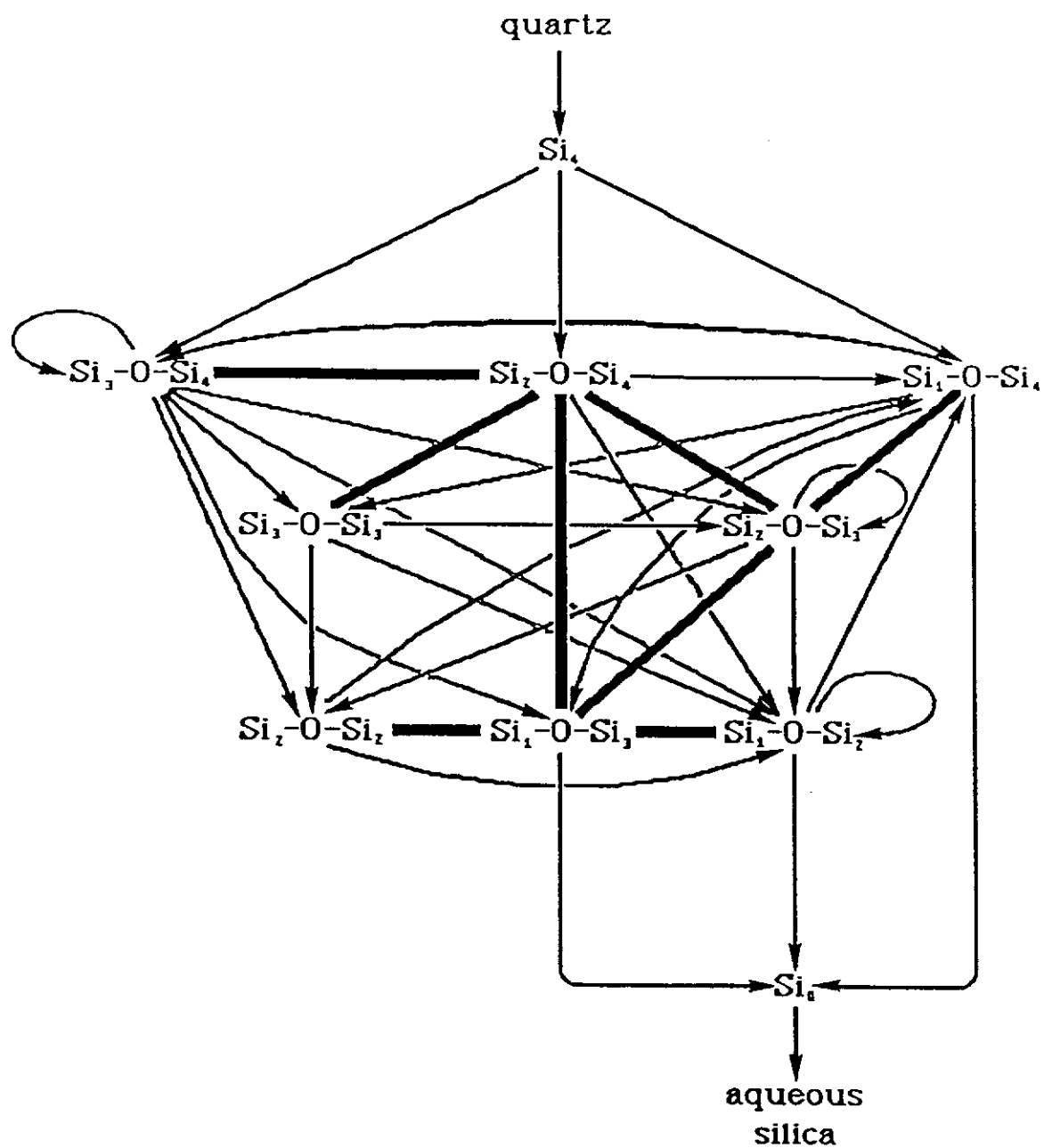
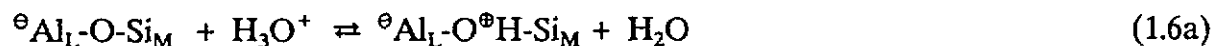


**Figure 1.6** Graph of the quartz dissolution mechanism. Each vertex or corner is a surface species and each directed line represents a reversible elementary reaction. Heavy lines are bi-directional reaction pathways. The arrows on the uni-directional reaction pathways point in the direction of the dissolution reaction.

Etch pits form at defects or dislocations in the crystal lattice where the excess energy of the reactants effectively lowers the activation energy for  $\equiv\text{Si-O-Si}\equiv$  bond hydrolysis. In addition, etch pits increase the number of ledges and hence, the number of  $\text{Si}_2$  and  $\text{Si}_1$  sites in the crystal surface. Examination of reacted mineral grains shows that dissolution occurs mainly at the edges of the grains and at etch pits (Berner and Holdren, 1977, 1979; Lasaga and Blum, 1986; Knauss and Wolery, 1988).

**1.6  $\equiv\text{Al-O-Si}\equiv$  Bond Hydrolysis Mechanism.** In addition to the hydrolysis of Si-O bonds, dissolution of aluminosilicate minerals involves hydrolysis of Al-O bonds. Because aluminum readily substitutes for silicon in aluminosilicate mineral structures, hydrolysis of  $\equiv\text{Al-O-Si}\equiv$  bonds probably follows the general pattern of acid- and base-catalyzed reactions described above for  $\equiv\text{Si-O-Si}\equiv$  bond hydrolysis. However, since the valence of aluminum is three, tetrahedrally coordinated aluminum carries excess electrons. Aluminum can satisfy its valence orbitals and reduce its formal charge by giving up one bond. In the  $\text{S}_{\text{N}}2$  mechanism, one bond is formed as another is broken in a concerted process, but when one bond is broken before the other is formed, the reaction follows an  $\text{S}_{\text{N}}1$  (unimolecular nucleophilic substitution) reaction pathway (Figure 1.5b). The  $\text{S}_{\text{N}}1$  reaction mechanism for hydrolysis of  $\equiv\text{Al-O-Si}\equiv$  bonds is:



Since the combined rates of the  $S_N2$  and  $S_N1$  reactions at the  $\equiv\text{Al-O-Si}\equiv$  sites is greater than the rate of the  $S_N2$  reaction alone, the minimum in the rate versus pH curve is shifted to a higher pH than the  $\text{pH}_{\text{pzc}}$ . The amount of the shift depends upon the relative rates of the  $S_N1$  and  $S_N2$  reactions. For albite, the minimum in the rate versus pH curve is about 4 pH units higher than the  $\text{pH}_{\text{pzc}}$  (Figure 1.7).

Another difference between albite dissolution and quartz dissolution is the apparent reaction order with respect to catalyst activity. As we have seen, the one-half order dependence of the quartz dissolution rate on catalyst activity is easily explained in terms of the stoichiometry of the  $\equiv\text{Si-O-Si}\equiv$  bond hydrolysis mechanism.

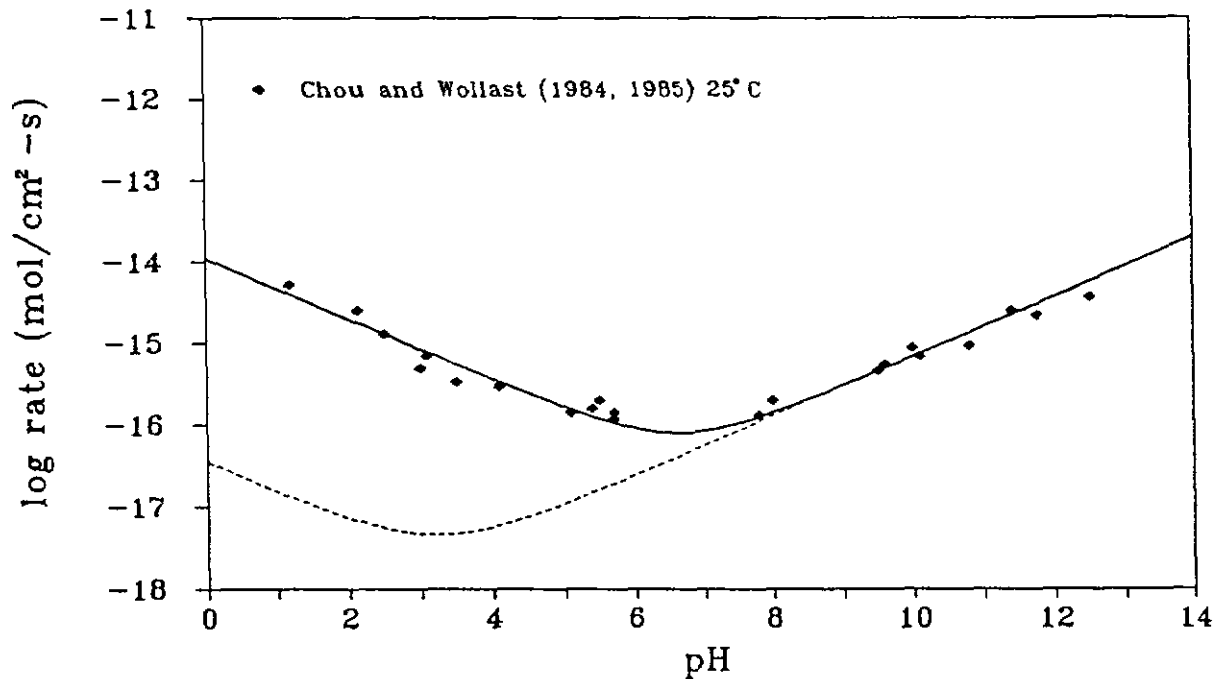


**Figure 1.7** Rates of  $S_N1$  (solid line) and  $S_N2$  (dashed line) reaction pathways for the acid-catalyzed hydrolysis of albite at 25°C. Notice that the  $S_N2$  pathway intersects the base catalyzed reaction at the  $\text{pH}_{\text{pzc}}$  for albite (about pH 3).

Applying this argument to albite dissolution, we would expect that the rate of aluminum release should be first order in catalyst concentration, while the rate of silicon release would be between one-half order (for  $\equiv\text{Si-O-Si}\equiv$  hydrolysis) and first order (for  $\equiv\text{Al-O-Si}\equiv$  hydrolysis) in catalyst activity. Instead, steady-state dissolution of albite approaches congruent dissolution (Chou and Wollast, 1984, 1985; Knauss and Wolery, 1986), and the steady-state dissolution rate is apparently one-third order in catalyst activity (Figure 1.3).

Chou and Wollast (1985) reported that dissolved aluminum retards the rate of albite dissolution. Their graph of the effect of aluminum concentration in solution on the logarithm of the dissolution rate is presented in Figure 1.8. When the steady-state albite dissolution rates are adjusted for the change in rate due to the presence of dissolved aluminum, the slopes of the "adjusted" log rate versus pH curves are one-half - the same as for quartz - as shown in Figure 1.9. The transient albite dissolution rate based on aluminum concentration is higher than the dissolution rate based on silicon release, but as the reaction approaches steady-state, the aluminum release rate approaches that for silicon. This suggests that the rate of hydrolysis of  $\equiv\text{Al-O-Si}\equiv$  is faster than the rate of  $\equiv\text{Si-O-Si}\equiv$  hydrolysis, and that as aluminum is removed from the mineral surface, the hydrolysis of  $\equiv\text{Si-O-Si}\equiv$  becomes rate-limiting.

**1.7 Albite Dissolution Mechanism and Rate Law.** There are fourteen obvious combinations of  $\text{Si}_L\text{-O-Al}_M$  bonds:  $\text{Si}_3\text{-O-Al}_4$ ,  $\text{Si}_2\text{-O-Al}_4$ ,  $\text{Si}_1\text{-O-Al}_4$ ,  $\text{Si}_4\text{-O-Al}_3$ ,  $\text{Si}_3\text{-O-Al}_3$ ,  $\text{Si}_2\text{-O-Al}_3$ ,  $\text{Si}_1\text{-O-Al}_3$ ,  $\text{Si}_4\text{-O-Al}_2$ ,  $\text{Si}_3\text{-O-Al}_2$ ,  $\text{Si}_2\text{-O-Al}_2$ ,  $\text{Si}_1\text{-O-Al}_2$ ,  $\text{Si}_4\text{-O-Al}_1$ ,  $\text{Si}_3\text{-O-Al}_1$ , and

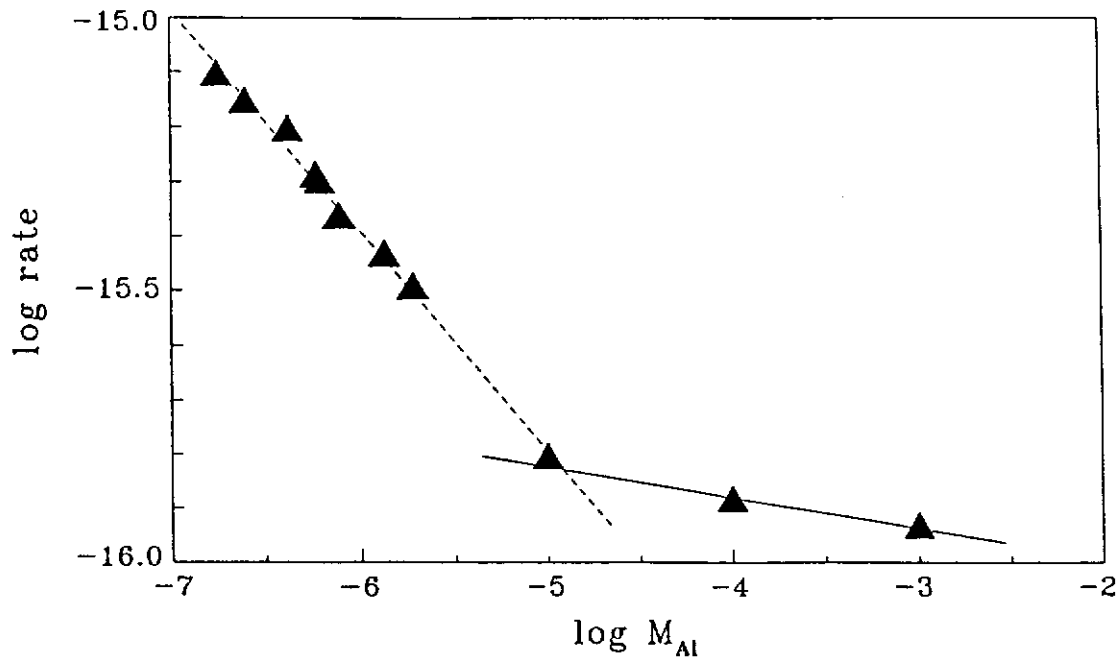


**Figure 1.8** Effect of aluminum concentration in solution on the rate of feldspar dissolution (from Chou and Wollast, 1985).

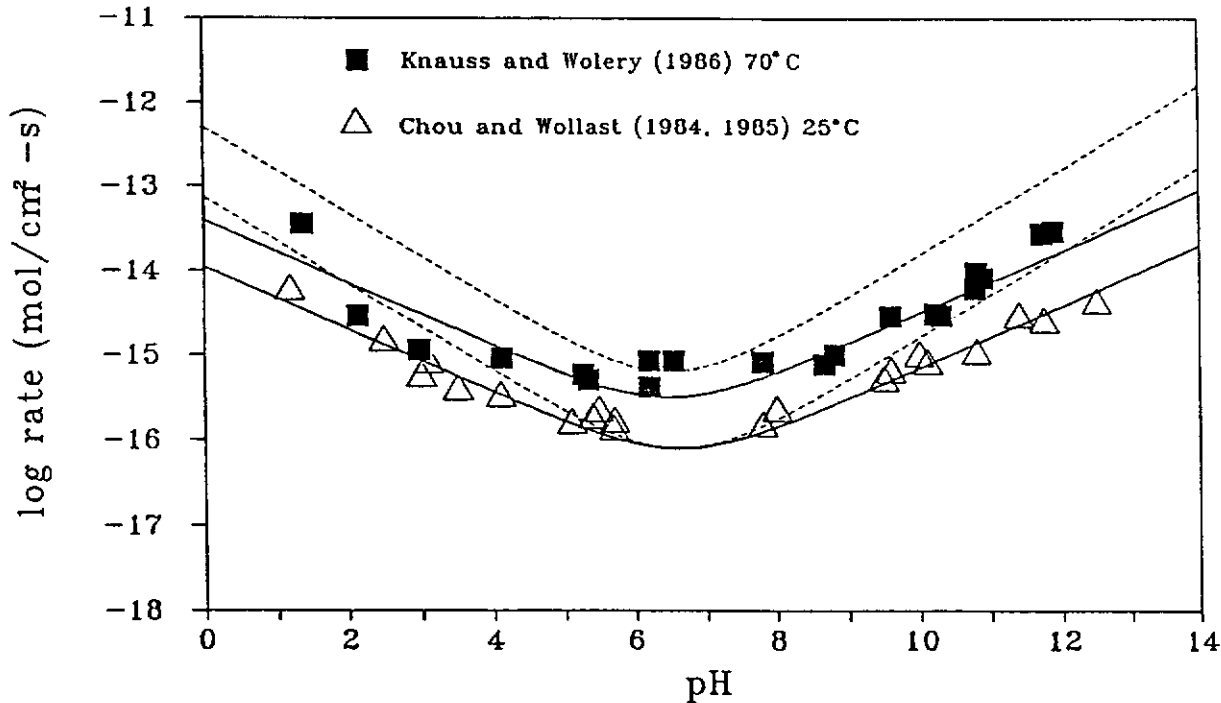


**Figure 1.9** Albite dissolution rates (solid lines) and rates adjusted for the effect of dissolved aluminum (dashed lines). The dashed lines are consistent with reaction orders with respect to catalyst concentration of one-half.

Si<sub>2</sub>-O-Al<sub>1</sub>. New aluminum is exposed to the crystal surface by reaction at Si<sub>3</sub>-O-Al<sub>4</sub>, Si<sub>2</sub>-O-Al<sub>4</sub>, and Si<sub>1</sub>-O-Al<sub>4</sub> sites, and aluminum passes into solution by reaction at Si<sub>4</sub>-O-Al<sub>1</sub>, Si<sub>3</sub>-O-Al<sub>1</sub>, and Si<sub>2</sub>-O-Al<sub>1</sub> sites. The rate,  $\mathfrak{R}_{Al}$ , at which aluminum goes into solution by the acid-catalyzed mechanism is:

$$\begin{aligned} \mathfrak{R}_{Al} = & \kappa_{34} [\text{Si}_3\text{-OH-Al}_4][\text{H}_2\text{O}] + \kappa_{24} [\text{Si}_2\text{-OH-Al}_4][\text{H}_2\text{O}] + \kappa_{14} [\text{Si}_1\text{-OH-Al}_4][\text{H}_2\text{O}] \\ & \text{(rate at which Al reaches the surface by an } S_{N2} \text{ mechanism)} \\ & + \lambda_{34} [\text{Si}_3\text{-OH-Al}_4] + \lambda_{24} [\text{Si}_2\text{-OH-Al}_4] + \lambda_{14} [\text{Si}_1\text{-OH-Al}_4] \\ & \text{(rate at which Al reaches the surface by an } S_{N1} \text{ mechanism)} \end{aligned} \quad (1.8a)$$

$$\begin{aligned} = & \kappa_{41} [\text{Si}_4\text{-OH-Al}_1][\text{H}_2\text{O}] + \kappa_{31} [\text{Si}_3\text{-OH-Al}_1][\text{H}_2\text{O}] + \kappa_{21} [\text{Si}_2\text{-OH-Al}_1][\text{H}_2\text{O}] \\ & \text{(rate at which Al enters the solution by an } S_{N2} \text{ mechanism)} \\ & + \lambda_{41} [\text{Si}_4\text{-OH-Al}_1] + \lambda_{31} [\text{Si}_3\text{-OH-Al}_1] + \lambda_{21} [\text{Si}_2\text{-OH-Al}_1] \\ & \text{(rate at which Al enters the solution by an } S_{N1} \text{ mechanism)} \end{aligned} \quad (1.8b)$$

where  $\kappa_{LM}$  and  $\lambda_{LM}$  are the rate constants for  $S_{N2}$  and  $S_{N1}$  reaction at Si<sub>L</sub>-O-Al<sub>M</sub> sites, respectively.  $\mathfrak{R}_{Al}$  is also equivalent to the steady-state rate of albite dissolution,  $\mathfrak{R}_{ab}$ , because of the stoichiometry of the global reaction (equation (1.3)).

The rate at which aqueous silica appears in solution via an acid-catalyzed reaction is given by:

$$\begin{aligned} \mathfrak{R}_{Si} = & k_{34} [\text{Si}_3\text{-OH}^+\text{-Si}_4][\text{H}_2\text{O}] + k_{24} [\text{Si}_2\text{-OH}^+\text{-Si}_4][\text{H}_2\text{O}] + k_{14} [\text{Si}_1\text{-OH}^+\text{-Si}_4][\text{H}_2\text{O}] \\ & + \kappa_{43} [\text{Si}_4\text{-OH-Al}_3][\text{H}_2\text{O}] + \kappa_{42} [\text{Si}_4\text{-OH-Al}_2][\text{H}_2\text{O}] + \kappa_{41} [\text{Si}_4\text{-OH-Al}_1][\text{H}_2\text{O}] \\ & + \lambda_{43} [\text{Si}_4\text{-OH-Al}_3] + \lambda_{42} [\text{Si}_4\text{-OH-Al}_2] + \lambda_{41} [\text{Si}_4\text{-OH-Al}_1] \end{aligned} \quad (1.9a)$$

$$\begin{aligned}
&= k_{14} [\text{Si}_1\text{-OH}^+\text{-Si}_4][\text{H}_2\text{O}] + k_{13} [\text{Si}_1\text{-OH}^+\text{-Si}_3][\text{H}_2\text{O}] + k_{12} [\text{Si}_1\text{-OH}^+\text{-Si}_2][\text{H}_2\text{O}] \\
&\quad + \kappa_{14} [\text{Si}_1\text{-OH-Al}_4][\text{H}_2\text{O}] + \kappa_{13} [\text{Si}_1\text{-OH-Al}_3][\text{H}_2\text{O}] + \kappa_{12} [\text{Si}_1\text{-OH-Al}_2][\text{H}_2\text{O}] \\
&\quad + \lambda_{14} [\text{Si}_1\text{-OH-Al}_4] + \lambda_{13} [\text{Si}_1\text{-OH-Al}_3] + \lambda_{12} [\text{Si}_1\text{-OH-Al}_2] \qquad (1.9b)
\end{aligned}$$

$$= 3 \mathfrak{R}_{ab}$$

If the  $S_{N1}$  rates are much faster than the  $S_{N2}$  rates, the rate terms containing  $\kappa_{ij}$  will be negligible compared to the terms with  $\lambda_{ij}$ , so effectively, there are three pathways by which aluminum reaches the crystal surface, and six pathways for silicon. The rates of these elementary reactions depend upon concentrations of surface species and on the kinetic parameters for each reaction. Clearly, much more information is needed about the species on a feldspar surface in order to verify this hypothesis and actually estimate rates.

**1.8 Calculation of Kinetic Parameters.** From the rate data presented in Figures 1.2 and 1.3, we might have expected that there is sufficient rate data to calculate kinetic parameters - activation energies and pre-exponential factors - for quartz and albite dissolution. In fact, kinetic parameters have been calculated for quartz and albite dissolution based on bulk dissolution rates (Table 1.1). But the link between transition-state theory rate expressions and Arrhenius rate expressions (Glasstone, et al, 1941; Benson, 1976) places a restriction on the Arrhenius rate constant - viz. that it applies to an elementary reaction. By accepting a transition-state theory description of reaction rates in condensed phase reactions, we also accept the basic underlying assumptions of

the more restrictive theory. Therefore, the kinetic parameters reported in Table 1.1 are apparent rather than true activation energies and pre-exponential factors.

To calculate true kinetic parameters, the bulk dissolution rate data must first be converted to the appropriate basis. For example, the apparent one-half order dependence of the quartz dissolution rate on catalyst activity is an artifact of expressing the dissolution rate in terms of the rate of appearance of aqueous silica. According to the stoichiometry of the elementary reactions in the  $\equiv\text{Si-O-Si}\equiv$  catalyzed hydrolysis mechanism, the dissolution rate is first order in catalyst activity and two product molecules are formed per hydrolyzed bond. In other words, the basis for the bulk rate of quartz dissolution is the number of moles of silica appearing in solution per second per  $\text{cm}^2$ , but the basis for the elementary reaction is the number of moles of  $\equiv\text{Si-O-Si}\equiv$  bonds broken per second.

**Table 1.1** Activation energies and pre-exponential factors reported for quartz and feldspar dissolution.

	$E_{\text{act}}$ (kJ/mole-K)	$\log_{10}A$
<u>Quartz</u>		
Rimstidt and Barnes (1980)	67.4 - 76.6	not reported
Robinson (1982)	78.3	0.433
Knauss and Wolery (1988)	108.4	-1.3
Bird, et al. (1986)	51 - 55	not reported
<u>Albite</u>		
Helgeson, et al (1984)	90	-1



When a single pathway limits the reaction rate of a complex reaction network, the bulk rate depends upon the rate of the rate-limiting step. We have just found that the rate laws for both quartz and albite dissolution involve multiple independent reaction pathways operating in parallel. If the contributions of these individual reaction pathways to the bulk rate cannot be distinguished, we cannot calculate meaningful activation energies from the bulk rate data. The relative contribution of each reaction to the bulk rate depends upon the magnitudes of the rate constants and on the surface concentrations of the key reactive species. A global treatment masks the contributions of individual elementary reactions. We could calculate a global activation energy from the bulk quartz dissolution rate data based only on the experimental data presented in Figure 1.2, but as long as the bulk rate has significant, and possibly different, contributions from two or three reaction pathways, we can have no confidence that this calculated activation energy relates to any process on a molecular level.

Within a series of experiments, the sample preparation is probably uniform so that a consistent pattern emerges on a graph of log rate versus pH, but it is likely that samples prepared by different investigators using the same sample preparation techniques have different ratios of  $\text{Si}_3$  to  $\text{Si}_2$  sites in the surface. *Even if the surface compositions were known to be the same in experiments conducted at different temperatures, the calculated activation energy would still not be related to a single elementary reaction but would represent an unknown average for two or more elementary reactions.*

The variation in the activation energies calculated by various researchers for quartz and albite dissolution underlines the importance of surface characterization techniques. Estimates of the activation energy for quartz dissolution ranges from 67 to 110 kJ/mol (Table 1.1), and for albite, Helgeson calculated an activation energy of 83 kJ/mol. But the feldspar involves breaking at least three times as many Si-O or Al-O bonds per mole as are required for quartz. The most reasonable explanation is that the reported rates of dissolution depend upon the relative concentrations of different types of surface sites, and that for both quartz and feldspar dissolution experiments, these concentrations are unknown.

**1.9 Quartz Dissolution Rate Experiments.** A thorough test of the  $\equiv\text{Si-O-Si}\equiv$  bond hydrolysis mechanism and rate laws presented in this thesis requires a considerable body of information and many experiments. However, some aspects of the mechanism and the corresponding rate law can be partially tested by a relatively simple series of experiments. Except for the data of Kamiya, et al. (1974), there is no evidence that the rate of dissolution depends upon the pH below the  $\text{pH}_{\text{pzc}}$ . The mechanism predicts that the rate of quartz dissolution depends upon the pH at pH values less than about 3 and that the reaction is one-half order with respect to  $[\text{H}^+]$ .

To test this pH dependence, quartz dissolution experiments were carried out at room temperature (25°C) in a packed bed reactor using a natural quartz sand. These experiments were primarily designed to obtain the quartz dissolution rate data at low pH. One consequence of the experiment design was that the dissolution rate

experiments could also be used to test an alternative reactor geometry and sample preparation technique.

For this study, a well-sorted quartz sand, Ottawa sand in the 20 to 28 mesh (0.841 to 0.595 mm opening) size range, was tumbled with 500 mesh silicon carbide grit for two weeks in deionized water to remove the deeply etched surface of the as-received material. After the tumbling, the silicon carbide and quartz were separated and the quartz was fluidized with demineralized water until the effluent was clear of fine particles. Surface areas of the treated (unreacted) and the reacted quartz were determined by three-point BET gas adsorption with a Quantasorb instrument using nitrogen in a helium carrier. The treated material had a surface area of 766 cm<sup>2</sup>/g, and the material that had been reacted had a surface area of 903 cm<sup>2</sup>/g.

The calculated initial rates of quartz dissolution from these experiments are compared with published quartz dissolution rates in Figure 1.10. The rate data from these experiments follow the same pattern of acid- and base-catalyzed reactions as the other quartz dissolution rate data. However, the new rates are consistently about two orders of magnitude faster than expected based on the published quartz dissolution rates at 25°C. Careful examination of the mineral surface by SEM shows that the tumbling did not completely remove the etched surface of the sand, so that the sand surface had many more imperfections than the surfaces of crushed quartz crystals used in other dissolution experiments (Figure 1.11).

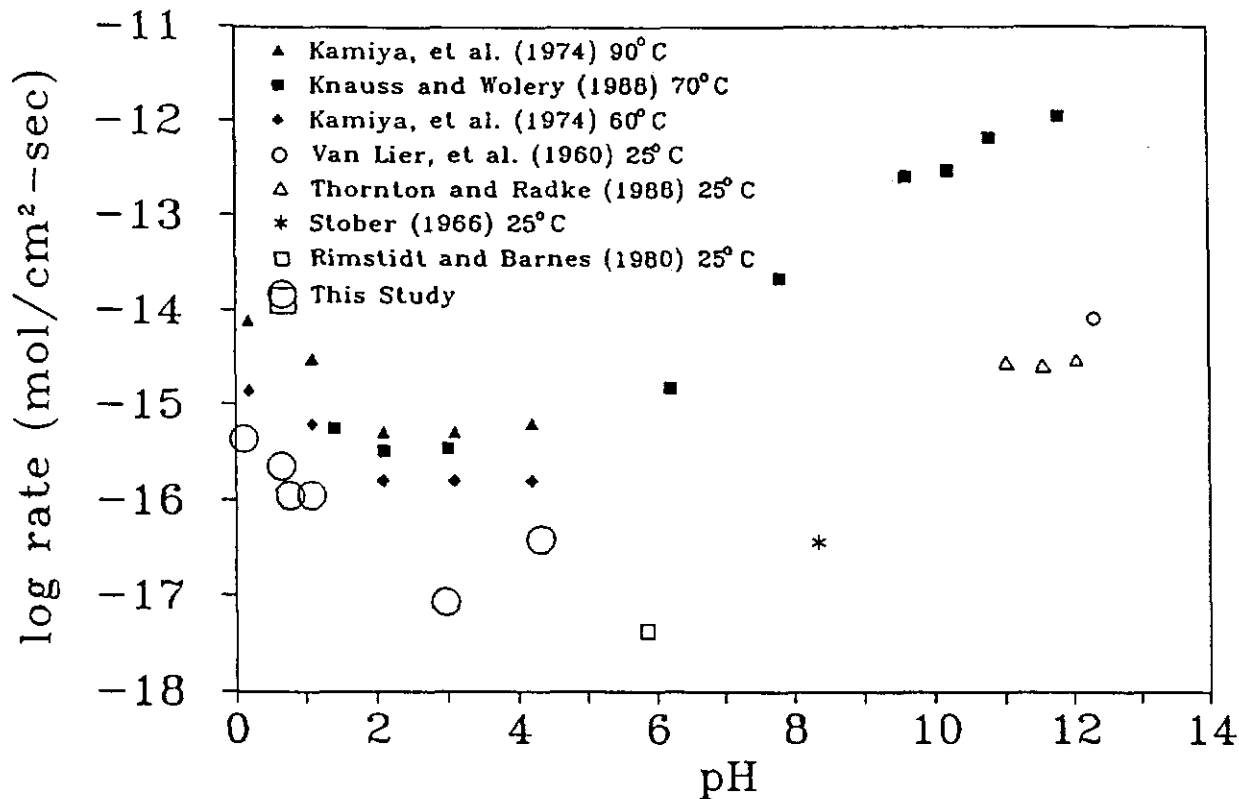


**Figure 1.10** Comparison of the experimentally determined quartz dissolution rates (this study) with published quartz dissolution rates.

Although the quartz dissolution rates are higher than expected, these experiments are an important confirmation of several aspects of the proposed reaction mechanism. First, the rate of quartz dissolution was shown to depend upon the solution pH at low pH. Next, the dissolution rate data are consistent with the expected one-half order with respect to pH, and the minimum in the rate appears to be at about a pH of 3 - close to the  $pH_{pzc}$ . Had crushed quartz been used in these experiments rather than Ottawa sand, the results would probably have been sufficiently consistent with the existing 25°C data that the questions about calculating activation energies from the bulk rate data would not have arisen.



100 $\mu$



10 $\mu$

**Figure 1.11** SEM photographs of the surfaces of (a) tumbled quartz (Ottawa) sand and (b) crushed quartz (from Knauss and Wolcny, 1988). Notice the smooth surface and sharp edges on the crushed quartz compared to the relatively rough surface of the tumbled quartz. The sand grain also shows a smooth fracture surface (arrow) similar to the smooth fractured surface of the crushed quartz.

**1.10 Conclusions and Recommendations.** The basic approach to dissolution kinetics presented in this thesis - developing a comprehensive set of elementary reactions, reducing this set to a few key reactions and relating the observed dissolution rate to the rates of the key elementary reactions - provides a method and a conceptual framework for future studies of mineral dissolution rates. The most important conclusions of this thesis are as follows:

- Quartz and albite dissolution proceed via acid- and base-catalyzed hydrolysis of  $\equiv\text{Si-O-Si}\equiv$  and/or  $\equiv\text{Si-O-Al}\equiv$  bonds.
- Acid- and base-catalyzed hydrolysis of  $\equiv\text{Si-O-Si}\equiv$  bonds follows an  $S_N2$  reaction pathway. The acid-catalyzed hydrolysis of  $\equiv\text{Al-O-Si}\equiv$  bonds can follow either an  $S_N1$  or an  $S_N2$  reaction pathway.
- The fractional order in catalyst activity of the quartz and albite dissolution rates results from the stoichiometry of the rate-limiting steps.
- Aqueous aluminum retards the rate of reaction to give an apparent reaction order with respect to catalyst concentration that is less than one-half order. Presumably, other multi-valent cations also retard the dissolution rate.
- The minimum rate occurs at the pH where the predominant mechanism changes from acid-catalyzed to base-catalyzed. When the acid-catalyzed mechanism follows an  $S_N2$  reaction pathway, this pH is the  $\text{pH}_{\text{pzc}}$ . When the acid-catalyzed mechanism follows an  $S_N1$  reaction pathway, the minimum rate occurs at a pH that is higher than the  $\text{pH}_{\text{pzc}}$ .
- The bulk rate of dissolution includes contributions from multiple, independent, parallel reaction pathways, and the relative rates of reaction for these pathways depends upon the surface morphology of the mineral sample.
- Rate laws based on simplified versions of the comprehensive mechanisms for reaction at  $\equiv\text{Si-O-Si}\equiv$  and  $\equiv\text{Si-O-Al}\equiv$  sites relate the observed bulk dissolution rates to the rates of elementary reactions.
- Calculation of kinetic parameters from the bulk dissolution rate data requires knowledge of the individual contributions of these various pathways be known. Both the rate constants and the concentrations of surface species must be known.
- Many of the elementary reaction steps are common to the reaction mechanisms for both quartz and albite and might be expected in the mechanisms of other aluminosilicate minerals.

A number of experiments are suggested by these results. The most important experiments involve measuring the concentrations of the key surface species and the rate constants associated with reaction at these sites. The rate of reaction at  $\text{Si}_3\text{-O-Si}_4$  sites could be measured using samples having extremely smooth surfaces and no defects. Polished slabs, cylinders or spheres of synthetic quartz crystals could be used for these experiments. The tumbled samples described in Chapter 6 were intended to approach polished spheres, and with more careful preparation, tumbled sand might be an appropriate starting material for mineral dissolution experiments.

All sample preparation techniques need to be examined carefully and techniques for analyzing mineral surfaces need to be developed. Some sample preparation techniques, for example acid washes, are useful in removing ultrafine particles from crushed samples, but strong acids can also nucleate etch pits when defects are present.

In addition to dissolution rate experiments, information is needed about the  $\text{pH}_{\text{pzc}}$  as a function of temperature for many minerals. This information along with dissolution rate data could be used to test the hypothesis that  $\text{S}_{\text{N}1}$  and  $\text{S}_{\text{N}2}$  reaction mechanisms operate simultaneously when aluminum is tetrahedrally coordinated in the crystal structure. If the minimum rate of dissolution of a mineral occurs at a pH higher than the  $\text{pH}_{\text{pzc}}$ , we can calculate an entropy difference corresponding to the difference between the  $\text{S}_{\text{N}1}$  and the  $\text{S}_{\text{N}2}$  mechanisms, and if this entropy difference is the same for a number of minerals, we could then predict the dissolution rate behavior for a mineral from knowledge of the  $\text{pH}_{\text{pzc}}$ . We also need to measure the effect of aluminum and

other aqueous ion concentrations on the rate of dissolution of quartz and other minerals.

The mechanisms and rate laws presented in this thesis for quartz and albite dissolution should apply with only slight modifications to other aluminosilicate minerals that contain aluminum in tetrahedral coordination in the crystal structure - other feldspars, feldspathoids, and zeolites. Other mineral groups - pyroxenes, amphiboles, clays, micas, garnets, etc. - contain aluminum, magnesium, and iron in octahedral coordination. The effect of octahedral aluminum, magnesium and iron in the crystal structure on the rate of dissolution is unknown.

The ideas presented in this thesis provide much of the necessary theoretical basis for further developments of geochemical kinetics. The major contributions are (1) the recognition that the dissolution of quartz and albite proceeds via catalyzed hydrolysis of  $\equiv\text{Si-O-Si}\equiv$  and/or  $\equiv\text{Si-O-Al}\equiv$  bonds, (2) a comprehensive reaction mechanism for catalyzed bond hydrolysis, (3) a simplified mechanism and rate law that relates the observed bulk dissolution rates to the rates of elementary reactions, and (4) the recognition that activation energies cannot be calculated without knowing the relative rates of the various parallel pathways.



## Chapter 2

### Geochemical Kinetics - A Review of the State-of-the-Art

**2.1 Introduction and Background.** Chemical reactions between rocks and water are generally complex in the sense that several solid phases and multiple reactions are coupled or in competition for reactants which are transported through a common liquid phase. The state of a complex reaction system - which phases are present and the amounts and compositions of those phases - is determined by the path of the reaction and the rate of progress along the reaction path rather than solely from thermodynamic equilibrium considerations. However, many previous attempts to model rates of rock-water reactions have largely assumed near-equilibrium conditions for most of the possible reactions in a system (Helgeson, 1968; Helgeson, et al., 1970; Helgeson, 1971; Helgeson and Murphy, 1983; Helgeson, et al., 1984).

For example, consider Helgeson and Murphy's (1983) description of the reaction path for microcline,  $\text{KAlSi}_3\text{O}_8$ , dissolution in a closed system. Figure 2.1 (modified after Helgeson and Murphy, 1983) is an activity diagram for the system  $\text{K}_2\text{O}-\text{Al}_2\text{O}_3-\text{SiO}_2-\text{H}_2\text{O}-\text{HCl}$  at  $25^\circ\text{C}$ , 1 bar and unit activity for  $\text{H}_2\text{O}$ . The various fields in Figure 2.1 are the regions of stability of mineral phases within the system which are in equilibrium with the solution, and the dashed line shows the calculated reaction path. Early in the reaction, microcline dissolves congruently by:



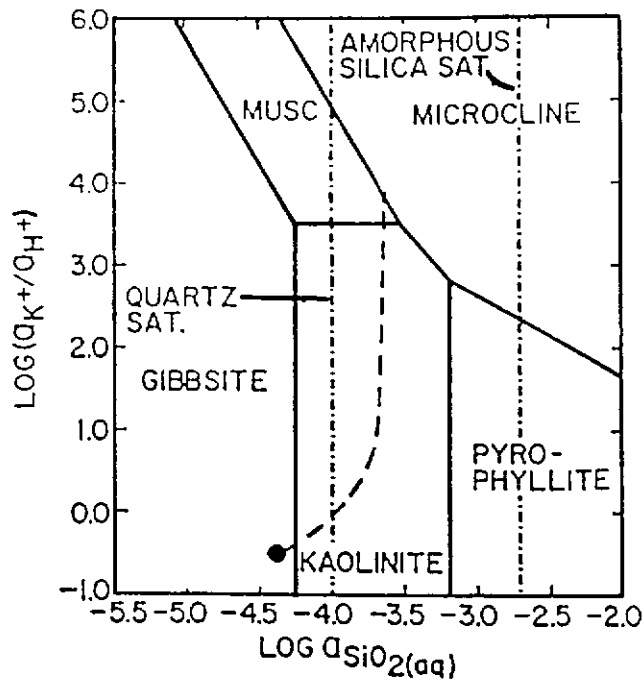
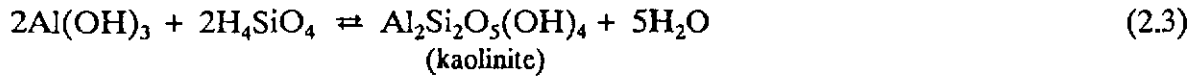


**Figure 2.1** Activity diagram for the system  $K_2O-Al_2O_3-SiO_2-H_2O-HCl$  at  $25^\circ C$ , 1 bar and unit activity for  $H_2O$  (modified after Helgeson and Murphy, 1983). Helgeson and Murphy's (1983) calculated reaction path for microcline dissolution is shown as the dashed line. The solid lines are the boundaries of the mineral stability fields in equilibrium with the solution.

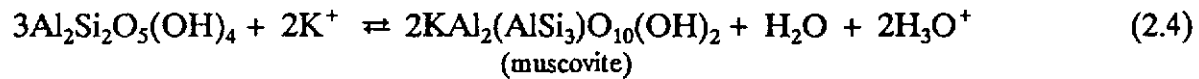
At some later time, gibbsite,  $Al(OH)_3$ , saturates and precipitates:



Helgeson and Murphy (1983) assume that gibbsite precipitation is very rapid so that the aqueous solution is near equilibrium with solid gibbsite. As the reaction proceeds, microcline continues to dissolve while gibbsite precipitates and aqueous silica,  $H_4SiO_4$ , builds up in solution. The next phase to saturate is kaolinite,  $Al_2Si_2O_5(OH)_4$ , which precipitates at the expense of the gibbsite and aqueous silica:



Once again, the reaction is assumed to be near equilibrium. As shown in Figure 2.1, the solution becomes saturated with respect to quartz,  $\text{SiO}_2$ , but Helgeson and Murphy do not allow quartz precipitation. Presumably, this is because precipitation of quartz at low temperatures is superseded by precipitation of amorphous silica which has the higher solubility. In any case, the solution remains supersaturated with respect to quartz. Muscovite,  $\text{KAl}_2(\text{AlSi}_3)\text{O}_{10}(\text{OH})_2$ , precipitates at the expense of kaolinite at high pH by:



which is, once again assumed to be a near equilibrium process. Finally, after all these reaction steps reach equilibrium, microcline reaches saturation with respect to the aqueous solution.

This discussion of microcline dissolution is typical of systems where most of the possible reactions are constrained to be always near equilibrium. Here, a maximum of three solid phases can coexist at any time: microcline which is dissolving and whatever phase or phases are thermodynamically stable with respect to the solution composition. For example, Helgeson and Murphy (1983) allow gibbsite and kaolinite to coexist only at the equilibrium boundary between the two mineral stability fields - for the solution to enter the kaolinite stability field, gibbsite must vanish.

But it is the kinetics rather than the thermodynamics that determines whether or not a saturated phase will precipitate. This point is tacitly recognized by Helgeson and Murphy (1983) in that quartz is allowed to saturate without precipitating. When the near-equilibrium assumptions are abandoned - if, for example, the rate of precipitation of gibbsite is very much higher than the rate of precipitation of kaolinite - gibbsite will continue to form even when kaolinite is thermodynamically the more stable phase. To accurately model the temporal behavior of a multi-phase reaction system, the near-equilibrium assumption must be considerably modified.

In many natural geological systems, it is not possible to estimate the time scale needed for reaction - time scales for weathering of minerals cited by Colman and Dethier (1986) range from  $10^{-3}$  to  $10^7$  years - but the presence of a near-equilibrium mineral assemblage suggests that the reaction time scale in natural systems is short compared to the time scale of fluid circulation. Fluid circulation times in natural hydrothermal systems can be of the order of hundreds to thousands of years (Pearson and Truesdell, 1978; Vuataz and Goff, 1986; Goff, et al., 1987). However, under the conditions encountered or expected in engineered systems such as man-made geothermal reservoirs or nuclear waste repositories, fluid residence times may be considerably shorter - on the order of hours to days - than rock-water reaction times (Grigsby, et al., 1989; Grigsby and Tester, 1989). In some applications, it may be crucial to accurately predict the rates of rock-aqueous fluid interactions for extremely long times (Brookins, 1984). For these systems, the assumption that most reactions are near equilibrium places artificial constraints on a reacting system model by reducing the

set of highly coupled reactions to a few more or less independent reactions. Furthermore, rate constants used in geochemical kinetic models are generally extracted from experiments which are inappropriately designed for determination of the fundamental kinetic parameters.

The importance of understanding rates of chemical reactions in geologic systems is growing. In addition to the general scientific interest in fundamental rock-water reaction kinetics, there are a number of practical applications where modeling coupled heat transfer, fluid flow, chemical reactions, and changes in rock mechanical properties is essential. Probably the most important and immediate applications of geochemical kinetics involve the geologic storage of nuclear waste (Brookins, 1984). Heating of a repository by radioactive decay of the waste, changes in the water table, failure of canisters, and unexpected tectonic events (such as earthquakes and volcanic eruptions) could release radionuclides into groundwater. Retardation of radioactive species transport by absorption or precipitation, alteration of the host rock mineralogy, and changes in permeability of the rock due to mineral dissolution and precipitation all involve chemical reaction rates. Thus, knowledge of the rates and mechanisms of rock-water reactions is critical in designing and evaluating a potential repository. Similar direct applications of this research can be found in a number of related fields involving the environment (chemical waste migration, leaching of mine tailings, effects of acid rain), energy production (performance of man-made geothermal reservoirs, reinjection of flashed geothermal brines, in-situ coal gasification, in-situ oil shale retorting, acid stimulation of oil wells), mineral recovery (solution mining, ore leaching),

and geology and geochemistry (ore deposition, hydrothermal alteration, chemical weathering).

Rock- and mineral-water reactions have been studied for well over one hundred years, but within the past twenty years there has been renewed interest in determining mineral solubility and reaction kinetics under a wide variety of reaction conditions. Much of the early work focused on determining the stability fields of minerals which crystallize from igneous melts as a function of the water content of the melt (Stern and Wyllie, 1981). Other studies examined alteration reactions which accompany metamorphism and/or weathering of rocks (Moody, 1979; Garrels and Christ, 1965). However, with the advent of rapid and sensitive analytical chemical methods, increasing emphasis has been placed on studying the aqueous phase in addition to the solid phases. This shift in emphasis has been driven by developments in such diverse fields as geothermal energy exploration and development (Fournier and Rowe, 1966; Henley, et al., 1984), studies of hydrothermal ore deposits (Barnes, 1967), and environmental protection.

The increased interest in rates of mineral-water reactions has not, in general, been accompanied by adequate understanding of chemical kinetics. Only within the past five years has the geochemical community abandoned the "parabolic", "linear" and "logarithmic" rate laws (see section 2.3) in favor of transition-state theory. Unfortunately, transition-state theory is being adopted without certain essential concepts. In particular, the concept of an elementary reaction (as opposed to an

overall reaction) is absent in several recent papers which employ transition-state theory (see, for example Rimstidt and Barnes, 1980; Aagaard and Helgeson, 1982). It is not unusual to find researchers describing an "activated complex" which is based on the stoichiometry of an overall rather than an elementary reaction. These points are illustrated by the discussions in this chapter.

**2.2 Experimental Methodology.** A major factor in the results obtained from experimental kinetic studies involves the particular experimental techniques used in the experiments. Typical experimental conditions in studies of quartz and feldspar dissolution are presented in Table 2.1.

To accelerate reaction rates, mineral or rock samples are usually crushed or ground to very fine particle sizes. Most researchers report specific surface areas measured by BET adsorption ( $N_2$  or Ar) even though it is generally recognized that BET areas overestimate the reactive surface area (Helgeson, et al., 1984). Many wash the samples with water, acetone or acid mixtures to remove ultrafine particles and surface damage caused by the grinding process. Holdren and Speyer (1985a, 1987) studied feldspar dissolution rates as a function of particle size and found that rates do not necessarily increase with decreasing particle diameter in the particle size range from 300 to 40  $\mu m$  (50 to 400 mesh). They suggest that dissolution occurs primarily at dislocations or defects in the crystal structure and that the dissolution rate depends more on defect density than on exposed surface area.

**Table 2.1 Typical experimental conditions for mineral dissolution studies reported by various investigators.**

Researcher	Mineral <sup>a</sup>	Particle Size Range ( $\mu\text{m}$ ) <sup>b</sup>	Solution or Reactor Volume (ml)	Solid Mass (g)	Specific Surface Area (BET) ( $\text{m}^2/\text{g}$ )	Reactor Type <sup>c</sup>
Wollast (1967)	feldspar	?	?	?	?	Semi-Batch
Busenberg and Clemency (1976)	feldspar	<37	1000	50	0.8-1.8	Semi-Batch
Lagache (1976)	Or <sub>39</sub> Ab <sub>43</sub>	?	30	0.1-0.8	0.03-0.25	Batch
Petrovic, et al. (1976)	Or <sub>86</sub> Ab <sub>14</sub>	100-600	10	0.1	?	Batch
Chou and Wollast (1984, 1985)	Ab <sub>100</sub>	50-200	29	3	0.046	Fluidized Bed
Holdren and Speyer (1985a)	Or <sub>87</sub> Ab <sub>13</sub>	<30-600	475	4.75	0.034-1.34	Semi-Batch
Holdren and Speyer (1985b)	Or <sub>20</sub> Ab <sub>80</sub>	<38-600	50	3	0.053-0.072	CSTR
Knauss and Wolery (1986)	Ab <sub>100</sub>	75-125	2.2 <sup>d</sup>	1	0.077-0.092	DPB
Kamiya, et al. (1974)	quartz	150-200	300	1	?	Semi-Batch
Rimstidt and Barnes (1982)	quartz	100-1000	?	?	0.92	Semi-Batch
Knauss and Wolery (1988)	quartz	75-125	2.2 <sup>d</sup>	1	0.046	DPB
Thornton and Radke (1988)	quartz	?	?	?	?	Semi-Batch

<sup>a</sup>Or - orthoclase (KAlSi<sub>3</sub>O<sub>8</sub>), Ab - albite (NaAlSi<sub>3</sub>O<sub>8</sub>)

<sup>b</sup>? - not reported

<sup>c</sup>CSTR - continuously stirred tank reactor  
DPB - differential packed bed reactor

<sup>d</sup>K. Knauss, personal communication, 1988



Most of the experiments were conducted in batch or semi-batch reactors. While these reactors are relatively simple to operate, they have several distinct disadvantages. First, since the concentrations of the components in solution are constantly increasing during the course of an experiment, it is possible for secondary minerals to saturate and precipitate from solution. It is also likely that the buildup of reaction products could slow the reaction rate (ie. as the solution approaches equilibrium with the dissolving mineral). Batch reactors must be quenched and dismantled to remove samples, so several experiments have to be run to get enough data points for plotting concentration versus time. Semi-batch reactors are an improvement over batch reactors since samples of the solution can be periodically withdrawn for analysis, however, the results must then be corrected for changing volume during the experiment.

Several researchers (Chou and Wollast, 1984, 1985; Holdren and Speyer, 1985b, 1986; Knauss and Wolery, 1986, 1988) used flow-through reactors rather than batch reactors because of the relative ease of controlling or changing fluid composition during an experiment. In particular, the use of flow-through reactors allows the fluid composition to be maintained at conditions which prevent the precipitation of secondary phases. All of the groups mentioned above assumed that the reactors performed as perfectly-mixed batch or continuously-stirred tank reactors (CSTR's), but none of the investigators actually demonstrated that this assumption was valid.

The idealized perfectly-mixed reactor is called a CSTR (continuously-stirred tank reactor). For a CSTR, there is no accumulation of material in the reactor so the

effluent composition is necessarily equal to the average composition of the fluid within the vessel (Levenspiel, 1962; Carberry, 1976). This leads to a very simple reactor performance equation for the rate of reaction:

$$\mathfrak{R} = k_{\text{eff}} C_{\text{out}} = \dot{q} (C_{\text{out}} - C_{\text{in}}) \quad (2.5)$$

where  $\mathfrak{R}$  is the bulk rate of the reaction,  $k_{\text{eff}}$  is the apparent first-order rate constant,  $\dot{q}$  is the volumetric flow rate through the reactor and  $C_{\text{out}}$  and  $C_{\text{in}}$  are the concentration of any species in the output and input streams to the reactor. Thus, the reaction rate can be easily determined from the parameters on the right-hand side of equation (2.5).

Chou and Wollast's (1984, 1985) experiments were conducted in a fluidized bed reactor (Figure 2.2) which was typically loaded with about 3 grams of crushed material and 20 to 30 ml of fluid (see Chou and Wollast, 1984, 1985 for the details of their experiments). Two size fractions (100 to 200 mesh and 50 to 100 mesh) were used, and the starting material was washed to remove fine particles which are generated during crushing. Input flow rates were 0.15 or 0.23 ml/min. To maintain sufficient fluid velocity to fluidize the particles, most of the effluent from the reactor was recycled to the reactor inlet. The recycle ratio - the ratio of the recycle flow rate to the inlet (or outlet) flow rate - was of the order of 17 to 30 (recycle rates of 2.5 to 6.8 ml/min). This value of the recycle ratio is high enough for the reactor to behave as an ideal CSTR (Carberry, 1976), so the perfectly-mixed assumption is appropriate.

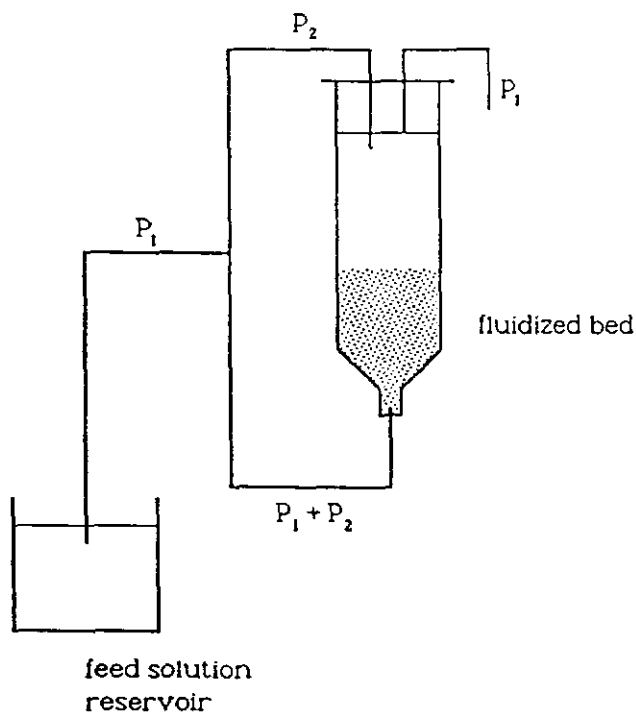


**Figure 2.2** Schematic fluidized bed reactor used by Chou and Wollast (1984, 1985) in their studies of feldspar dissolution.

Another reaction vessel which approaches the perfectly-mixed condition is Holdren and Speyer's (1985b, 1986) stirred flow-cell reactor (Figure 2.3). The cell is initially charged with 3 grams of crushed and washed material of various size fractions along with 50 ml of solution, and the solution flow rate is maintained at approximately 0.025 ml/min (1.5 ml/hr). The interior of the cell is stirred by a magnetic stirring bar which is suspended in the solution. Holdren and Speyer (1986) report that finer size fractions were kept suspended by the stirring, and that the coarser fractions formed a conical pile below the stirring bar. The mean residence time of the reactor is 33 hours. Given the high stirring rate and the long residence time, this vessel clearly approaches CSTR behavior.

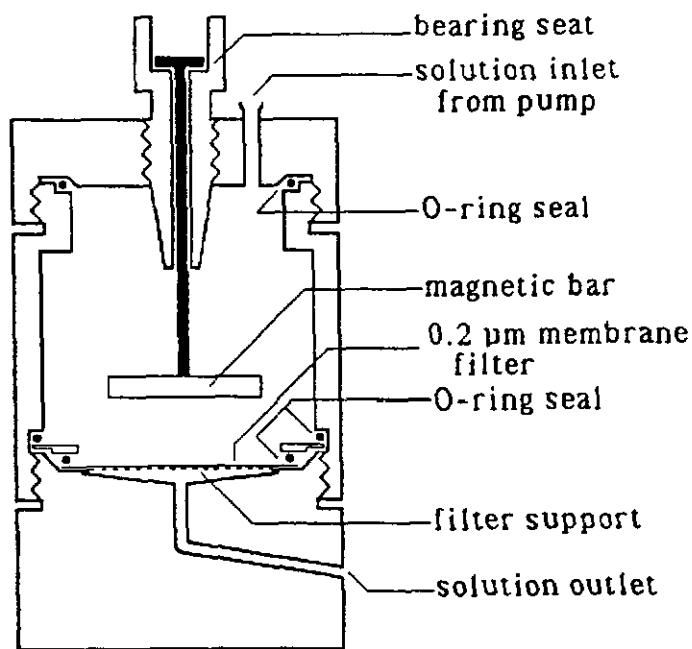


**Figure 2.3** Schematic stirred flow cell reactor used by Holdren and Speyer (1985b, 1986) in their studies of feldspar dissolution.

Knauss and Wolery (1986, 1988) conducted experiments in a single-pass flow reactor containing 1 gram of crushed (120 to 200 mesh) material which had been washed with isopropanol to remove fine particles (Figure 2.4). They report a bed depth of about 0.1 cm and volumetric and (superficial) linear flow rates of 35 cm<sup>3</sup>/day and 7 cm/day, respectively. K. Knauss, (personal communication, 1988) reports reactor internal dimensions of 2.0 cm internal diameter by 0.7 cm high. He also corrects the linear flow rate based on the open reactor internal diameter to 11 cm/day rather than the reported 7 cm/day.

From the information presented by Knauss and Wolery (1986, 1988), it is not possible to demonstrate that the perfectly-mixed assumption holds. The ratio of bed

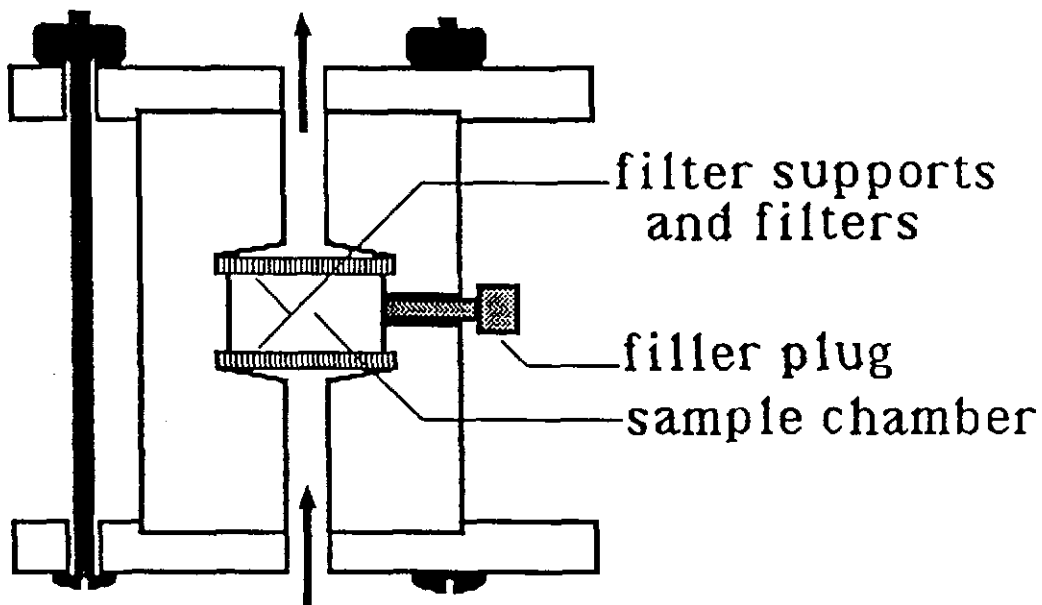


**Figure 2.4** Schematic differential packed bed reactor used by Knauss and Wolery (1986, 1988) in studies of quartz and feldspar dissolution.

length to bed diameter ( $L/d$ ) for this reactor is very small (0.039), so this reactor looks similar to a differential slice through a packed bed reactor. Ideally, such a differential slice can be treated as a CSTR (Carberry, 1976). However, uneven distribution of the mineral across the bed - particularly near the walls of the reactor - or the presence of a single large particle within the bed could lead to preferential flow through one portion of the bed. Some fraction of the fluid would manage to pass through the bed without contacting the mineral while the remainder of the fluid would experience a longer contact time. On average, the fluid would have the same mean residence time as the ideal case, but the mean contact time would be different. To reduce the potential for channeling, typical packed bed designs use  $L/d$  ratios of at least 5 and preferably above 10. To test for channeling through the bed, K. Knauss (personal

communication, 1988) conducted experiments at several different flow rates. Presumably flow distribution through the thin bed does not pose a problem since the results of these experiments were essentially identical. However, channeling would occur over a range of flow rates, so these experiments do not preclude the possibility of uneven flow distribution within the differential packed bed.

In all of the reaction vessels discussed above, the ratio of solid mass to fluid volume is very small, and the mean residence times are of the order of days. An induction period of several days duration is usually required at the start of each experiment to completely flush out the reaction vessel. Typical reaction times range from 100 to 300 hours, but some experiments run for several months.

In much of the earlier experimental work reported in Table 2.1, the solid phases were not carefully characterized before and after completion of the experiment. In order to correlate changes in fluid composition with changes in the reacted solid, mineral surfaces must be examined by SEM or electron microprobe. Techniques such as x-ray photoelectron spectroscopy can be used to study compositional changes within the surface.

**2.3 Geochemical Rate Laws.** A great deal of geochemical rate data has been correlated by the empirical equation:

$$\frac{dQ}{dt} = kt^n \quad (2.7)$$

where Q is the mass transferred per unit area (moles/cm<sup>2</sup>) which is a function of time, k is the "parabolic rate constant" (moles/cm<sup>2</sup>-sec<sup>n+1</sup>), and n is 0 for linear kinetics, -1/2 for parabolic kinetics and -1 for logarithmic kinetics (Helgeson, 1971; Luce et al., 1972; Grandstaff, 1977; White and Classen, 1979; Lahann and Robertson, 1980; Lin and Clemency, 1981). While equation (2.7) may be fitted to geochemical rate data by adjusting the value of k, it is not a true rate law in that the rate is not an explicit function of concentrations of reactants or products. Since the rate as correlated by this equation is independent of the accumulation of products and of the disappearance of reactants, equation (2.7) cannot predict the approach to equilibrium.

Lasaga (1981) describes a phenomenological approach to geochemical kinetics.

For a general overall irreversible reaction:



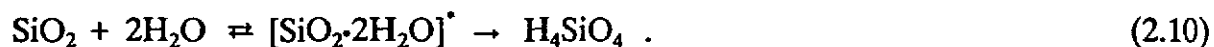
where the lower case letter is the stoichiometric coefficient and the uppercase letter represents a component in the reaction, the rate of reaction,  $\mathfrak{R}$ , is given by:

$$\mathfrak{R} = \frac{-1}{a} \frac{d\{A\}}{dt} = \frac{-1}{b} \frac{d\{B\}}{dt} = \dots = \frac{1}{p} \frac{d\{P\}}{dt} = \frac{1}{r} \frac{d\{R\}}{dt} = \dots \quad (2.9a)$$

$$= k \{A\}^{\alpha} \{B\}^{\beta} \dots \{P\}^{\gamma} \{R\}^{\epsilon} \dots \quad (2.9b)$$

where the curly brackets indicate component concentrations, and  $k$  is the rate constant which has units of  $(\text{concentration})^{1-\alpha-\beta\dots\text{etc}}/(\text{time})$ . The reaction orders,  $\alpha$ ,  $\beta$ ,  $\pi$ ,  $\rho$  ..., in equation (2.9b) are real numbers (not necessarily equal to the stoichiometric coefficients) determined by fitting experimental data to equation (2.9b). The rate expression represented by this equation is a typical global rate law. Global rate laws are frequently used in describing the kinetics of industrial chemical processes, but they seldom contain real mechanistic information and usually apply over limited ranges of temperature and composition. They have rarely been applied to geochemical reactions.

Transition-state theory (TST) (Eyring, 1935; Evans and Polyani (1935) has been used to describe the reaction rates for quartz dissolution (Rimstidt and Barnes, 1984) and feldspar dissolution (Aagaard and Helgeson, 1982; Helgeson, et al, 1984). However, it is clear that the underlying assumptions and limitations of TST are not fully appreciated since both of these applications violate some of the assumptions of transition-state theory. For example, the reaction mechanism cited by Rimstidt and Barnes (1984) for quartz dissolution is simply the overall reaction with an "activated complex" inserted into the reaction:



However, because equation (2.10) does not give any details of the molecular processes that occur during the reaction, this is not an elementary reaction. Furthermore,  $[\text{SiO}_2 \cdot 2\text{H}_2\text{O}]^*$  is not a realistic activated complex.

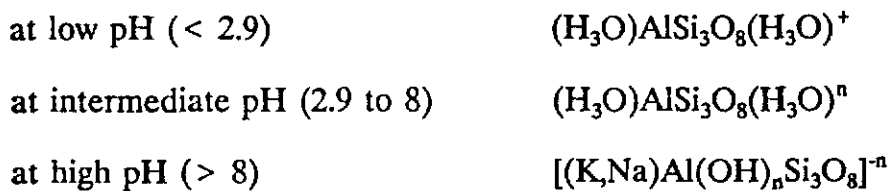


Aagaard and Helgeson (1982) and Helgeson, et al. (1984) derive a general rate equation for aluminosilicate reactions from transition-state theory:

$$\mathfrak{R} = k (\prod_i a_i^{-m_i}) (1 - \exp(A/\sigma RT)) \quad (2.11)$$

where  $\mathfrak{R}$  and  $k$  are the rate of and the rate constant for the reaction (both in moles/cm<sup>2</sup>-sec),  $a_i$  is the activity of the  $i^{\text{th}}$  species in the reaction,  $m_i$  is the stoichiometric coefficient of the  $i^{\text{th}}$  species in the  $j^{\text{th}}$  reaction,  $A$  is the chemical affinity of the reaction, and  $\sigma$  is the "average stoichiometric number, ... equal to the ratio of the rate of decomposition of the activated complex to that of the overall reaction" (Helgeson, et al. 1984).

They describe aluminosilicate dissolution - especially feldspar dissolution - as the breakdown of certain pH dependent, activated complexes at the feldspar surface. The complexes are postulated to have the stoichiometry:



where  $n$  "represents the number of moles of interstitial H<sub>2</sub>O dipoles or hydroxyl ions in the surface configuration of atoms corresponding to the activated complex per mole of reactive feldspar" (Helgeson, et al. 1984). The value of  $n$  is not necessarily the same in the intermediate and the high pH ranges. According to this mechanism, the

rate-limiting step at low pH is the release of the entire H-feldspar complex, eg.  $[(\text{H}_3\text{O})\text{AlSi}_3\text{O}_8(\text{H}_3\text{O})]^+$ , from the feldspar structure by the simultaneous rupture of five Si-O (or Al-O) bonds as shown in Figure 2.5 (from Aagaard and Helgeson, 1982). The rate of reaction for each activated complex is given by equation (2.11) with values for the rate constants and for n being estimated by fitting the rate equations to experimental data. The final form of this rate law is empirically represented as:

$$R = k_{\text{acid}} (a_{\text{H}^+})^a + k_{\text{neutral}} + k_{\text{basic}} (a_{\text{H}^+})^b \quad (2.12)$$

where  $k_{\text{acid}}$ ,  $k_{\text{neutral}}$  and  $k_{\text{basic}}$  are the rate constants for the various pH ranges and a and b are the slopes of the log rate versus pH data.

A serious objection to Aagaard and Helgeson's (1982) and Rimstidt and Barnes (1984) use of transition-state theory is the choice of activated complexes. In Aagaard and Helgeson's (1982) mechanism, the release of an entire formula unit of feldspar to solution from the mineral surface due to the simultaneous breaking of five widely separated Si-O or Al-O bonds is inconsistent with the accepted concept of the transition state. Glasstone, et al. (1941) describe the reaction process in TST in terms of converting translational energy of the reactants into vibrational energy of the products. However, only translational motion directed along the reaction coordinate can lead to reaction, and this energy conversion process only occurs at one bond at a time. To circumvent this restriction, sequential processes could be invoked, but this immediately leads to the choice of a much simpler transition state.

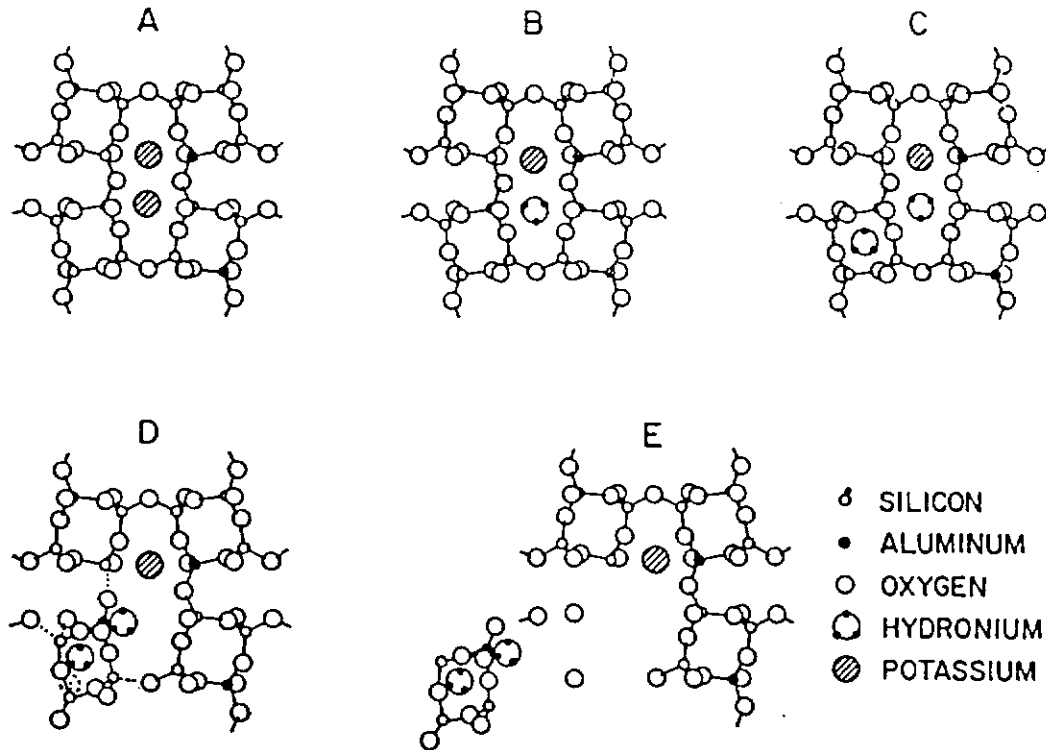


**Figure 2.5** Aagaard and Helgeson's (1982) mechanism of potassium feldspar dissolution in acid solutions. The initial feldspar structure is shown in (a). Exchange of a hydronium ion for a potassium ion (b), and addition of an interstitial hydronium ion (c) form the "activated complex" (d) which has the stoichiometry  $(\text{H}_2\text{O})\text{AlSi}_3\text{O}_8(\text{H}_3\text{O})^+$ . In (e), the "activated complex" is released to aqueous solution.

For multiple reaction systems, Helgeson (1968), Helgeson, et. al., (1969), Helgeson, et. al., (1970), and Helgeson and Murphy (1983) define the relative rate of reaction  $i$  with respect to reaction  $j$  as:

$$\mathfrak{R}_{\text{rel}} = \frac{d\xi_i/dt}{d\xi_j/dt} = \frac{d\xi_i}{d\xi_j} \quad (2.13)$$

where  $\xi_i$  is the extent of reaction for reaction  $i$ . For each reaction  $i$  in the system, the change in species activity can be related to changes in  $\xi_i$  for that reaction by:

$$\frac{d\xi_i}{dt} = \frac{1}{\nu_n^i} \frac{d[C_n^i]}{dt} \quad (2.14)$$

where  $\nu_n^i$  and  $[C_n^i]$  are respectively the stoichiometric coefficient and the activity of species  $n$  in reaction  $i$ . A number of basic reactions are then combined into an overall reaction for the entire system, and the extent of this overall reaction is specified as  $\xi$ .

Following Helgeson's approach, given an initial composition (initial concentrations and masses of phases), the distribution of species and the activities and activity coefficients for each species in solution are calculated. Once the internal state of the initial aqueous phase is determined, the state of equilibrium between the aqueous phase and each solid phase (or potential phase) is evaluated. When undersaturated or supersaturated phases are identified, reversible reactions between the aqueous phase and the appropriate solid phases are invoked to redistribute mass among the aqueous phase and solid phases. These reactions proceed according to the relative rates of reaction defined by equation (2.14) referenced to the overall rate of reaction. When all of the equilibrium and mass balance constraints have been satisfied, the extent of reaction for the overall reaction,  $\xi$ , is incremented and the cycle is repeated until global equilibrium is achieved.

There are several deficiencies inherent in this technique. First of all, the choice of values for the relative rates is almost completely arbitrary. Experimental data are used to guide the choice of the relative rates in that reactions which are observed to be faster have the higher relative rates. However, these relative rates bear no true

relationship to the rates of elementary reactions in the system. In systems involving more than one reaction, specification of relative rates for two reactions will lead to incorrect results unless one reaction is always much faster than the other reaction. In a real system, the relative rates of reaction for two or more reactions change as the reaction progresses: one reaction will initially approach equilibrium more rapidly than the other and its rate will decrease relative to the slower reactions. Helgeson and Murphy (1983) attempted to correct for this difficulty by specifying new relative rates at each new value of  $\xi$ . However, by introducing this degree of variability in the choice of the relative reaction rates, they remove much of the credibility that the model may have contained.

**2.4 Quartz Dissolution Kinetics.** Because of its importance both geologically and industrially, quartz ( $\text{SiO}_2$ ) has been studied intensively. Quartz is one of the most common minerals in nature, and synthetic quartz crystals of high purity are grown industrially, for example, for use as oscillators in telecommunications equipment. Quartz solubility in aqueous solutions has been examined as a function of temperature, pressure and salinity by a number of investigators (Kennedy, 1950; Kitahara, 1960; Morey, et al, 1962; Siever, 1962; Fournier and Rowe, 1966; Crerar and Anderson, 1971; Mackenzie and Gees, 1971; Voloson, et al., 1972). Others have studied the rate of dissolution of quartz in pure water (Kitahara, 1960; Van Lier, et al., 1960; Siebert, et al., 1962; Weill and Fyfe, 1964; Stober, 1966; Rimstidt and Barnes, 1980; and Robinson, 1982) and as a function of pH (Kamiya, et al, 1974; Knauss and Wolery, 1988; Thornton and Radke, 1988).

Quartz dissolution is a congruent process (i.e. one mole of aqueous silica,  $\text{H}_4\text{SiO}_4$ , appears in solution for every mole of quartz,  $\text{SiO}_2$ , that leaves the solid phase) which follows the overall reaction (Van Lier, et al., 1960; Rimstidt and Barnes, 1980; Robinson, 1982; Knauss and Wolery, 1988):



As discussed above, Rimstidt and Barnes (1980) write this reaction with an intermediate "activated complex",  $[\text{SiO}_2 \cdot 2\text{H}_2\text{O}]^*$ , and derive a rate law for the appearance of aqueous silica as a function of time using transition-state theory:

$$\frac{d [\text{H}_4\text{SiO}_4]}{dt} = \frac{A}{M} \gamma_{\text{H}_4\text{SiO}_4} (k_f [\text{SiO}_2] [\text{H}_2\text{O}]^2 - k_r [\text{H}_4\text{SiO}_4]) \quad (2.16)$$

where the square brackets indicate the activity of the species,  $\gamma_{\text{H}_4\text{SiO}_4}$  is the activity coefficient of aqueous silica,  $k_f$  and  $k_r$  are the rate constants for the forward and reverse directions,  $A$  is the "relative" interfacial area of quartz and  $M$  is the "relative" mass of water in the system. Rimstidt and Barnes (1980) normalize the interfacial area and the fluid volume to a "standard" system which has an interfacial area,  $A_0$ , of  $1 \text{ m}^2$  and a mass,  $M_0$ , of  $1 \text{ kg}$  of water.

Equation (2.16) is essentially identical to the empirical rate law used by Van Lier, et al. (1960), Tester, et al. (1977), and Robinson (1982) to describe quartz

dissolution kinetics as a function of the degree of undersaturation:

$$\frac{d \{H_4SiO_4\}}{dt} = k a^* (\{H_4SiO_4\}^{sat} - \{H_4SiO_4\}) \quad (2.17)$$

In this equation, the curly brackets indicate species concentrations,  $k$  is the first order rate constant for the reaction and  $a^*$  is the ratio of the interfacial surface area to the fluid volume. Note that the compositional driving force is written in terms of species activities in equation (2.16) and in terms of species concentrations in equation (2.17). Thus, the rate constants for equation (2.16) cannot be directly compared with the rate constants for equation (2.17) without converting the rate laws to the same basis. In this case, the conversion is given by

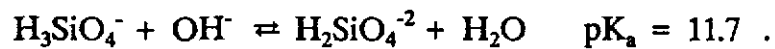
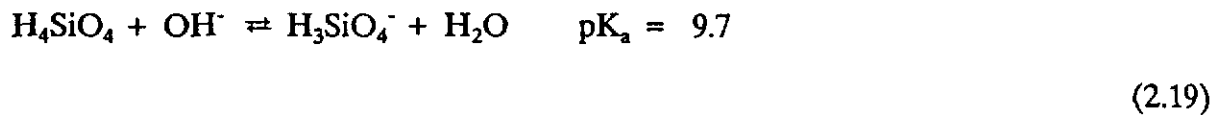
$$k = k_r \frac{M_0 \gamma_{H_4SiO_4}}{A_0 \rho_{H_2O}} \quad (2.18)$$

where  $\rho_{H_2O}$  is the density of water. Rimstidt and Barnes (1980) set the value of  $\gamma_{H_4SiO_4}$  equal to unity since the solution is dilute.

The effect of pH on the rate of quartz dissolution has been studied in detail only recently. Knauss and Wolery (1988) studied the rate quartz dissolution over the pH range from 1.4 to 11.8 at a temperature of 70°C. Their experiments were conducted in the single-pass flow reactor described above. Thornton and Radke (1988) examined

the rate of quartz dissolution and precipitation as a function of pH in the range 11 to 12 and at temperatures of 23 and 70°C. They used 500 ml teflon bottles suspended in a constant temperature bath as semi-batch reactors. Aliquots of the solution withdrawn for analysis at various times. Thornton and Radke (1988) do not present details of the particle size, mass of solid, mass of solution, or initial composition of the solution used in their experiments.

Above a pH of about 9.7 (at 25°C), silica speciation in solution becomes important as the silicic acid ionizes according to the reactions:



To account for the effect of aqueous silica speciation on the dissolution or precipitation rate, Thornton and Radke (1988) write the rate law for quartz dissolution as:

$$\mathfrak{R} = k_1 - k_{-1,0}[\text{H}_4\text{SiO}_4] - k_{-1,1}[\text{H}_3\text{SiO}_4^-] - k_{-1,2}[\text{H}_2\text{SiO}_4^{2-}] \quad (2.20)$$

where  $k_1$  is the initial dissolution rate and  $k_{-1,0}$ ,  $k_{-1,1}$  and  $k_{-1,2}$  are the quartz deposition rate constants corresponding to the various monomeric silica species. Using a material balance on Si along with the equilibrium constants for equations (2.19), this equation can be rewritten in a form equivalent to equation (2.17).



In addition to providing experimental data, Thornton and Radke (1988) present a mechanism for quartz dissolution which is shown in Figure 2.6a. In their mechanism, a tetrahedral silicate group is described as a primary, secondary or tertiary group depending on the number of bonds connecting the silica tetrahedron with the quartz surface (see Figure 2.6b). They assume that aqueous silica adsorbs to the quartz surface according to a Langmuir isotherm and that reaction at a tertiary silicate group is the rate-limiting step in the mechanism. The effects of pH are not included since they did not observe a pH dependence of the quartz dissolution rate in the range pH range they studied (11 to 12).

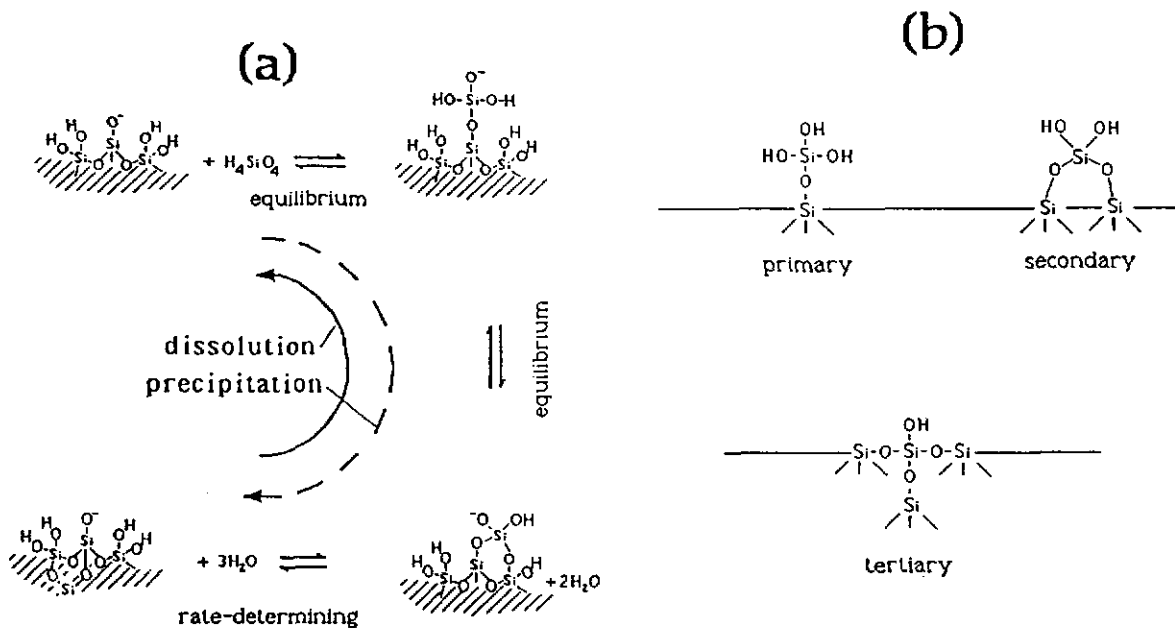


**Figure 2.6** (a) Thornton and Radke's (1988) mechanism of quartz dissolution and precipitation from aqueous solution. (b) representation of "primary", "secondary" and "tertiary" silicate groups at the quartz-water interface (from Thornton and Radke, 1988).

Kamiya, et al (1974) studied the effects of salt concentrations and low pH ( $0 < \text{pH} < 5$ ) on quartz dissolution using 500 ml polyethylene bottle as a semi-batch reactor. They suspended 1 gram of powdered quartz (150 to 200 mesh) in 300 ml of aqueous solution having various NaCl and HCl concentrations. Aliquots of the solution were withdrawn at intervals for analysis. Sample preparation techniques and specific surface areas of the powdered quartz used in their experiments were not reported.

Quartz dissolution rates reported by various investigators are presented as a function of pH in Figure 2.7. For pH values greater than 5, the rate of dissolution increases linearly with pH, and in the pH range from 2 to 5, the dissolution rate appears to be independent of pH. The rates based on the data of Kamiya, et al., (1974) are initial rates interpreted from their curves of silicon concentrations versus time for a number of pH values. Because specific surface areas are not reported, the vertical position of this data set is somewhat arbitrary. By placing the rates of Kamiya, et al. (1974) where they appear in the figure, I have assumed that these rates bracket the rates which would appear if Knauss and Wolery had extended their experiments to lower pH. The rationale for choosing to present the data of Kamiya, et al (1974) will be clear after the discussion of reaction mechanism in Chapter 3.

**2.5 Feldspar Dissolution Kinetics.** In contrast with quartz dissolution described above, feldspar dissolution is an incongruent process, that is, reaction products do not appear in solution in ratios which correspond to the stoichiometry of the dissolving phase (for a brief description of the feldspar minerals and feldspar nomenclature,

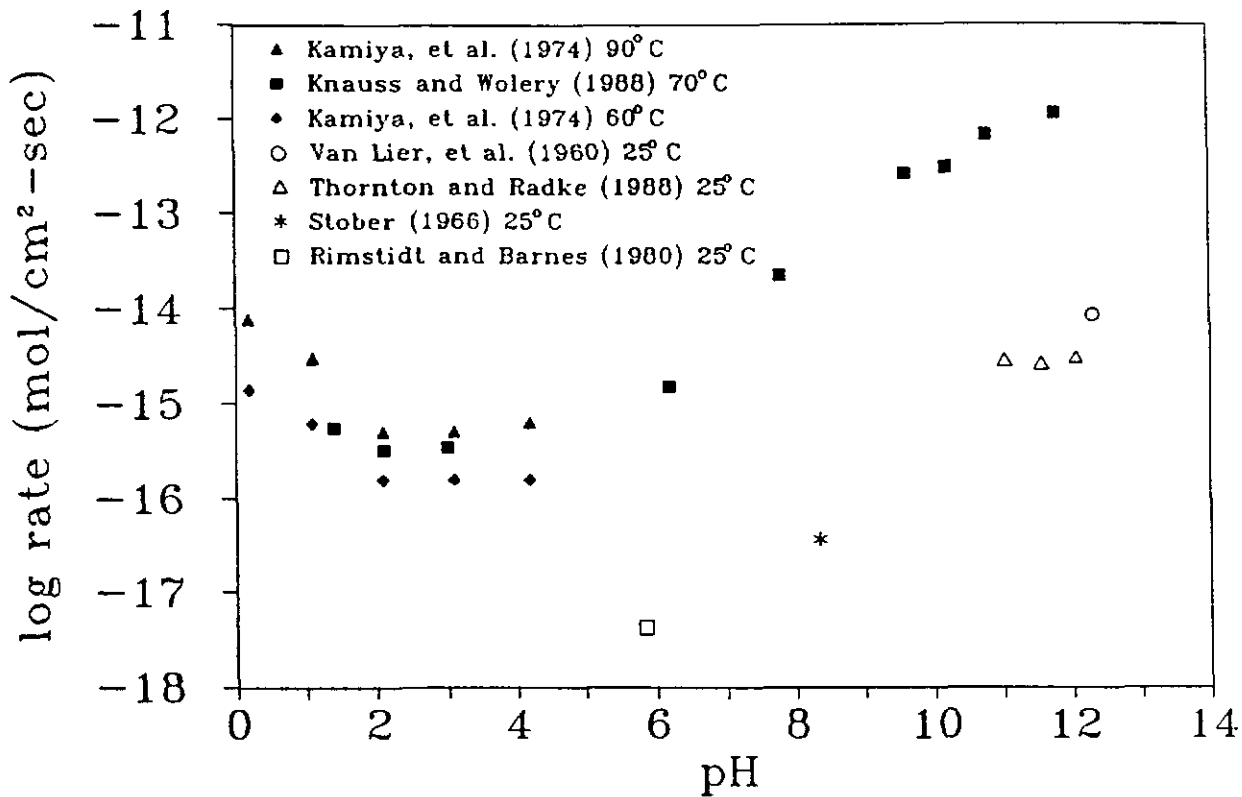
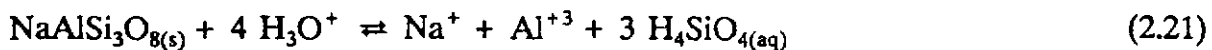


**Figure 2.7** Quartz dissolution rates as a function of pH from data reported in the literature. Because Kamiya, et al (1974) did not report specific surface areas for their quartz samples, the vertical position of this data set is arbitrarily chosen to match the data of other investigators. However, the positions of these data points relative to each other are fixed.

please turn to Appendix A). The overall reaction for feldspar dissolution is:



Covering of the mineral surface by either a leached residuum or by the precipitation of reaction products from solution was offered as an explanation for both the incongruent nature of the reaction and for the observed "parabolic" kinetics (where the concentration is proportional to  $t^{1/2}$ ) in the early stages of a dissolution experiment. (Parabolic rate laws are discussed in Section 2.2.) This type of behavior was attributed

to diffusion limitations within the hypothesized surface layer (Wollast, 1967; Helgeson, 1971, 1972; Paces, 1973; Busenberg and Clemency, 1976; White and Classen, 1979; Chou and Wollast, 1984, 1985). Using data from the literature, Lasaga (1984) calculated the thickness of the surface layer which would be formed due to leaching of a feldspar surface or precipitation of a covering layer to be of the order of 100-1000 Å, and Chou and Wollast (1984) calculated leached layer thicknesses of 30 Å for Na and 15 Å for Al in their studies of albite dissolution. However, Chou and Wollast only examined the surfaces of their reacted feldspar with scanning electron microscopy (SEM) which cannot analyze the composition of surface layers. Other experimental studies of reacted feldspar surfaces using x-ray photoelectron spectroscopy (XPS) indicate that there is no uniform coating of precipitated reaction products and no leached layer with a thickness greater than 15 Å (Petrovic, et al., 1976; Berner, 1978).

Lagache (1965, 1976) argued that for diffusion control of feldspar dissolution rates, the rate should be proportional to the product of the mineral surface area ( $s$ ) and the square root of time ( $t^{1/2}$ ). However, her experiments show a different functional form (roughly  $[st]^{1/2}$ ), so she concluded that feldspar dissolution rates are not controlled by diffusion. Berner (1978) showed that activation energies considerably in excess of 15 to 20 kJ/mole (4 to 5 kcal/mole) indicate surface reaction rather than diffusion control. Thus, the apparent activation energy for feldspar dissolution of 83 kJ/mole (20 kcal/mole) (Helgeson, et al., 1984) suggests that feldspar dissolution rates are limited by surface reaction rates.

Dibble and Tiller (1981) proposed that the rate-limiting step changes during the progress of the reaction. They invoke surface processes such as detachment at a kink or a ledge, surface or ledge diffusion, desorption from the surface to the adjacent liquid layer, and finally diffusion through a fluid boundary layer. Any of these steps may be rate-limiting under certain conditions, and Dibble and Tiller derive "linear", "logarithmic" and "parabolic" rate laws which correspond to different rate-limiting steps (see section 2.2).

Holdren and Berner (1979), Grandstaff (1980), and Petrovic (1981a,b) suggested that ultrafine particles which result from sample preparation techniques adhere to larger grains and that rapid dissolution of these ultrafine particles is responsible for the apparent parabolic rates of dissolution of a number of minerals. Linear (ie. zero order) kinetics invariably result when the ultrafine particles are removed (Berner, 1978; Lasaga, 1984).

Parabolic rates may also result from a phenomena reported by Holdren and Adams (1982) and Holdren (1983) who mixed aqueous solutions of  $\text{AlCl}_3 \cdot 6\text{H}_2\text{O}$ ,  $\text{Na}_2\text{SiO}_3 \cdot 9\text{H}_2\text{O}$  and a pH buffer in a single reaction vessel and followed the progress of the reaction by withdrawing samples for analysis. All three solutions were added at constant rates so that the total mass of each component in the reaction vessel increased linearly with time. Analysis of the reacting mixture showed that the amount of silica in solution only increased parabolically, proportional to  $t^{1/2}$ , rather than linearly with time. Presumably this is due to precipitation of aluminosilicates having various Si/Al ratios.

Holdren (1983) reports that some of this effect is due to complexing of Al by the pH buffers.

Experimentally determined feldspar dissolution rates are shown as a function of pH in Figure 2.8. In this figure, the rate of dissolution (moles of feldspar/cm<sup>2</sup>-s) is a minimum at a pH of 7, and the rate increases linearly with pH at both lower and higher values of the pH. The slope of the rate versus pH curve at low pH is equal in magnitude but opposite in sign to the slope of the curve at high pH.

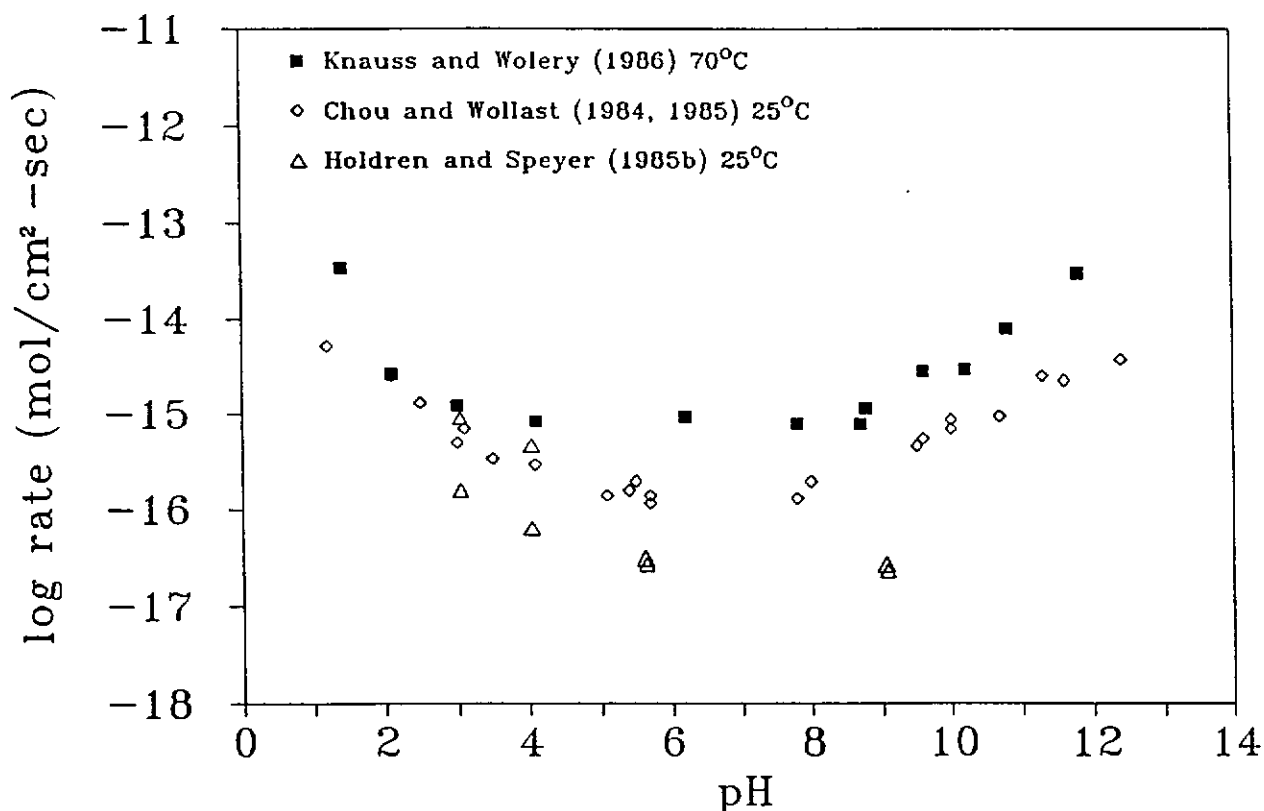


Figure 2.8 Feldspar dissolution rates as a function of pH from data reported in the literature.

Lasaga (1984) suggested that the fractional order dependence on  $H^+$  of the rate of dissolution of several minerals is due to the presence of several types of surface sites having different adsorption and reaction energies. He also suggested that the minimum in the rate versus pH curve might be related to the pH at which the surface has no net charge - the  $pH_{pzc}$  - and that the "U-shaped" nature of the rate versus pH curve is due to the amphoteric nature of aluminum in solution. These questions about the reaction order of the dissolution with respect to hydrogen ion concentration, the location of the minimum in the rate versus pH curve, and the shape of the rate versus pH curve are key points in understanding the kinetics of rock-water reactions and are major topics addressed in this thesis.

## Chapter 3

### Thesis Motivation and Objectives

Progress in chemical kinetics research is largely driven by the need for incorporating reaction mechanisms and rates in the design and scale-up of industrial chemical processes. Detailed reaction kinetics can help in optimizing the utilization of resources - raw materials, energy, process equipment, time - for chemical processes, and this optimization translates into economic benefit. Because most industrially produced chemicals are organic, organic reaction mechanisms and rates have been and continue to be the most thoroughly studied class of reactions.

The state-of-the-art of geochemical kinetics stands in sharp contrast with chemical kinetics in the chemical process industries. At the present time, there is no direct economic incentive for studying geochemical reactions, thus, the development of realistic reaction mechanisms and rate laws for geochemical reactions lags far behind organic reaction kinetics. However, the economic incentive for geochemical kinetics research is growing largely due to the need for long-term solutions to the problem of nuclear waste disposal.

*Much of the "modern" revolution in geochemical kinetics is actually old. Transition-state theory, for example, made its geological debut in 1980 forty-five years after its general introduction. The use of "parabolic" rate laws for describing reaction rates was only discontinued in the early 1980's, but no geochemical reaction has ever*



been described as a bimolecular nucleophilic substitution (for example), even though this terminology and all it implies has long been used in describing organic reactions. The advantages of flow-through reactors over batch or semi-batch reactors have recently been discussed in the geochemical literature, but reactor design and analysis is not generally understood outside of the chemical engineering literature.

Feldspar dissolution rates have been studied intensively for the last fifteen years without the development of a true reaction mechanism. Even quartz dissolution is not as well understood as is generally thought, as evidenced by the recent papers on the pH dependence of the quartz dissolution rate (Knauss and Wolery, 1988; Thornton and Radke, 1988). Because of their complexity, and because of the lack of progress with feldspar reaction mechanisms, other aluminosilicates - micas, clays, zeolites, olivines, pyroxenes - have received much less attention.

The primary objectives of this thesis are (1) to develop detailed reaction mechanisms for specific geochemical reactions, (2) to derive rate laws corresponding to those reaction mechanisms, and (3) to evaluate the kinetic parameters in the derived rate laws. By accomplishing these objectives, other goals will also be met: (4) to provide a conceptual framework into which geochemical kinetics studies may be fit, and (5) discover what specific information is required for future developments.

Reaction mechanisms for aluminosilicate dissolution reactions are proposed in Chapter 4, and rate laws corresponding to these mechanisms are derived in Chapter 5.

Certain aspects of the proposed mechanisms can be tested by relatively simple experiments, and the experimental studies designed to verify some of these predictions are presented in Chapter 6. While the experimental results generally confirm several aspects of the proposed mechanisms and rate laws, they also expose a major complication with estimation of kinetic parameters as discussed in Chapter 7.

No thesis is complete without several interesting side issues being raised. In the course of this research, there are two which might be of general interest. Appendix B presents a general method of evaluating kinetic parameters for complex reaction networks given a reaction mechanism or for predicting the behavior of a complex system once the kinetic parameters are known. Appendix C describes a method of estimating thermochemical parameters for aluminosilicate minerals using bond additivity.

## Chapter 4

### Mechanisms of Aluminosilicate Dissolution Reactions

The lack of detailed reaction mechanisms is the major factor that limits the progress of studies of reaction kinetics in geochemical systems. Experiments such as those conducted by Chou and Wollast (1984, 1985), Holdren and Speyer (1985b) and Knauss and Wolery (1986, 1988) show that the rates of quartz and albite dissolution depend on the solution pH and to a lesser degree on the solution composition, and Aagaard and Helgeson (1982) developed rate equations to describe the dissolution rate of quartz, feldspar, and other aluminosilicate minerals. However these rate equations are not based on reaction mechanisms composed of elementary reactions. Rather, they are an elaborate curve-fitting exercise.

Activation energies and pre-exponential factors have been reported for quartz and albite dissolution (see Table 4.1). For a variety of reasons, these kinetic parameters are incomplete or unsatisfactory. First of all, the parameters are not based on any realistic reaction mechanism. By default, kinetic parameters are assigned to an overall reaction which is treated as if it were an elementary reaction. Transition-state theory is often employed to describe the reaction rates, but since the reaction mechanisms are based on overall reactions, this approach usually violates some of the basic assumptions of transition-state theory.

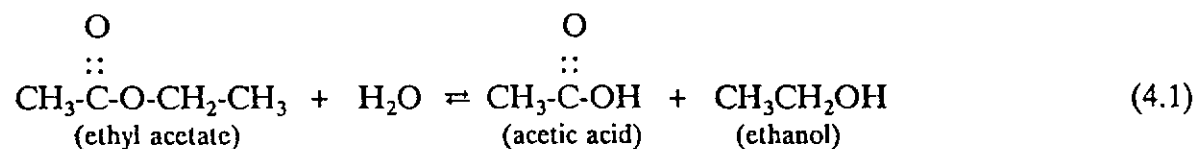
**Table 4.1** Activation energies and pre-exponential factors reported for quartz and feldspar dissolution.

	$E_{act}$ (kJ/mole-K)	$\log_{10}A$
<i>Quartz</i>		
Rimstidt and Barnes (1980)	67.4 - 76.6	not reported
Robinson (1982)	78.3	0.433
Knauss and Wolery (1988)	108.4	-1.3
Bird, et al. (1986)	51 - 55	not reported
<i>Albite</i>		
Helgeson, et al (1984)	90	-.1

Another difficulty arises when the overall reaction actually consists of several independent, parallel pathways. Under some conditions of temperature, pressure or solution composition, one of the pathways may dominate the kinetics, but as conditions change, other pathways may become important. In a reaction network involving many elementary reactions, each elementary reaction has its own transition state, activation energy and pre-exponential factor. Reactions in series may be adequately described by overall kinetic parameters as long as one step in the series is always the rate-limiting step, but overall kinetic parameters cannot account for changes in the relative importance of parallel pathways. For example, a change in the solution pH can shift quartz dissolution from the primarily acid-catalyzed mechanism to a regime where the base-catalyzed mechanism dominates. To which of these reactions do the reported parameters apply? Does the acid-catalyzed reaction necessarily have the same activation energy or pre-exponential factor as the base-catalyzed reaction? These questions can only be addressed by the proper use of detailed and comprehensive reaction mechanisms in the appropriate kinetic models.

**4.1 Acid- and Base-Catalyzed Hydrolysis of Epoxides: an Analog for Aluminosilicate Reaction Mechanisms.** Quartz and feldspar dissolution rates depend on solution pH in a way that is qualitatively similar to the pH dependence of C-O bond hydrolysis in esters and epoxides. For example, the rates of ethyl acetate and isobutylene oxide hydrolysis are shown as a function of solution pH in Figure 4.1 (after Kirby, 1972; Long and Pritchard, 1956). Ethyl acetate hydrolysis rates (Figure 4.1a) increase linearly with the pH as it changes from a pH of about 5.3. This is very similar to the quartz and feldspar dissolution rates shown in Figures 2.7 and 2.8. The isobutylene oxide hydrolysis rates show a distinct flattening at intermediate pH values which is qualitatively similar to the flattening in the feldspar rates.

Although ester and epoxide hydrolysis rates depend upon pH, the overall reactions are independent of pH. For example, stoichiometry of ethyl acetate hydrolysis in acidic or basic solutions is written as:



H<sup>+</sup> and/or OH<sup>-</sup> participate in this reaction as catalysts, and therefore, the increase in rate correlates with increasing catalyst concentration. Ester and epoxide hydrolysis mechanisms are described as acid-catalyzed, base-catalyzed or pH-independent.

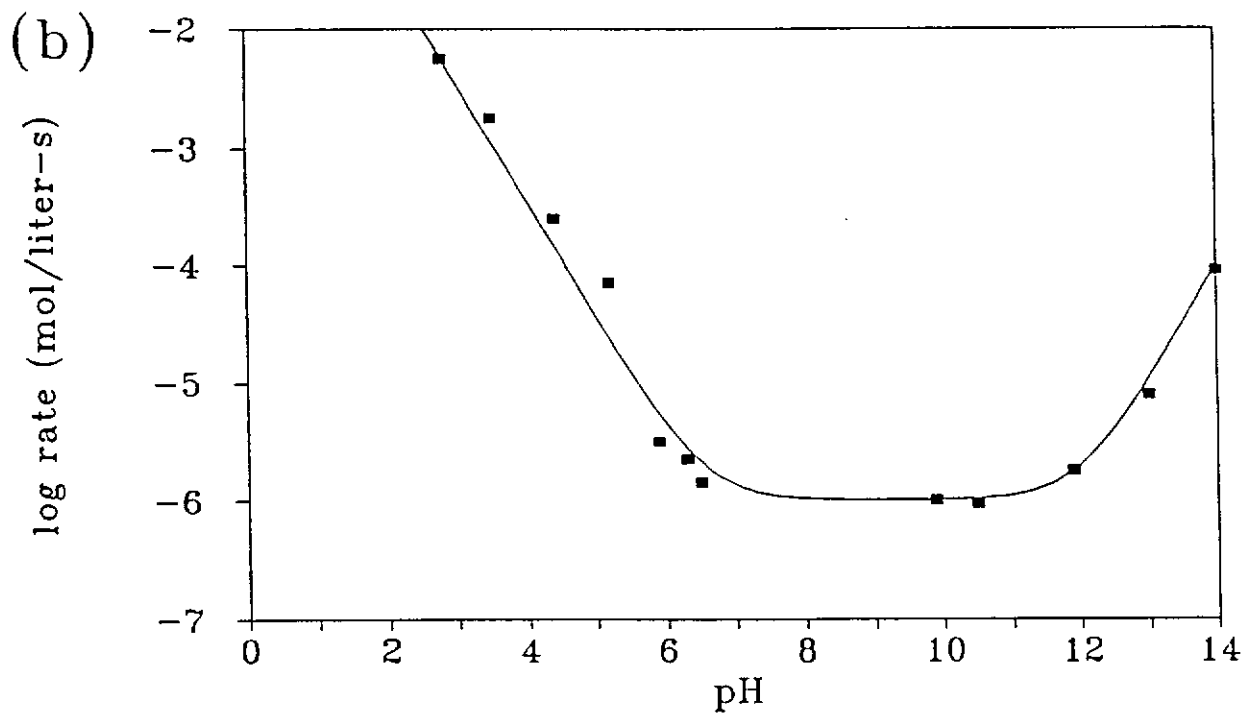
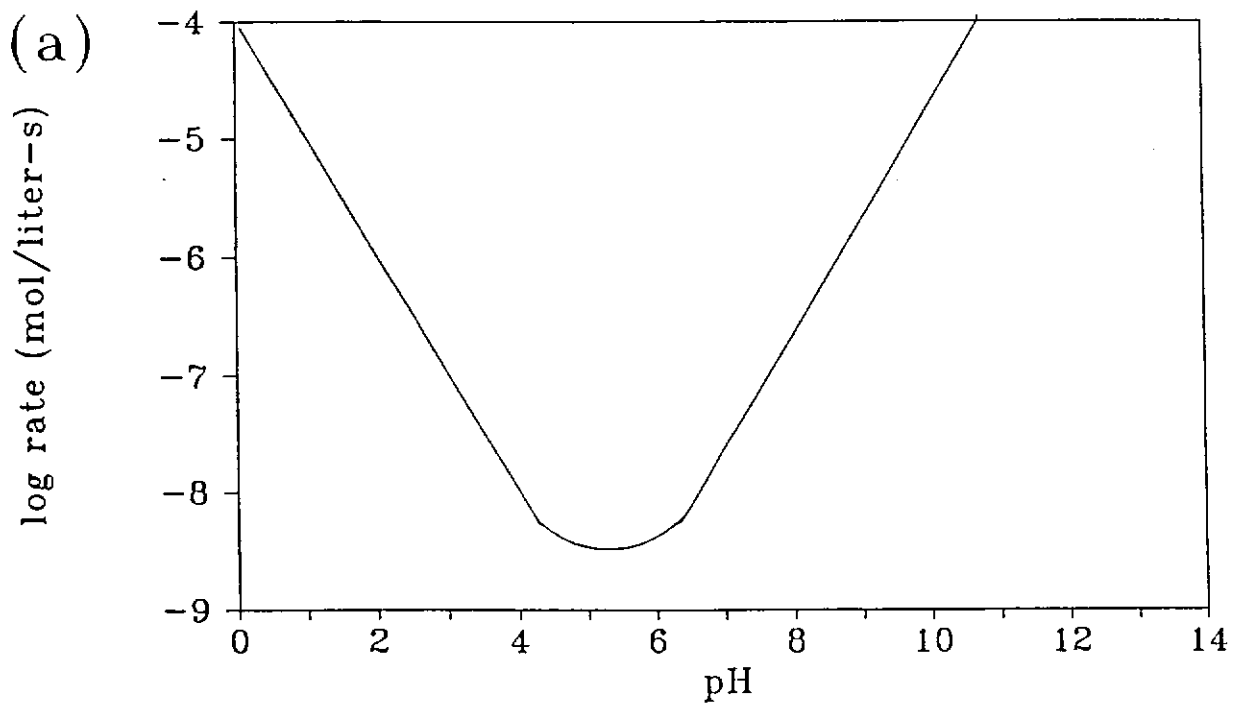


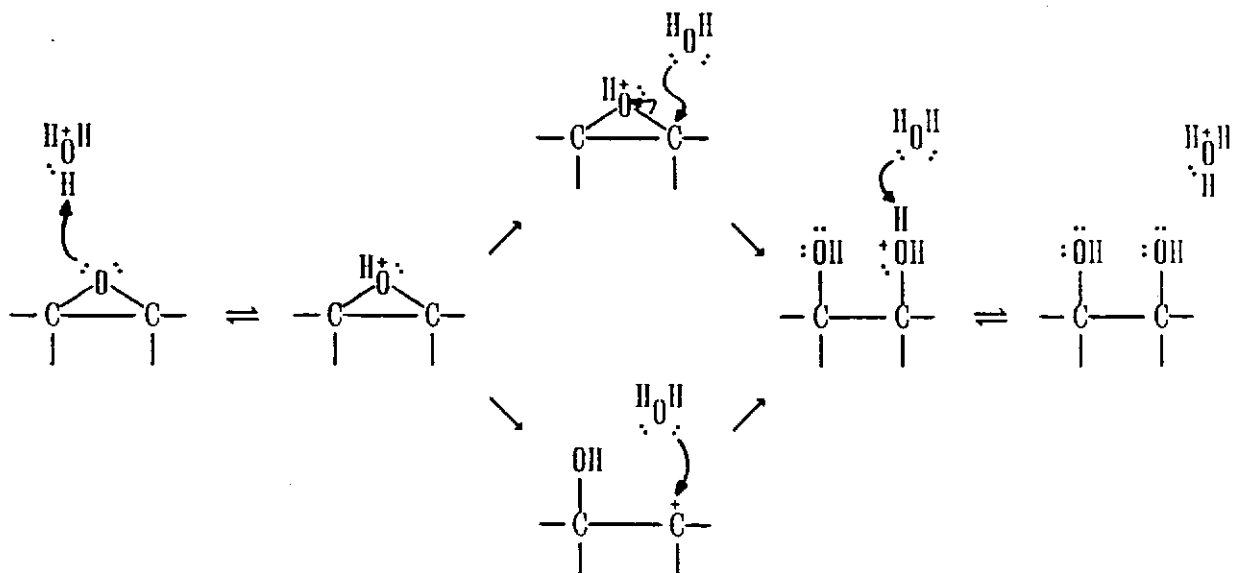
**Figure 4.1** Hydrolysis rates of (a) Ethyl acetate (after Kirby, 1972) and (b) isobutylene oxide (after Long and Pritchard, 1956) as a function of pH at 25°C. At low pH, both reactions are catalyzed by  $H^+$ , and at high pH,  $OH^-$  catalyzes the reactions. Isobutylene oxide also reacts by a pH independent reaction at intermediate pH.

Examination of the rate versus pH curves in Figure 4.1 suggests that ester hydrolysis is more similar to quartz and feldspar rate curves than is epoxide hydrolysis since the latter has a pH-independent region. However, the epoxide hydrolysis reaction mechanism is a better model for aluminosilicate reaction mechanisms for two reasons. In epoxides and aluminosilicates, the reactive site is a  $\equiv\text{T}-\text{O}-\text{T}\equiv$  position where the  $\equiv\text{T}$ - designates a tetrahedrally coordinated (or  $\text{sp}^3$  hybridized) atom (carbon in epoxides, silicon or aluminum in aluminosilicates). On the other hand, the reactive site in esters is a  $\text{T}-\text{O}-\text{D}$  site where the  $\text{D}$  is a carbonyl group. The carbonyl carbon is  $\text{sp}^2$  hybridized (trigonal planar symmetry) rather than  $\text{sp}^3$  hybridized (tetrahedral symmetry).

The second way in which the epoxide hydrolysis mechanism is preferable to the ester hydrolysis mechanism as a model for aluminosilicate reactions involves the internal rotations of the molecules. The epoxide ring prevents rotation about the C-O bonds, but the C-O bonds in the ester can rotate freely or are only slightly hindered by gauche-type interactions. In aluminosilicate minerals, the tetrahedral positions are fixed by the crystal structure so that there is no rotation about a T-O bond.

The epoxide hydrolysis mechanism is shown schematically in Figure 4.2 (after Gould, 1959). In the acid-catalyzed mechanism, a hydrogen is abstracted from a hydronium molecule by the epoxide oxygen. The resulting epoxide ion can react further along one of two paths. The upper path in Figure 4.2a shows an  $\text{S}_{\text{N}}2$  (bimolecular nucleophilic substitution) reaction at one of the epoxide carbons. A water molecule is the nucleophile (attacking group) and the protonated epoxide oxygen is the leaving

(a) *Acid-Catalyzed Mechanism*



(b) *Base-Catalyzed Mechanism*

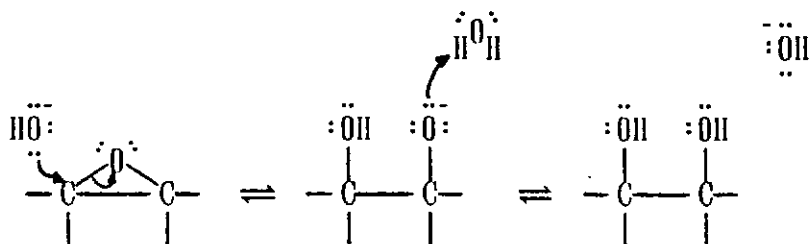


Figure 4.2 (a) Acid- and (b) base-catalyzed mechanisms of epoxide hydrolysis (after Gould, 1959).

group. This reaction opens the epoxide ring. The excess proton is then abstracted by a water molecule to regenerate the acid. In the lower path, the reaction follows an S<sub>N</sub>1



(unimolecular nucleophilic substitution) pathway through a carbocation intermediate. Addition of a water molecule at the carbocation is followed by abstraction of the excess proton by another water molecule.

The base-catalyzed mechanism follows an  $S_N2$  type reaction where the hydroxide ion attacks one of the epoxide carbons to open the ring. The epoxide oxygen is left with three lone pairs of electrons. This oxygen then abstracts a hydrogen from a water molecule to regenerate the base. The final product of both the acid- and base-catalyzed mechanisms is a diol.

In addition to the acid- and base-catalyzed mechanisms, epoxides also are hydrolyzed by a pH-independent reaction. This "water" reaction involves the nucleophilic attack by a water molecule on the epoxide ring carbons (Long and Pritchard, 1956) similar to the base-catalyzed mechanism shown in Figure 4.2b. For the pH-independent reaction of isobutylene oxide, the selectivity toward the labeled oxygen entering at the primary carbon is about 65% compared to about 80% for the base-catalyzed reaction. Long and Pritchard (1956) suggest this lower selectivity toward the primary site is due to water being a weaker nucleophile than hydroxide. Based on these mechanisms, we would expect the epoxide hydrolysis reaction rate to be first order, minus first order and zero order in  $[H^+]$  for the acid-catalyzed, base-catalyzed and pH-independent reactions, respectively; and these reaction orders are indeed observed within the accuracy of the experimental data presented in Figure 4.1.

Long and Pritchard (1956) studied the mechanisms of propylene oxide and isobutylene oxide hydrolysis as a function of pH in experiments with labeled water ( $\text{H}_2\text{O}^{18}$ ). Their results are presented in Table 4.2. In acid solutions, 70% (propylene oxide) to 100% (isobutylene oxide) of the entering oxygen atoms bonded at the branched rather than the primary carbon. Since secondary and tertiary carbon atoms form more stable carbocations than primary carbons, Long and Pritchard's results suggest that the  $\text{S}_{\text{N}}1$  reaction path is preferred. For the base-catalyzed mechanism, they found reaction at the primary carbon for both propylene and isobutylene oxides which is interpreted as  $\text{S}_{\text{N}}2$  reaction at the less sterically hindered site (the primary carbon).

**Table 4.2** Percentage of  $^{18}\text{O}$  entering the epoxide at the primary carbon in Long and Pritchard's (1956) studies of epoxide hydrolysis mechanisms.

	Hydrolysis Conditions	Primary Carbon
Propylene Oxide	acid	26 - 34
	neutral	61 - 67
	basic	78 - 82
Isobutylene Oxide	acid	0 - 1
	neutral*	9 - 20
	basic	90 - 92

\*Because the pH dropped during the course of the reaction, these results include a significant contribution from the acid-catalyzed reaction.

Long, et al. (1957) suggested that the entropy of activation for an  $S_N2$  reaction should be different from that of an  $S_N1$  reaction since the  $S_N2$  reaction involves a specific water molecule in the transition state while the  $S_N1$  reaction does not. For acid-catalyzed ester hydrolysis, the activation entropies for  $S_N1$  and  $S_N2$  reactions are about 30 J/mol-K and -92 J/mol-K, respectively. For acid-catalyzed epoxide hydrolysis, the activation entropy for  $S_N1$  reactions is about -16 J/mol-K. Since even the unsubstituted epoxides (ethylene and propylene oxide) showed activation entropies in this range, Long, et al. (1957) concluded that the  $S_N1$  reaction dominates in acid-catalyzed epoxide hydrolysis. Thus, the amount of labeled oxygen entering the primary carbon in the acid-catalyzed hydrolysis of propylene oxide reflects the relative  $S_N1$  reactivity between primary and secondary carbons.

#### **4.2 Acid- and Base-Catalyzed Mechanisms for Aluminosilicate Hydrolysis.**

Quartz and feldspar dissolution involve hydrolysis of Si-O and Al-O bonds rather than the hydrolysis of C-O bonds. The reactive sites in the mineral surface consist of  $\equiv\text{Si-O-Si}\equiv$  or  $\equiv\text{Si-O-Al}\equiv$  bond sequences (note: Si and Al are each bound to three additional oxygen atoms symbolized by " $\equiv$ "). Experimentally determined quartz and feldspar dissolution rates are shown as a function of pH in Figures 2.7 and 2.8. In both of these figures, the dissolution rates increase linearly with  $[\text{H}^+]$  in the highly acid and highly basic pH ranges. Although the data of Kamiya, et al (1974) are of lesser quality than the other data presented in Figure 2.7, these data indicate a pH dependence for quartz dissolution at low pH.

Quartz and feldspar hydrolysis rates show fractional order dependence on  $[H^+]$  rather than the first order dependence observed in epoxide hydrolysis. The apparent reaction order with respect to  $[H^+]$  was found for quartz (and for albite) dissolution rates by superimposing the different data sets using a constant offset value for each data set (see Figure 4.3). Superimposing the individual data sets allows us to weight each point equally in the calculation of the slope. The slope and intercept were calculated using linear regression, and the best offset value for each data set was chosen by maximizing the correlation coefficient. The details and results of the regression are presented in Table 4.3. To the 95% confidence level, the reaction order with respect to  $[H^+]$  should be  $0.560 \pm 0.143$  for quartz and  $0.313 \pm .073$  for albite in the acid range and  $-0.494 \pm .040$  for quartz and  $-0.354 \pm 0.048$  for feldspar in the basic range.

For the sake of simplicity, we will temporarily describe the reaction order with respect to  $[H^+]$  in terms of simple fractions - 1/2 for quartz, 1/3 for albite:

$$R_{qtz} = k_a [H^+]^{0.5} + k_b [H^+]^{-0.5} \quad (4.2a)$$

$$R_{ab} = k_a [H^+]^{0.33} + k_b [H^+]^{-0.33} \quad (4.2b)$$

A comparison of equation (4.2a) with the quartz dissolution rate data is presented in Figure 4.4a; a similar comparison of the feldspar dissolution rates with equation (4.2b) is shown in Figure 4.4b. Notice that in both cases the equation matches the data

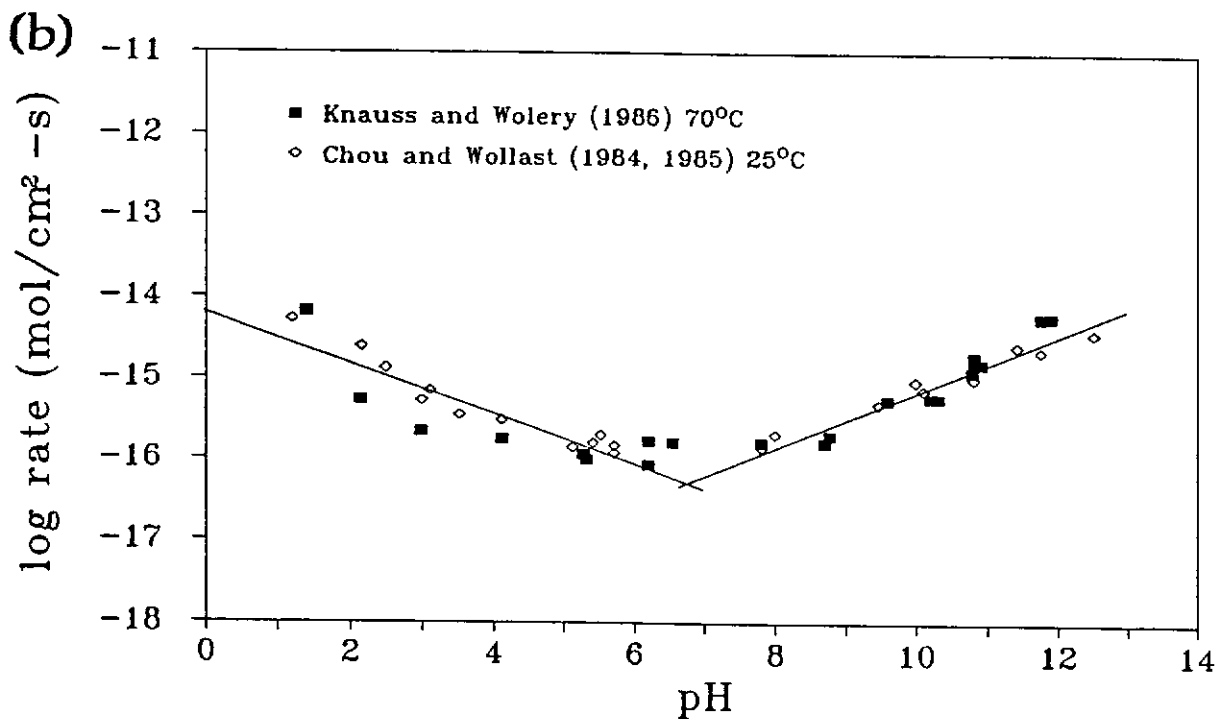
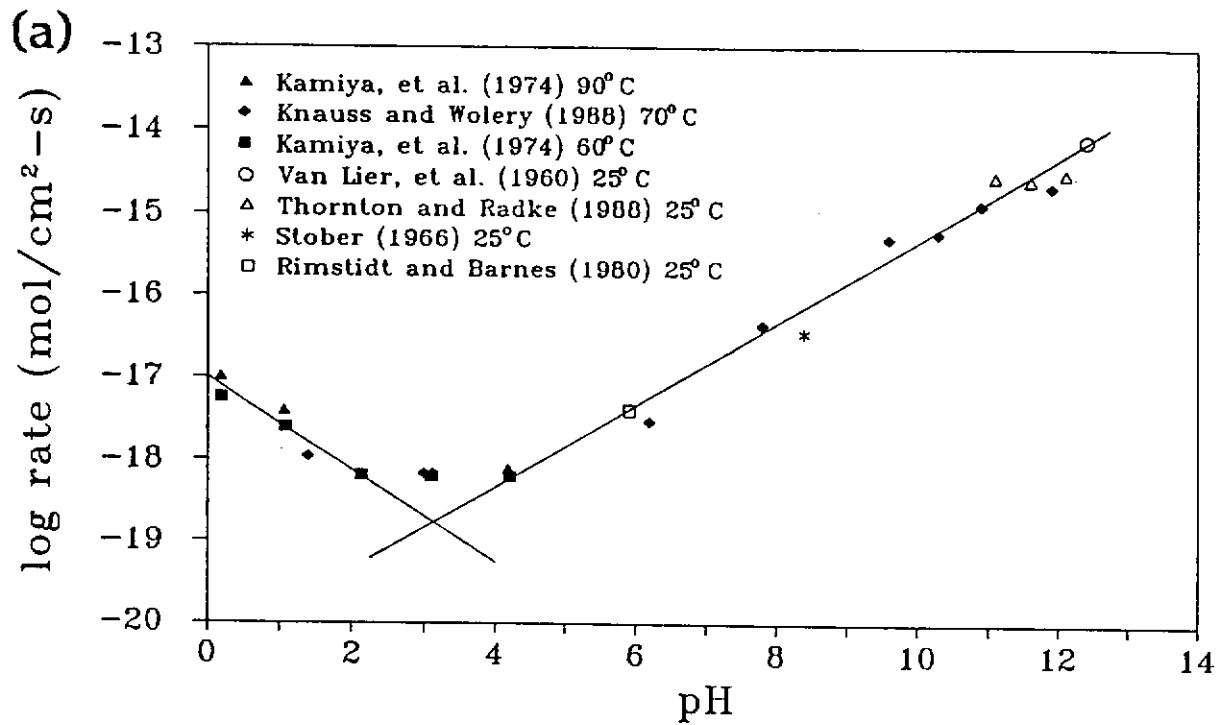


**Figure 4.3** Superposition of (a) the quartz dissolution rate data sets, and (b) the feldspar dissolution rate data sets. The rates for each data set (for example, the quartz dissolution rate data at 25°C) are offset by a constant value as discussed in Table 4.3.

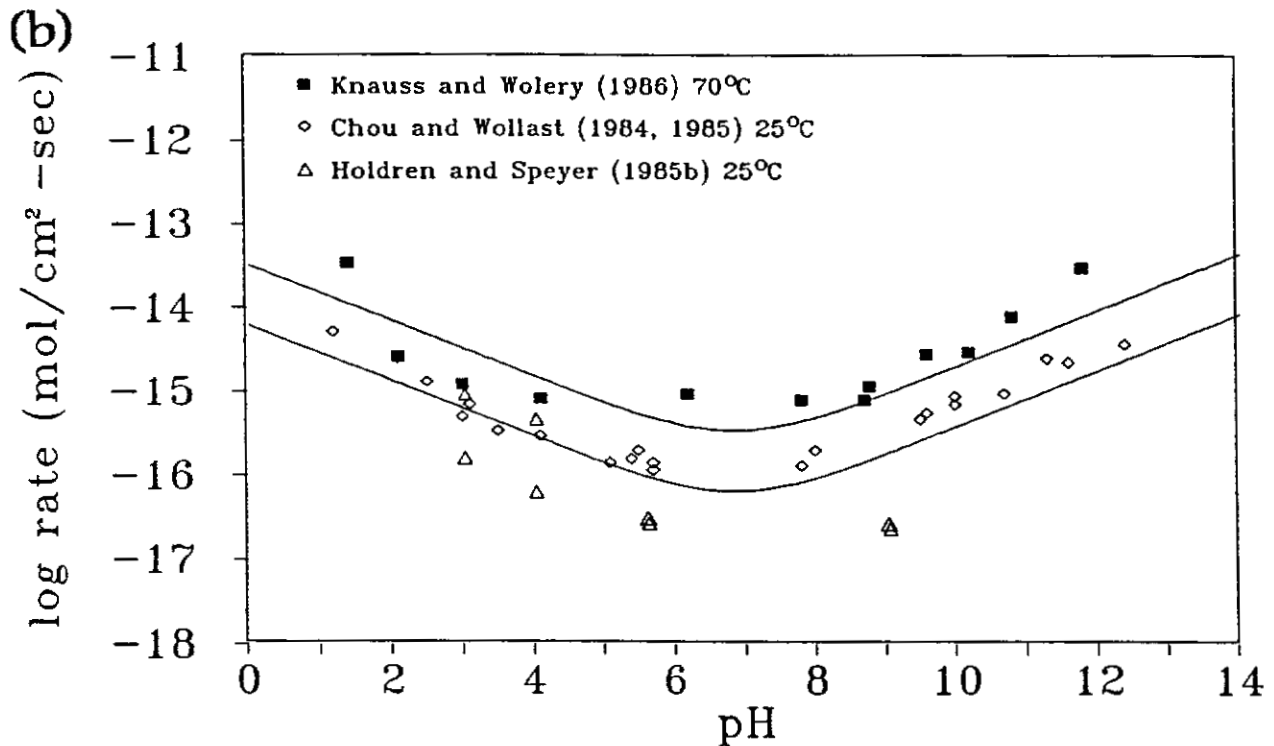
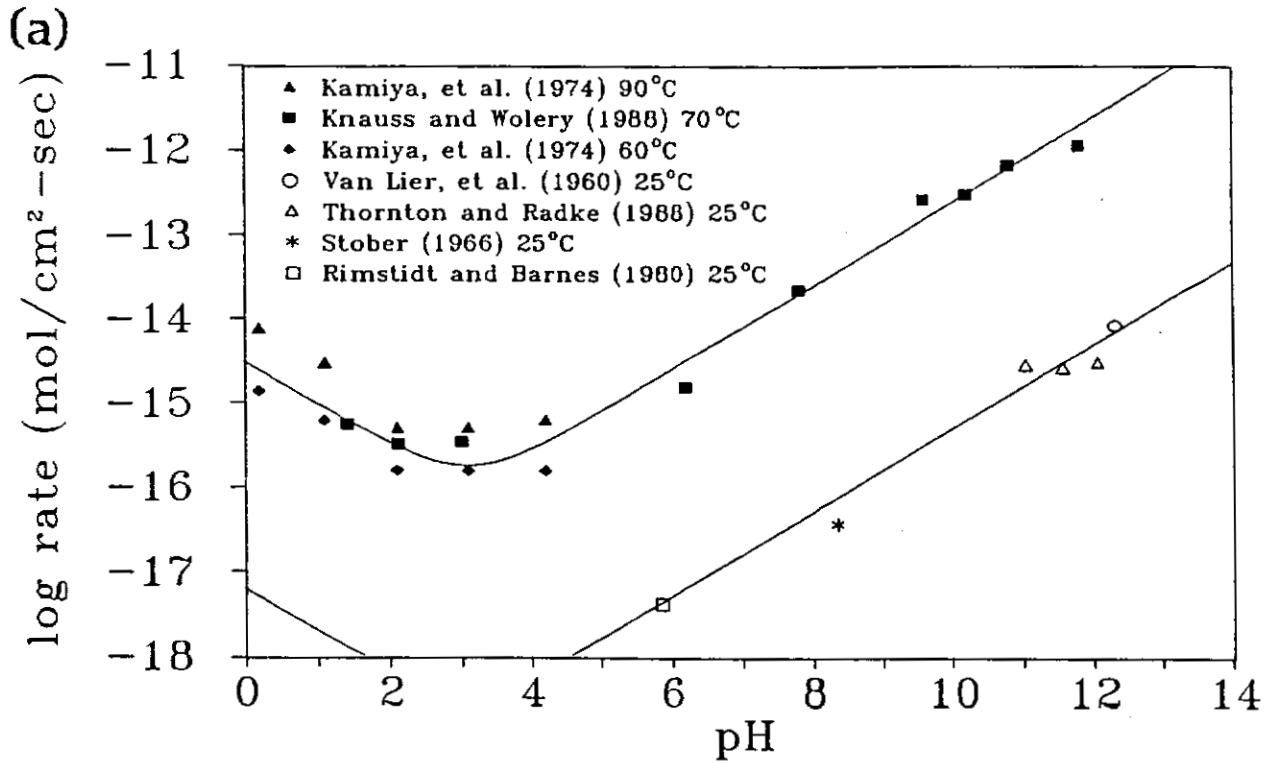


**Figure 4.4** Comparison of (a) equation (4.2a) with the published quartz dissolution rate data, and (b) equation (4.2b) with feldspar dissolution rate data.

**Table 4.3** Regression of quartz and albite reaction rate data to find the reaction order with respect to  $[H^+]$  for the quartz and albite dissolution reactions. The quartz data sets and offsets to the rate data used in the regression are: Knauss and Wolery (1988) 70°C, -2.7; Kamiya, et al. (1974) 60°C, -2.4; Kamiya, et al. (1974) 90°C, -2.9; all 25°C data, 0.0. For albite, the data sets are: Knauss and Wolery (1986) 70°C, -0.715; Chou and Wollast (1984, 1985) 25°C, 0.0.

	Quartz		Albite	
	Acid	Base	Acid	Base
pH range	0.2-2.14	4.2-12.4	1.39-5.7	7.8-12.5
number of data points	8	14	22	22
slope	0.560	-0.494	0.313	-0.354
intercept	-17.00	-20.31	-14.15	-18.68
correlation coefficient	0.938	0.984	0.801	0.921
$t_{\alpha/2}$	2.447	2.179	2.086	2.086
95% confidence interval on slope	0.143	0.040	0.073	0.048
95% confidence interval on intercept	0.217	0.045	0.318	0.211

without the need to invoke a pH-independent mechanism. Values for the  $k$ 's used in equations (4.2a) and (4.2b) are derived from the intercepts and offsets presented in Table 4.3.

The fractional order of the pH dependence suggests that quartz and feldspar dissolution are more complicated than the simple mechanism of epoxide hydrolysis shown in Figure 4.2. Indeed, each of these reactions is in reality a series of reactions

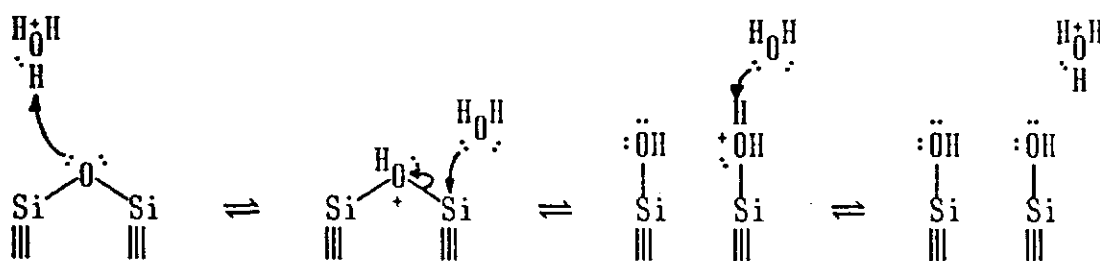
starting with tetrahedra newly-exposed to the mineral surface and ending with aqueous silica and aqueous aluminum ions in solution. The complete mechanism for mineral dissolution includes all of the reaction steps required to remove an  $\text{SiO}_4$  (or  $\text{AlO}_4$ ) tetrahedron from the crystal surface into aqueous solution.

*4.2.1  $\equiv\text{Si-O-Si}\equiv$  Hydrolysis Mechanism.* Based on the epoxide hydrolysis mechanisms discussed above, I propose that  $\equiv\text{Si-O-Si}\equiv$  bonds are hydrolyzed via acid- and base-catalyzed mechanisms as shown in Figure 4.5. In contrast with the acid-catalyzed epoxide hydrolysis mechanism, the acid-catalyzed mechanism shown in Figure 4.5 only includes one reaction pathway. Although there is not sufficient information to distinguish between an  $\text{S}_{\text{N}}2$  and an  $\text{S}_{\text{N}}1$  reaction pathway for the  $\equiv\text{Si-O-Si}\equiv$  hydrolysis, there are several reasons to believe that the acid-catalyzed  $\equiv\text{Si-O-Si}\equiv$  reaction proceeds through an  $\text{S}_{\text{N}}2$  pathway rather than the  $\text{S}_{\text{N}}1$  pathway preferred by the epoxides. First of all, atoms in the second row of the Periodic Table can extend their valence shells more readily than first row elements, and thus, activation energies for  $\text{S}_{\text{N}}2$  reactions would be lower for silicon than for carbon (Benson, 1976). Next, the other ligands on the epoxide carbons are either carbon or hydrogen both of which act as electron donors to the epoxide carbons. The electron donating effect of carbon ligands stabilizes carbocations on the epoxide carbon. In the silicates, however, the other ligands attached to a silicon are oxygens which withdraw the electrons from the silicon atoms. Thus, there is no tendency to stabilize silicon cations. Finally, the argument used by Long, et al. (1957) to decipher the mechanism of ethylene oxide hydrolysis can also be applied here. The activation entropy for an  $\text{S}_{\text{N}}2$  reaction should be more negative than



the activation entropy for an  $S_N1$  reaction because the  $S_N2$  reaction involves a specific water molecule in the transition state. This point will be discussed in more detail when we consider the possibility of  $S_N1$  reactions at tetrahedral aluminum sites in Section 4.2.2 and in Section 5.3.2. For the present time, we will assume that the acid-catalyzed  $\equiv\text{Si-O-Si}\equiv$  hydrolysis reaction proceeds through an  $S_N2$  pathway.

*Acid-Catalyzed Mechanism*



*Base-Catalyzed Mechanism*

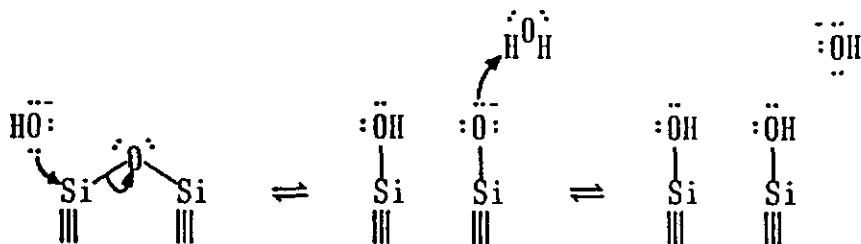


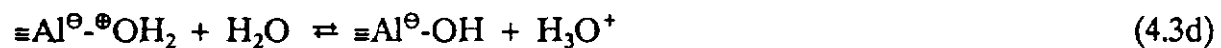
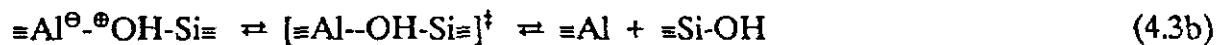
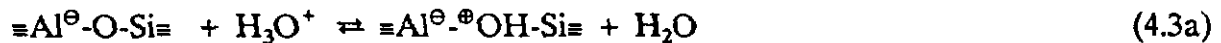
**Figure 4.5** Schematic acid- and base-catalyzed mechanisms for  $\equiv\text{Si-O-Si}\equiv$  bond hydrolysis.

In Figure 4.5, only one oxygen atom is shown attached to the two silicon atoms involved in the reaction. However, each silicon is also attached to three other oxygen atoms (represented by " $\equiv$ ") which can be bridging oxygens (oxygen atoms that "bridge" between two silicon atoms) or "terminal" oxygens (which are hydroxyl groups). We will adopt the terminology of Thornton and Radke (1988) and describe silicon atoms having one, two and three bridging oxygens as a "primary", "secondary" and "tertiary" silicons, respectively.

Although bridging oxygens are not distinguished from hydroxyls in Figure 4.5, the rate of hydrolysis of an  $\equiv\text{Si-O-Si}\equiv$  bond depends on the nature of the next-nearest neighbor ligands. For example, the transition state for a primary silicate tetrahedron is "looser" than the transition state for a secondary or tertiary silicon because there is very little restriction on the movement of the lateral hydroxyls (ie. ligands not involved in the reaction) as they go from tetrahedral symmetry ( $\text{sp}^3$  hybridized) to trigonal planar symmetry ( $\text{sp}^2$  hybridized) and back to tetrahedral symmetry (Figure 4.6a). A "loose" transition state implies a larger pre-exponential factor in the Arrhenius expression for the rate constant, and therefore a faster reaction rate (Benson, 1976). On the other hand, the motion of lateral bridging oxygens in a tertiary silicate tetrahedron is restricted by the bonds to the crystal structure that resist the formation of the trigonal bipyramidal  $\text{S}_{\text{N}}2$  transition state. This transition state is much "tighter". Moreover, the activation energy for tertiary silicate tetrahedra is higher than for primary or secondary silicate tetrahedra because energy is consumed in deforming the lateral bonds to the crystal structure, so with both a tight transition state and a high

activation energy, reaction at a tertiary silicate tetrahedron should be much slower than reaction at primary or secondary sites. This point is particularly important if the hydrolysis reaction proceeds through an  $S_N2$  mechanism.

**4.2.2  $\equiv Al-O-Si \equiv$  Hydrolysis Mechanism.** In addition to the hydrolysis of Si-O bonds, dissolution of other aluminosilicate minerals involves hydrolysis of Al-O bonds.  $\equiv Al-O-Si \equiv$  bond hydrolysis should follow the general pattern of  $\equiv Si-O-Si \equiv$  bond hydrolysis shown in Figure 4.5. However, there are some important differences between hydrolysis of  $\equiv Al-O-Si \equiv$  and  $\equiv Si-O-Si \equiv$  bonds. First, the valence of aluminum is three, so an aluminum bound to four oxygens carries a negative charge. Aluminum can give up one of its four oxygens and still fill its valence shell. Instead of forming a cation, the aluminum loses its net negative charge. This is an  $S_N1$  (unimolecular nucleophilic substitution) mechanism as shown schematically in Figure 4.6b. The elementary reactions in this reaction mechanism are given by:



Since the combined rates of the  $S_N2$  and  $S_N1$  reactions at the  $\equiv Al-O-Si \equiv$  sites is greater than the rate of the  $S_N2$  reaction alone, the minimum in the rate versus pH curve is shifted to a higher pH than the  $pH_{pzc}$ . The amount of the shift depends upon

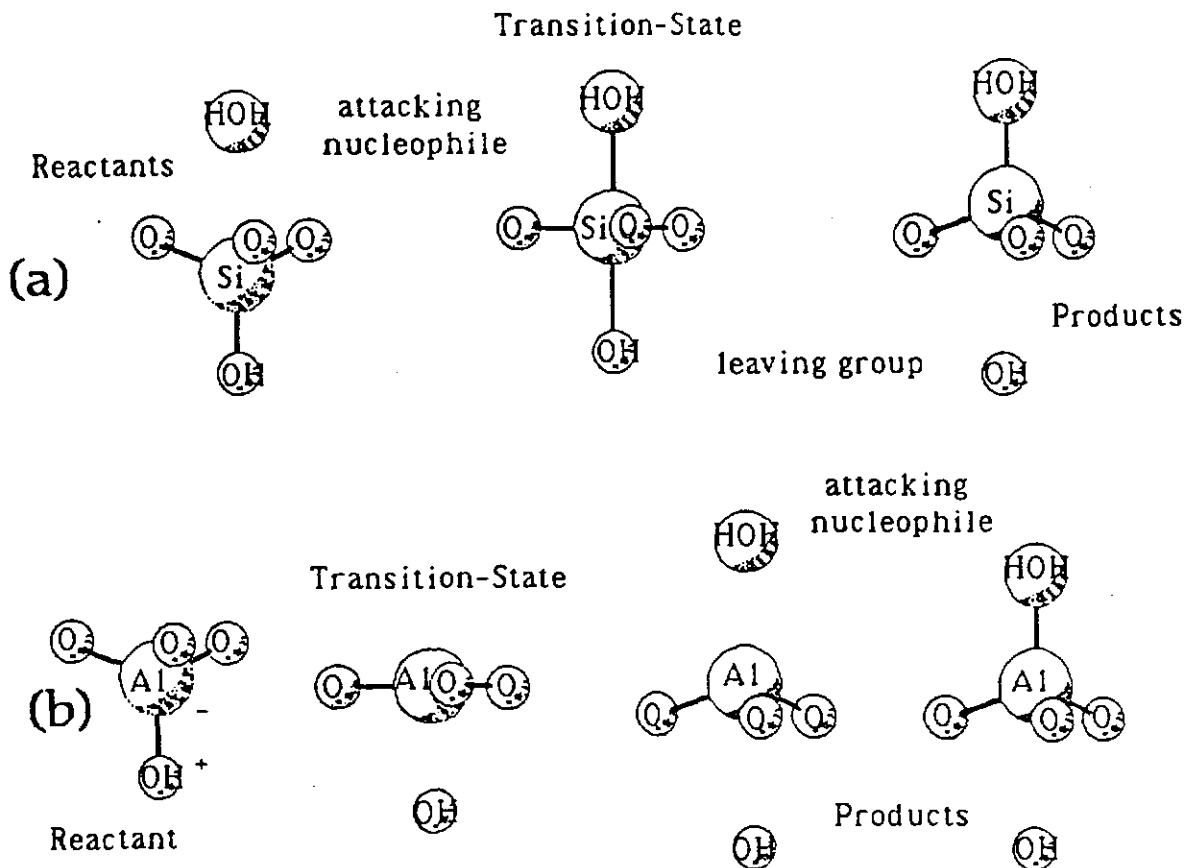


**Figure 4.6** Mechanism of (a) an  $S_N2$  reaction showing the trigonal bipyramidal transition state and inversion of the  $SiO_4$  tetrahedron, and (b) a unimolecular ( $S_N1$ ) bond fission reaction with subsequent attack by a nucleophile (water molecule).

the relative rates of the  $S_N1$  and  $S_N2$  reactions. For albite, the minimum in the rate versus pH curve is about 4 pH units higher than the  $pH_{pzc}$ .

The Al-O bond is also more polar than the Si-O bond since it has a higher difference in electronegativity (2.0 for Al-O versus 1.7 for Si-O). An oxygen bridging between a silicon and an aluminum will carry a larger net negative charge than an oxygen which bridges two silicons. For an  $S_N2$  reaction in acid solutions, the first step of the reaction is to protonate a bridging oxygen. Because of its greater negative

charge, the  $\equiv\text{Al-O-Si}\equiv$  oxygen should be more easily protonated than  $\equiv\text{Si-O-Si}\equiv$  oxygens, so an  $\text{S}_{\text{N}}2$  reaction at an  $\equiv\text{Al-O-Si}\equiv$  bond should be faster than an  $\text{S}_{\text{N}}2$  reaction at an  $\equiv\text{Si-O-Si}\equiv$  bond. Since the  $\equiv\text{Al-O-Si}\equiv$  sites could possibly react by both  $\text{S}_{\text{N}}1$  and  $\text{S}_{\text{N}}2$  mechanisms while reactions at  $\equiv\text{Si-O-Si}\equiv$  sites are restricted to the  $\text{S}_{\text{N}}2$  mechanism, the presence of aluminum in tetrahedral sites in a crystal structure will affect the rate of dissolution.

*4.2.3 Successive Reactions at a Specific Tetrahedral Atom.* For each reaction at a  $\equiv\text{T-O-T}\equiv$  site, only one of the T atoms passes through the trigonal bipyramidal transition state. The T atom containing the higher number of hydroxyls is more likely to pass through the transition state since it has the looser activated complex. When the two T atoms have the same number of hydroxyls, neither will be energetically favored. The combinations having the highest activation energy and the lowest pre-exponential factor are those sites with two silicons having no more than one terminal group (hydroxyl) per silicon atom. All other reactive sites will have looser transition states.

A schematic reaction coordinate-energy diagram for the reaction sequence at a given T atom is presented in Figure 4.7. Each peak represents the transition state for the reaction at one of the bridging oxygens. Only three peaks are shown since a T is brought to the crystal surface by previous reaction of another T atom, and on average, each silicon atom only passes through two transition states (on average, only two Si-O bonds are broken per silicon atom). In the case where the entire surface of the mineral is covered by silicon atoms having three bridging oxygens each, some of the silicon

atoms may have to pass through the transition state three times. Only the most important features of the reaction are shown in this diagram; the details of the reaction mechanism - protonation of bridging oxygens and regeneration of the catalyst by transfer of a hydrogen atom - are not shown since they are energetically small compared with the activation energy for the reaction.

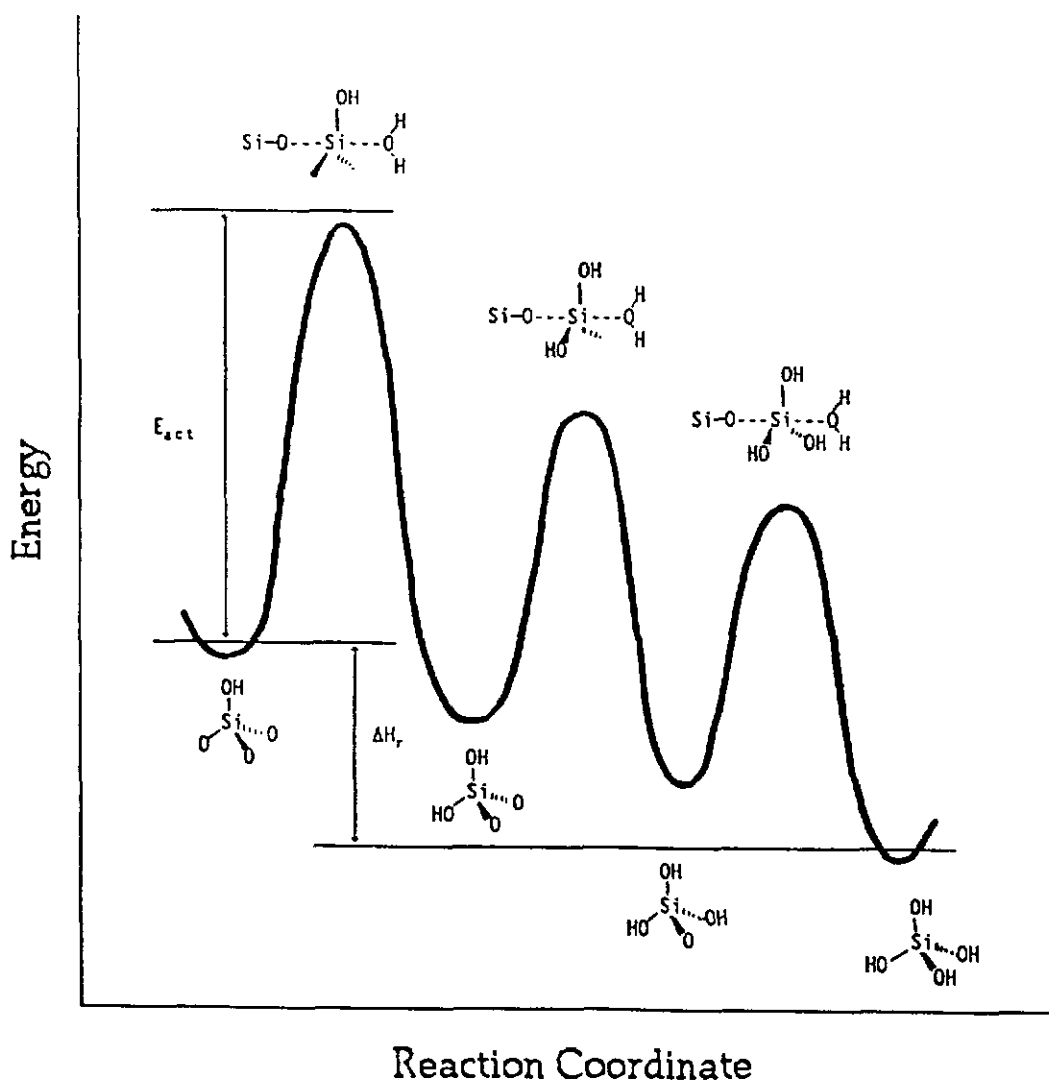


**Figure 4.7** Reaction coordinate-energy diagram for successive reactions at a particular tetrahedral site. Each peak corresponds to the activated complex and each valley corresponds to a stable surface species as shown in the figure.

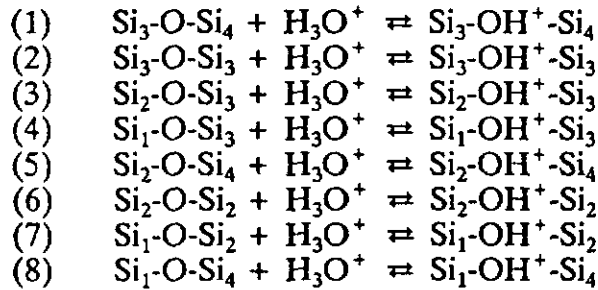
As discussed above, the activation energy is highest for a reaction in which a tertiary T atom passes through the transition state. Subsequent reactions have lower activation energies. The lowest activation energy corresponds to reaction where all of the non-reacting ligands are hydroxyl groups which have relatively unrestricted movement. If reaction at these other sites is relatively rapid, the surface concentration of primary and secondary silicates will be small compared to the concentration of tertiary silicates.

**4.3 Quartz Dissolution Mechanism.** The mechanisms presented in the previous sections describe the reactions occurring at a single  $\equiv\text{T-O-T}\equiv$  bond where the ligands to the tetrahedral atoms are not specified. However, quartz dissolution involves reaction at each oxygen in the quartz crystal structure, and the types of ligands - hydroxyls or bridging oxygens - attached to the silicons will affect the reactivity at an  $\equiv\text{Si-O-Si}\equiv$  site.

Let  $\text{Si}_L$  represent a silicon atom with L bridging oxygens. Eight combinations of  $\text{Si}_L\text{-O-Si}_M$  groups are possible:  $\text{Si}_3\text{-O-Si}_4$ ,  $\text{Si}_3\text{-O-Si}_3$ ,  $\text{Si}_2\text{-O-Si}_3$ ,  $\text{Si}_1\text{-O-Si}_3$ ,  $\text{Si}_2\text{-O-Si}_4$ ,  $\text{Si}_2\text{-O-Si}_2$ ,  $\text{Si}_1\text{-O-Si}_2$ , and  $\text{Si}_1\text{-O-Si}_4$ . (Note:  $\text{Si}_4\text{-O-Si}_4$  is an interior bond, not a surface moiety, and  $\text{Si}_1\text{-O-Si}_1$  is a dimer of silicic acid in solution.) Each of these combinations is a potential reaction site having its own acid- and base-catalyzed reaction mechanisms. The "elementary" reactions which describe reaction at all of these sites is the quartz dissolution mechanism given in Table 4.4.

**Table 4.4 Elementary reactions for the detailed quartz dissolution mechanism.**

Protonation Reactions:



Acid-Catalyzed  $S_N2$  Reactions:

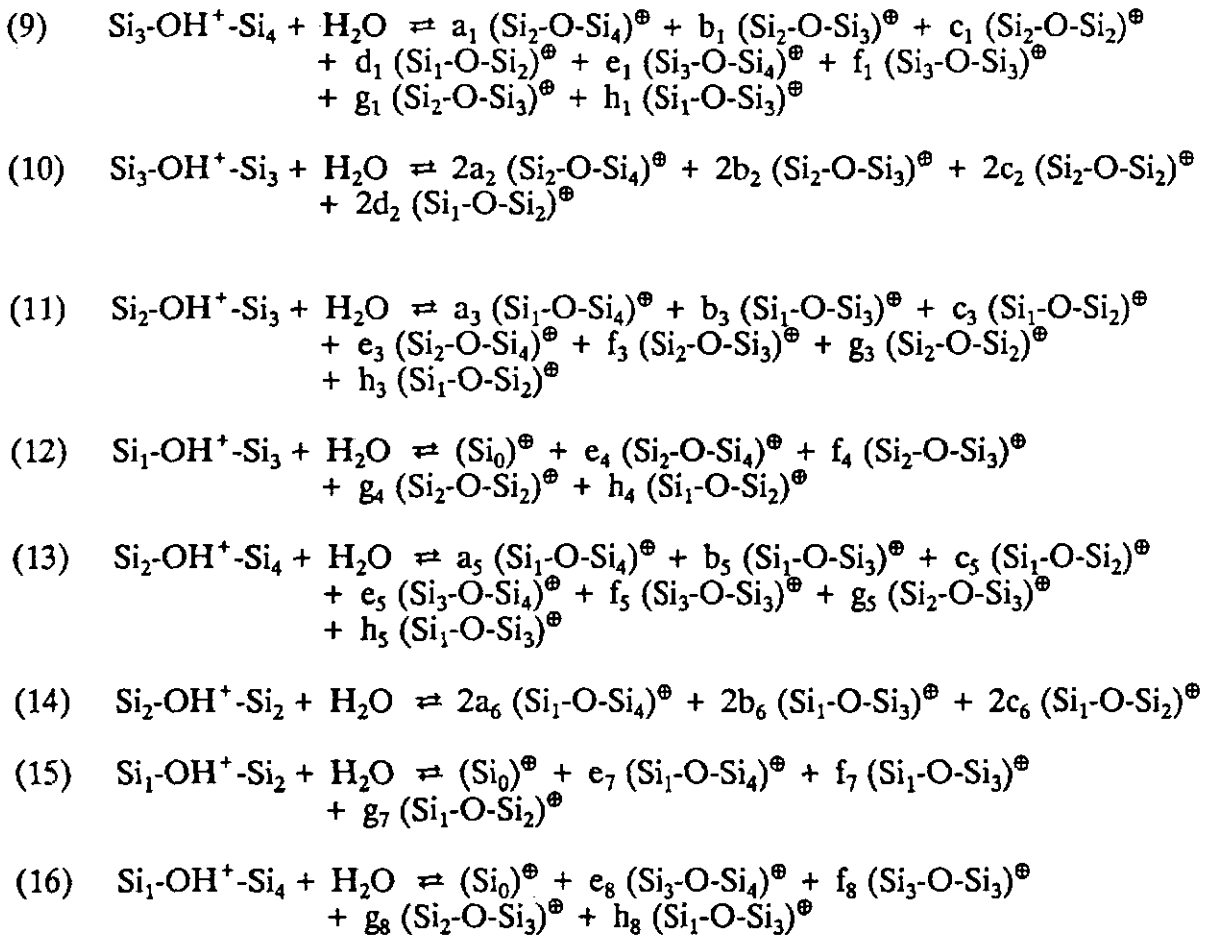
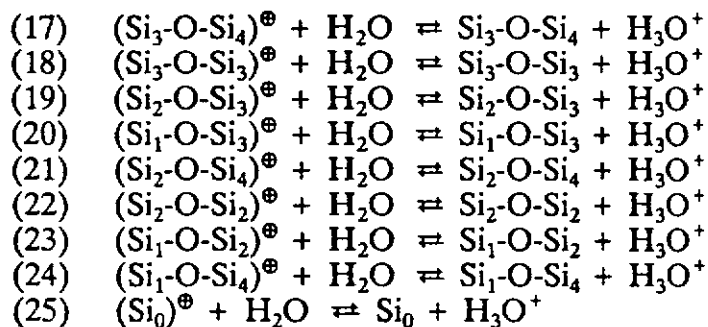




Table 4.4 (continued)

Acid Catalyst Regeneration:



Base-Catalyzed  $S_N2$  Reactions:

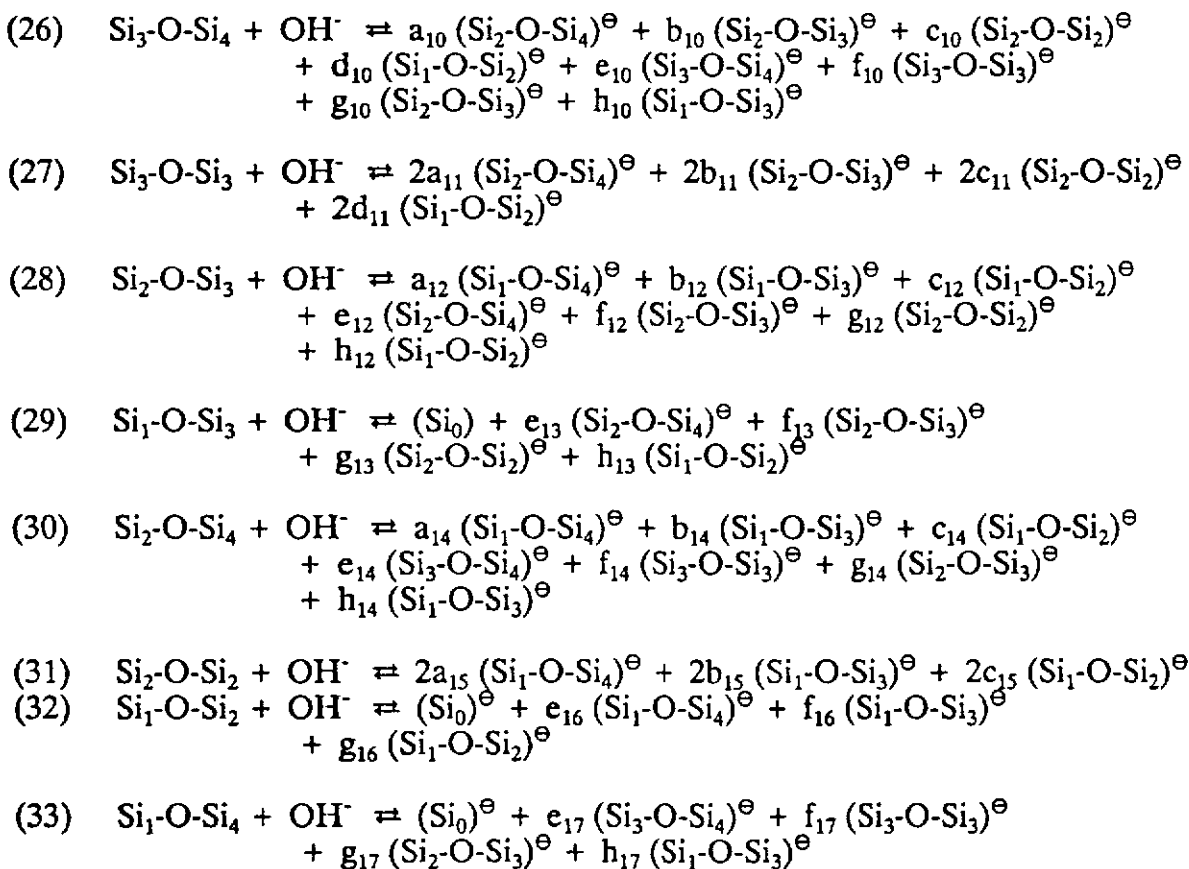
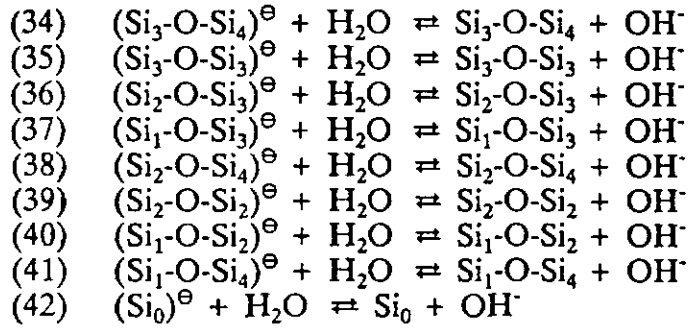


Table 4.4 (continued)

Base Catalyst Regeneration:



Three groups of acid-catalyzed reactions and two groups of base-catalyzed reactions appear in Table 4.4. These groups correspond to protonation,  $S_N2$  reaction and catalyst regeneration at each type of reactive site on the quartz surface. The  $S_N2$  reaction reduces the number of bridging oxygens attached to each of the two silicons involved in the reaction by one. Thus, an  $\text{Si}_3\text{-O-Si}_4$  group reacts to produce one  $\text{Si}_2$  and one  $\text{Si}_3$ . Two bridging oxygens are attached to the  $\text{Si}_2$  and three are attached to the  $\text{Si}_3$ . Each of these bridging oxygen atoms is attached to a silicon atom which, in turn, can have one, two, three, or four bridging oxygens. Let  $a_1$  denote the fraction of  $\text{Si}_2\text{-O-Si}_4$  groups that are formed by this reaction. Similarly,  $b_1$ ,  $c_1$ , and  $d_1$  denote the fraction of  $\text{Si}_2\text{-O-Si}_3$ ,  $\text{Si}_2\text{-O-Si}_2$ , and  $\text{Si}_2\text{-O-Si}_1$  groups formed, respectively, while  $e_1$ ,  $f_1$ ,  $g_1$ , and  $h_1$  indicate the fraction of  $\text{Si}_3\text{-O-Si}_4$ ,  $\text{Si}_3\text{-O-Si}_3$ ,  $\text{Si}_3\text{-O-Si}_2$ , and  $\text{Si}_2\text{-O-Si}_1$  groups, respectively. In Table 4.4, the  $a_i$  through  $d_i$  refer to the products formed by the first silicon in the reactant while the  $e_i$  through  $h_i$  refer to the product formed by the second silicon in the reactant. The  $a_i$  terms in reactions (9) through (16) and (26) through (33) in Table 4.4

are undetermined multipliers representing the unknown stoichiometry of the reaction at each type of reaction site. These undetermined multipliers are subject to the constraints:

$$a_i + b_i + c_i + d_i = 1 \quad (4.4a)$$

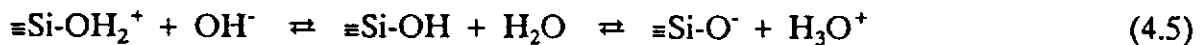
$$e_i + f_i + g_i + h_i = 1 \quad (4.4b)$$

Notice that each of the  $S_N2$  reactions in Table 4.4 is a not a true elementary reaction but is a composite of several elementary reactions. For example, we might find that some fraction,  $a_1$ , of the reactions at an  $Si_3-OH^+-Si_4$  site produce  $Si_2-O-Si_4$  as one of the products, but the other product of the reaction could be  $Si_3-O-Si_4$ ,  $Si_3-O-Si_3$ ,  $Si_2-O-Si_3$ , or  $Si_1-O-Si_3$ . Let  $e_1$ ,  $f_1$ ,  $g_1$ , and  $h_1$  represent the fraction of the  $a_1$  reactions that have  $Si_3-O-Si_4$ ,  $Si_3-O-Si_3$ ,  $Si_2-O-Si_3$ , and  $Si_1-O-Si_3$ , respectively, as the second product. From Table 4.5, we can see that the fraction of the total reactions at an  $Si_3-O-Si_4$  site that give  $Si_2-O-Si_4$  and  $Si_3-O-Si_4$  as products is given by the coefficient,  $a_1e_1$ . Thus, reaction (9) in Table 4.4 is the sum of the elementary reactions given in Table 4.5. The activation energies and pre-exponential factors for each of these reactions should be the same, so the rates of each of these reactions depends upon the surface concentrations of  $Si_3$ ,  $Si_2$ , and  $Si_1$  species. As long as we are concerned only with the rate of quartz dissolution, the combined "elementary" reactions in Table 4.4 can be used to describe the rates.

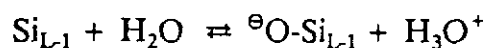
**Table 4.5** Elementary reactions which add to give the composite reaction (9) in Table 4.4. The coefficient of the elementary reaction gives the product distribution for reaction at an Si<sub>3</sub>-O-Si<sub>4</sub> site.

Coefficient		Elementary Reaction
(9a)	a <sub>1</sub> e <sub>1</sub>	Si <sub>3</sub> -OH <sup>+</sup> -Si <sub>4</sub> + H <sub>2</sub> O ⇌ (Si <sub>2</sub> -O-Si <sub>4</sub> ) <sup>⊕</sup> + (Si <sub>3</sub> -O-Si <sub>4</sub> ) <sup>⊕</sup>
(9b)	a <sub>1</sub> f <sub>1</sub>	Si <sub>3</sub> -OH <sup>+</sup> -Si <sub>4</sub> + H <sub>2</sub> O ⇌ (Si <sub>2</sub> -O-Si <sub>4</sub> ) <sup>⊕</sup> + (Si <sub>3</sub> -O-Si <sub>3</sub> ) <sup>⊕</sup>
(9c)	a <sub>1</sub> g <sub>1</sub>	Si <sub>3</sub> -OH <sup>+</sup> -Si <sub>4</sub> + H <sub>2</sub> O ⇌ (Si <sub>2</sub> -O-Si <sub>4</sub> ) <sup>⊕</sup> + (Si <sub>2</sub> -O-Si <sub>3</sub> ) <sup>⊕</sup>
(9d)	a <sub>1</sub> h <sub>1</sub>	Si <sub>3</sub> -OH <sup>+</sup> -Si <sub>4</sub> + H <sub>2</sub> O ⇌ (Si <sub>2</sub> -O-Si <sub>4</sub> ) <sup>⊕</sup> + (Si <sub>1</sub> -O-Si <sub>3</sub> ) <sup>⊕</sup>
(9e)	b <sub>1</sub> e <sub>1</sub>	Si <sub>3</sub> -OH <sup>+</sup> -Si <sub>4</sub> + H <sub>2</sub> O ⇌ (Si <sub>2</sub> -O-Si <sub>3</sub> ) <sup>⊕</sup> + (Si <sub>3</sub> -O-Si <sub>4</sub> ) <sup>⊕</sup>
(9f)	b <sub>1</sub> f <sub>1</sub>	Si <sub>3</sub> -OH <sup>+</sup> -Si <sub>4</sub> + H <sub>2</sub> O ⇌ (Si <sub>2</sub> -O-Si <sub>3</sub> ) <sup>⊕</sup> + (Si <sub>3</sub> -O-Si <sub>3</sub> ) <sup>⊕</sup>
(9g)	b <sub>1</sub> g <sub>1</sub>	Si <sub>3</sub> -OH <sup>+</sup> -Si <sub>4</sub> + H <sub>2</sub> O ⇌ (Si <sub>2</sub> -O-Si <sub>3</sub> ) <sup>⊕</sup> + (Si <sub>2</sub> -O-Si <sub>3</sub> ) <sup>⊕</sup>
(9h)	b <sub>1</sub> h <sub>1</sub>	Si <sub>3</sub> -OH <sup>+</sup> -Si <sub>4</sub> + H <sub>2</sub> O ⇌ (Si <sub>2</sub> -O-Si <sub>3</sub> ) <sup>⊕</sup> + (Si <sub>1</sub> -O-Si <sub>3</sub> ) <sup>⊕</sup>
(9i)	c <sub>1</sub> e <sub>1</sub>	Si <sub>3</sub> -OH <sup>+</sup> -Si <sub>4</sub> + H <sub>2</sub> O ⇌ (Si <sub>2</sub> -O-Si <sub>2</sub> ) <sup>⊕</sup> + (Si <sub>3</sub> -O-Si <sub>4</sub> ) <sup>⊕</sup>
(9j)	c <sub>1</sub> f <sub>1</sub>	Si <sub>3</sub> -OH <sup>+</sup> -Si <sub>4</sub> + H <sub>2</sub> O ⇌ (Si <sub>2</sub> -O-Si <sub>2</sub> ) <sup>⊕</sup> + (Si <sub>3</sub> -O-Si <sub>3</sub> ) <sup>⊕</sup>
(9k)	c <sub>1</sub> g <sub>1</sub>	Si <sub>3</sub> -OH <sup>+</sup> -Si <sub>4</sub> + H <sub>2</sub> O ⇌ (Si <sub>2</sub> -O-Si <sub>2</sub> ) <sup>⊕</sup> + (Si <sub>2</sub> -O-Si <sub>3</sub> ) <sup>⊕</sup>
(9l)	c <sub>1</sub> h <sub>1</sub>	Si <sub>3</sub> -OH <sup>+</sup> -Si <sub>4</sub> + H <sub>2</sub> O ⇌ (Si <sub>2</sub> -O-Si <sub>2</sub> ) <sup>⊕</sup> + (Si <sub>1</sub> -O-Si <sub>3</sub> ) <sup>⊕</sup>
(9m)	d <sub>1</sub> e <sub>1</sub>	Si <sub>3</sub> -OH <sup>+</sup> -Si <sub>4</sub> + H <sub>2</sub> O ⇌ (Si <sub>1</sub> -O-Si <sub>2</sub> ) <sup>⊕</sup> + (Si <sub>3</sub> -O-Si <sub>4</sub> ) <sup>⊕</sup>
(9n)	d <sub>1</sub> f <sub>1</sub>	Si <sub>3</sub> -OH <sup>+</sup> -Si <sub>4</sub> + H <sub>2</sub> O ⇌ (Si <sub>1</sub> -O-Si <sub>2</sub> ) <sup>⊕</sup> + (Si <sub>3</sub> -O-Si <sub>3</sub> ) <sup>⊕</sup>
(9o)	d <sub>1</sub> g <sub>1</sub>	Si <sub>3</sub> -OH <sup>+</sup> -Si <sub>4</sub> + H <sub>2</sub> O ⇌ (Si <sub>1</sub> -O-Si <sub>2</sub> ) <sup>⊕</sup> + (Si <sub>2</sub> -O-Si <sub>3</sub> ) <sup>⊕</sup>
(9p)	d <sub>1</sub> h <sub>1</sub>	Si <sub>3</sub> -OH <sup>+</sup> -Si <sub>4</sub> + H <sub>2</sub> O ⇌ (Si <sub>1</sub> -O-Si <sub>2</sub> ) <sup>⊕</sup> + (Si <sub>1</sub> -O-Si <sub>3</sub> ) <sup>⊕</sup>

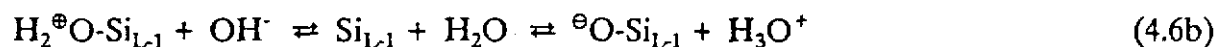
One of the reaction products for each S<sub>N</sub>2 reaction is left with a net charge which is shown as a ⊕ or ⊖ in Table 4.4. We cannot predict which of the products carries this charge. Although we might expect that any excess electrical charges would be quickly removed by the appropriate catalyst regeneration reaction, solid aluminosilicate surfaces in contact with liquids often retain excess surface charge (Stumm and Morgan, 1981). The surface charge is determined by equilibrium between surface silanol groups (≡Si-OH) and the solution:



Uncharged products of the  $S_N2$  reactions may also become charged via the reverse of a catalyst regeneration reaction. Thus, the catalyst regeneration reactions are involved in fixing the surface charge of the crystal. Another important factor in fixing the surface charge is the pH of the solution. Consider the regeneration of the catalyst from the reaction of  $Si_L-O-Si_M$  where the excess charge resides with the  $Si_{L-1}$  silicon:



or



When the solution is acidic, terminal hydroxyl groups are protonated, and under basic conditions, the terminal hydroxyl groups lose hydrogens. Thus, depending on the pH, the crystal surface may have a net positive charge, a net negative charge or no charge at all. The pH at which the surface has no net charge is called the point of zero charge,  $pH_{pzc}$ . The  $pH_{pzc}$  for quartz, amorphous silica and for silica gels is reported to be in the range  $pH_{pzc} \approx 1.5$  to 3.5 (Iler, 1979; Stumm and Morgan, 1981). The surface charge density of amorphous silica particles as a function of pH and electrolyte concentration is shown in Figure 4.8 (from Bolt, 1957). It is apparent from this figure that there is a range in pH over which the surface charge is very small and that the width of this range depends upon electrolyte concentration. The  $pH_{pzc}$  from this figure

is about 3 which is the same pH as the minimum in the quartz dissolution rate and the point at which the predominant quartz dissolution mechanism changes from acid- to base-catalyzed.

For quartz dissolution, the dissolution rate is defined in terms of the rate of appearance of aqueous silica in the solution. In the mechanism presented in Table 4.4, aqueous silica,  $\text{Si}_0$ , is produced by the acid-catalyzed reactions (12), (15) and (16) and by the base-catalyzed reactions (29), (32) and (33). All of the other reactions in this mechanism involve reactants and products that are surface species and are not observed

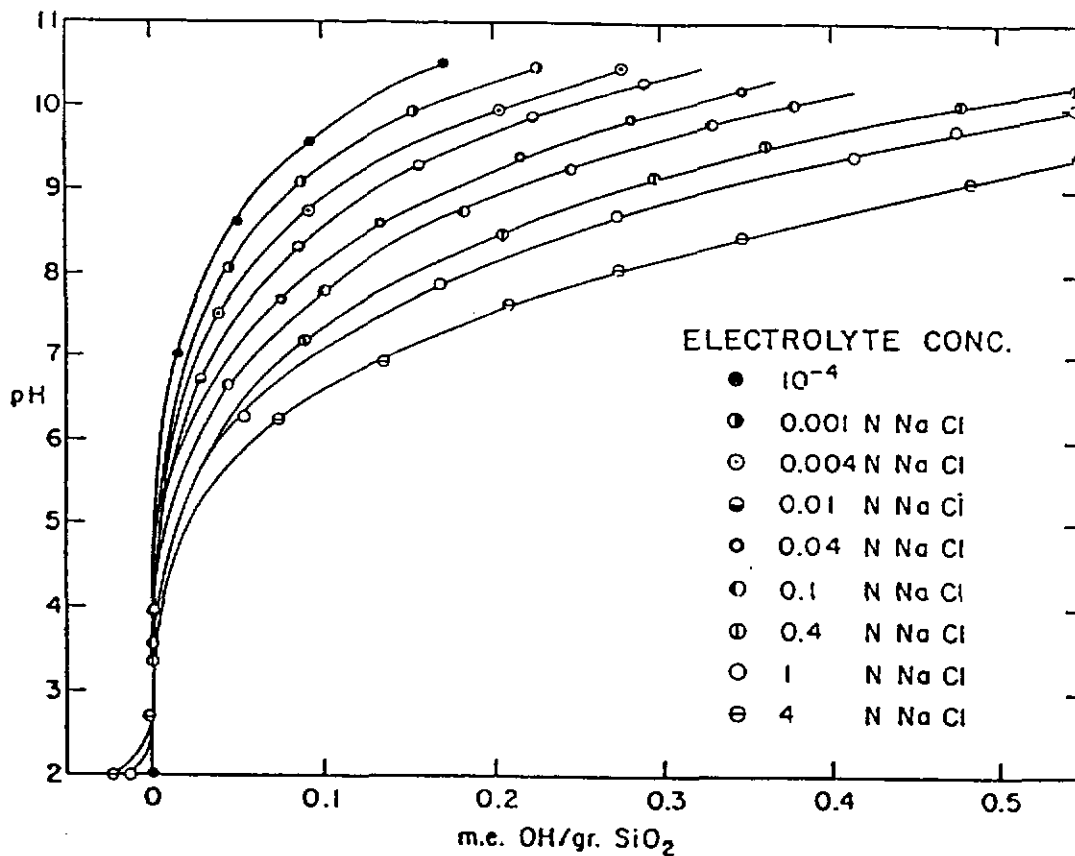


**Figure 4.8** Surface charge density as a function of pH and electrolyte concentration for an amorphous silica sol (from Bolt, 1957).

before, during or after the reaction. The fact that most of the reactants and products are species that cannot be observed experimentally limits the utility of this comprehensive quartz dissolution mechanism.

**4.4 Feldspar Dissolution Mechanism.** In addition to the hydrolysis of Si-O bonds, feldspar dissolution involves hydrolysis of Al-O bonds. There are fourteen combinations of  $\text{Si}_L\text{-O-Al}_M$  bonds:  $\text{Si}_3\text{-O-Al}_4$ ,  $\text{Si}_2\text{-O-Al}_4$ ,  $\text{Si}_1\text{-O-Al}_4$ ,  $\text{Si}_4\text{-O-Al}_3$ ,  $\text{Si}_3\text{-O-Al}_3$ ,  $\text{Si}_2\text{-O-Al}_3$ ,  $\text{Si}_1\text{-O-Al}_3$ ,  $\text{Si}_4\text{-O-Al}_2$ ,  $\text{Si}_3\text{-O-Al}_2$ ,  $\text{Si}_2\text{-O-Al}_2$ ,  $\text{Si}_1\text{-O-Al}_2$ ,  $\text{Si}_4\text{-O-Al}_1$ ,  $\text{Si}_3\text{-O-Al}_1$ , and  $\text{Si}_2\text{-O-Al}_1$ . Reaction at each site can follow the  $\text{S}_{\text{N}2}$  acid- or base-catalyzed mechanism or the (acid-catalyzed)  $\text{S}_{\text{N}1}$  mechanism. Reactions at the fourteen  $\equiv\text{Al-O-Si}\equiv$  sites are in addition to the reactions at the eight  $\equiv\text{Si-O-Si}\equiv$  sites described above for the quartz dissolution mechanism. Not counting the protonation and catalyst regeneration reactions, there are 58 independent elementary reactions in the feldspar dissolution mechanism: acid- and base-catalyzed reactions at the eight  $\equiv\text{Si-O-Si}\equiv$  sites (16 reactions) along with acid-catalyzed  $\text{S}_{\text{N}1}$  and  $\text{S}_{\text{N}2}$  reactions and the base-catalyzed  $\text{S}_{\text{N}2}$  reaction at the fourteen  $\equiv\text{Al-O-Si}\equiv$  sites (42 reactions).

Aluminum sites are brought to the crystal surface by reaction at  $\text{Si}_3\text{-O-Al}_4$ ,  $\text{Si}_2\text{-O-Al}_4$ , and  $\text{Si}_1\text{-O-Al}_4$  sites, and aluminum passes into solution by reaction at  $\text{Si}_4\text{-O-Al}_1$ ,  $\text{Si}_3\text{-O-Al}_1$ , and  $\text{Si}_2\text{-O-Al}_1$  sites. Silicon sites reach the surface by reaction at  $\text{Si}_3\text{-O-Si}_4$ ,  $\text{Si}_2\text{-O-Si}_4$ ,  $\text{Si}_1\text{-O-Si}_4$ ,  $\text{Al}_3\text{-O-Si}_4$ ,  $\text{Al}_2\text{-O-Si}_4$ , and  $\text{Al}_1\text{-O-Si}_4$  sites, and aqueous silica is formed by reaction at  $\text{Si}_1\text{-O-Si}_4$ ,  $\text{Si}_1\text{-O-Si}_3$ ,  $\text{Si}_1\text{-O-Si}_2$ ,  $\text{Al}_4\text{-O-Si}_1$ ,  $\text{Al}_3\text{-O-Si}_1$ , and  $\text{Al}_2\text{-O-Si}_1$  sites.

As with the comprehensive mechanism for quartz dissolution, the detailed feldspar dissolution mechanism requires information about the composition of the surface of the dissolving mineral. The fact that the surface species concentrations cannot be measured limits the utility of these comprehensive mechanisms developed in this chapter. In Chapter 5, we will use these comprehensive reaction mechanisms to develop a simplified mechanism that contains all the relevant kinetics of the comprehensive mechanisms and will derive rate laws for these simplified mechanisms.



## Chapter 5

### Rate Laws for Quartz and Albite Dissolution

To test a reaction mechanism against experimental data, each elementary reaction in the mechanism must first be translated into a mathematical equation - a rate law - which relates the rate of that reaction to observable parameters such as species concentrations. It is usually possible to find several different sets of elementary reactions that can be fit to the reaction rate data, and no matter how well a mechanism fits the rate data, it is not necessarily a unique description of the observable behavior of the reaction. We cannot *prove* that a reaction occurs by a particular mechanism, we can only show that a mechanism is consistent with the experimental rate data.

There are several levels of at which mechanisms can be profitably analyzed. Certainly, the most information is contained in the detailed analysis of the mechanism - that is, in solving the set of rate equations for the entire mechanism. However, simultaneous solution of large numbers of equations often requires complex mathematical techniques which tend to overshadow the kinetics while providing meager additional insight into the reaction processes. An important simplification is obtained when the system of equations is reduced to a set of rate-limiting steps - only the slowest elementary step along each reaction path is included in the analysis. The risk here is in choosing the appropriate reaction as the rate-limiting step, and this approach does not work well when several reactions along a single reaction pathway have nearly the same intrinsic rates. The simplest level of analysis involves empirical rate laws in which

most of the kinetic insight is sacrificed for the simplicity of a very few rate equations that capture the essential behavior of the reacting system. In this chapter, we will use a combination of these approaches in analyzing quartz dissolution kinetics.

**5.1 Rate Laws for Elementary Reactions in Solution.** In the gas phase, the forward rate of an elementary reaction is proportional to the product of the species concentrations. However, under the conditions at which gas phase reactions are studied, pure gases and gas mixtures often exhibit ideal (or nearly ideal) behavior. Except for very dilute solutions, mixing behavior is often very non-ideal in condensed phases. To correct for the non-ideal behavior of species in aqueous solution, the rates of reactions in solution are explicitly written as proportional to the product of the reactant activities rather than concentrations (Glasstone, et al. 1941; Adamson, 1979; Moore and Pearson, 1981; Francisco, et al., in press).

On the other hand, reaction stoichiometry for reactions in aqueous solution follow mass action laws: reactants combine in fixed proportions which are directly related to the reactant species concentrations. Changes in species concentrations are proportional to reaction rates which, in turn, depend upon species activities. For example, consider the elementary reaction in solution whose mechanism is given by equation (5.1):



The rate of change of species concentrations is given by the stoichiometry of the reaction:

$$\mathfrak{R} = - \frac{1}{\nu_A} \frac{d\{A\}}{dt} = - \frac{1}{\nu_B} \frac{d\{B\}}{dt} = \frac{1}{\nu_P} \frac{d\{P\}}{dt} \quad (5.2)$$

where  $\nu_i$  is the stoichiometric coefficient of species  $i$  in the elementary reaction. The forward rate of this reaction depends upon species activities and is written empirically as:

$$\mathfrak{R}_{\text{forward}} = k_1 [A] [B] \quad (5.3)$$

where  $k_1$  is the rate constant and  $[A]$  and  $[B]$  are the activities of species A and B, respectively. The rate of the reverse reaction also depends upon species activities:

$$\mathfrak{R}_{\text{reverse}} = k_{-1} [P] \quad (5.4)$$

where  $k_{-1}$  is the rate constant for the reverse reaction and  $[P]$  is the activity of P. The net rate of the reaction is the difference between the forward and reverse rates:

$$\mathfrak{R}_{\text{net}} = k_1 [A] [B] - k_{-1} [P] \quad (5.5)$$

At equilibrium, the net rate is zero, and equation (5.5) can be rearranged to give:

$$\frac{k_1}{k_{-1}} = \frac{[P]}{[A][B]} = K^{eq} \quad (5.6)$$

where  $K^{eq}$  is the thermodynamic equilibrium constant for the elementary reaction (equation (5.1)).

**5.2 Rate Expressions for the Quartz Dissolution Mechanism.** Rate expressions corresponding to the reactions in Table 4.4 are presented in Table 5.1. According to the rate laws for elementary reactions discussed above, the forward rates of elementary reactions depend on reactant activities. Since the reactants for each elementary reaction in Table 4.5 are identical, the rate expressions for the forward reactions are also identical, and the same rate expression holds for the forward rate of reaction (9) in Table 4.4 which is the composite of the reactions in Table 4.5.

Our concern here is with quartz dissolution, so the rate expressions for the rate-limiting steps (the acid- and base-catalyzed  $S_N2$  reactions) will not include the contributions from the reverse reactions to avoid the complication of dealing with the set of elementary reactions presented in Table 4.5 and equivalent reactions for each of the other  $S_N2$  reactions in Table 4.4. Proton transfer reactions - protonation and catalyst regeneration - are observed to be much faster than the hydrolysis reactions (see Chou and Wollast, 1984, 1985; Holdren and Speyer, 1985b; Knauss and Wolery, 1986), and so, are near equilibrium.

**Table 5.1** Rate laws for the elementary reactions in Table 4.4.

Protonation Reactions:

- (1)  $\mathfrak{R}_1 = k_1 [\text{Si}_3\text{-O-Si}_4][\text{H}_3\text{O}^+] - k_{-1} [\text{Si}_3\text{-OH}^+\text{-Si}_4]$
- (2)  $\mathfrak{R}_2 = k_2 [\text{Si}_3\text{-O-Si}_3][\text{H}_3\text{O}^+] - k_{-2} [\text{Si}_3\text{-OH}^+\text{-Si}_3]$
- (3)  $\mathfrak{R}_3 = k_3 [\text{Si}_2\text{-O-Si}_3][\text{H}_3\text{O}^+] - k_{-3} [\text{Si}_2\text{-OH}^+\text{-Si}_3]$
- (4)  $\mathfrak{R}_4 = k_4 [\text{Si}_1\text{-O-Si}_3][\text{H}_3\text{O}^+] - k_{-4} [\text{Si}_1\text{-OH}^+\text{-Si}_3]$
- (5)  $\mathfrak{R}_5 = k_5 [\text{Si}_2\text{-O-Si}_4][\text{H}_3\text{O}^+] - k_{-5} [\text{Si}_2\text{-OH}^+\text{-Si}_4]$
- (6)  $\mathfrak{R}_6 = k_6 [\text{Si}_2\text{-O-Si}_2][\text{H}_3\text{O}^+] - k_{-6} [\text{Si}_2\text{-OH}^+\text{-Si}_2]$
- (7)  $\mathfrak{R}_7 = k_7 [\text{Si}_1\text{-O-Si}_2][\text{H}_3\text{O}^+] - k_{-7} [\text{Si}_1\text{-OH}^+\text{-Si}_2]$
- (8)  $\mathfrak{R}_8 = k_8 [\text{Si}_1\text{-O-Si}_4][\text{H}_3\text{O}^+] - k_{-8} [\text{Si}_1\text{-OH}^+\text{-Si}_4]$

Acid-Catalyzed  $S_N2$  Reactions:

- (9)  $\mathfrak{R}_9 = k_9 [\text{Si}_3\text{-OH}^+\text{-Si}_4][\text{H}_2\text{O}]$
- (10)  $\mathfrak{R}_{10} = k_{10} [\text{Si}_3\text{-OH}^+\text{-Si}_3][\text{H}_2\text{O}]$
- (11)  $\mathfrak{R}_{11} = k_{11} [\text{Si}_2\text{-OH}^+\text{-Si}_3][\text{H}_2\text{O}]$
- (12)  $\mathfrak{R}_{12} = k_{12} [\text{Si}_1\text{-OH}^+\text{-Si}_3][\text{H}_2\text{O}]$
- (13)  $\mathfrak{R}_{13} = k_{13} [\text{Si}_2\text{-OH}^+\text{-Si}_4][\text{H}_2\text{O}]$
- (14)  $\mathfrak{R}_{14} = k_{14} [\text{Si}_2\text{-OH}^+\text{-Si}_2][\text{H}_2\text{O}]$
- (15)  $\mathfrak{R}_{15} = k_{15} [\text{Si}_1\text{-OH}^+\text{-Si}_2][\text{H}_2\text{O}]$
- (16)  $\mathfrak{R}_{16} = k_{16} [\text{Si}_1\text{-OH}^+\text{-Si}_4][\text{H}_2\text{O}]$

Acid Catalyst Regeneration:

- (17)  $\mathfrak{R}_{17} = k_{17} [(\text{Si}_3\text{-O-Si}_4)^\oplus][\text{H}_2\text{O}] - k_{-17} [\text{Si}_3\text{-O-Si}_4][\text{H}_3\text{O}^+]$
- (18)  $\mathfrak{R}_{18} = k_{18} [(\text{Si}_3\text{-O-Si}_3)^\oplus][\text{H}_2\text{O}] - k_{-18} [\text{Si}_3\text{-O-Si}_3][\text{H}_3\text{O}^+]$
- (19)  $\mathfrak{R}_{19} = k_{19} [(\text{Si}_2\text{-O-Si}_3)^\oplus][\text{H}_2\text{O}] - k_{-19} [\text{Si}_2\text{-O-Si}_3][\text{H}_3\text{O}^+]$
- (20)  $\mathfrak{R}_{20} = k_{20} [(\text{Si}_1\text{-O-Si}_3)^\oplus][\text{H}_2\text{O}] - k_{-20} [\text{Si}_1\text{-O-Si}_3][\text{H}_3\text{O}^+]$
- (21)  $\mathfrak{R}_{21} = k_{21} [(\text{Si}_2\text{-O-Si}_4)^\oplus][\text{H}_2\text{O}] - k_{-21} [\text{Si}_2\text{-O-Si}_4][\text{H}_3\text{O}^+]$
- (22)  $\mathfrak{R}_{22} = k_{22} [(\text{Si}_2\text{-O-Si}_2)^\oplus][\text{H}_2\text{O}] - k_{-22} [\text{Si}_2\text{-O-Si}_2][\text{H}_3\text{O}^+]$
- (23)  $\mathfrak{R}_{23} = k_{23} [(\text{Si}_1\text{-O-Si}_2)^\oplus][\text{H}_2\text{O}] - k_{-23} [\text{Si}_1\text{-O-Si}_2][\text{H}_3\text{O}^+]$
- (24)  $\mathfrak{R}_{24} = k_{24} [(\text{Si}_1\text{-O-Si}_4)^\oplus][\text{H}_2\text{O}] - k_{-24} [\text{Si}_1\text{-O-Si}_4][\text{H}_3\text{O}^+]$
- (25)  $\mathfrak{R}_{25} = k_{25} [(\text{Si}_0)^\oplus][\text{H}_2\text{O}] - k_{-25} [\text{Si}_0][\text{H}_3\text{O}^+]$

Table 5.1 (Continued)

Base-Catalyzed  $S_N2$  Reactions:

- (26)  $\mathfrak{R}_{26} = k_{26} [\text{Si}_3\text{-O-Si}_4][\text{OH}^-]$   
 (27)  $\mathfrak{R}_{27} = k_{27} [\text{Si}_3\text{-O-Si}_3][\text{OH}^-]$   
 (28)  $\mathfrak{R}_{28} = k_{28} [\text{Si}_2\text{-O-Si}_3][\text{OH}^-]$   
 (29)  $\mathfrak{R}_{29} = k_{29} [\text{Si}_1\text{-O-Si}_3][\text{OH}^-]$   
 (30)  $\mathfrak{R}_{30} = k_{30} [\text{Si}_2\text{-O-Si}_4][\text{OH}^-]$   
 (31)  $\mathfrak{R}_{31} = k_{31} [\text{Si}_2\text{-O-Si}_2][\text{OH}^-]$   
 (32)  $\mathfrak{R}_{32} = k_{32} [\text{Si}_1\text{-O-Si}_2][\text{OH}^-]$   
 (33)  $\mathfrak{R}_{33} = k_{33} [\text{Si}_1\text{-O-Si}_4][\text{OH}^-]$

Base Catalyst Regeneration:

- (34)  $\mathfrak{R}_{34} = k_{34} [(\text{Si}_3\text{-O-Si}_4)^\ominus][\text{H}_2\text{O}] - k_{-34} [\text{Si}_3\text{-O-Si}_4][\text{OH}^-]$   
 (35)  $\mathfrak{R}_{35} = k_{35} [(\text{Si}_3\text{-O-Si}_3)^\ominus][\text{H}_2\text{O}] - k_{-35} [\text{Si}_3\text{-O-Si}_3][\text{OH}^-]$   
 (36)  $\mathfrak{R}_{36} = k_{36} [(\text{Si}_2\text{-O-Si}_3)^\ominus][\text{H}_2\text{O}] - k_{-36} [\text{Si}_2\text{-O-Si}_3][\text{OH}^-]$   
 (37)  $\mathfrak{R}_{37} = k_{37} [(\text{Si}_1\text{-O-Si}_3)^\ominus][\text{H}_2\text{O}] - k_{-37} [\text{Si}_1\text{-O-Si}_3][\text{OH}^-]$   
 (38)  $\mathfrak{R}_{38} = k_{38} [(\text{Si}_2\text{-O-Si}_4)^\ominus][\text{H}_2\text{O}] - k_{-38} [\text{Si}_2\text{-O-Si}_4][\text{OH}^-]$   
 (39)  $\mathfrak{R}_{39} = k_{39} [(\text{Si}_2\text{-O-Si}_2)^\ominus][\text{H}_2\text{O}] - k_{-39} [\text{Si}_2\text{-O-Si}_2][\text{OH}^-]$   
 (40)  $\mathfrak{R}_{40} = k_{40} [(\text{Si}_1\text{-O-Si}_2)^\ominus][\text{H}_2\text{O}] - k_{-40} [\text{Si}_1\text{-O-Si}_2][\text{OH}^-]$   
 (41)  $\mathfrak{R}_{41} = k_{41} [(\text{Si}_1\text{-O-Si}_4)^\ominus][\text{H}_2\text{O}] - k_{-41} [\text{Si}_1\text{-O-Si}_4][\text{OH}^-]$   
 (42)  $\mathfrak{R}_{42} = k_{42} [(\text{Si}_0)^\ominus][\text{H}_2\text{O}] - k_{-42} [\text{Si}_0][\text{OH}^-]$

Consider the rate expression for one of the acid-catalyzed elementary reactions

[reaction (9), Table 4.4]:

$$\mathfrak{R}_9 = k_9 [\text{Si}_3\text{-OH}^+\text{-Si}_4][\text{H}_2\text{O}] \quad (5.7)$$

If the protonation reaction for  $\text{Si}_3\text{-OH}^+\text{-Si}_4$  [ie. reaction (1), Table 4.4] is in equilibrium, we can express  $[\text{Si}_3\text{-OH}^+\text{-Si}_4]$  in terms of  $[\text{Si}_3\text{-O-Si}_4]$  and  $[\text{H}_3\text{O}^+]$  using equation (5.6):

$$[\text{Si}_3\text{-OH}^+\text{-Si}_4] = K^{\text{eq}} [\text{Si}_3\text{-O-Si}_4][\text{H}_3\text{O}^+] \quad (5.8)$$

and substitute this expression into equation (5.7):

$$\mathfrak{R}_9 = k_9 K^{\text{eq}} [\text{Si}_3\text{-O-Si}_4][\text{H}_3\text{O}^+][\text{H}_2\text{O}] \quad (5.9)$$

The base-catalyzed reaction mechanisms do not involve a preliminary protonation step, and the rate of these reactions is taken directly from Table 5.1:

$$\mathfrak{R}_{26} = k_{26} [\text{Si}_3\text{-O-Si}_4][\text{OH}^-] \quad (5.10)$$

Notice that the rate of each  $S_{\text{N}}2$  reaction given in Table 4.4 [reactions (9) through (16) and (26) through (33)] can be written in a form that is first order in catalyst activity. However, the result of each of these  $S_{\text{N}}2$  reactions is the production of *two* Si-OH species from one Si-O-Si. Any linear combination of these reactions will give the same result: two product Si's per catalyst molecule. *Thus, on a per product Si basis, each of these reactions consumes 0.5  $\text{H}_3\text{O}^+$  molecules.*

As discussed in Chapter 4, the rate of quartz dissolution, which is given on a per  $\text{H}_4\text{SiO}_{4(\text{aq})}$  basis, is one-half order in  $[\text{H}_3\text{O}^+]$  (or  $[\text{H}^+]$ ) for the acid-catalyzed reaction and one-half order in  $[\text{OH}^-]$  for the base-catalyzed reaction. Furthermore, since the acid-catalyzed mechanism requires that the surface bonds be protonated prior to the addition of a water molecule and reaction at an  $\text{=Si-O-Si=}$  site, the acid-catalyzed

mechanism is predominant at a pH less than the  $\text{pH}_{\text{pzc}}$  ( $\text{pH} \approx 3$ ) for quartz. The importance of Kamiya, et al.'s (1974) data is apparent: it supports the prediction of one-half order dependence of the quartz dissolution rate on pH at low pH. This pH dependence is not clearly defined in Knauss and Wolery's (1988) data on quartz dissolution at 70°C, and there is no data on the pH dependence of the quartz dissolution rate at 25°C and low pH. Experiments (discussed in Chapter 6) conducted to test the pH dependence of the quartz dissolution rate at low pH and 23°C confirmed the one-half order  $[\text{H}^+]$  (or  $[\text{H}_3\text{O}^+]$ ) dependence of the quartz dissolution rate at low pH.

*5.2.1 Comprehensive Rate Expression for Quartz Dissolution.* In a network of coupled reactions, the rate of change of a species concentration is given by:

$$\frac{d \{\text{Si}_L\text{-OH}^+\text{-Si}_M\}}{dt} = \sum_i \nu_i \mathfrak{R}_i \quad (5.11)$$

where  $\nu_i$  and  $\mathfrak{R}_i$  are the stoichiometric coefficient of the species and rate of the  $i^{\text{th}}$  reaction, respectively; and the summation is carried out over all elementary reactions. For example, the rate of change of  $\text{Si}_3\text{-O-Si}_4$  concentration with time is

$$\frac{d \{\text{Si}_3\text{-OH}^+\text{-Si}_4\}}{dt} = (e_1 - 1)\mathfrak{R}_9 + e_5\mathfrak{R}_{13} + e_8\mathfrak{R}_{16} \quad (5.12)$$

where the  $(e_1 - 1)$  term indicates that  $e_1$  moles of  $\text{Si}_3\text{-OH}^+\text{-Si}_4$  are produced by reaction



(9) in Table 4.4 for every mole of  $\text{Si}_3\text{-OH}^+\text{-Si}_4$  that is consumed in the reaction. The reaction network for a system of reactions is formed by writing equation (5.12) for every component in the system. This set of rate expressions is listed in Table 5.2.

**Table 5.2** Rate equations for the change in surface species concentrations with time for the acid-catalyzed  $\text{S}_{\text{u}2}$  reactions given in Table 4.4. The  $\mathfrak{R}_i$  are given in Table 5.1.

---


$$\begin{aligned} \frac{d \{ \text{Si}_3\text{-OH}^+\text{-Si}_4 \}}{dt} &= (e_1-1)\mathfrak{R}_9 + e_5\mathfrak{R}_{13} + e_8\mathfrak{R}_{16} \\ \frac{d \{ \text{Si}_3\text{-OH}^+\text{-Si}_3 \}}{dt} &= f_1\mathfrak{R}_9 - \mathfrak{R}_{10} + f_{13}\mathfrak{R}_5 + b_8\mathfrak{R}_{16} \\ \frac{d \{ \text{Si}_2\text{-OH}^+\text{-Si}_3 \}}{dt} &= (b_1+g_1)\mathfrak{R}_9 + 2b_2\mathfrak{R}_{10} + (b_3-1)\mathfrak{R}_{11} + b_4\mathfrak{R}_{12} + g_5\mathfrak{R}_{13} + c_8\mathfrak{R}_{16} \\ \frac{d \{ \text{Si}_1\text{-OH}^+\text{-Si}_3 \}}{dt} &= h_1\mathfrak{R}_9 + f_3\mathfrak{R}_{11} - \mathfrak{R}_{12} + (b_5+h_5)\mathfrak{R}_{13} + 2b_6\mathfrak{R}_{14} + b_7\mathfrak{R}_{15} + d_8\mathfrak{R}_{16} \\ \frac{d \{ \text{Si}_2\text{-OH}^+\text{-Si}_4 \}}{dt} &= a_1\mathfrak{R}_9 + 2a_2\mathfrak{R}_{10} + a_3\mathfrak{R}_{11} + a_4\mathfrak{R}_{12} - \mathfrak{R}_{13} \\ \frac{d \{ \text{Si}_2\text{-OH}^+\text{-Si}_2 \}}{dt} &= c_1\mathfrak{R}_9 + 2c_2\mathfrak{R}_{10} + c_3\mathfrak{R}_{11} + c_4\mathfrak{R}_{12} - \mathfrak{R}_{14} \\ \frac{d \{ \text{Si}_1\text{-OH}^+\text{-Si}_2 \}}{dt} &= d_1\mathfrak{R}_9 + 2d_2\mathfrak{R}_{10} + (d_3+g_3)\mathfrak{R}_{11} + d_4\mathfrak{R}_{12} + c_5\mathfrak{R}_{13} + 2c_6\mathfrak{R}_{14} \\ &\quad + (c_7-1)\mathfrak{R}_{15} \\ \frac{d \{ \text{Si}_1\text{-OH}^+\text{-Si}_4 \}}{dt} &= e_3\mathfrak{R}_{11} + a_5\mathfrak{R}_{13} + 2a_6\mathfrak{R}_{14} + a_7\mathfrak{R}_{15} - \mathfrak{R}_{16} \\ \frac{d \{ \text{Si}_0 \}}{dt} &= \mathfrak{R}_{12} + \mathfrak{R}_{15} + \mathfrak{R}_{16} \end{aligned}$$

The rate equations given in Table 5.2 can be written in matrix notation as:

$$\underline{\dot{s}} = \underline{L} \underline{r} \quad (5.13)$$

where  $\underline{\dot{s}}$  and  $\underline{r}$  are vectors whose elements are the time derivative of the species concentrations and the rates of the reactions, respectively:

$$\underline{\dot{s}} = \frac{d}{dt} \begin{bmatrix} \{Si_3-OH^+-Si_4\} \\ \vdots \\ \{Si_1-OH^+-Si_4\} \\ \{Si_0\} \end{bmatrix}, \quad \underline{r} = \begin{bmatrix} \mathfrak{R}_1 \\ \vdots \\ \mathfrak{R}_n \end{bmatrix} \quad (5.14)$$

and the elements of the variable matrix,  $\underline{L}$ , are the "stoichiometric" coefficients of the reaction rates given by the set of rate equations in Table 5.2. Although there are nine rate equations in Table 5.2, only seven of the first eight are independent. In principle, we can solve for  $\underline{r}$  if we know  $\underline{\dot{s}}$  and  $\underline{L}$  by inverting  $\underline{L}$  and premultiplying both sides by  $\underline{L}^{-1}$ :

$$\underline{r} = \underline{L}^{-1} \underline{L} \underline{r} = \underline{L}^{-1} \underline{\dot{s}}. \quad (5.16)$$

Under steady-state conditions, the concentrations of surface species should not change, so the first eight terms of  $\underline{\dot{s}}$  are equal to zero. The last term of  $\underline{\dot{s}}$  is the rate at which

$\text{Si}_1$ 's leave the surface which is the same as the rate with which aqueous silica appears in solution. The value for this term comes from experimental data. Since all but the last term of  $\underline{s}$  are zero, the rate vector,  $\underline{r}$ , is determined by the last column of  $\underline{\underline{L}}^{-1}$ . Each term in this column must be positive for the individual terms in the rate vector to be positive.

There are 40 undetermined multipliers and 11 constraints (giving a total of 29 independent undetermined multipliers) in  $\underline{\underline{L}}$ . Even with the requirement that the individual terms of  $\underline{r}$  be positive, this system of equations is severely underdetermined, and without additional information or constraints, cannot be solved.

*5.2.2 Graph of the Quartz Dissolution Mechanism.* Comprehending the interrelationships in a large set of reactions such as the quartz dissolution mechanism in Table 4.4 can be very difficult. A complex reaction network is often easier to visualize when presented in graphical form. A graph of the acid-catalyzed quartz dissolution mechanism is shown in Figure 5.1. The corners (or vertices) of the graph are labeled as the various  $\equiv\text{Si-O-Si}\equiv$  moieties, and the lines connecting the vertices (the edges) correspond to chemical reactions. Each line is directed from the reactant to one of the possible products of the reaction and is labeled with the stoichiometric coefficient of the product (that is, the appropriate element of  $\underline{\underline{L}}$ ) for that reaction. The heavy lines indicate bi-directional connections between the two species, ie. each interconnection has a parallel interconnection that has the opposite direction so that the reactant for one of the reaction pathways is the product for the other pathway.

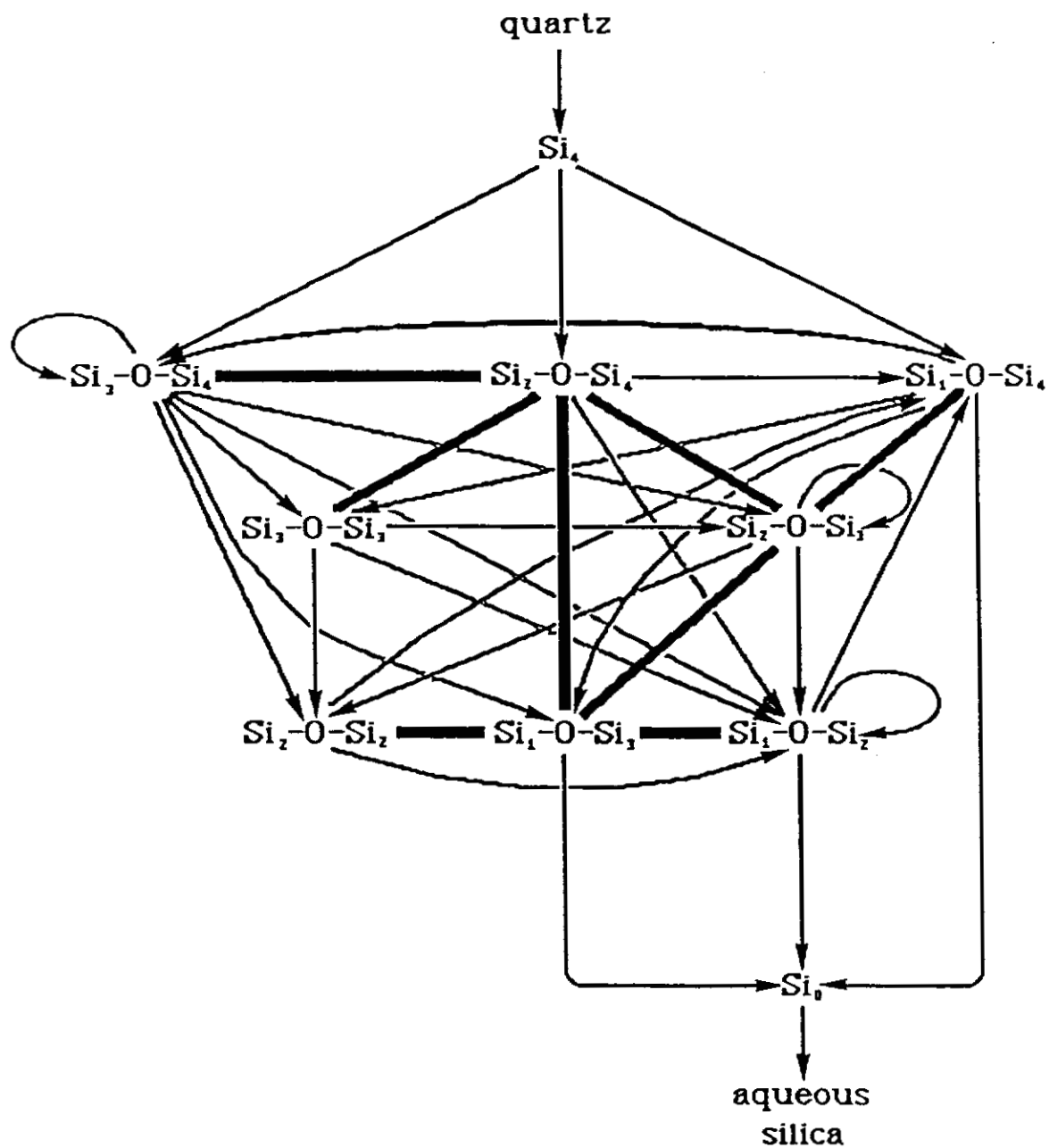


**Figure 5.1** Graph of the quartz dissolution mechanism. Each vertex is a surface species and each directed line represents one or more reversible elementary reactions from Table 5.2. The arrows point in the direction of the dissolution reaction. Complete cycles that include only two vertices (or bi-directional connections) are shown as heavy lines.

These pairs of parallel lines represent reversible reaction pathways, and not reversible reactions. In fact, each directed line is a reversible reaction where the direction indicates the pathway for dissolution. A bi-directional pair of reactions forms a closed cycle between two surface species. Other closed cycles also exist in Figure 5.1, but not all of these cycles are reversible. The reversibility of closed cycles can be important in determining possible reaction pathways. Even though microscopic reversibility is subsumed in the individual directed lines in Figure 5.1, under conditions far from equilibrium, reversible reactions can behave irreversibly.

Although there may not be a direct reaction pathway from one particular  $\equiv\text{Si-O-Si}\equiv$  species to every other  $\equiv\text{Si-O-Si}\equiv$  species in Figure 5.1, there is at least one closed cycle that connects every  $\equiv\text{Si-O-Si}\equiv$  species into the network. At the top and bottom of the graphs in Figure 5.1 are the bulk crystal species,  $\text{Si}_4$ , and aqueous silica,  $\text{Si}_0$ . Aqueous silica is produced by reactions (12), (15) and (16) in Table 4.4. Reaction at  $\text{Si}_3\text{-O-Si}_4$ ,  $\text{Si}_2\text{-O-Si}_4$ , and  $\text{Si}_1\text{-O-Si}_4$  sites brings material from the bulk crystal to the surface. This reaction mechanism is essentially a chain reaction mechanism where reaction at  $\text{Si}_3\text{-O-Si}_4$ ,  $\text{Si}_2\text{-O-Si}_4$ , and  $\text{Si}_1\text{-O-Si}_4$  sites are the "initiation" steps, reaction at  $\text{Si}_1\text{-O-Si}_4$ ,  $\text{Si}_1\text{-O-Si}_3$ , and  $\text{Si}_1\text{-O-Si}_2$  sites are the "termination" steps, and all other reactions are the "propagation" steps. At steady-state, the rate at which crystalline material arrives at the surface must equal the rate of production of aqueous silica:

$$\begin{aligned}
 & k_9 [\text{Si}_3\text{-OH}^+\text{-Si}_4][\text{H}_2\text{O}] + k_{13} [\text{Si}_2\text{-OH}^+\text{-Si}_4][\text{H}_2\text{O}] + k_{16} [\text{Si}_1\text{-OH}^+\text{-Si}_4][\text{H}_2\text{O}] \quad (5.17) \\
 & = k_{16} [\text{Si}_1\text{-OH}^+\text{-Si}_4][\text{H}_2\text{O}] + k_{12} [\text{Si}_1\text{-OH}^+\text{-Si}_3][\text{H}_2\text{O}] + k_{15} [\text{Si}_1\text{-OH}^+\text{-Si}_2][\text{H}_2\text{O}]
 \end{aligned}$$

This rate is also equal to the bulk rate of quartz dissolution,  $\mathfrak{R}_{\text{qtz}}$ , which is expressed in terms of the rate of appearance of silica in solution.

According to equation (5.17), the rate of quartz dissolution is the sum of the rates of three reactions:

$$\mathfrak{R}_{\text{qtz}} = k_9 [\text{Si}_3\text{-OH}^+\text{-Si}_4][\text{H}_2\text{O}] + k_{13} [\text{Si}_2\text{-OH}^+\text{-Si}_4][\text{H}_2\text{O}] + k_{16} [\text{Si}_1\text{-OH}^+\text{-Si}_4][\text{H}_2\text{O}] \quad (5.17a)$$

But which of these reactions are important in determining the rate? It may be that one reaction dominates the kinetics while the other two are relatively unimportant. On the other hand, two or even all three may contribute significantly to the overall rate.

From the discussion in Chapter 4 on the relative reactivity of the various groups, we expect that  $k_9 \ll k_{13} < k_{16}$ , but we have no direct measurement of the relative importance of  $k_9 [\text{Si}_3\text{-OH}^+\text{-Si}_4]$ ,  $k_{13} [\text{Si}_2\text{-OH}^+\text{-Si}_4]$ , and  $k_{16} [\text{Si}_1\text{-OH}^+\text{-Si}_4]$ . The  $\text{Si}_3\text{-O-Si}_4$ ,  $\text{Si}_2\text{-O-Si}_4$ , and  $\text{Si}_1\text{-O-Si}_4$  sites may be related to bulk surface, "ledge" and "kink" sites, respectively, as shown in Figure 5.2. Dissolution at ledge and kink sites is much more rapid than at the bulk surface sites, but the concentrations of ledge and kink sites is much less than the concentration of bulk surface sites. Etch pits form at defects or dislocations in the crystal lattice where the excess energy of the reactants effectively lowers the activation energy for  $\equiv\text{Si-O-Si}\equiv$  bond hydrolysis. In addition, etch pits increase the number of ledges and hence, the number of  $\text{Si}_2$  and  $\text{Si}_1$  sites in the crystal surface.

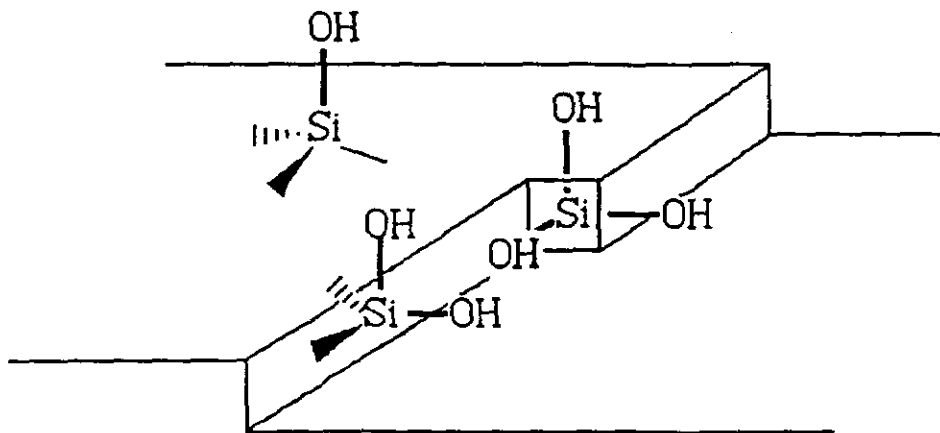


**Figure 5.2.** Idealized quartz surface showing the relationship between  $Si_3$ ,  $Si_2$  and  $Si_1$  sites and bulk surface, ledge and kink sites.

**5.3 Rate Expressions for Feldspar Dissolution Kinetics.** The comprehensive mechanism for quartz dissolution explains the observed pH dependence of quartz dissolution in terms of two mechanisms operating in parallel - the acid- and base-catalyzed mechanisms - and shows why the acid-catalyzed mechanism is favored at pH values lower than the  $pH_{pzc}$ . The graph of this mechanism suggests that the tendency to form etch pits can be interpreted in terms of the relative rates of several competing initiation reactions. When the reactions involving the substitution of aluminum in the tetrahedral sites are included, there are far too many reaction pathways for the feldspar mechanism to be graphed.

There are two major differences between the rate data for feldspar dissolution and that for quartz dissolution. First, the slopes of the log rate versus pH lines (Figures 2.6 and 2.7) are about one-third in the case of feldspar dissolution rather than the more easily explained slope of one-half observed for quartz dissolution. Second, the pH at which the predominant mechanism changes from acid- to base-catalysis is apparently not related to the  $\text{pH}_{\text{pzc}}$  for feldspar which is approximately a pH of 2 to 3 (Stumm and Morgan, 1981).

*5.3.1 Effect of Dissolved Aluminum on the Feldspar Dissolution Rate.* Chou and Wollast (1985) reported that dissolved aluminum retards the rate of feldspar dissolution. Their graph of the effect of aluminum concentration in solution on the logarithm of the dissolution rate is presented in Figure 5.3. The slope of this graph is reported to be -0.385 log units per log unit change in aluminum molarity. If the inhibiting effect of aqueous aluminum is independent of pH, we can use this data to "adjust" the steady-state rate of feldspar dissolution for the aluminum content in the solution.

Steady-state feldspar dissolution rates reported by Chou and Wollast (1984, 1985) and Knauss and Wolery (1986) are calculated from the reactor effluent solution composition as reported in Chapter 2. Aluminum concentrations in the reactor effluent were back-calculated from the reported steady-state dissolution rates. The change in aluminum molarity depends upon the choice of the "zero" aluminum concentration. Since the detection limit for aluminum in aqueous solution using graphite furnace



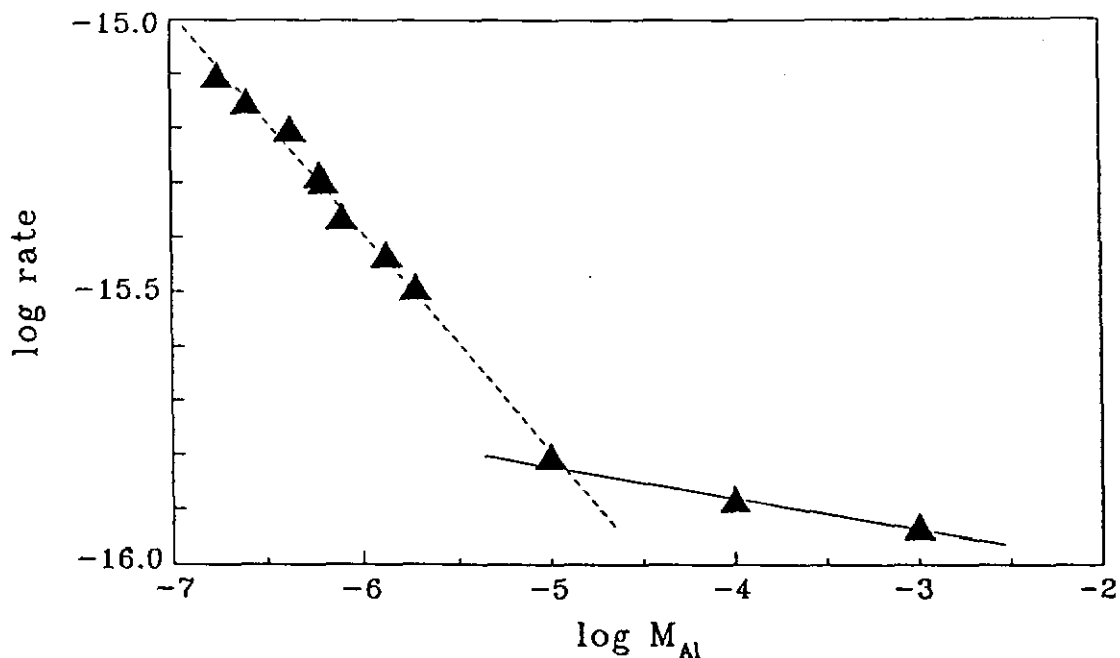


**Figure 5.3** Effect of dissolved aluminum concentration of the rate of dissolution of feldspar (from Chou and Wollast, 1985).

atomic absorption spectrophotometry is approximately  $10^{-7}$  M, the "zero" aluminum concentration was chosen to be  $10^{-8}$  M. We can calculate the change in feldspar dissolution rate due to dissolved aluminum from the slope of the log rate versus log aluminum molarity graph in Figure 5.3. The "adjusted" feldspar dissolution rates are compared with the reported rates in Figure 5.4. The slopes of the "adjusted" log rate versus pH curves are one-half - the same as for quartz.

When the rates have been corrected for the inhibiting effect of the aluminum concentration in solution, feldspar dissolution is one-half order in catalyst concentration. This result is not surprising since the elementary reactions for feldspar dissolution have

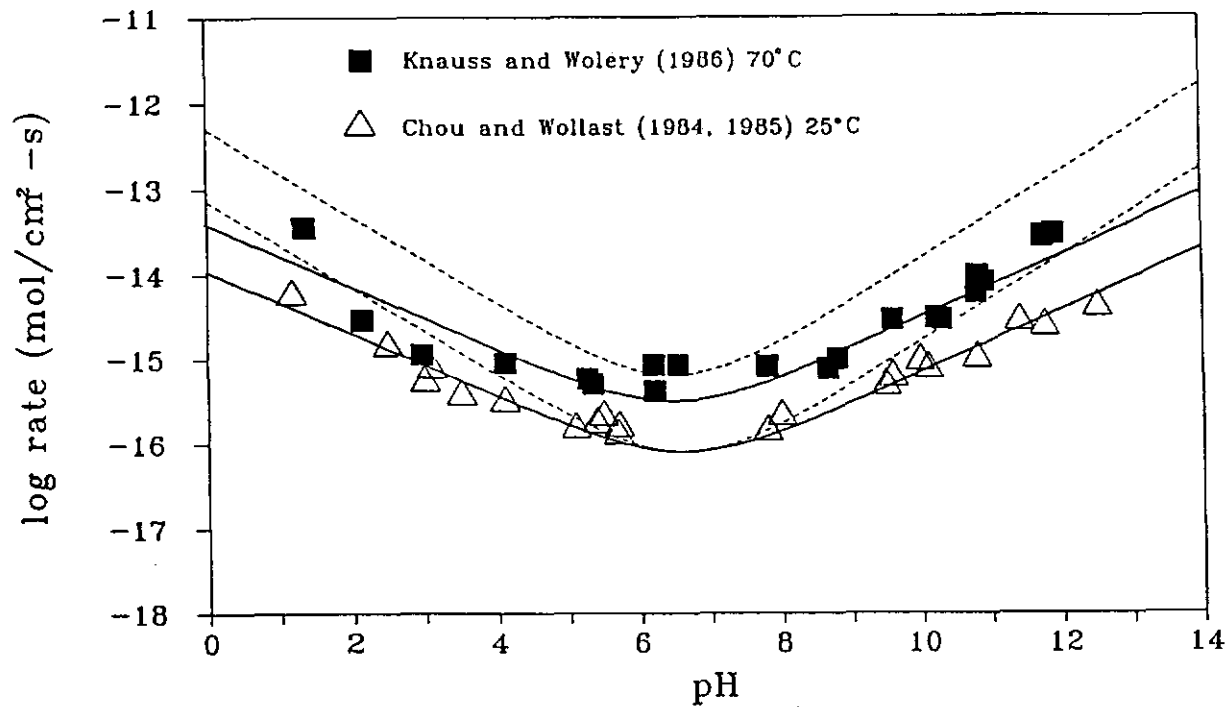
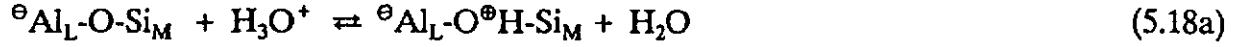


**Figure 5.4** Albite dissolution rates (solid lines) and rates adjusted for the effect of dissolved aluminum (dashed lines). The dashed lines are consistent with reaction orders with respect to catalyst concentration of one-half.

the same order with respect to catalyst concentration as the elementary reactions for quartz dissolution.

*5.3.2 The Effect of  $S_N1$  versus  $S_N2$  Mechanisms on the Rate of Feldspar Dissolution at Low pH.* Because the valence of aluminum is three, tetrahedrally coordinated aluminum carries excess electrons. Aluminum can satisfy its valence orbitals and reduce its formal charge by giving up one bond. In the  $S_N2$  mechanism, one bond is formed as another is broken in a concerted process, but when one bond is broken before the other is formed, the reaction follows an  $S_N1$  (unimolecular nucleophilic substitution) reaction pathway (Figure 4.6b). The  $S_N1$  reaction mechanism for

hydrolysis of  $\equiv\text{Al-O-Si}\equiv$  bonds is:



The combined rates of the  $S_N2$  and  $S_N1$  reactions at the  $\equiv\text{Al-O-Si}\equiv$  sites is greater than the rate of the  $S_N2$  reaction alone, the minimum in the rate versus pH curve is shifted to a higher pH than the  $\text{pH}_{\text{pzc}}$ . The amount of the shift depends upon the relative rates of the  $S_N1$  and  $S_N2$  reactions. Rate expressions for  $S_N1$  and  $S_N2$  reactions at a particular  $\equiv\text{Si-O-Al}\equiv$  site are given by:

$$\mathfrak{R}_{S_N1} = k_I [\text{Si-OH}^+\text{-Al}] = k_I K^{\text{eq}} [\text{Si-O-Al}][\text{H}_3\text{O}^+] \quad (5.19a)$$

$$\mathfrak{R}_{S_N2} = k_{II} [\text{Si-OH}^+\text{-Al}][\text{H}_2\text{O}] = k_{II} K^{\text{eq}} [\text{Si-O-Al}][\text{H}_3\text{O}^+][\text{H}_2\text{O}] \quad (5.19b)$$

where  $K^{\text{eq}}$  is the equilibrium constant for the protonation reaction and  $k_I$  and  $k_{II}$  are the unimolecular and bimolecular rate constants. Both mechanisms have the same order with respect to catalyst concentration, and on the graph of log rate versus pH, the rates would appear as parallel lines. We are looking for an acid-catalyzed reaction whose rate describes a line parallel to the experimental rate data and which intersects the base-catalyzed rate at a pH of about 3 which is about the  $\text{pH}_{\text{pzc}}$  for albite (Stumm

and Morgan, 1981). This line, shown in Figure 5.5, corresponds to a rate that is about two and a half orders of magnitude lower than the experimental rate data.

The ratio of the  $S_N1$  to  $S_N2$  reaction rates (equation 5.19a divided by 5.19b) is:

$$\frac{\mathfrak{R}_{S_N1}}{\mathfrak{R}_{S_N2}} = \frac{k_I}{k_{II} [\text{H}_2\text{O}]} \approx 10^{2.5} \quad (5.20)$$

Rate constants for elementary reactions can be written in terms of an enthalpy and an entropy of activation using rate expressions for elementary reactions from transition-state theory (Glasstone, et al, 1941; etc.):

$$k_I = \frac{ek_B T}{h} \exp \left[ \frac{\Delta S^\ddagger}{R} \right] \exp \left[ \frac{-\Delta H^\ddagger}{RT} \right] \quad (5.21)$$

where  $k_B$ ,  $h$  and  $R$  are Boltzmann's, Planck's and the ideal gas constants, respectively, and  $\Delta S^\ddagger$  and  $\Delta H^\ddagger$  are the entropy and enthalpy of activation. The ratio of the  $S_N1$  to the  $S_N2$  rates is given by:

$$\frac{\mathfrak{R}_{S_N1}}{\mathfrak{R}_{S_N2}} = \frac{1}{[\text{H}_2\text{O}]} \exp \left[ \frac{\Delta S_I^\ddagger - \Delta S_{II}^\ddagger}{R} \right] \exp \left[ \frac{-\Delta H_I^\ddagger + \Delta H_{II}^\ddagger}{RT} \right] \quad (5.22)$$

Because the transition state for both the  $S_N1$  and  $S_N2$  reactions involves the trigonal bipyramidal ( $sp^2$  hybridized) geometry, the activation enthalpies for both reaction paths

should be the same. If  $\Delta H_I^\ddagger \approx \Delta H_{II}^\ddagger$ , then the difference in activation entropy corresponding to the ratio of rates of  $10^{2.5}$  is 81.3 J/mole-K (assuming  $[H_2O] = 55.5$  molar). This result is in very good agreement with the difference in activation entropies of 80 to 125 J/mole-K between  $S_N1$  and  $S_N2$  mechanisms for acid-catalyzed hydrolysis reactions within the same class of compounds (Long, Pritchard and Stafford, 1957).

Rate data for feldspar dissolution at 25° and 70°C are shown as a function of pH in Figure 5.6. Also shown in this figure are lines representing the "Al adjusted" rates for the base-catalyzed and the  $S_N1$  and  $S_N2$  acid-catalyzed reactions. These lines are

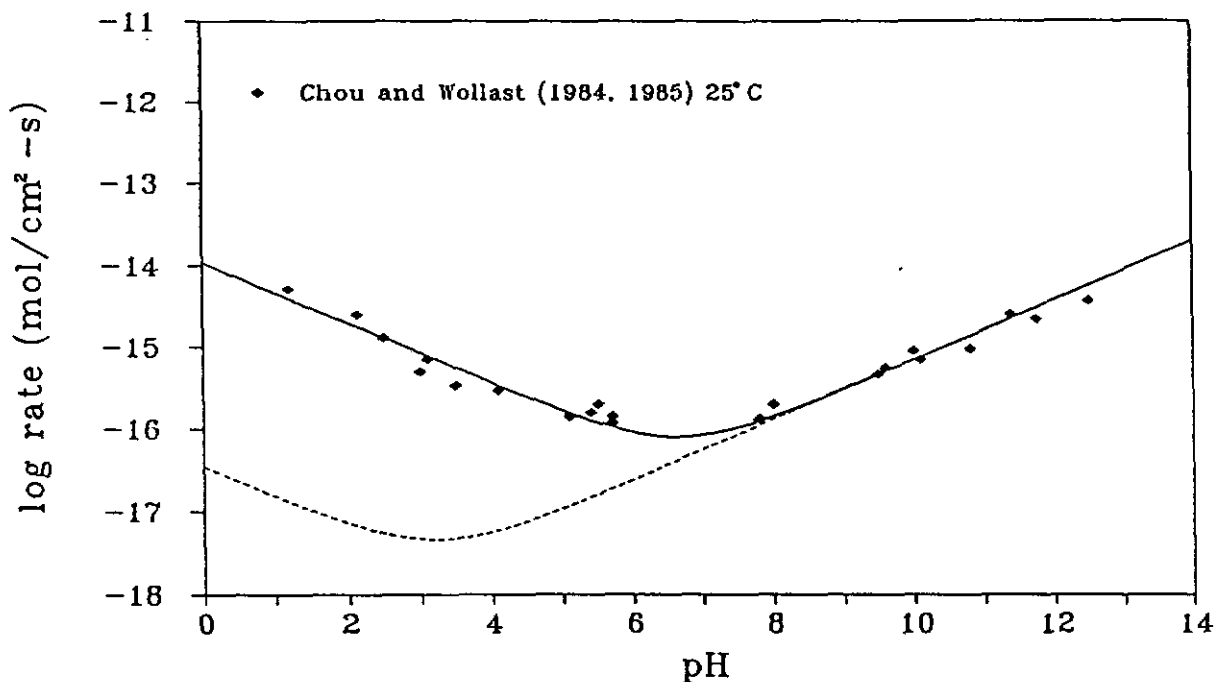


**Figure 5.5** Rates of  $S_N1$  (solid line) and  $S_N2$  (dashed line) reaction pathways for the acid-catalyzed hydrolysis of albite at 25°C. Notice that the  $S_N2$  pathway intersects the base-catalyzed reaction at the  $pH_{pzc}$  for albite (about pH 3).

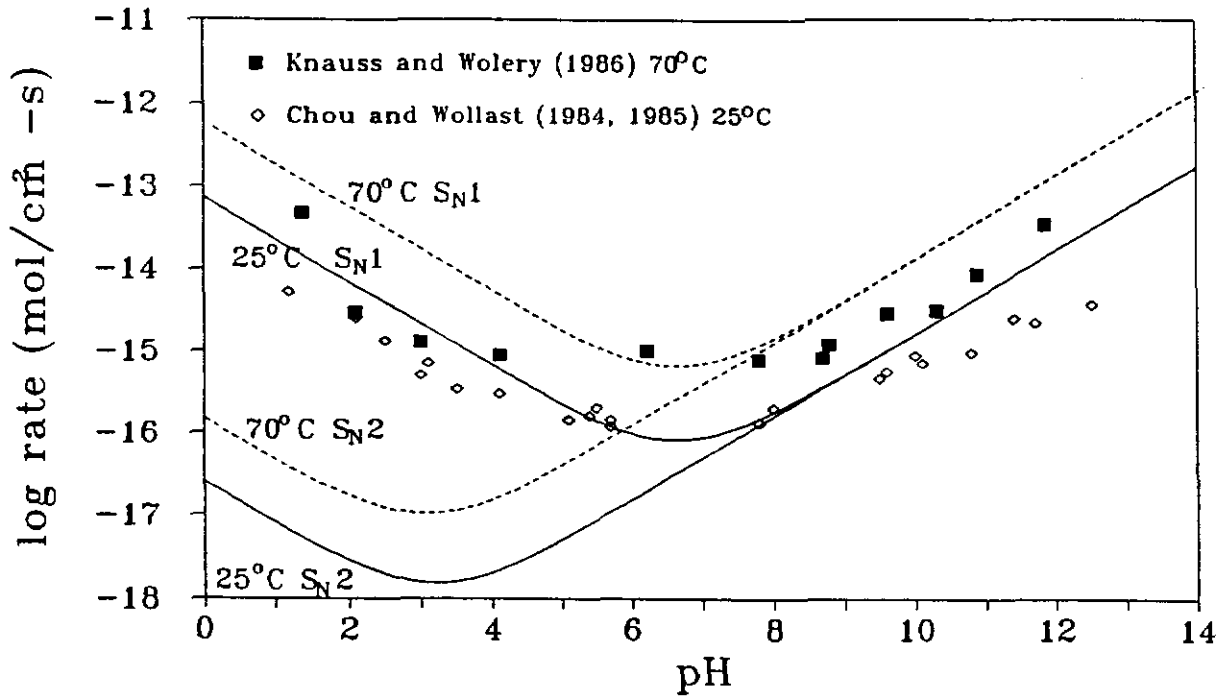


**Figure 5.6** Comparison of feldspar dissolution rate data with the adjustments for aluminum concentration effects and the incorporation of both  $S_N1$  and  $S_N2$  reaction mechanisms.

compared with the quartz dissolution rate data in Figure 5.7. The similarity between the  $S_N2$  rates for feldspar and quartz dissolution is striking but perhaps not surprising since the development of the reaction mechanisms for both minerals has proceeded in parallel.

By analogy with the rate expression for quartz dissolution developed in section 5.2, we can write a rate expression for feldspar dissolution. New aluminum sites are exposed to the crystal surface by reaction at  $Si_3-O-Al_4$ ,  $Si_2-O-Al_4$ , and  $Si_1-O-Al_4$  sites, and aluminum passes into solution by reaction at  $Si_4-O-Al_1$ ,  $Si_3-O-Al_1$ , and  $Si_2-O-Al_1$  sites. The rate,  $\mathfrak{R}_{Al}$ , at which aluminum goes into solution by the acid-catalyzed mechanism

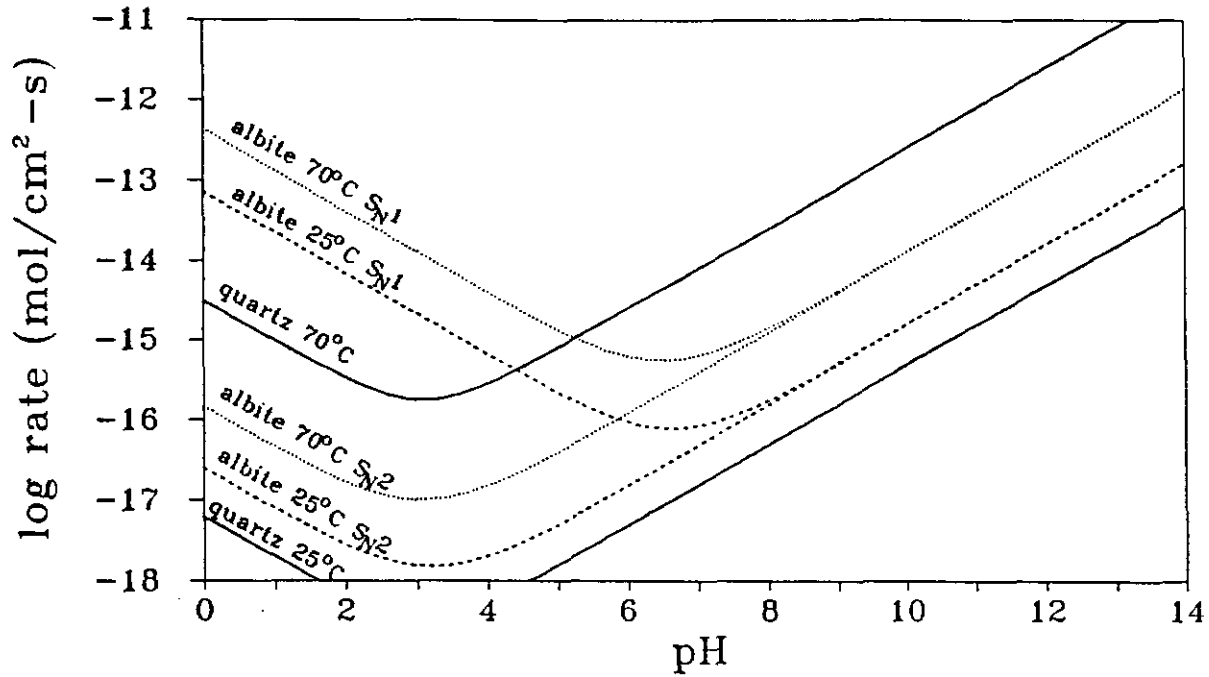


**Figure 5.7** Comparison of the adjusted feldspar dissolution rates with quartz dissolution rate data.

is given by:

$$\begin{aligned}
 \mathfrak{R}_{Al} = & \kappa_{34} [\text{Si}_3\text{-OH-Al}_4][\text{H}_2\text{O}] + \kappa_{24} [\text{Si}_2\text{-OH-Al}_4][\text{H}_2\text{O}] + \kappa_{14} [\text{Si}_1\text{-OH-Al}_4][\text{H}_2\text{O}] \\
 & \text{(rate at which Al reaches the surface by an } S_N2 \text{ mechanism)} \\
 & + \lambda_{34} [\text{Si}_3\text{-OH-Al}_4] + \lambda_{24} [\text{Si}_2\text{-OH-Al}_4] + \lambda_{14} [\text{Si}_1\text{-OH-Al}_4] \\
 & \text{(rate at which Al reaches the surface by an } S_N1 \text{ mechanism)}
 \end{aligned}
 \tag{5.23a}$$

$$\begin{aligned}
 = & \kappa_{41} [\text{Si}_4\text{-OH-Al}_1][\text{H}_2\text{O}] + \kappa_{31} [\text{Si}_3\text{-OH-Al}_1][\text{H}_2\text{O}] + \kappa_{21} [\text{Si}_2\text{-OH-Al}_1][\text{H}_2\text{O}] \\
 & \text{(rate at which Al enters the solution by an } S_N2 \text{ mechanism)} \\
 & + \lambda_{41} [\text{Si}_4\text{-OH-Al}_1] + \lambda_{31} [\text{Si}_3\text{-OH-Al}_1] + \lambda_{21} [\text{Si}_2\text{-OH-Al}_1] \\
 & \text{(rate at which Al enters the solution by an } S_N1 \text{ mechanism)}
 \end{aligned}
 \tag{5.23b}$$

where  $\kappa_{LM}$  and  $\lambda_{LM}$  are the rate constants for  $S_N2$  and  $S_N1$  reaction at  $Si_L-O-Al_M$  sites, respectively.  $\mathfrak{R}_{Al}$  is also equivalent to the steady-state rate of albite dissolution,  $\mathfrak{R}_{ab}$ , because of the stoichiometry of the global reaction for albite dissolution (equation (1.3)).

The rate at which aqueous silica appears in solution via an acid-catalyzed reaction is given by:

$$\begin{aligned} \mathfrak{R}_{Si} = & k_{34} [Si_3-OH^+-Si_4][H_2O] + k_{24} [Si_2-OH^+-Si_4][H_2O] + k_{14} [Si_1-OH^+-Si_4][H_2O] \\ & + \kappa_{43} [Si_4-OH-Al_3][H_2O] + \kappa_{42} [Si_4-OH-Al_2][H_2O] + \kappa_{41} [Si_4-OH-Al_1][H_2O] \\ & + \lambda_{43} [Si_4-OH-Al_3] + \lambda_{42} [Si_4-OH-Al_2] + \lambda_{41} [Si_4-OH-Al_1] \end{aligned} \quad (5.24a)$$

$$\begin{aligned} = & k_{14} [Si_1-OH^+-Si_4][H_2O] + k_{13} [Si_1-OH^+-Si_3][H_2O] + k_{12} [Si_1-OH^+-Si_2][H_2O] \\ & + \kappa_{14} [Si_1-OH-Al_4][H_2O] + \kappa_{13} [Si_1-OH-Al_3][H_2O] + \kappa_{12} [Si_1-OH-Al_2][H_2O] \\ & + \lambda_{14} [Si_1-OH-Al_4] + \lambda_{13} [Si_1-OH-Al_3] + \lambda_{12} [Si_1-OH-Al_2] \end{aligned} \quad (5.24b)$$

$$= 3 \mathfrak{R}_{ab}$$

If the  $S_N1$  rates are much faster than the  $S_N2$  rates, the rate terms containing  $\kappa_{ij}$  will be negligible compared to the terms with  $\lambda_{ij}$ , so effectively, there are three pathways by which aluminum reaches the crystal surface, and six pathways for silicon. The rates of these elementary reactions depend upon concentrations of surface species and on the kinetic parameters for each reaction. A comparison of the terms in equations (5.23) and (5.24) suggests that the rate of release of aluminum is independent



of the silicon release rate. However, if the reaction at  $\equiv\text{Si-O-Al}\equiv$  sites is rapid by comparison with reaction at  $\equiv\text{Si-O-Si}\equiv$  sites, the surface would become depleted in aluminum sites and the rate of dissolution would be limited by the rate of breaking  $\equiv\text{Si-O-Si}\equiv$  bonds. That this might be the case is suggested by the non-stoichiometric nature of feldspar dissolution during the transient stages of a dissolution rate experiment. During these early stages, aluminum is released to solution faster than silicon, and the relative release rate approaches stoichiometric proportions as steady-state is reached (Chou and Wollast, 1984, 1985; Holdren and Speyer, 1985; Knauss and Wolery, 1986).

In Chapters 4 and 5, we developed reaction mechanisms consisting of sets of elementary reactions and derived rate expressions for those mechanisms. Inferences drawn from these mechanisms and rate laws are in good agreement with experimentally observed results. For example, the reaction order with respect to catalyst concentration is apparently due to the stoichiometry of the elementary reactions for both quartz and albite dissolution as long as the rate is not retarded by ions in solution. Experiments were conducted to demonstrate the one-half order dependence of the quartz dissolution rate on  $[\text{H}^+]$  at low pH, and these experiments are discussed in Chapter 6.

Another strong point of the mechanism is the explanation of the minimum in the log rate versus pH curve. Proton exchange between the solution and the mineral surface fix the surface charge at a given pH. The rate of acid-catalyzed reactions depends upon whether the reaction proceeds via bimolecular or unimolecular reaction

pathways. For aluminum sites in feldspar, the unimolecular pathway is about two and one-half orders of magnitude faster than the bimolecular pathway. When the acid-catalyzed reaction follows an  $S_N2$  pathway, the minimum rate occurs at the  $pH_{pzc}$ , and for  $S_N1$  reactions, the minimum rate is at a pH higher than the  $pH_{pzc}$ .

The rate laws derived in this chapter suggest that there are multiple pathways by which the constituents of crystalline quartz or albite enter the aqueous phase, and the relative importance of these pathways depends upon the composition of the surface and on the rate constants of the key elementary reactions. The presence of multiple parallel reaction pathways explains the importance of surface morphology to experimentally determined bulk dissolution rates. This point is discussed in more detail in Chapter 7.

## Chapter 6

### Experimental Tests of the Proposed Mechanisms and Rate Laws

Verification of the  $\equiv\text{Si-O-Si}\equiv$  and  $\equiv\text{Si-O-Al}\equiv$  bond hydrolysis mechanisms and rate laws presented in Chapters 4 and 5, requires a considerable body of experimental data. For a given mineral, we need to know the  $\text{pH}_{\text{pzc}}$  as a function of temperature, dissolution rates as a function of pH at several temperatures, the surface morphology - especially, the fraction of the surface covered by  $\text{Si}_3\text{-O-Si}_4$ ,  $\text{Si}_2\text{-O-Si}_4$ , and  $\text{Si}_1\text{-O-Si}_4$  sites, the effect of aluminum and other trivalent cations in solution on the hydrolysis rate, and for minerals such as clays and micas, the reactivity of octahedrally coordinated aluminum in the crystal structure. Unfortunately, only part of these data are currently available in the literature.

The Si-O bond hydrolysis mechanism and the corresponding rate law can be partially tested by a relatively straight forward experiment. The mechanism predicts that the rate of quartz dissolution depends on  $[\text{H}^+]$  at pH values less than about 3 and that the reaction is one-half order with respect to  $[\text{H}^+]$ . To test this  $[\text{H}^+]$  dependence, quartz dissolution experiments were carried out at room temperature in a packed bed reactor using a natural quartz sand. These experiments were primarily designed to obtain the quartz dissolution rate data at low pH and room temperature. An additional benefit of the experiment design was that the dissolution rate experiments could also be used to test an alternative reactor geometry and sample preparation technique. The sample preparation techniques and the reactor design and analysis for these

experiments are described in detail in this chapter along with the results of the experiments. These experimental results are discussed in Chapter 7 in the context of calculating kinetic parameters from bulk dissolution rate data.

**6.1 Experiment Design.** The experimental apparatus for this study is shown schematically in Figure 6.1. A 1-liter Nalgene bottle was used as the feed solution reservoir. The cap of this bottle was fitted with a gas inlet and a liquid outlet. Argon gas from a large liquid dewar supplied gas pressure to the pressure regulator which controlled the pressure head in the feed solution reservoir.

The liquid outlet from the feed solution reservoir was connected via teflon tubing to the stainless steel needle valve at the base of the reaction vessel. The reaction vessel is a teflon-coated, stainless steel filter holder which has been slightly modified for this application. The base of the filter holder contains a filter support which serves as a bed support and flow distributor. Feed solutions were changed by closing the valve at the reactor inlet, crimping the argon supply tubing on the high pressure side of the pressure regulator and bleeding the pressure from the feed solution reservoir. The feed solution bottle was unscrewed carefully and replaced with a fresh bottle of feed solution. Much care was taken to prevent air from entering the reactor feed line. After the new bottle was in place, the feed solution was pressurized and the valve to the reactor inlet was opened.

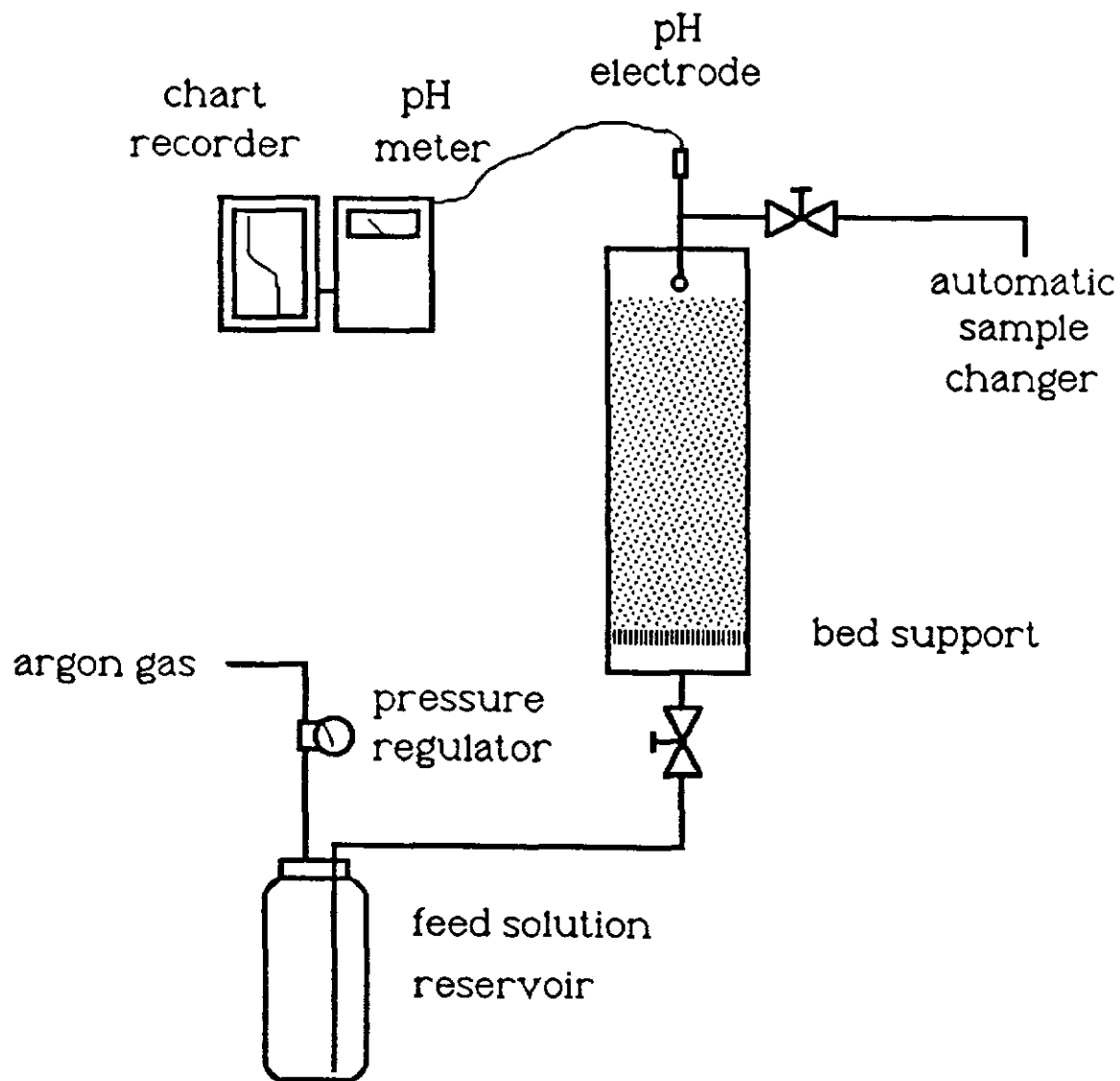


**Figure 6.1** Schematic drawing of the experimental apparatus used in these experiments. The reaction vessel is a high-pressure filter that is constructed of teflon-coated stainless steel. All wetted parts in the system are polyethylene, teflon or teflon-coated except for the two valves which are stainless steel.

The top of the reaction vessel was modified to accept a 1/4 inch O.D. epoxy body pH electrode. This electrode was continuously monitored by a pH meter, with the outlet pH recorded on a chart recorder. The reactor effluent passed through a stainless steel needle valve to a very small internal diameter teflon tubing. This tubing provided back-pressure to the pressure regulator which controlled the fluid flow rate. Samples were collected in 30 ml polyethylene vials by an automatic sample changer which advanced at approximately one hour intervals. Except for the two stainless steel valves and the glass bulb of the pH electrode, the wetted parts for the entire system are polyethylene, epoxy, or teflon.

The internal diameter and length of the reaction vessel are 4.13 cm and 15.24 cm, respectively. The total internal volume of the reactor is 216.8 ml. In preparation for the experiments, the reactor was loaded with 288.0 g of quartz sand which was prepared as described below. The valve at the reactor inlet was closed, and the vessel was evacuated using a standard vacuum pump. After the vessel was evacuated, feed solution was drawn into the reactor by slowly opening the valve to the feed solution reservoir. This filling procedure eliminates air bubbles that might be trapped in the bed or below the flow distributor. The void fraction in the bed was measured in a separate test to be 39.2%.

Flow rates were measured by weighing the individual sample vials after collection of the samples, transferring the fluid to 30 ml Nalgene bottles and reweighing the empty sample vials. The electronic balance reported weights to the hundredth of a

gram, so the truncation error in weighing the samples is of the order of  $10^{-2}$  g. The time at which the automatic sampler advanced was recorded by hand directly on the sample vials. For those samples that did not have times recorded, the starting times were interpolated between known times. The error in recording the starting time is of the order of 3 seconds, and the maximum deviation between a measured time and an interpolated time is 20 seconds. For a constant flow rate of 20 g/hr, this maximum difference between the actual and the interpolated sample advance time gives an error of 0.11g which gives a relative error of 0.55%.

To account for possible evaporation losses, one vial was filled with deionized water and its weight was monitored as a function of time over several days. The rate of weight loss determined from this vial was used to correct the flow rates and the concentrations of the samples. The rate of evaporation was 0.8 g/day when the sample vials were covered and 1.4 g/day without the cover.

The raw data for the dissolution experiments - recorded and interpolated sample advance times, mass of the sample plus the vial, mass of the empty vial, calculated flow rates, corrections for evaporation losses, measured concentrations, concentrations corrected for evaporation, etc. - are reported in Appendix D. These data are summarized in Table 6.1.

A tracer experiment using a Na-fluorescein dye tracer was performed to measure the residence time distribution in the packed bed. The experimental apparatus was

**Table 6.1 Summary of the results of the quartz dissolution rate experiments. The reported time is the time the sample changer advanced. Measured sample masses were corrected for evaporation applying an average evaporation rate over the time from sample collection to measurement of the sample mass. This correction for evaporation was then used to correct the flow rate and the HNO<sub>3</sub> and silica concentrations.**

S/N	Date	Time	Total Mass (g)	Tare (g)	Sample Mass (g)	Sample Mass (g)	Meas. Flow Rate (ml/hr)	Corr. Flow Rate (ml/hr)	Corr. HNO <sub>3</sub> Conc. (molar)	Calc. pH	Meas. pH	Meas. Silica Conc. (ppb)	Corr. Silica Conc. (ppb)
<b>Deionized Water Feed</b>													
1	09/30/88	17:32	23.40	9.29	14.11	15.34					3.92	1	1
20	10/01/88	12:16	31.66	8.96	22.70	22.87	23.01	23.19			5.80	10	9
21	10/01/88	13:15	31.87	9.25	22.62	22.73	22.93	23.05			4.30	19	19
											4.20	18	18
<b>Change feed to 5.3 N HNO<sub>3</sub> about 10:00 3 Oct</b>													
35	10/03/88	10:01	26.77	9.26	17.51	19.24	17.40	19.12	5.075	-0.84		80	
69	10/04/88	20:14	23.77	9.22	14.55	15.17	14.46	15.07	0.018	1.84		150	137
70	10/04/88	21:14	23.62	9.27	14.35	14.93	14.26	14.84	5.150	-0.81		3010	2888
									5.205	-0.83		2490	2393
<b>Change feed to 1.0 N HNO<sub>3</sub> about 23:00 4 Oct</b>													
72	10/04/88	23:15	25.28	9.26	16.02	16.54	15.92	16.43	1.015	0.13		80	
101	10/06/88	08:18	25.26	9.26	16.00	16.07	15.90	15.96	4.786	-0.76		1450	1405
102	10/06/88	09:19	25.25	9.08	16.17	16.20	16.07	16.10	1.055	0.12		960	956
									1.035	0.13		960	958
<b>Change feed to 0.31 N HNO<sub>3</sub> about 10:00 6 Oct</b>													
105	10/06/88	10:18	26.98	9.30	17.68	18.49	17.58	18.38	0.314	0.65		0	
127	10/07/88	08:14	26.65	9.23	17.42	17.52	17.56	17.66	1.000	0.16		880	841
128	10/07/88	09:13	27.15	9.09	18.06	18.12	18.20	18.27	0.300	0.67		600	597
									0.305	0.66		590	588
<b>Deionized Water Feed</b>													
140	10/17/88	11:53	25.20	9.10	16.10	18.51	16.04	18.45			3.40	15	
160	10/18/88	07:57	24.04	9.26	14.78	16.54	14.73	16.48			4.05	169	147
161	10/18/88	08:58	23.69	9.10	14.59	16.32	14.54	16.26			3.40	120	107
											3.42	132	118
<b>Change feed to 0.1 N HNO<sub>3</sub> about 09:10 18 Oct</b>													
162	10/18/88	09:58	23.86	9.00	14.86	16.56	14.81	16.50	0		1.22	0	107
185	10/19/88	09:03	24.76	9.22	15.54	16.49	15.48	16.43			3.51	119	107
186	10/19/88	10:03	27.31	9.25	18.06	18.97	17.99	18.90	0.242	0.77		348	328
												354	337



used as described above except that the automatic sample changer was set to a sampling interval of 15 minutes. Fluorescein concentrations were measured spectrophotometrically using a Beckman model 25 UV-visible spectrophotometer. By simply changing feed solution bottles, the fluorescein tracer was introduced as a step change in inlet composition. The results of the tracer experiment are presented in Section 6.4.1.

**6.2 Sample Preparation, Characterization and Chemical Analysis.** Sample preparation techniques generally include crushing, sieving and washing of the solid particles to remove the fines which react much more quickly than larger particles. However, crushing disrupts the mineral surface and washing with strong acids and bases can initiate etch pits. Both of these effects increase the amount of high energy surface area available to solution. Ideally, the mineral samples should be smooth, uniform spheres, and for some minerals, this ideal can be approached using natural samples. For this study, a well-sorted quartz sand was chosen as the experimental material. Two pounds of Ottawa sand in the 20 to 28 mesh (0.841 to 0.595 mm opening) size range were washed for about 10 minutes with concentrated nitric acid to remove iron stains. This material, along with an equal weight of 500 mesh silicon carbide grit, was tumbled for two weeks in deionized water to smooth the surfaces of the sand grains. After tumbling and separating the silicon carbide from the quartz, the quartz was fluidized in a 2-liter graduated cylinder with deionized water until the effluent was clear of fine particles. The quartz was rinsed with ethanol to remove the water before being dried at 100°C. The dried sand was hand-sorted to remove any remaining contamination.

SEM photographs of the surface before and after the washing procedure are presented in Figure 6.2. Notice that the unwashed sample has many fine particles ( $< 1 \mu\text{m}$  diameter) attached to the surface and that the surface is deeply etched. The fine particles are effectively removed in the photograph of the washed material, and the etched surface has been smoothed by tumbling. Surface areas of the treated (unreacted) and the reacted quartz were determined by three-point BET gas adsorption with a Quantasorb instrument using nitrogen in a helium carrier. The analyses were performed by John F. Baytos of the Explosives Technology Group (M-1) of the Los Alamos National Laboratory. The treated material had a surface area of  $766 \text{ cm}^2/\text{g}$ , and the material that had been reacted had a surface area of  $903 \text{ cm}^2/\text{g}$ . Although the instrument was not designed to measure surface areas of less than  $5000 \text{ cm}^2/\text{g}$ , the results of the three analyses were linear (correlation coefficients of 0.984 and 0.998 for the treated and the reacted material, respectively) suggesting that the measurements are accurate even though they were below the operating range of the instrument.

Acidic feed solutions were prepared from J.T. Baker Analytical Grade ("Baker Instra Analyzed" for trace metal analysis) nitric acid (70% wt) using demineralized water from a purification system that continuously recycled the water through mixed bed demineralizers, sub-micron filters and a reverse osmosis unit. The electrical conductivity of this water is  $10^{-18} \text{ M}\Omega\text{-cm}$ . Measured concentrations of the acidic feed solutions were 5.08, 1.04, 0.39, and 0.23 normal  $\text{HNO}_3$ . All solutions were prepared in polyethylene labware and stored in new Nalgene bottles.

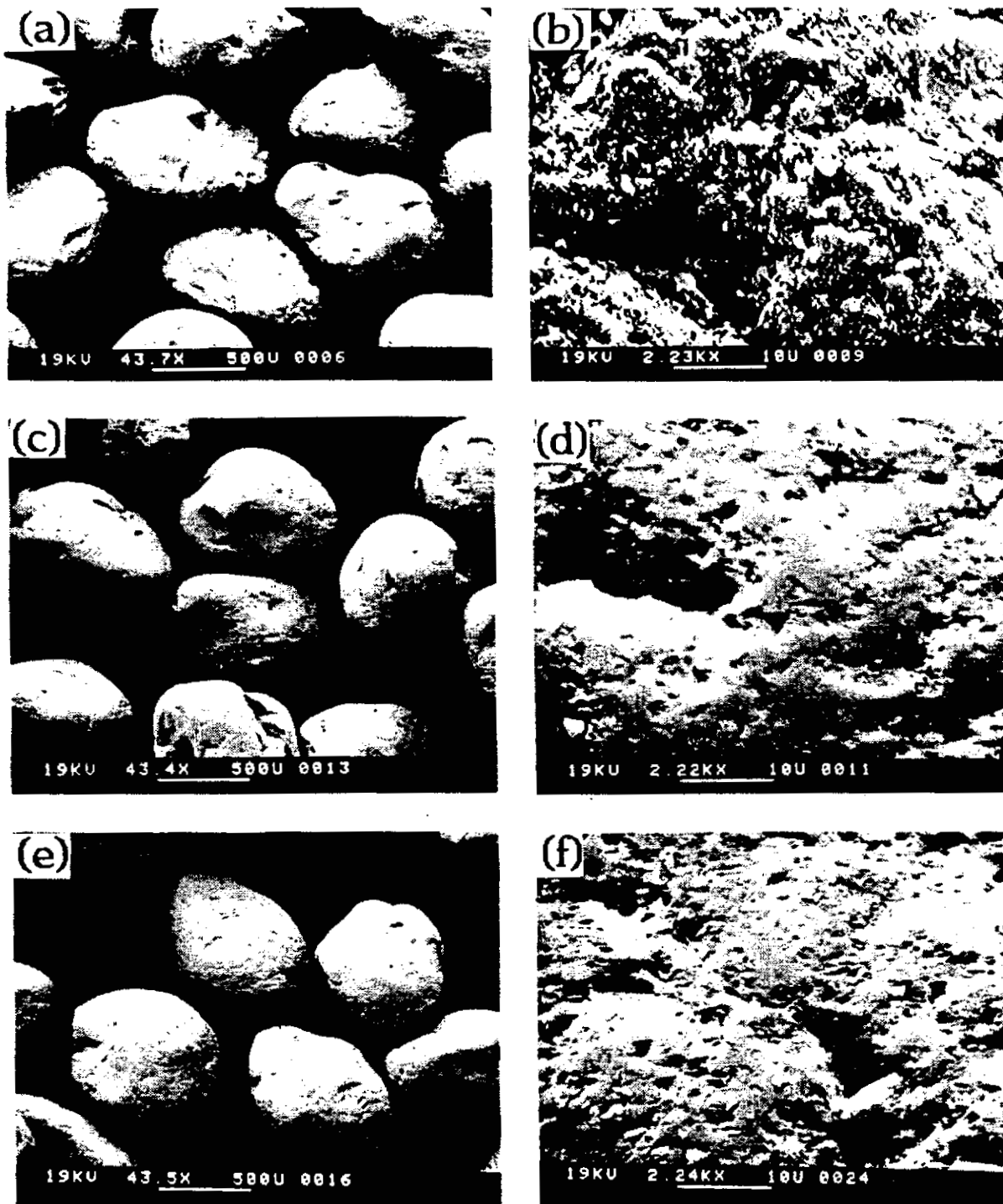


**Figure 6.2** SEM photographs of the quartz sand used in these experiments. (a) and (b) show the sand before any treatment to remove fine particles and surface roughness, (c) and (d) are after tumbling and fluidization to remove fines, and (e) and (f) are reacted sand. The magnification of (a), (c) and (e) is about 43.5 x, and the magnification of (b), (d) and (f) is about 2230 x.

Solutions were analyzed for silica at 251.61 nm using a Perkin-Elmer model 5500 inductively coupled plasma emission spectrograph. In the absence of interfering species, this emission line gives the highest sensitivity for silicon, and the detection limit for aqueous silica is of the order of 1 ppb. Three readings were taken per sample, and the average of these readings is presented in Table 6.1. Analyses were performed by Dale Counce of the Geology and Geochemistry Group (ESS-1) of the Los Alamos National Laboratory.

Wherever possible, the pH was measured by a standard glass pH electrode. Acid and base concentrations of feed solutions and effluent samples were measured using a Fisher Computer Aided Titrimeter system which was programmed to search for endpoints. The titrant was 0.1 N H<sub>2</sub>SO<sub>4</sub> solution which was prepared from Baker Dilut-it™ ampoules using demineralized water. A measured amount of 0.1 N KOH was added to acid samples before they were titrated to raise the pH above 10.

**6.3 Reactor Design and Analysis.** An integral part of any experimental study of reaction kinetics is the chemical reactor. There are several reactor types which can be used to study dissolution kinetics. Depending on the application, one type of reactor may be more suitable than others. Flow-through reactors are increasingly used in preference to batch and semi-batch reactors in mineral dissolution rate experiments (Chou and Wollast, 1984, 1986; Holdren and Speyer, 1985b; Knauss and Wolery, 1986, 1988). The advantages of flow-through reactors over batch or semi-batch reactors were discussed briefly in Chapter 2. The major advantage of flow-through reactors is that

the solution composition in the reactor can easily be controlled or changed, and precipitation of secondary phases can be prevented. Under steady-state conditions, reaction products are removed from the reactor as fast as they are formed - that is, there is no accumulation of material in the reaction vessel - so the interpretation of the reaction rate data is relatively easy.

Three flow-through reactor designs have been used extensively: a stirred tank reactor (Holdren and Speyer, 1986), a fluidized bed reactor (Chou and Wollast, 1984, 1985), and a differential packed bed reactor (Knauss and Wolery, 1986, 1988). Ideally, each of these reactors behaves as a continuously-stirred tank reactor (CSTR). In a CSTR, there are no spatial inhomogeneities in the fluid composition, so the effluent composition is identical to the composition of the fluid in the reactor. The performance of a CSTR is obtained by performing a material balance:

$$V \frac{dC}{dt} = \dot{q} C_{in} - \dot{q} C_{out} + \mathfrak{R} \quad (6.1)$$

where  $V$  is the fluid volume in the reactor,  $C$  is the concentration of a species in the solution,  $\dot{q}$  is the volumetric flow rate and  $\mathfrak{R}$  is the rate of the reaction. Since the solution in the reactor is spatially uniform, the effluent has the same composition as the fluid in the reactor, so  $C_{out} = C$ . Under steady-state conditions the rate is given by:

$$\mathfrak{R} = \dot{q} (C - C_{in}) \quad (6.2)$$

One consequence of the CSTR material balance equation (equation (6.1)) is that residence time distribution (RTD) is an exponential function of time. Consider the case where there is no reaction occurring in the vessel. If at a time  $t_0$ , the feed to a CSTR is suddenly changed from a stream containing no tracer to one which has a tracer concentration given by  $C_0$ , then the concentration of the tracer in the effluent is given by:

$$\frac{C}{C_0} = 1 - \exp[-(t-t_0)/\tau] \quad (6.3)$$

where  $\tau$  is the mean residence time which is also equal to  $V/\dot{q}$  (see, for example, Levenspiel, 1972; Carberry, 1976). Equation (6.3) can be solved to give the time required to replace a given fraction of the original fluid in the reactor. For example, to replace 98% of the fluid (ie.  $C/C_0 = 0.98$ ) requires a time equal to 3.91 times the mean residence time.

In the flow-through reactors discussed above, the time to steady-state conditions ( $\tau_{ss}$ ) is long - of the order of 20 to 100 hours for the fluidized bed (Chou and Wollast, 1984, 1985), 190 hours for the stirred tank (Holdren and Speyer, 1986) and 100 to 500 hours for the differential reactor (Knauss and Wolery, 1986, 1988). Mean residence times were calculated from the reported reactor fluid volumes and flow rates (see Table 6.2). The number of reactor volumes required to reach steady-state ( $\tau_{ss}/\tau$ ) varies from about six for the stirred tank to about 320 for the differential packed bed. As discussed above, 98% of the fluid in the an ideal CSTR is replaced in four reactor volumes, so

**Table 6.2** Characteristics of flow-through reactors reported in the literature.

V (ml)	$\dot{q}$ (ml/hr)	$\tau$ (hr)	$\tau_{ss}$ (hr)	$\tau_{ss}/\tau$
<i>Fluidized Bed (Chou and Wollast 1984, 1985)</i>				
28.5	13.8	2.07	20	10
22.2	9.0	2.47	100	41
29.5	13.8	2.14	50	23
<i>Stirred Tank (Holdren and Speyer 1985b, 1986)</i>				
50.0	1.5	33.3	190	6
<i>Differential Packed Bed (Knauss and Wolery 1986, 1988)</i>				
2.2	1.5	1.51	120	80
2.2	1.5	1.51	480	319

values of  $\tau_{ss}/\tau$  greater than about 10 could be an indication that there is stagnant volume or channeling somewhere in the reactor.

In addition to the long times required to come to steady-state, there are other potential problems with these reactors. In the fluidized bed and to a lesser extent in the stirred tank reactor, mechanical abrasion of the dissolving particles could enhance the dissolution rate. Holdren and Speyer (1986) report that the agitation in the stirred tank was insufficient to suspend the coarser solid particles which formed a conical pile of solids below the impeller. In this case, the contact between the phases is not completely uniform, so the stirred tank reactor may deviate from ideal CSTR behavior.

Non-uniform contacting between the phases is also a potential problem in Knauss and Wolery's (1986, 1988) differential packed bed reactor if flow channeling occurs.

Another feature of these reactors is that they are very dilute. Typically, the reactor is loaded with 1 to 3 grams of solid and 20 to 50 ml of fluid. To be able to detect reaction products in the reactor effluent, very low feed rates and high mineral surface areas are used. Mineral samples are typically ground to particle diameters of 50 to 400 microns to increase the surface area, but Holdren and Speyer (1985, 1987) report that the rate of dissolution of alkali feldspars does not necessarily increase linearly with specific surface area in this particle size range. They suggest that defects in the crystal structure control the rate of dissolution and that grinding below a certain size does not expose new defects at the same rate that new surface area is exposed.

Some of the experimental difficulties described above - abrasion, non-uniform contact between the phases, low solid/liquid ratios - can be alleviated by using a packed bed reactor. In contrast with the CSTR's, the fluid composition in a packed bed reactor is not spatially uniform but varies along the axis of the reactor. Radial variations in fluid composition are also possible, but are relatively unimportant in an isothermal reactor. Radial variations can be partially alleviated by a flow distributor at the inlet to the bed.

Under ideal conditions, a packed bed will behave as a plug flow reactor (PFR) where all the entering molecules have the same residence time in the reactor. Because



the fluid composition is not uniform throughout a packed bed, it is more difficult to analyze the data from this type of reactor. Consider the schematic drawing of a packed bed reactor shown in Figure 6.3. A material balance on the control volume gives

$$\frac{\partial C}{\partial t} = D \frac{\partial^2 C}{\partial x^2} - u \frac{\partial C}{\partial x} + \mathfrak{R} \quad (6.4)$$

where  $D$  is the axial dispersion coefficient,  $C$  is the concentration of an aqueous species which is produced by dissolution of the bed material,  $x$  is the distance along the axis of the reactor, and  $\mathfrak{R}$  is the rate of the reaction. When  $\mathfrak{R}$  is zero, equation (6.4) describes axial dispersion in a plug flow reactor (Levenspiel, 1972). Under steady-state conditions, the left hand side of equation (6.4) is zero. Equation (6.4) can be rewritten in dimensionless form as

$$\frac{d^2 \Psi}{d\xi^2} - Pe \frac{d\Psi}{d\xi} - Da\Psi = 0 \quad (6.5)$$

where the dimensionless concentration,  $\Psi$ , dimensionless axial distance,  $\xi$ , Peclet number,  $Pe$ , and the Damköhler number,  $Da$ , are defined by:

$$\Psi = \frac{C^{sat} - C}{C^{sat} - C_{in}}, \quad \xi = \frac{x}{L}, \quad Pe = \frac{uL}{D}, \quad Da = \frac{L^2 \mathfrak{R}}{D C}$$

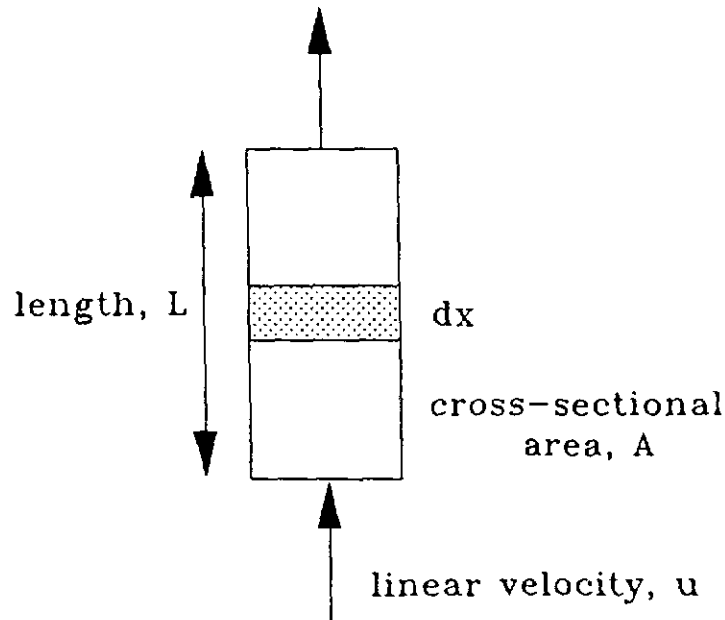


**Figure 6.3** Schematic cross-section of a packed bed reactor. The performance equation for the reactor is derived by performing a material balance on the control volume shown in the figure.

$C^{sat}$  and  $C_{in}$  are the saturation concentration and the feed concentration for the aqueous species,  $L$  is the length of the packed bed, and the Peclet and Damköhler numbers are, respectively, the ratios of the convection velocity to the dispersion velocity and the chemical reaction velocity to the dispersion velocity.

The value for the Peclet number can be deduced from tracer experiments, and when this value is large, transport by dispersion is insignificant relative to bulk flow convection. On the other hand, when  $Da$  is large, the reaction velocity is larger than the dispersion velocity so the reaction rate will be limited by mixing of reactants rather than by the reaction kinetics.

For large  $Pe$ , the dispersive term in equation (6.5) can be neglected, and the steady-state material balance equation is simplified to:

$$\frac{\partial C}{\partial \xi} = \frac{L}{u} \mathfrak{R} = \tau \mathfrak{R} \quad (6.6)$$

A major difference between the analysis of CSTR and PFR behavior is seen in the form of equations 6.2 and 6.6. For the CSTR, the rate is proportional to the outlet concentration while the rate in a PFR is proportional to the axial concentration gradient. Thus, for the PFR, the rate law must be integrated to find the outlet concentration while the rate law need not be known to find an expression for the rate in the CSTR case.

With an appropriate rate law, equation (6.6) can be integrated to give the species concentration as a function of dimensionless distance,  $\xi$ . When the concentration of the reaction products are well below the saturation concentration, the rate is given by the forward rate of the rate-limiting step. We are interested in the rate expressed on a per mole of  $H_4SiO_4$  basis, so the stoichiometric coefficients (hence the reaction orders) of each of the reactants are 1/2:

$$\mathfrak{R} = k_f \{a^* [C^{surf}] [H_3O^+]\}^{1/2} \quad (6.7)$$

where  $[C^{\text{surf}}]$  is the activity of the surface species that is involved in the reaction, and  $a^*$  is the ratio of the interfacial surface area to the fluid volume in the packed bed. For reaction (9) in Table 4.4,  $[C^{\text{surf}}]$  refers to the activity of  $\text{Si}_3\text{-O-Si}_4$  moieties, and for reaction (13),  $[C^{\text{surf}}]$  refers to  $\text{Si}_2\text{-O-Si}_4$  sites. The solution to equation (6.6) with a rate law given by equation (6.7) is:

$$C(\xi) = C_{\text{in}} + k_f \tau \{a^* [C^{\text{surf}}] [\text{H}_3\text{O}^+]\}^{1/2} \xi \quad (6.8)$$

This equation can also be written in terms of the dimensionless concentration,  $\Psi(\xi)$ , as

$$\Psi(\xi) = \frac{C^{\text{sat}} - C(\xi)}{C^{\text{sat}} - C_{\text{in}}} = 1 - \frac{k_f \tau \{a^* [C^{\text{surf}}] [\text{H}_3\text{O}^+]\}^{1/2} \xi}{C^{\text{sat}} - C_{\text{in}}} \quad (6.8a)$$

Because the concentration [equation (6.8)] or the dimensionless concentration [equation (6.8a)] is a linear function of the distance along the bed, as long as  $[\text{H}^+]$  and  $[C^{\text{surf}}]$  are constant, the change in concentration with respect to axial distance,  $dC/dx$ , is constant throughout the bed. Since the reaction rate is proportional to  $dC/dx$ , the reaction rate is also constant. When  $C_{\text{in}}$  is equal to zero, the rate given by differentiating equation (6.8) is the initial rate.

As reaction products accumulate, the reverse or precipitation reaction becomes important. On a per mole of  $\text{H}_4\text{SiO}_4$  basis, the rate expression for the reverse (precipitation) reaction is first order in aqueous silica concentration and first order in

surface sites, and the net rate is given by:

$$\begin{aligned} \mathfrak{R} &= k_f \{a^* [C^{\text{surf}}] [H_3O^+]\}^{1/2} - k_r a^* [C^{\text{surf}}] [C] \\ &= k_f \{a^* [C^{\text{surf}}] [H_3O^+]\}^{1/2} - k_r a^* [C^{\text{surf}}] \gamma_C C \end{aligned} \quad (6.9)$$

where  $\gamma_C$  is the activity coefficient of component C in the aqueous solution. Substituting this expression for the rate term in equation (6.6) we find the concentration profile in the packed bed is given by:

$$\frac{C^{\text{sat}} - C}{C^{\text{sat}} - C_{\text{in}}} = \exp \{-k_r a^* [C^{\text{surf}}] \gamma_C \xi \tau\} \quad (6.10)$$

or, at the bed outlet ( $\xi = 1$ ):

$$\frac{C^{\text{sat}} - C_{\text{out}}}{C^{\text{sat}} - C_{\text{in}}} = \exp \{-k_r a^* [C^{\text{surf}}] \gamma_C \tau\}. \quad (6.10a)$$

In contrast with the linear concentration profile given by equation (6.8a), the concentration profile given by equation (6.10) is an exponential. The relationship between the two concentration profiles is shown in Figure 6.4. Notice that equation (6.8a) is tangent to equation (6.10) at the reactor entrance, and that equation (6.10) is written in terms of the rate of the reverse reaction while equation (6.8) contains rate parameters for the forward reaction.

To deduce the rate of the forward reaction in a packed bed geometry where the reverse reaction is important, we must first calculate the value of the coefficient of  $\tau$  in equation (6.10):

$$k_r a^* [C^{\text{surf}}] \gamma_C = - \frac{1}{\tau} \ln \frac{C^{\text{sat}} - C_{\text{out}}}{C^{\text{sat}} - C_{\text{in}}} \quad (6.11)$$

Numerical evaluation of  $k_r a^* [C^{\text{surf}}] \gamma_C$  requires knowledge of the saturation concentration or experimental determining the outlet concentration as a function of  $\tau$ . This coefficient is then be related to the coefficient of  $\xi$  in equation (6.8) using equation (6.9) and the fact that the net rate is zero when  $[C] = [C^{\text{sat}}]$ :

$$k_r a^* [C^{\text{surf}}] C^{\text{sat}} = - \frac{[C^{\text{sat}}]}{\tau} \ln \frac{C^{\text{sat}} - C_{\text{out}}}{C^{\text{sat}} - C_{\text{in}}} \quad (6.12)$$

$$= k_f \{a^* [C^{\text{surf}}] [H_3O^+]\}^{1/2} / \tau \quad (6.12a)$$

Thus, the rate of the forward reaction is found from the rate of the reverse reaction and the saturation concentration.

Although the analysis of a packed bed reactor is more complicated than for a CSTR, there are some advantages to the packed bed reactor. In a packed bed, the amount of surface area exposed to a given fluid volume can be much larger than for

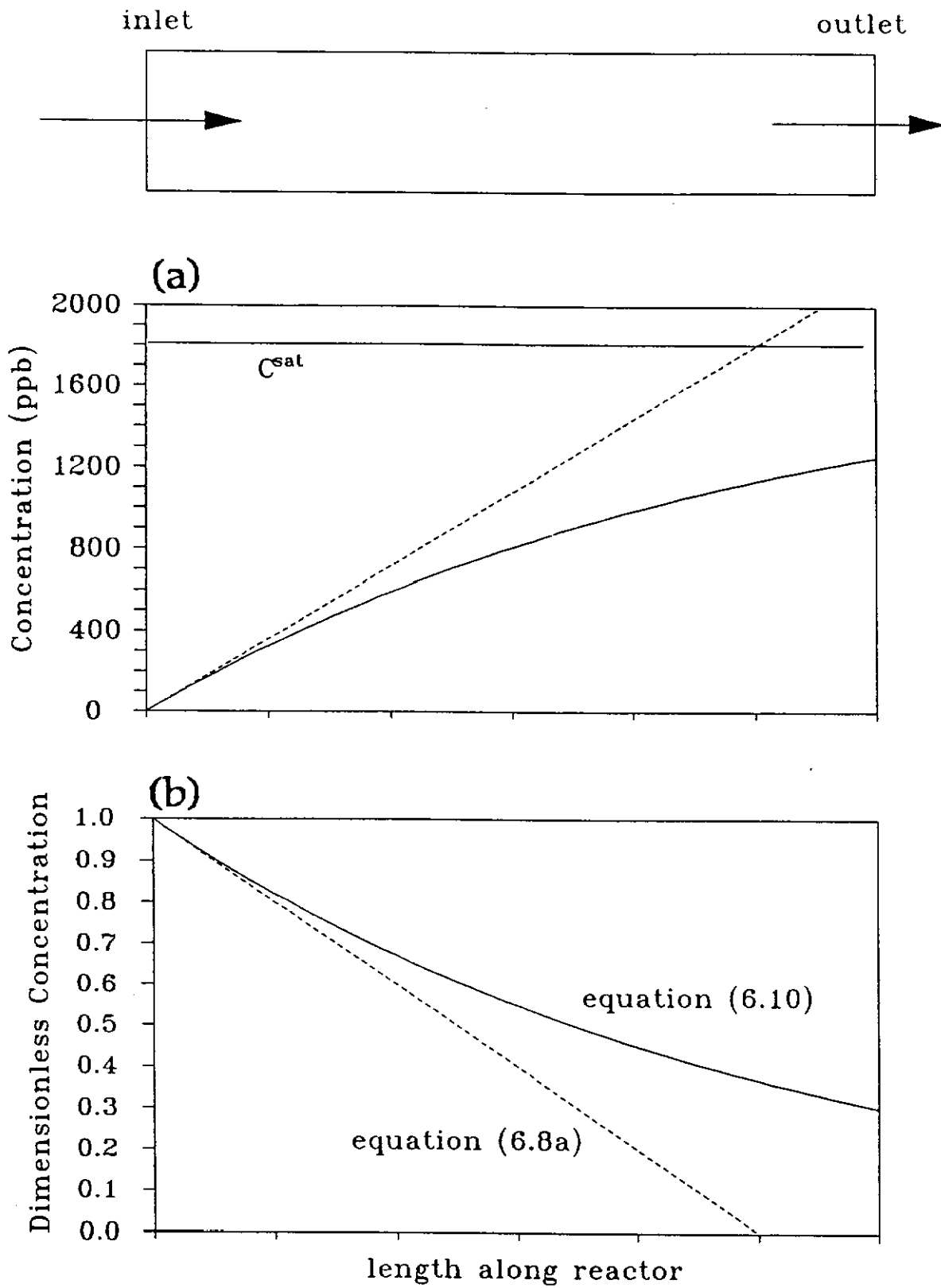


**Figure 6.4** (a) Concentration profile and (b) dimensionless concentration profile in a packed bed reactor.

any of the other flow-through reactors. This reduces the need for grinding particles to very fine sizes and allows the use of higher flow rates. Because there is no motion of the particles, abrasion is not a problem. Fluid channeling is much less likely than in a differential packed bed reactor, and it is simple to test for channeling by performing a tracer experiment.

A major difference in the analysis of dissolution rate data from a packed bed (PFR) geometry and a CSTR geometry involves the form of the reactor performance equation. For the PFR, the bulk rate is proportional to the derivative of concentration with length along the reactor. Calculation of a reaction profile requires integration of the rate with respect to length along the reactor axis. For the CSTR, the bulk rate is proportional to the difference in concentration between the reactor outlet and inlet. When this concentration difference is small, slight errors in measuring the concentrations in the inlet and outlet streams can lead to large errors in the estimate of the dissolution rate for a CSTR. The integration of the performance equation for the PFR smoothes out some analytical error but introduces a constant that must be evaluated by applying the boundary conditions. A major goal of performing dissolution experiments is to test the form of and to evaluate kinetic parameters for a rate law. While it is possible to obtain bulk rate data from a CSTR outside the context of a rate law, evaluation of PFR data requires a rate law, and so, analysis of PFR rate data is automatically a partial test of the rate law.



**6.4 Experimental Results.** Quartz dissolution rate experiments were carried out in the packed bed geometry discussed above to test for pH dependence. The results of the various experiments are summarized in Table 6.1, and the raw data is presented in Appendix D. In addition to the dissolution rate experiments, a tracer experiment was conducted in the reactor to characterize the dispersion in the packed bed. The tracer data are discussed in the next section before considering the dissolution rate data.

*6.4.1 Determination of the Residence Time Distribution for the Packed Bed Reactor.*

The mathematical basis for evaluating the performance of chemical reactors using inert tracers is very well-developed in the chemical engineering literature (Danckwerts, 1953, 1958; Levenspiel, 1962). The exit age or residence time distribution (RTD), is measured by injecting a mass of tracer as a pulse into the reactor inlet. The measured tracer concentration in the reactor effluent is called  $C(t)$ . Under steady-flow conditions, the mean residence time,  $\tau$ , is the first moment of the distribution given by

$$\tau = \frac{V}{\dot{q}} = \frac{\int_0^{\infty} t C(t) dt}{\int_0^{\infty} C(t) dt} \simeq \frac{\sum t_i C_i \Delta t_i}{\sum C_i \Delta t_i} \quad (6.13)$$

The variance or spread of the distribution is given by the second moment of the distribution:

$$\sigma^2 = \frac{\int_0^{\infty} (t - \tau)^2 C(t) dt}{\int_0^{\infty} C(t) dt} \approx \frac{\Sigma(t_i - \tau)^2 C_i \Delta t_i}{\Sigma C_i \Delta t_i} \quad (6.14)$$

If the input to the reactor involves a step change in inlet concentration rather than simply a pulse of tracer, the response at the outlet is simply the integral of the response to a pulse.

A 9 ppm solution of Na-fluorescein dye was used as the tracer, and the reactor effluent was collected as described in section 6.1 using a 15 minute sampling interval. Na-fluorescein is readily determined to sub-ppm levels using a UV spectrophotometer at a wavelength of 493 nm. The absorbance follows Beer's law up to concentrations of about 10 ppm. However, the absorbance decreases with pH below a pH of about 8. To prevent this loss of absorbance, the feed solution pH was adjusted with  $\text{NaHCO}_3$  and  $\text{NaOH}$  to be approximately 10.

A Beckman model 25 UV-visible spectrophotometer with a flow-through cell was used for the analyses. This model can be adjusted to display concentration units directly. Since the absolute concentrations of tracer are not necessary, the background

solution (baseline) was adjusted to a concentration of zero while the feed concentration was set to unity. The sample concentrations, then, are automatically normalized with respect to the feed and background concentrations.

Dye concentrations for the samples collected during the tracer experiment are plotted as a function of time in Figure 6.5 and the concentration and flow rate data are presented in Table 6.3. To calculate the mean residence time and the variance for this tracer test, the concentration data was numerically differentiated with respect to flow rate (rather than time since the flow rate was not steady during the tracer experiment). The mean residence time and the variance were then calculated using equations (6.13) and (6.14). At a flow rate of 13.15 ml/hr, the mean residence time and variance are 8.38 hours and 0.167 hr<sup>2</sup>, respectively. The mean contact time is 5.32 hours (70 ml bed void volume ÷ 13.15 ml/hr), and the difference between the mean residence time and the mean contact time is equal to the reactor headspace volume (38.15 ml) plus the volume (≈4 ml) of the feed tube (42.15 ml ÷ 13.15 ml/hr = 3.21 hr).

For small amounts of dispersion, the solution to the axial dispersion model, equation (6.4), is (Levenspiel, 1972)

$$C = \frac{1}{2(\pi D/uL)^{1/2}} \exp - \frac{(t - \tau)^2}{4D/uL} \quad (6.15)$$

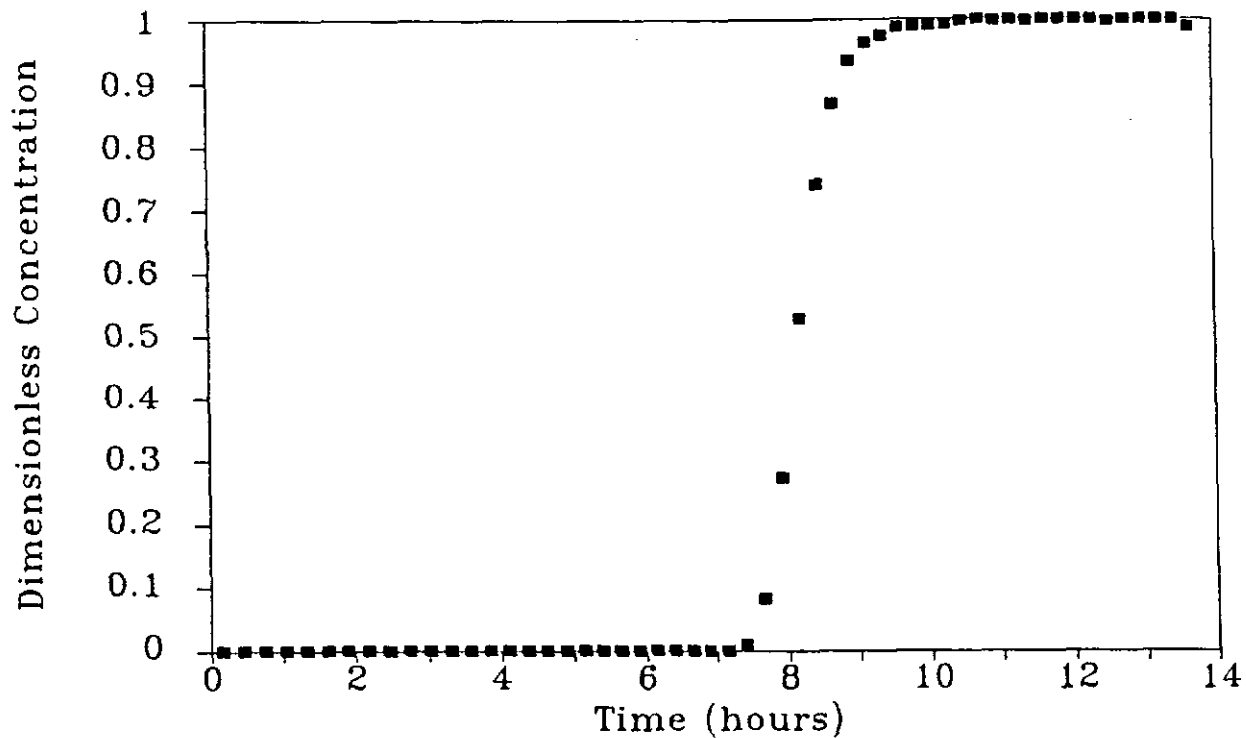


**Figure 6.5** Normalized Na-Fluorescein dye concentrations as a function of time for the packed bed tracer experiment. The concentrations are normalized automatically by setting the spectrophotometer to read the feed concentration as 1.000 and the background concentration as 0.000.

For small extents of dispersion, the shape of the residence time distribution curve is insensitive to boundary conditions (Levenspiel, 1962). Equation (6.15) is a normal distribution with a mean of  $\tau$  and a variance of  $\sigma^2 = 2\tau^2 D/uL = 2\tau^2/Pe$ . By integrating equation (6.15), the experimentally determined tracer concentrations can be compared with the axial dispersion model for small amounts of dispersion. This comparison is shown in Figure 6.6. The fit of the axial dispersion model to the experimental data was optimized by adjusting the mean residence time to 8.35 hours. The RMS difference between the experimental data points and the axial dispersion model is 0.016 hours.

**Table 6.3 Na-fluorescein concentrations from the dye tracer experiment. The elapsed time is the actual time that the automatic sampler advanced. The calculated time is figured for a constant flow rate of 0.22 ml/min.**

Elapsed Time (min)	Mass (g)	Cumulative Mass (g)	Calculated Time (min)	Na-fluorescein Concentration (dimensionless)
0	3.76	3.76	9.66	0.00
15	4.03	7.79	28.05	0.00
30	3.92	11.71	45.93	0.00
45	3.77	15.48	63.14	0.00
60	3.65	19.13	79.79	0.00
75	3.81	22.94	97.18	0.00
90	3.74	26.68	114.24	0.00
106	3.67	30.35	130.99	0.00
121	3.66	34.01	147.69	0.00
136	3.63	37.64	164.25	0.00
151	3.75	41.39	181.36	0.00
166	3.78	45.17	198.61	0.00
181	3.64	48.81	215.22	0.00
196	3.51	52.32	231.24	0.00
211	3.43	55.75	246.89	0.00
226	3.46	59.21	262.68	0.00
241	3.45	62.66	278.42	0.00
256	3.46	66.12	294.21	0.00
271	3.29	69.41	309.22	0.00
286	3.28	72.69	324.18	0.00
301	3.29	75.98	339.20	0.00
316	3.28	79.26	354.16	0.00
331	3.28	82.54	369.13	0.00
346	3.25	85.79	383.96	0.00
362	3.26	89.05	398.84	0.00
377	3.29	92.34	413.85	0.00
392	3.36	95.70	429.18	0.00
407	3.38	99.08	444.60	0.01
422	3.54	102.62	460.76	0.08
437	3.50	106.12	476.73	0.27
452	3.33	109.45	491.92	0.53
467	3.20	112.65	506.52	0.74
482	3.12	115.77	520.76	0.87
497	3.21	118.98	535.41	0.94
512	3.00	121.98	549.09	0.96
527	2.96	124.94	562.60	0.97
542	3.01	127.95	576.34	0.99
557	2.96	130.91	589.84	0.99
572	2.97	133.88	603.39	0.99

**Table 6.3** (continued)

Elapsed Time (min)	Mass (g)	Cumulative Mass (g)	Calculated Time (min)	Na-fluorescein Concentration (dimensionless)
587	2.96	136.84	616.90	0.99
602	2.97	139.81	630.45	1.00
618	2.94	142.75	643.87	1.00
633	2.93	145.68	657.24	1.00
648	2.98	148.66	670.84	1.00
663	2.97	151.63	684.39	1.00
678	2.97	154.60	697.94	1.00
693	2.97	157.57	711.49	1.00
708	2.98	160.55	725.09	1.00
723	2.98	163.53	738.69	1.00
738	2.98	166.51	752.29	1.00
753	2.99	169.50	765.93	1.00
768	2.99	172.49	779.57	1.00
783	3.00	175.49	793.26	1.00
798	3.01	178.50	807.00	1.00
813	3.02	181.52	820.78	0.99

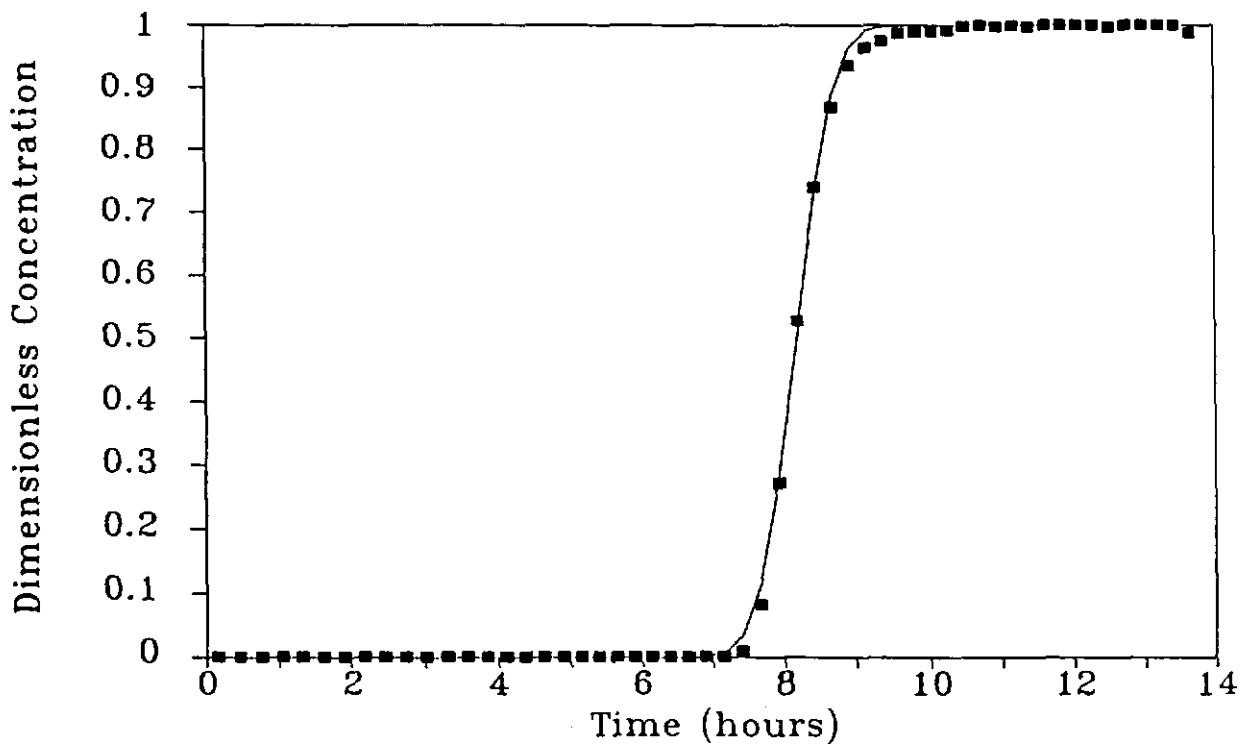


**Figure 6.6** Comparison of the tracer concentration data with the axial dispersion model for small extents of dispersion (equation (6.15)).

The excellent fit of the axial dispersion model to the tracer data allows the direct evaluation of the Peclet number. For this tracer experiment,  $Pe = 874$ . As discussed above, large values for the Peclet number mean that the diffusion term in equation (6.5) is negligible compared with the convection term. Thus, for the packed bed reactor, the reactor performance is adequately described by equation (6.6).

*6.4.2 Calculation of the Solution pH.* A pH electrode was inserted in the reactor effluent stream to continuously monitor the pH. The electrode was standardized with commercially available pH 4 and pH 7 buffer solutions, and for pH values above 0.5, the pH electrode gave reasonable readings. However, the electrode response in the stronger acid solutions ( $> 1.0 \text{ N HNO}_3$ ) was very non-linear, and negative values of pH were measured. It is not unusual for the slope adjustment to change over broad ranges of pH, and the negative pH readings may indicate that the slope correction set by calibrating with the buffer solutions was not appropriate that far outside the pH 4 to 7 range.

If both the hydrogen ion concentration and the activity coefficient of hydrogen in the aqueous solution are known, the pH can be approximated. The hydrogen ion concentrations were measured by titration as described in section 6.1.2, and the results are tabulated in Table 6.1. A comparison of the acid contents of the feed solutions and the effluent solutions shows that steady-state concentrations of nitric acid in the reactor effluent are very close to the feed concentrations of nitric acid.

Two methods were used to estimate the mean ionic activity coefficient. The first is the empirical correlation of Meissner (Meissner and Tester, 1972; Meissner, 1980) and the second is Pitzer's (1979) ion interaction approach. Meissner and Tester (1972) defined a reduced mean ionic activity coefficient,  $\Gamma$ , as:

$$\Gamma = \gamma^{1/|z_+z_-|} \quad (6.16)$$

where  $\gamma$  is the mean ionic activity coefficient and  $z_+$  and  $z_-$  are the charge on the cation and anion, respectively. When experimentally determined values of  $\Gamma$  for solutions of single electrolytes are plotted against the ionic strength,  $I$ , a family of curves is formed. Part of this family of curves is shown in Figure 6.7. An analytical expression has been developed for the curve family, and each curve is represented by a single parameter,  $q$  (Meissner, 1980):

$$\Gamma = [1 + B(1 + 0.1 I)^q - B] \Gamma^* \quad (6.17)$$

where

$$B = 0.75 - 0.065 q$$

$$\log_{10}\Gamma^* = \frac{-0.5107 I^{1/2}}{1 + C I^{1/2}}$$

$$C = 1 + 0.055 q \exp(-0.023I^3)$$

$$I = 0.5 \sum m_i z_i^2$$



Published values for the mean ionic activity coefficient of various nitric acid solutions (Conway, 1952; Harned and Owen, 1958; Dobos, 1975) were used to find the best value for  $q$ . As shown in Figure 6.7, up to an ionic strength of 0.5,  $q$  is approximately equal to 5, but for ionic strengths above 1.5,  $q$  is about 3.7.

Pitzer (1979) suggested that short-range ion association effects become increasingly important as the ionic strength increases. These ion association effects in solution are analogous to the intermolecular forces between pairs of molecules in a real gas which, for the gas, are described by the second virial coefficient. Pitzer (1979) extends the analogy by adding a "second virial coefficient" to the Debye-Hückel limiting law. For a single-component electrolyte solution (Pitzer, 1979):

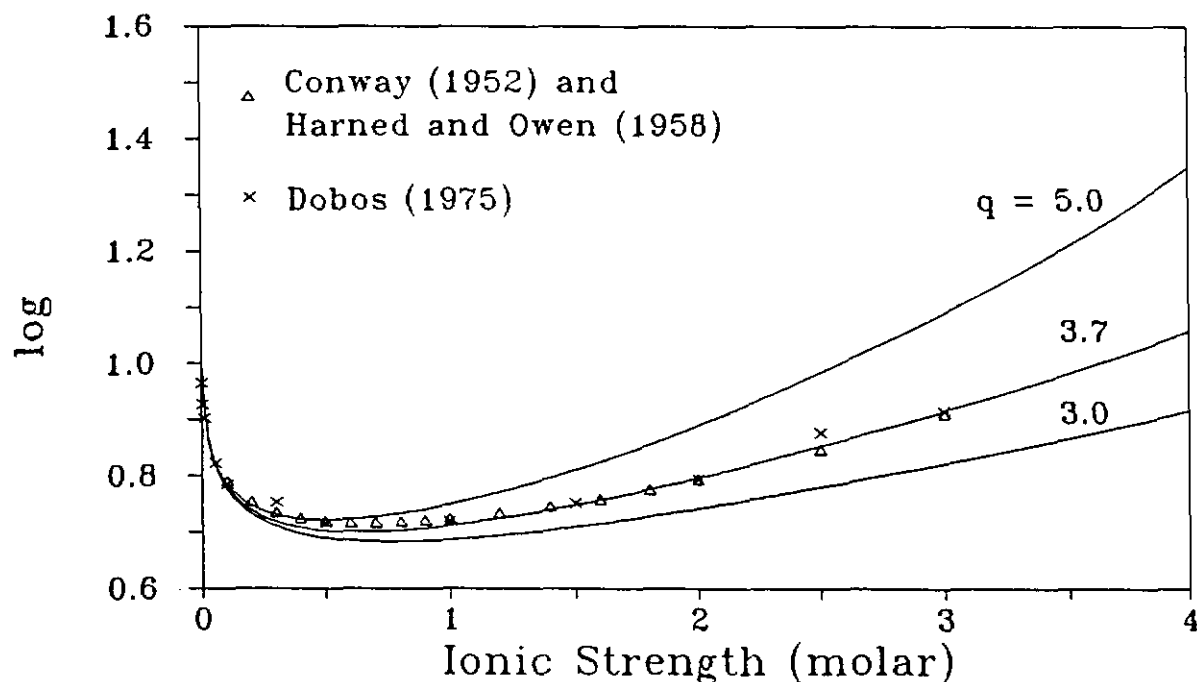


**Figure 6.7** Comparison of a portion of Meissner's (1980) family of curves of reduced mean ionic activity coefficient,  $\Gamma$ , with experimental values for the mean ionic activity coefficient for  $\text{HNO}_3$  at  $25^\circ\text{C}$  (from Conway, 1952; Harned and Owen, 1958; and Dobos, 1975).

$$\ln \gamma_{\pm} = |z_+ z_-| f^{\gamma} + 2 m \frac{(\nu_+ \nu_-)}{(\nu_+ + \nu_-)} B^{\gamma} + 3 m^2 \frac{(\nu_+ \nu_-)}{(\nu_+ + \nu_-)} C^{\phi} \quad (6.18)$$

where

$$f^{\gamma} = -A_{\phi} [I^{1/2}/(1 + 1.2 I^{1/2}) + (2/1.2) \ln (1 + 1.2 I^{1/2})]$$

$$B^{\gamma} = 2\beta^{(0)} + 2\beta^{(1)}[1 - (1 + 2I^{1/2} - 2I) \exp (-2I^{1/2})]/(4I)$$

$A_{\phi}$  is the Debye-Hückel osmotic coefficient (at 25°C,  $A_{\phi} = 0.3910$ ), and for nitric acid,  $\beta^{(0)} = 0.1119$ ,  $\beta^{(1)} = 0.3206$  and  $C^{\phi} = 0.0010$  (Pitzer, 1979).

The mean ionic activity coefficients for nitric acid (Conway, 1952; Harned and Owen, 1958; Dobos, 1975) are compared with Meissner's (1980) model ( $q = 3.7$ ) and with Pitzer's (1979) model in Figure 6.8. While both activity coefficient models are reasonably close to the experimental data, Pitzer's model fits the data slightly better over the entire range.

Values for the pH calculated from these model activity coefficients and ionic strengths are shown in Figure 6.9. As shown in the figure, there is no real difference between the pH values calculated by Meissner's (1980) empirical method and those calculated by Pitzer's (1979) method. One interesting feature of this graph is that the calculated pH is less than zero at ionic strengths greater than about 1.35. There are at least two ways in which the apparent negative pH values could arise. First, if some fraction of the  $\text{HNO}_3$  does not dissociate in the solution, the apparent ionic strength

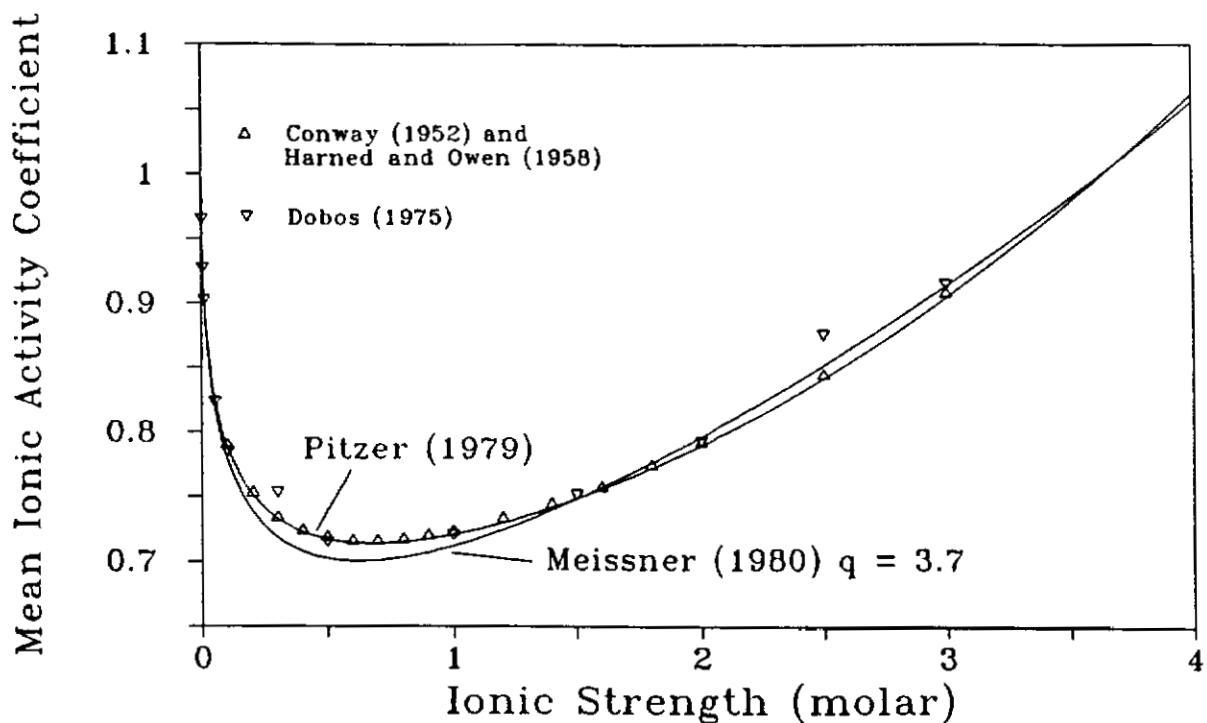


**Figure 6.8** Comparison of the experimental values for the mean ionic activity coefficient for  $\text{HNO}_3$  (Conway, 1952; Harned and Owen, 1958; Dobos, 1975) with Meissner's (1980) and Pitzer's (1979) models for calculating activity coefficients.

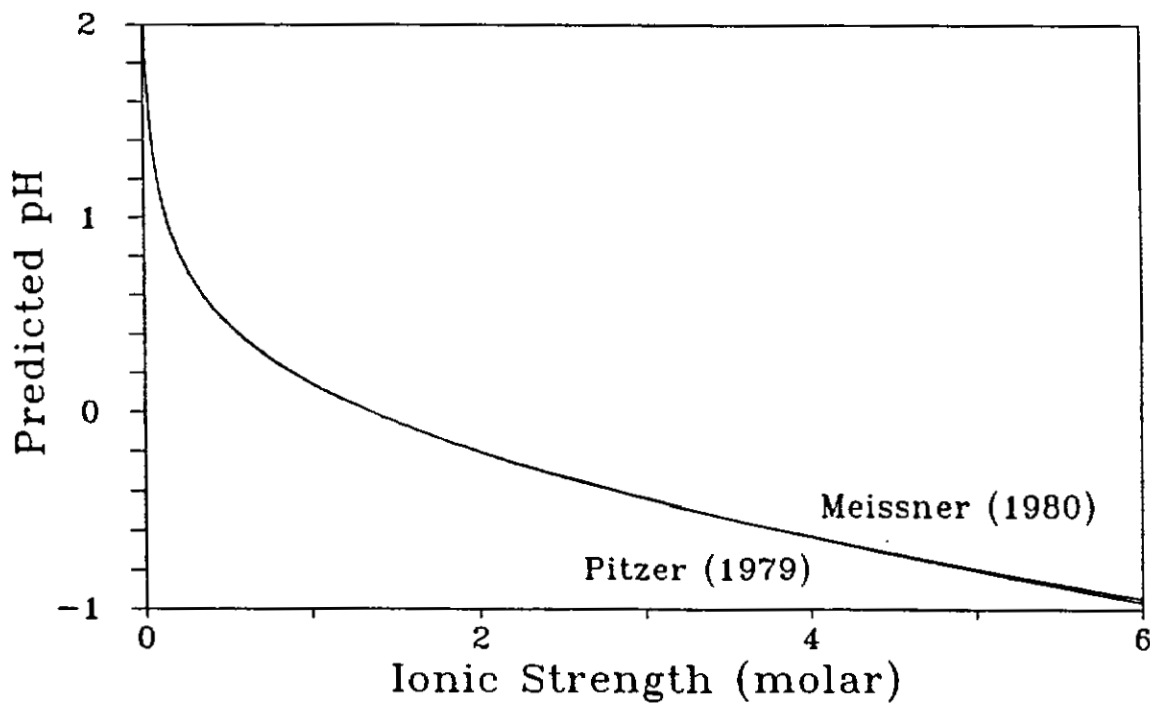


**Figure 6.9** Calculated pH versus ionic strength for Meissner's (1980) and for Pitzer's (1979) activity coefficient models.

based on 100% dissociation would be higher than the true ionic strength. For example, Dobos (1975) reports the degree of dissociation of 0.1 N, 1.0 N and concentrated nitric acid solutions to be 0.92, 0.82 and 0.096, respectively.

Another adjustment must be made for disproportionation of the  $\text{HNO}_3$  in solution:



If this reaction contributes significantly to the speciation, then the hydrogen ion concentration is reduced relative to the nitrate concentration, and the ionic strength is reduced since only two ions are produced from two  $\text{HNO}_3$  molecules instead of the four that would result from complete dissociation of the acid.

Two sets of nitric acid dilutions were prepared to test the pH calculations. The measured pH values and the nitric acid concentrations determined by titration are presented in Table 6.4. These data are also compared with the calculated pH values in Figure 6.10. Below an ionic strength of about 0.6, these data sets are within about 0.1 pH units of the calculated pH values. Above an ionic strength of 0.6, the pH electrode would not give stable readings. Because of the good agreement among the activity coefficient models, published data on mean ionic activity coefficients for  $\text{HNO}_3$  solutions and the measured pH of nitric acid solutions, we can have reasonable confidence in our calculated pH values.

**Table 6.4** Ionic strength and pH measured for various HNO<sub>3</sub> solutions. The ionic strength was determined by adding 5.0 ml of 0.1 N KOH to 1.0 ml of sample and then titrating with 0.1 N H<sub>2</sub>SO<sub>4</sub>.

Measured pH	Titrant Volume (ml)	Ionic Strength (molar)	Mean Ionic Activity Coefficient	Calculated pH
1.52	4.62	0.038	0.837	1.498
1.36	4.39	0.061	0.809	1.307
1.26	4.24	0.076	0.795	1.219
1.18	3.95	0.105	0.775	1.089
1.11	3.71	0.129	0.763	1.007
0.95	2.75	0.225	0.732	0.783
3.903	0.00		1.000	
1.454	4.32	0.034	0.843	1.543
1.179	4.33	0.067	0.803	1.269
0.903	3.59	0.141	0.758	0.971
0.577	3.54	0.292	0.719	0.678
0.419	2.81	0.438	0.705	0.510
0.300	2.13	0.574	0.701	0.396

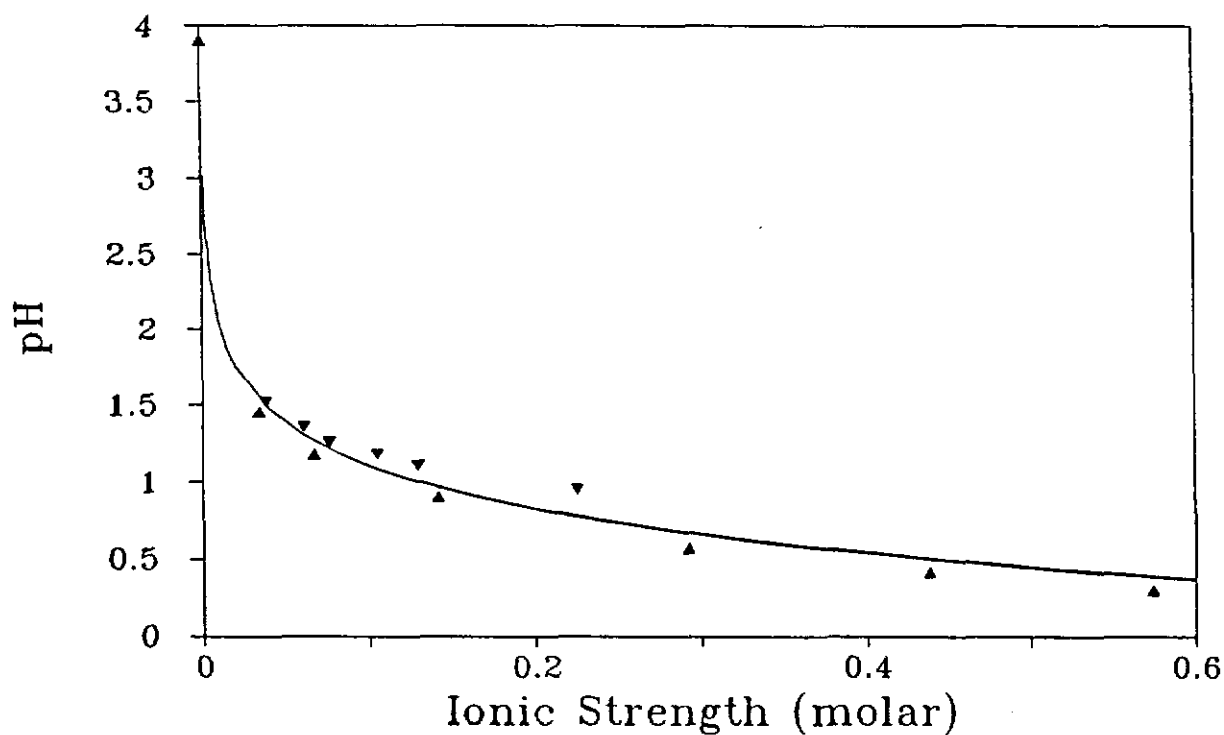


**Figure 6.10** Comparison of calculated pH values with experimentally measured values of pH for various HNO<sub>3</sub> solutions

*6.4.3 Quartz Dissolution Results.* Silica concentrations in the feed solutions and the reactor effluent samples are presented in Appendix D along with silica concentrations corrected for evaporation losses between the time of collection and the time of analysis. For the most part, these corrections are negligible. Measured and evaporation corrected silica concentrations in the reactor effluent are plotted as a function of time in Figure 6.11a. Similar plots for pH and flow rate are shown in Figures 6.11b and 6.11c. Note that the time required to approach steady-state ( $\tau_{ss}$ ) is of the order of 12 hours, in excellent agreement with the mean residence time determined by the tracer experiment. Although there is a considerable amount of scatter in the silica data, the silica concentrations do approach steady-state values. These steady-state silica concentrations were determined by averaging the concentrations which occurred after the transient changes had passed. Measurements more than two standard deviations away from the mean were excluded from the data set. The averaged steady-state silica concentrations are presented in Table 6.5.

To calculate the rate of quartz dissolution using equation (6.10), we must know the quartz saturation concentration. Quartz saturation concentrations are thought to be independent of pH below a pH of about 8 (Iler, 1979; Knauss and Wolery, 1988; Thornton and Radke, 1988). The saturation concentration for each of the nitric acid feeds was measured by reacting 10.0 grams of quartz sand in 15 ml of the acid for two weeks. Silica concentrations were determined as described above, and the saturation concentrations are shown in Table 6.5.

**Table 6.5** Experimentally determined quartz saturation concentrations at low pH, steady-state outlet silica concentrations from the packed bed reactor, and calculated rates of quartz dissolution.

HNO <sub>3</sub> Concentration (molar)	pH	Silica Saturation Concentration (ppb)	Steady-State Silica Concentration (ppb)	Flow Rate (ml/hr)	log rate (mol/cm <sup>2</sup> -s)
1.00	0.12	1800	960	16.5	-15.36
0.31	0.65	1720	580	17.1	-15.64
0.10	0.76*	1440	335	16.5	-15.93
0.10	1.07*	1440	335	16.5	-15.93
0.00	4.30		120	16.6	-16.40
0.00	3.00		20	23.0	-17.05

\* The measured pH is 1.07 and the calculated pH is 0.76 as described in the text.

The initial rates of quartz dissolution were calculated using equations (6.8) and (6.12). The rate law embedded in equation (6.8) does not account for the reverse (precipitation) reaction. In computing the rate from equation (6.8), the term,  $k_f \{a^* [C^{surf}] [H_3O^+]\}^{1/2}$ , was calculated from measured values of  $C(\xi)$ ,  $C_{in}$  and  $\tau$ . These calculated rates are shown as the open squares in Figure 6.12. When the reverse reaction is considered (equation (6.12)), the rates are slightly lower as shown by the open diamonds in Figure 6.12. The rates reported in Table 6.5 are calculated from equation (6.12). For one of the runs, the pH could be measured as well as calculated. The calculated pH is 0.755 compared to a measured pH of 1.07. The difference between the calculated and the measured pH is larger than expected - about 0.3 pH

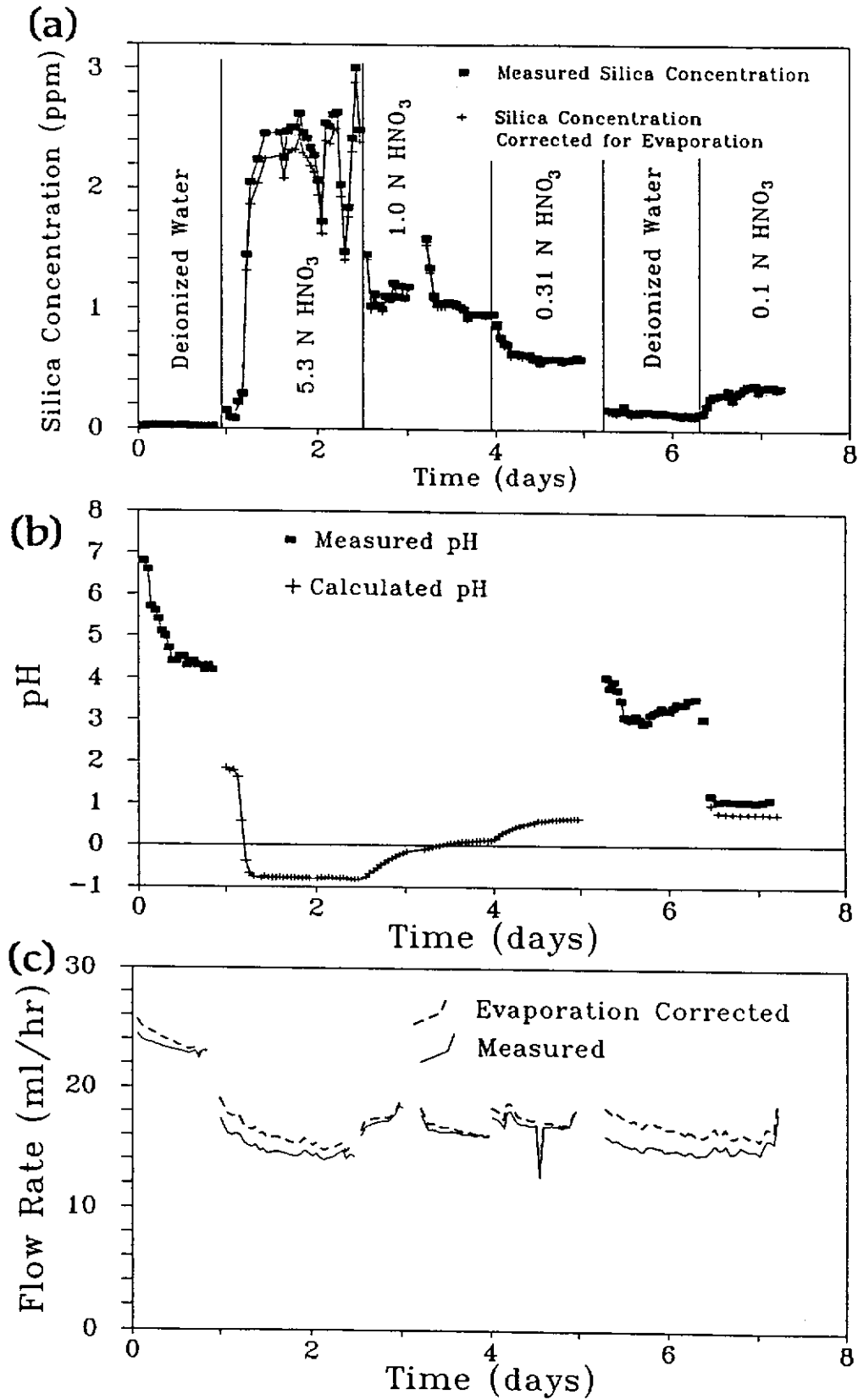


**Figure 6.11** Measured (■) and calculated (+) values for (a) silica concentration, (b) pH, and (c) flow rate for the quartz dissolution rate experiments in the packed bed reactor. Feed solutions are labeled on the graph. The major breaks shown at about days 1 and 5 are of several days duration each; the time axis for these graphs is compressed to show the important features of the experimental results.



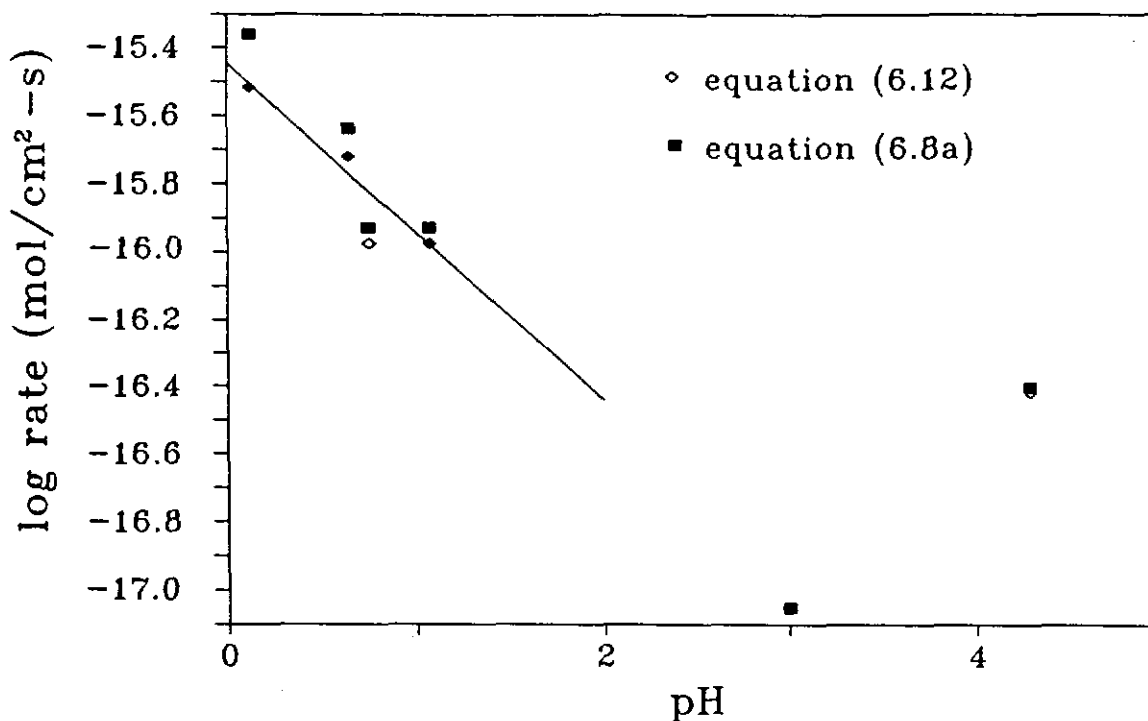


**Figure 6.12** Results of the quartz dissolution rate studies on Ottawa sand. The open squares are the rates calculated using equation (6.8), and the diamonds correspond to the rates calculated from equation (6.12). The solid diamonds were used in calculating the least squares line.

units, and is as yet unexplained<sup>1</sup>. For this case, the log rate is plotted versus both the measured and the calculated pH values in Figure 6.12. A least squares line was calculated using the measured pH rather than the calculated pH for the one point is shown in Figure 6.12. The slope of this line is -0.59 ( $2\sigma = 0.1$ ), in reasonably good agreement with the predicted value of -0.5.

<sup>1</sup>If the volume of sample titrated was actually 2.0 ml rather than the 1.0 ml recorded, the calculated pH agrees very well with the measured pH. However, the samples have been discarded and this point cannot be tested.

*6.4.4 Comparison with Previous Results.* The results of these dissolution rate experiments are compared with published quartz dissolution rates in Figure 6.13. Although the rate data from these experiments follow the same pattern of acid- and base-catalyzed reactions as the other quartz dissolution rate data, they are consistently one to two orders of magnitude faster than expected based on the published quartz dissolution rates at 25°C.

Some of this difference could be due to inaccuracies in the measurement of the BET surface area, but it is more likely that the difference results from the differences between the sand surface and the surfaces of crushed quartz crystals used in other dissolution experiments. For example, compare the SEM photographs of a treated but unreacted Ottawa sand grain (Figure 6.14a) and a fragment of crushed quartz crystal (from Knauss and Wolery, 1988) (Figure 6.14b). The outer surface of the sand grain is considerably smoother than the original sand as shown in Figure 6.2, but it is still rough compared with the smooth surface seen in the fracture at the right side of Figure 6.14a and with the fractured surface shown in Figure 6.14b. A smooth surface such as a fracture surface would consist mainly of  $\text{Si}_3\text{-OH}$  moieties with  $\text{Si}_2\text{-(OH)}_2$  groups present at the sharp corners and edges of the grain. On the other hand, a rough surface would have ledges and etch pits and a much higher fraction of the surface covered by  $\text{Si}_2\text{-(OH)}_2$  groups. Thus, it is plausible that the main reason for the differences between the quartz dissolution rates measured using the tumbled Ottawa sand and crushed quartz lies in the relative importance of reaction at  $\text{Si}_3$  sites versus reaction at  $\text{Si}_2$  sites. For the crushed quartz, most of the surface is covered by the

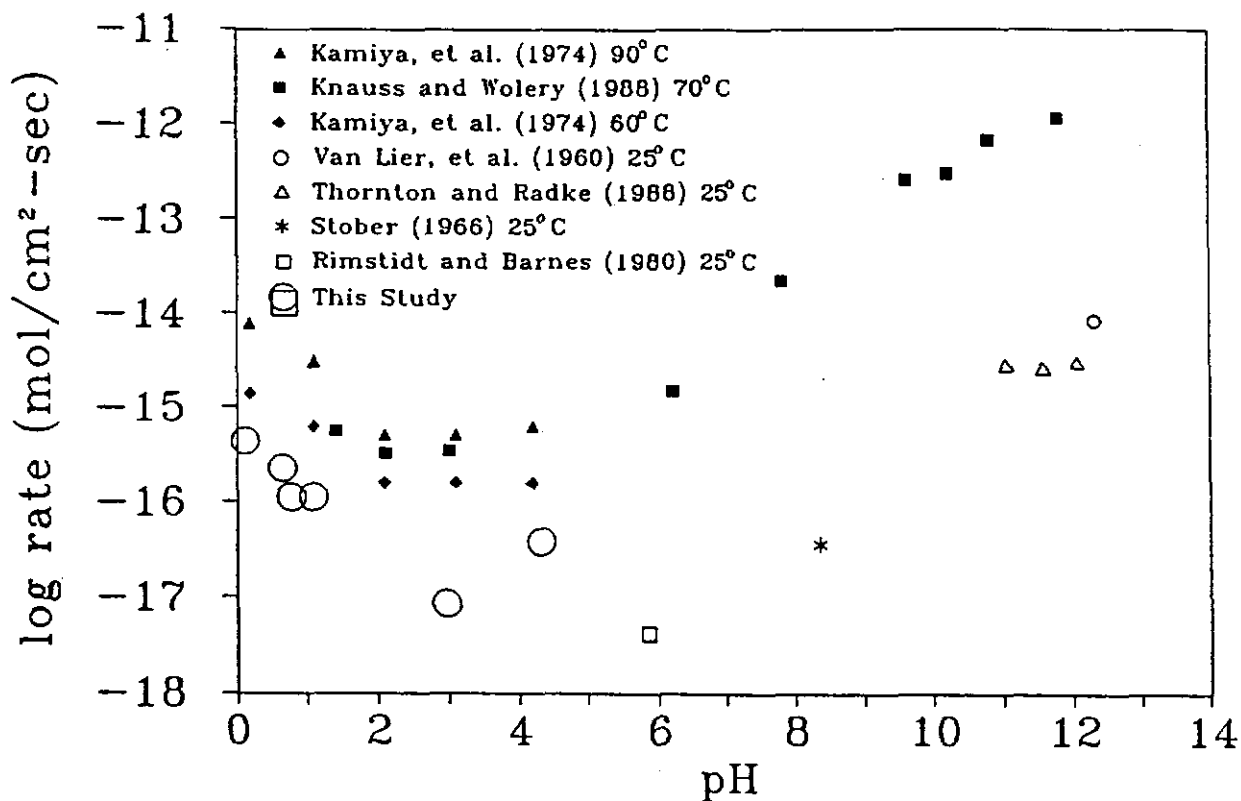
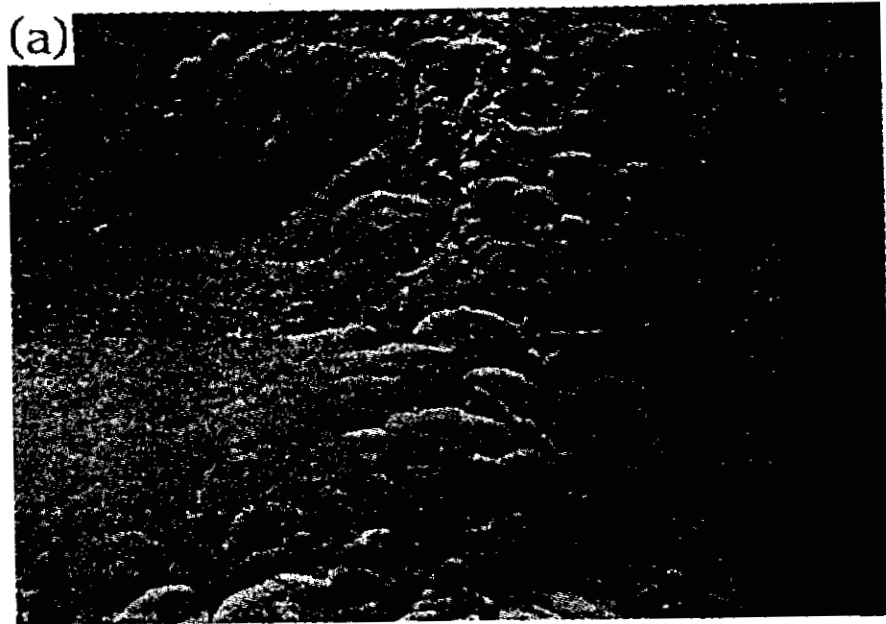


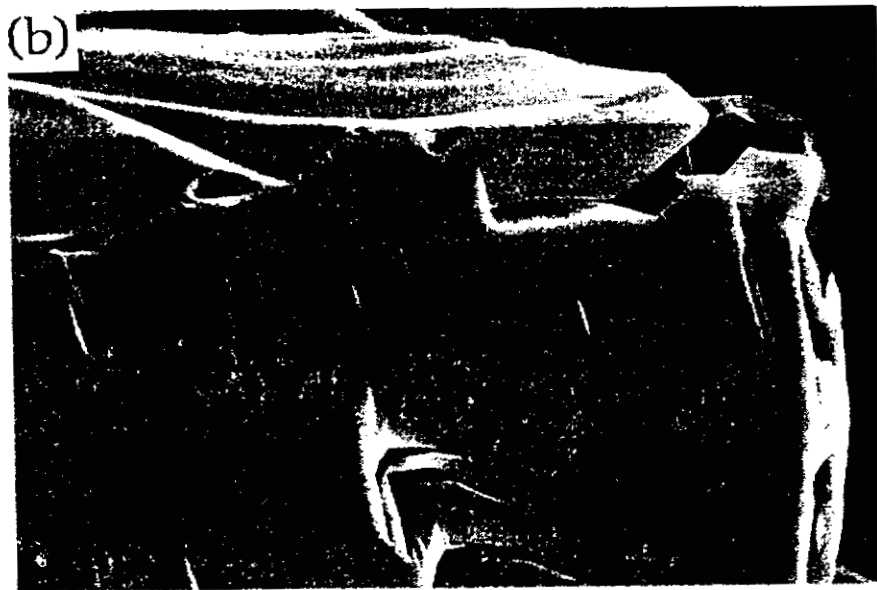
**Figure 6.13** Results of the quartz dissolution rate experiments compared with published quartz dissolution rate data. Notice that the quartz dissolution rate increases with  $[H^+]$  at low pH. The rates from this study are considerably higher than expected based on the 25°C data shown in the Figure.

relatively less reactive  $Si_3-OH$  groups, but for the Ottawa sand, the proportion of  $Si_2-(OH)_2$  sites is higher because the tumbling did not completely smooth the surface of the grains.

Although the quartz dissolution rates are higher than expected, the experiments described in this chapter are an important confirmation of several aspects of the proposed reaction mechanism. First, the rate of quartz dissolution was shown to depend upon the solution pH at low pH. Next, the dissolution rate data are consistent with the expected one-half order with respect to pH. Finally, the minimum in the rate



100 $\mu$



10 $\mu$

**Figure 6.14** SEM photographs of (a) a grain of Ottawa sand from these experiments and (b) the crushed quartz used by Knauss and Wolery (1988). Fracture surfaces in (a) (at the arrow) and (b) are very smooth compared with the outside surface of the sand grain.

appears to be at about a pH of 3 - close to the  $\text{pH}_{\text{pzc}}$ . In addition, these experiments show that the packed bed reactor can be used in mineral dissolution experiments as well as CSTR type reactors.

## Chapter 7

### Discussion of the Theoretical and Experimental Results and Recommendations for Future Work

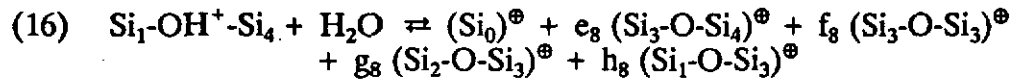
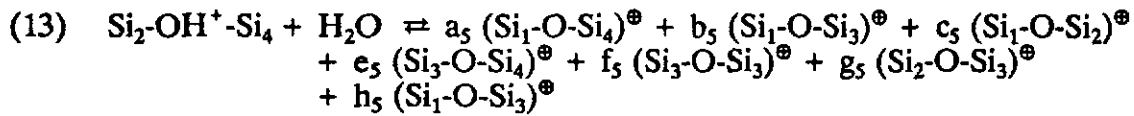
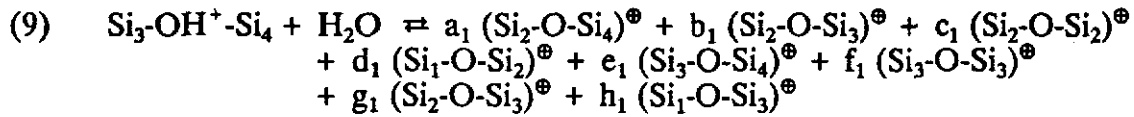
**7.1 Discussion of the Results.** In Chapters 4 and 5, we developed a mechanism for describing the acid- and base-catalyzed hydrolysis of  $\equiv\text{Si-O-Si}\equiv$  bonds and derived rate laws that account for the dependence of the rate on pH. The experiments described in Chapter 6 confirm the pH dependence of the quartz dissolution rate at low pH and support the mechanistic prediction that the rate is one-half order in catalyst ( $[\text{H}^+]$  or  $[\text{OH}^-]$ ) activity.

At this point, we might expect that there is sufficient rate data to calculate intrinsic kinetic parameters - activation energies and pre-exponential factors - for quartz and albite dissolution. Since the reaction rate data for quartz and albite dissolution are based on the stoichiometry of overall reactions, we must first convert the rate data to the appropriate basis before attempting to calculate kinetic parameters. There is, however, a further complication. The activation energy is proportional to the derivative of the natural logarithm of the *rate constant* for an elementary reaction with respect to the reciprocal temperature:

$$E_{\text{act}} = -R \frac{d \ln k}{d(1/T)} \quad (7.1)$$

The dissolution rate data presented in Figures 5.6 and 6.13 give bulk dissolution rates, not rate constants, so the bulk rate must be related to the rate of one or more key elementary reactions.

The relationship between the bulk rate of quartz dissolution and the rates of the rate-limiting elementary reactions was discussed in Chapter 5. The derived rate law for acid-catalyzed quartz dissolution includes contributions from three independent elementary reactions (reactions 9, 13 and 16 in Table 4.4) that operate in parallel:



Each reaction occurs at a particular surface site: reaction (9) occurs at  $\text{Si}_3\text{-O-Si}_4$  sites, reaction (13) occurs at  $\text{Si}_2\text{-O-Si}_4$  sites, and reaction (16) occurs at  $\text{Si}_1\text{-O-Si}_4$  sites. The bulk dissolution rate is given by equation (5.17a):

$$\mathfrak{R}_{\text{qtz}} = k_9 [\text{Si}_3\text{-OH}^+\text{-Si}_4][\text{H}_2\text{O}] + k_{13} [\text{Si}_2\text{-OH}^+\text{-Si}_4][\text{H}_2\text{O}] + k_{16} [\text{Si}_1\text{-OH}^+\text{-Si}_4][\text{H}_2\text{O}] \quad (5.17a)$$

If the contributions of these two reaction pathways cannot be distinguished, we cannot calculate meaningful activation energies from the bulk rate data. The relative

contribution of each reaction to the bulk rate depends upon the magnitudes of the rate constants,  $k_9$  and  $k_{13}$ , and on the surface concentrations of the key reactive species -  $\text{Si}_3\text{-O-Si}_4$  and  $\text{Si}_2\text{-O-Si}_4$ . Smooth mineral surfaces should be covered mostly by  $\text{Si}_3\text{-O-Si}_4$ , but at edges, ledges and dislocations,  $\text{Si}_2\text{-O-Si}_4$  should predominate as shown in Figure 5.2.

The importance of sample preparation and surface characterization techniques becomes evident when the various rates measured for quartz dissolution are examined. Most investigators crush the minerals and wash to remove the fines (see Table 2.1). These crushed samples typically have relatively smooth cleavage surfaces bounded by sharp edges (see Figure 6.14b). Thus, most of the surface of the "crushed and washed" samples would be covered by the  $\text{Si}_3$  sites, but most of the dissolution would occur at the edges and etch pits. Examination of reacted mineral grains shows that dissolution occurs mainly at the edges of the grains and at etch pits (Knauss and Wolery, 1988; others).

Etched surfaces such as are shown in the SEM photographs (Figure 6.2) of the Ottawa sand used in the experiments described in Chapter 6 should have a much higher surface concentration of  $\text{Si}_2$  sites because of the relatively rough surface. Clearly, tumbling the sand for two weeks did not completely remove the etched surface, so ledges and pits abound. The surface concentration of  $\text{Si}_2$  sites would be much higher for these samples than for the crushed quartz samples, and this is reflected in the fact that the rate of dissolution measured for tumbled sand is about two orders of



magnitude higher than would be expected based on the rates measured for crushed quartz at 25°C by other investigators.

Within a series of experiments, the sample preparation is uniform so that a consistent pattern emerges on a graph of log rate versus pH, but it is not clear that the samples prepared by different investigators using the same sample preparation techniques have the same ratio of Si<sub>3</sub> to Si<sub>2</sub> sites in the surface. We might calculate a reasonable activation energy from the bulk quartz dissolution rate data based only on the experiments using crushed quartz, but as long as the bulk rate has significant, and possibly different, contributions from two reaction pathways, we can have no confidence that this calculated activation energy relates to any real process. For example, it appears that the ratio of Si<sub>3</sub> to Si<sub>2</sub> sites may have been approximately the same in the 25° quartz dissolution rate experiments of Van Lier, et al. (1960), Thornton and Radke (1988), Stober (1966) and Rimstidt and Barnes (1980) since these rate data define a line that is parallel to the 70°C data of Knauss and Wolery (1988) as shown in Figure 6.13. However, we cannot be sure that the Si<sub>3</sub> to Si<sub>2</sub> ratio is the same in these 25°C experiments as it is in the 70°C experiments. Even if the surface compositions were the same in the 70°C and the 25°C experiments, the calculated activation energy would still not be related to a single elementary reaction but would represent an unknown average for two or three elementary reactions. The variation in the activation energies calculated by various researchers for quartz dissolution (Table 4.1) underlines this point; estimates of the activation energy for quartz dissolution ranges from 67 to 110 kJ/mol.

To characterize the surface in a way that is useful for dissolution rate experiments, *both* the surface composition (the relative amounts of each of the surface species) and the total mineral surface area must be known. The surface composition serves to fix the relative rates of the two reaction paths. *Without this knowledge, we could not calculate reliable activation energies from the bulk dissolution rate data even if a series of dissolution experiments were conducted at different temperatures using perfectly uniform samples.* This information about surface species for aluminosilicate mineral samples is not only essential for calculating activation energies, it is also completely unavailable for all of the dissolution experiments described in this thesis. In fact, a technique for directly measuring the concentrations of  $\text{Si}_3$  and  $\text{Si}_2$  at a mineral surface in an aqueous environment is not known to this author.

The conclusion that there is not sufficient information available to calculate reliable activation energies even for quartz dissolution is important, particularly considering the number of experiments that have been conducted using quartz. However, even the pH dependence of the quartz dissolution rate was not clearly established until 1988 (Knauss and Wolery, 1988). The recent adoption of flow-through reactors has enabled a great many experiments to be conducted under a variety of conditions. Still, the major factor that has limited the rate of development of geochemical kinetics has been the lack of a unified geochemical kinetic theory to guide the experimental studies.

The ideas presented in this thesis provide much of the necessary theoretical basis for further developments of geochemical kinetics. The major contributions are (1) the recognition that the dissolution of quartz and albite proceeds via catalyzed hydrolysis of Si-O-Si and/or Si-O-Al bonds, (2) a comprehensive reaction mechanism for catalyzed bond hydrolysis, (3) a simplified mechanism and rate law that relates the observed bulk dissolution rates to the rates of elementary reactions, and (4) the recognition that activation energies cannot be calculated without knowing the relative rates of the various parallel elementary reaction pathways. The essential features of the reaction mechanisms and the corresponding rate laws developed in this thesis for quartz and albite dissolution are:

- 1) The dissolution reactions are catalyzed by  $H^+$  (or  $H_3O^+$ ) at low pH and by  $OH^-$  at high pH.
- 2) Many of the elementary reaction steps are common to the reaction mechanisms for both quartz and albite and might be expected in the mechanisms of other aluminosilicate minerals.
- 3) Only a few of these elementary steps are important in determining the bulk dissolution rate.
- 4) Because of the stoichiometry of the rate-limiting steps, the rates of the acid- and base-catalyzed reactions are one-half order in catalyst concentration for both minerals.
- 5) Aqueous aluminum retards the rate of reaction to give an apparent reaction order with respect to catalyst concentration that is less than one-half order. Presumably, other multi-valent cations also retard the dissolution rate.
- 6) The minimum dissolution rate for quartz occurs at the  $pH_{pzc}$  of quartz, and both the acid- and base-catalyzed reactions are interpreted as  $S_N2$  reaction mechanisms. For albite, the minimum rate occurs at a pH which is higher than the  $pH_{pzc}$  of albite because the acid-catalyzed reaction at tetrahedral aluminum sites in the albite structure can follow both the  $S_N2$  and the  $S_N1$  pathways.

7) The bulk rates of quartz and albite dissolution include contributions from at least two independent, parallel reaction pathways, and the relative rates of reaction for these pathways depends upon the surface morphology of the mineral sample.

8) The activation energy for an elementary reaction depends on the local environment at the reaction site and not on mineral bulk composition. Therefore, the rate and activation energy for a reaction at an Si<sub>2</sub>-O-Si<sub>4</sub> site be essentially the same in albite, quartz and other aluminosilicate minerals.

Some items in this list - for example, items (1), (4), (5) - are supported by direct evidence of experimental dissolution studies; other items - (5), (6) and (7) - provide mechanistic interpretations for features of dissolution rates that heretofore have been observed but not understood. All of the items are predictions that can be tested by experiment once the appropriate experiment design is developed.

**7.2 Recommendations for Further Work.** There are a number of experiments which should be performed to further test the proposed mechanisms and to solve certain problems that have been defined in this thesis. The most important recommendations for future work involve the independent measurement of the two key surface species and the rate constants associated with reaction at these two sites. In the absence of a technique for measuring concentrations of surface species, the first term in equation (5.18)

$$r_{qtz} = k_9 [Si_3-OH^+-Si_4][H_2O] + k_{13} [Si_2-OH^+-Si_4][H_2O] + k_{16} [Si_1-OH^+-Si_4][H_2O] \quad (5.17a)$$

could be measured if samples having extremely smooth surfaces and no edges could be prepared. The tumbled quartz sand samples described in Chapter 6 were intended to approach polished spheres, and with more careful preparation, tumbled sand might be an appropriate starting material for mineral dissolution experiments. Cylindrical geometries also can provide smooth surfaces with minimal corners or edges. It may be necessary to anneal samples to reduce or eliminate dislocations and defects.

Since a smooth surface should have different adsorption characteristics from a ledge or a pit, different surface sites could perhaps be measured by temperature programmed desorption of water. Sites binding water more tightly would desorb at slightly higher temperatures than the smooth surface, and this effect could be measured if the difference in site energy is sufficiently high.

When techniques for separating the contributions from the key elementary reactions are available, the experimental rate data taken by all previous investigators will not be useful in calculating kinetic parameters. Investigators wishing to fill this gap should plan on performing dissolution experiments as a function of pH at several different temperatures using the same starting material. This would eliminate the need to build composite data sets from isolated experiments which probably were not conducted under the same conditions using the same materials. Investigators should also choose reactor geometries that avoid the potential problems of flow maldistribution in the reactor, and tracer tests should be routinely be used to characterize reactor performance. Both the CSTR and the packed bed reactor can be

used for these experiments. The CSTR offers advantages when it is necessary to maintain low reaction product concentrations, and the calculations of bulk rates are easier using CSTR geometry.

In addition to dissolution rate experiments, information is needed about the  $\text{pH}_{\text{pzc}}$  as a function of temperature for many minerals. This information along with dissolution rate data could be used to test the hypothesis that  $\text{S}_{\text{N}1}$  and  $\text{S}_{\text{N}2}$  reaction mechanisms operate simultaneously when aluminum is tetrahedrally coordinated in the crystal structure. If the minimum rate of dissolution of a mineral occurs at a pH higher than the  $\text{pH}_{\text{pzc}}$ , we can calculate an entropy difference corresponding to the difference between the  $\text{S}_{\text{N}1}$  and the  $\text{S}_{\text{N}2}$  mechanisms, and if this entropy difference is the same for a number of minerals, we could then predict the dissolution rate behavior for a mineral from knowledge of the  $\text{pH}_{\text{pzc}}$ . We also need to measure the effect of aluminum and other aqueous ion concentrations on the rate of dissolution of quartz and other minerals.

The mechanisms and rate laws presented in this thesis for quartz and albite dissolution should apply with only slight modifications to other aluminosilicate minerals that contain aluminum in tetrahedral coordination in the crystal structure - other feldspars, feldspathoids, and zeolites. Other mineral groups - pyroxenes, amphiboles, clays, micas, garnets, etc. - contain aluminum, magnesium, and iron in octahedral coordination. The effect of octahedral aluminum, magnesium and iron in the crystal structure on the rate of dissolution is not characterized at this time.

The basic approach to dissolution kinetics presented - developing a comprehensive set of elementary reactions, reducing this set to a few key reactions and relating the observed dissolution rate to the rates of the key elementary reactions - provides a consistent methodology and conceptual framework for future studies of mineral dissolution rates.

## References

- Aagaard, P. and Helgeson, H.C. (1982) Thermodynamic and kinetic constraints on reaction rates among minerals and aqueous solutions. I. theoretical considerations. *Amer. J. Sci.* **282**: 237-285.
- Adamson, A.W. (1979) *Textbook of Physical Chemistry*. Academic Press, New York, NY, 953 pp.
- Barnes, H.L., ed. (1967) *Geochemistry of Hydrothermal Ore Deposits*. 2<sup>nd</sup> Edition. John Wiley and Sons, New York, NY, 798 pp.
- Benson, S.W. and Buss, J.H. (1958) Additivity rules for the estimation of molecular properties: thermodynamic properties. *J. Chem. Phys.* **29**: 546-572.
- Benson, S.W., Cruickshank, F.R., Golden, D.M., Gaugen, G.R., O'Neal, H.E., Rodgers, A.S., Shaw, R. and Walsh, R. (1968) Additivity rules for the estimation of thermochemical properties. *Chem. Rev.* **69**: 279-324.
- Benson, S.W. (1976) *Thermochemical Kinetics*. 2<sup>nd</sup> Edition. John Wiley and Sons, New York, NY, 320 pp.
- Berner, R.A. and Holdren, G.R. (1977) Mechanism of feldspar weathering: some observational evidence. *Geology* **5**: 369-372.
- Berner, R.A. (1978) Rate control of mineral dissolution under earth surface conditions. *Amer. J. Sci.* **278**: 1235-1252.
- Berner, R.A. and Holdren, G.R. (1979) Mechanism of feldspar weathering. II. observations of feldspars from soils. *Geochim. Cosmochim. Acta* **43**: 1173-1186.
- Bird, G., Boon, J. and Stone, T. (1986) Silica transport during steam injection into oil sands. I. dissolution and precipitation kinetics of quartz: new results and review of existing data. *Chemical Geology* **54**: 69-80.
- Bolt, G.H. (1957) Determination of the charge density of silica sols. *J. Phys. Chem.* **61**: 1166-1169.
- Brookins, D.G. (1984), *Geochemical Aspects of Radioactive Waste Disposal*. Springer-Verlag, New York, NY, 347 pp.
- Busenberg, E. and Clemency, C.V. (1976) The dissolution kinetics of feldspars at 25°C and 1 atm. CO<sub>2</sub> partial pressure. *Geochim. Cosmochim. Acta* **40**: 41-50.
- Carberry, J.J. (1976) *Chemical and Catalytic Reaction Engineering*. McGraw-Hill, New York, NY, 642 pp.



- Chen, C.H. (1975) A method of estimation of standard free energies of formation of silicate minerals at 298.15 K. *Amer. J. Sci.* 275: 801-817.
- Chou, L. and Wollast, R. (1984) Study of the weathering of albite at room temperature and pressure with a fluidized bed reactor. *Geochim. Cosmochim. Acta* 48: 2205-2217.
- Chou, L. and Wollast, R. (1985) Steady-state kinetics and dissolution mechanisms of albite. *Amer. J. Sci.* 285: 963-993.
- Colman, S.M. and Dethier, D.P. (1986) An overview of rates of chemical weathering. in S.M. Colman and D.P. Dethier, eds., *Rates of Chemical Weathering of Rocks and Minerals* Academic Press, Orlando, FL, 61-81.
- Conway, B.E. (1952) *Electrochemical Data*. Elsevier Publishing, New York, NY.
- Crerar, D.A., and Anderson, G.M. (1971) Solubility and solution reactions of quartz in dilute hydrothermal solutions. *Chemical Geology* 8: 107-122.
- Danckwerts, P.V. (1953) Continuous flow systems: distribution of residence times. *Chem. Eng. Sci.* 2: 1-13.
- Danckwerts, P.V. (1958) Local residence times in continuous flow systems. *Chem. Eng. Sci.* 9: 78-79.
- Deere, W.A., Howie, R.A. and Zussman, J. (1971) *An Introduction to the Rock-Forming Minerals*. John Wiley and Sons, New York, NY, 528 pp.
- Dibble, W.E. and Tiller, W.A. (1981) Non-equilibrium water/rock interactions. I. model for interface-controlled reactions. *Geochim. Cosmochim. Acta* 45: 79-92.
- Dobos, D. (1975) *Electrochemical Data*. Elsevier Publishing, New York, NY.
- Eigenmann, H.K., Golden, D.M. and Benson, S.W. (1973) Revised group additivity parameters for the enthalpies of formation of oxygen-containing organic compounds. *J. Phys. Chem.* 77: 1687-1691.
- Evans, M.G. and Polyani, M. (1935) *Trans. Faraday Soc.* 31: 875.
- Eyring, H. (1935) The activated complex in chemical reactions. *J. Chem. Phys.* 3: 107.
- Fessenden, R.J. and Fessenden, J.S. (1982) *Organic Chemistry*. 2<sup>nd</sup> Edition. PWS Publishers, Boston, MA, 1069 pp.
- Fournier, R.O. and Rowe, J.J. (1966) Estimation of underground temperatures from the silica content of waters from hot springs and wet-steam wells. *Amer. J. Sci.* 264: 685-697.

- Francisco, J.S., Hase, W.L. and Steinfeld J.I. (in press) *Chemical Kinetics and Dynamics*. Prentice Hall, Inc., Englewood Cliffs, NJ.
- Franklin, J.L. (1949) Prediction of heat and free energies of organic compounds. *Ind. Eng. Chem.* **41**: 1070-1076.
- Franklin, J.L. (1953) Calculation of the heats of formation of gaseous free radicals and ions. *J. Chem. Phys.* **21**: 2029-2033.
- Froment, G.F. (1975) Model discrimination and parameter estimation in heterogeneous catalysis. *AIChE J.*, **27**: 1043-1057.
- Garrels, R.M. and Christ, C.L. (1965) *Solutions, Minerals and Equilibria*. Freeman, Cooper and Company, San Francisco, CA, 450 pp.
- Glasstone, S., Laidler, K.J. and Eyring, H. (1941) *The Theory of Rate Processes*. McGraw-Hill, New York, NY, 611 pp.
- Glowinski, J. and Stocki, J. (1981) Estimation of kinetic parameters - initial guess generation method. *AIChE J.* **27**: 1041-1043.
- Goff, F., Truesdell, A.H., Grigsby, C.O., Janik, C.J., Shevenell, L.A., Paredes, J.R., Gutierrez, J.W., Trujillo, P.E., and Counce, D.A. (1987) Hydrogeochemical investigation of six geothermal sites in Honduras, Central America. Los Alamos National Laboratory report LA-10785-MS, 170 pp.
- Gould, E.S. (1959) *Mechanism and Structure in Organic Chemistry*. Holt, Rinehart, and Winston, New York, NY, pp. 291-294.
- Grandstaff, D.C. (1977) Some kinetics of bronzite orthopyroxene dissolution. *Geochim. Cosmochim. Acta* **43**: 1097-1103.
- Grandstaff, D.C. (1980) The dissolution rate of forsterite olivine from Hawaiian beach sand. *Proc. Third Intl. Symp. Water-Rock Interaction, Edmonton, Canada*, pp. 72-74.
- Grigsby, C.O., Tester, J.W., Trujillo, P.E., and Counce, D.A. (1989) Rock-water interactions in the Fenton Hill, New Mexico hot dry rock geothermal systems I. fluid mixing and chemical geothermometry. accepted for publication in *Geothermics*.
- Grigsby, C.O. and Tester, J.W. (1989) Rock-water interactions in the Fenton Hill, New Mexico hot dry rock geothermal systems II. modeling geochemical behavior. accepted for publication in *Geothermics*.
- Harned, H.S. and Owen, B.B. (1958) *The Physical Chemistry of Electrolyte Solutions*. 3<sup>rd</sup> Edition, Reinhold Publishing, New York, NY.

- Helgeson, H.C., Garrels, R.M. and Mackenzie, F.T. (1969) Evaluation of irreversible reactions in geochemical processes involving minerals and aqueous solutions - II applications. *Geochim. Cosmochim. Acta*, **33**: 455-481.
- Helgeson, H.C. (1968) Evaluation of irreversible reactions in geochemical processes involving minerals and aqueous solutions - I. thermodynamic relations. *Geochim. Cosmochim. Acta* **32**: 853-857.
- Helgeson, H.C., Brown, T.H., Nigrini, A. and Jones, T.A. (1970) Calculation of mass transfer in geochemical processes involving aqueous solutions. *Geochim. Cosmochim. Acta* **34**: 569-592.
- Helgeson, H.C. (1971) Kinetics of mass transfer among silicates and aqueous solutions. *Geochim. Cosmochim. Acta* **35**: 421-469.
- Helgeson, H.C. (1972) Kinetics of mass transfer among silicates and aqueous solutions: correction and clarification. *Geochim. Cosmochim. Acta* **36**: 1067-1070.
- Helgeson, H.C. and Murphy, W.M. (1983) Calculation of mass transfer among minerals and aqueous solutions as a function of time and surface area in geochemical processes - I. computational approach. *Mathematical Geology* **15**: 109-130.
- Helgeson, H.C., Murphy, W.M. and Aagaard, P. (1984) Thermodynamic and kinetic constraints on reaction rate among minerals and aqueous solutions. II. rate constants, effective surface area and the hydrolysis of feldspar. *Geochim. Cosmochim. Acta*, **48**: 2405-2432.
- Henley, R.W., Truesdell, A.H. and Barton, P.B. (1984) *Reviews in Economic Geology, 1. Fluid-Mineral Equilibria in Hydrothermal Systems*. Society of Economic Geologists, 267 pp.
- Himmelblau, D.M., Jones, C.R. and Bischoff, K.B. (1967) Determination of rate constants for complex kinetics models. *I & EC Fundamentals* **6**: 539-543.
- Holdren, G.R., and Berner, R.A. (1979) Mechanism of feldspar weathering - I. experimental studies. *Geochim. Cosmochim. Acta* **43**: 1161-1171.
- Holdren, G.R. and Adams, J.E. (1982) Parabolic dissolution kinetics of silicate minerals: an artifact of non-equilibrium precipitation processes? *Geology* **10**: 186-190.
- Holdren, G.R. (1983) The composition of early formed aluminosilicate precipitates: results from simulated feldspar dissolution studies. *Sciences Geologiques Memoir #71 Petrologie des alterations et des sols, Petrologie experimentale* **1**: 75-84.
- Holdren, G.R. and Speyer, P.M. (1985a) Reaction-rate-surface area relationships during the early stages of weathering -- I. initial observations. *Geochim. Cosmochim. Acta* **49**: 675-681.

- Holdren, G.R. and Speyer, P.M. (1985b) pH dependent changes in the rates and stoichiometry of dissolution of an alkali feldspar at room temperature. *Amer. J. Sci.* **285**: 994-1026.
- Holdren, G.R. and Speyer, P.M. (1986) Stoichiometry of alkali feldspar dissolution at room temperature and various pH values. in S.M. Colman and D.P. Dethier, eds., *Rates of Chemical Weathering of Rocks and Minerals*, Academic Press, Orlando, FL, 61-81.
- Holdren, G.R. and Speyer, P.M. (1987) Reaction rate-surface area relationships during the early stages of weathering. II. data on eight additional feldspars. *Geochim. Cosmochim. Acta* **51**: 2311-2318.
- Iler, R. (1979) *The Chemistry of Silica. Solubility, Polymerization, Colloid and Surface Properties, and Biochemistry*. John Wiley and Sons, New York, NY, 866pp.
- Jobak, K.G. and Reid, R.C. (1987) Estimation of pure-component properties from group-contributions. *Chem. Eng. Comm.* **57**: 233-243.
- Kamiya, H., Ozaki, A. and Imahashi, M. (1974) Dissolution rate of powdered quartz in acid solution. *Geochemical Journal (of Japan)*, **8**: 21-26.
- Kennedy, G.C. (1950) A portion of the system silica-water. *Economic Geology* **45**: 629-653.
- Kirby, A.J. (1972) Hydrolysis and formation of esters of organic acids. in Bamford, C.H. and Tipper, C.F.H., eds. *Comprehensive Chemical Kinetics 10. Ester Formation and Hydrolysis, Related Reactions*. Elsevier, Amsterdam, pp 57-202.
- Kitahara, S. (1960) The solubility equilibrium and the rate of solution of quartz in water at high temperatures and high pressures. *Review of Physical Chemistry of Japan* **30**: 122-130.
- Klincewicz, K.M. and Reid, R.C. (1984) Estimation of critical properties with group contribution methods. *AIChE Journal* **30**: 137-142.
- Knauss, K.G. and Wolery, T.J. (1986) Dependence of albite dissolution kinetics on pH and time at 25°C and 70°C. *Geochim. Cosmochim. Acta* **50**: 2481-2497.
- Knauss, K.G. and Wolery, T.J. (1988) The dissolution kinetics of quartz as a function of pH and time at 70°C. *Geochim. Cosmochim. Acta* **52**: 43-53.
- La Iglesia, A. and Aznar, A.J. (1986) A method of estimating the Gibbs energies of formation of zeolites. *Zeolites* **6**: 26-29.

- Lagache, M. (1965) Contributions a l'etude de l'alteration des feldspaths dans l'eau, entre 100 et 200°C, Sus diverses pressions de CO<sub>2</sub>, et application a la synthese des mineraux argibeux. *Bull. Soc. Fr. Mineral. Cristallogr.* **88**: 223-253.
- Lagache, M. (1976) New data on the kinetics of dissolution of alkali feldspars at 200°C in CO<sub>2</sub> charged water. *Geochim. Cosmochim. Acta*, **40**: 157-161.
- Lahann, R.W. and Roberson, H.E. (1980) Dissolution of silica from montmorillonite: effect of solution chemistry. *Geochim. Cosmochim. Acta* **44**: 1937-1943.
- Lasaga, A.C. (1981) Rate laws of chemical reactions. in A.C. Lasaga and R.J. Kirkpatrick, eds. *Kinetics of Geochemical Processes* Mineralogical Society of America, **8**: 1-67.
- Lasaga, A.C. (1984) Chemical kinetics of water-rock interactions. *J. Geophys. Res.* **89(B6)**: 4009-4025.
- Lasaga, A.C. and Blum, A.E. (1986) Surface chemistry, etch pits and mineral-water reactions. *Geochim. Cosmochim. Acta* **50**: 2363-2379.
- Levenspiel, O. (1962) *Chemical Reaction Engineering*. John Wiley and Sons, New York, NY, 578 pp.
- Lin, F.C. and Clemency, C.V. (1981) The kinetics of dissolution of muscovites at 25°C and 1 atm CO<sub>2</sub> partial pressure. *Geochim. Cosmochim. Acta* **45**: 571-576.
- Long, F.A. and Pritchard, J.G. (1956) Hydrolysis of substituted ethylene oxides in H<sub>2</sub>O<sup>18</sup> solutions. *J. Amer. Chem. Soc.* **78**: 2663-2667.
- Long, F.A., Pritchard, J.G. and Stafford, F.E. (1957) Entropies of activation and mechanism for the acid-catalyzed hydrolysis of ethylene oxide and its derivatives. *J. Amer. Chem. Soc.* **79**: 2362-2364.
- Luce, R.W., Bartlett, R.W. and Parks, G.A. (1972) Dissolution kinetics of magnesium silicates. *Geochim. Cosmochim. Acta* **36**: 35-50.
- Mackenzie, F.T. and Gees, R. (1971) Quartz: synthesis at earth-surface conditions. *Science* **173**: 533-534.
- Meissner, H.P. and Tester, J.W. (1972) Activity coefficients of strong electrolytes in aqueous solutions. *Ind. Eng. Chem. Process Des. Develop.* **11**: 128-133.
- Meissner, H.P. (1979) Prediction of activity coefficients of strong electrolytes in aqueous systems. *AIChE Symposium Series* **133(25)**: 495-511.
- Moody, J.B. (1979) Serpentinites, spilites and ophiolite metamorphism. *Canadian Mineralogist* **17**: 871-887.

- Moore, J.W. and Pearson, R.G. (1981) *Kinetics and Mechanism*. 3<sup>rd</sup> Edition. John Wiley and Sons, New York, NY, 455 pp.
- Morey, G.W., Fournier, R.O. and Rowe, J.J. (1962) The solubility of quartz in water in the temperature interval from 25°C to 300°C. *Geochim. Cosmochim. Acta* 26:
- Nriagu, J.O. (1975) Thermochemical approximations for clay minerals. *Am. Mineralogist* 60: 834-839.
- Paces, T. (1973) Steady-state kinetics and equilibrium between ground water and granitic rock. *Geochim. Cosmochim. Acta* 37: 2641-2663.
- Pearson, F.J. and Truesdell, A.H. (1978) Tritium in the waters of Yellowstone National Park, US Geological Survey Open-file Report 78-701.
- Petrovic, R., Berner, R.A. and Goldhaber, M.B. (1976) Rate control in dissolution of alkali feldspars - I. study of residual feldspar grains by x-ray photoelectron spectroscopy. *Geochim. Cosmochim. Acta* 40: 537-548.
- Petrovic, R. (1981a) Kinetics of dissolution of mechanically comminuted rock-forming oxides and silicates I. deformation and dissolution of quartz under laboratory conditions. *Geochim. Cosmochim. Acta*, 45: 1665-1674.
- Petrovic, R. (1981b) Kinetics of dissolution of mechanically comminuted oxides and silicates II. deformation and dissolution of oxides and silicates in the laboratory and at the earth's surface. *Geochim. Cosmochim. Acta* 45: 1675-1686.
- Pitzer, K.S. (1979) Theory: ion interaction approach. in R.M. Pytkowicz, ed., *Activity Coefficients in Electrolyte Solutions*. CRC Press, Boca Raton, FL. 1: 139-208.
- Rihani, D.N. and Doraiswamy, L.K. (1965) Estimation of heat capacity of organic compounds from group contributions. *I & EC Fundamentals* 4: 17-21.
- Rimstidt, J.D. and Barnes, H.L. (1980) The kinetics of silica-water reactions. *Geochim. Cosmochim. Acta* 44: 1683-1699.
- Robie, R.A., Hemingway, B.S. and Fisher, J.R. (1979) *Thermodynamic Properties of Minerals and Related Substances at 298.15 K and 1 Bar (10<sup>5</sup> Pascals) Pressure and at Higher Temperatures*. US Geological Survey Bulletin 1452, 456 pp.
- Robinson, B.A. (1982) Quartz Dissolution and Silica Deposition in Hot Dry Rock Geothermal Systems. MS Thesis, Department of Chemical Engineering, Massachusetts Institute of Technology, Cambridge, MA, 139 pp. also published as Los Alamos National Laboratory report LA-9404-T, available from NTIS.

- Siebert, H., Youdelis, W.V., Leja, J. and Lilje, E.O. (1962) The kinetics of the dissolution of crystalline quartz in water at high temperatures and high pressures. *Unit Processes in Hydrometallurgy* The Metallurgical Society of AIME Conference 24:
- Seinfeld, J.H. (1970) Nonlinear estimation theory. *Ind. Eng. Chem.* 62: 32-42.
- Shaw, R. (1971) Heats of formation of nitroaromatics: group additivity for solids. *J. Phys. Chem.* 75: 4047-4049.
- Siever, R. (1962) Silica solubility 0-200°C and the diagenesis of siliceous sediments. *Journal of Geology* 70: 127-150.
- Smyth, J.R. and Bish, D.L. (1988) *Crystal Structures and Cation Sites of the Rock-Forming Minerals*. Allen & Unwin, Inc., Winchester, MA, 332 pp.
- Souders, M., Matthews, C.S. and Hurd, C.O. (1949a) Relationship of thermodynamic properties to molecular structure: heat capacities and heat contents of hydrocarbon vapors. *Ind. Eng. Chem.* 41: 1037-1048.
- Souders, M., Matthews, C.S. and Hurd, C.O. (1949b) Relationship of thermodynamic properties to molecular structure: entropy and heat of formation of hydrocarbon vapors. *Ind. Eng. Chem.* 41: 1048-1056.
- Stern, C.R. and Wyllie, P.J. (1981) Phase relationships of I-type granite with water to 35 kilobars: the Dinkey Lakes biotite granite from the Sierra Nevada batholith. *J. Geophys. Res.* 86: 10412-10422.
- Stober, W. (1966) Formation of silicic acid in aqueous suspensions of different silica modifications. *Adv. Chem. Ser.* 67: 161-182.
- Stumm, W. and Morgan, J.J. 1981, *Aquatic Chemistry*. 2<sup>nd</sup> Edition. John Wiley and Sons, New York, NY, 780 pp.
- Tardy, Y. and Garrels, R.M. (1974) A method of estimating the Gibbs energies of formation of layer silicates. *Geochim. Cosmochim. Acta* 38: 1101-1116.
- Tester, J.W., Holley, C.E. and Blatz, L.A. (1977) Solution chemistry and scaling in hot dry rock geothermal systems. 83<sup>rd</sup> National meeting of the AIChE, Houston, Texas, March, 1977.
- Thinh, T.P., Duran, J.L. and Ramalho, R.S (1971) Estimation of ideal gas heat capacities of hydrocarbons from group contribution techniques. *I & EC Proc. Des. Dev.* 10: 576-582.
- Thornton, S.D. and Radke, C.J. (1988) Dissolution and condensation kinetics of silica in alkaline solution. *SPE Reservoir Engineering* vol?: 743-752.

- van Lier, J.A., deBruyn, P.L. and Overbeek, J.T.G. (1960) The solubility of quartz," *J. Phys. Chem.*, **64**: 1625-1682.
- Voloson, A.G., Khodakovskiy, I.G. and Ryzhenko, B.N. (1972) Equilibria in the system  $\text{SiO}_2\text{-H}_2\text{O}$  at elevated temperatures along the lower three-phase curve. *Geochemistry International* **9**: 362-377.
- Verma, K.K. and Doraiswamy, L.K. (1965) Estimation of heats of formation of organic compounds. *I & EC Fundamentals* **4**: 389-396.
- Vuataz, F.D. and Goff, F. (1986) Isotope geochemistry of thermal and non-thermal waters in the Valles caldera, Jemez Mountains, New Mexico. *J. Geophys. Res.* **91(B2)**: 1835-1853.
- Watanabe, K. and Himmelblau, D.M. (1983) One variety of quick estimation schemes for parameters in kinetic models. *AIChE Journal* **29**: 789-795.
- Wei, J. (1962) Axiomatic treatment of chemical reaction systems. *J. Chem. Phys.* **36**: 1578-1584.
- Wei, J. and Prater, C.D. (1962) The structure and analysis of complex reaction systems. *Advances in Catalysis* **13**: 203-392.
- Weill, D.F. and Fyfe, W.S. (1964) The solubility of quartz in  $\text{H}_2\text{O}$  in the range 1000-4000 bars and 400-550°C. *Geochim. Cosmochim. Acta* **28**: 1243-1255.
- White, A.F. and Classen, H.C. (1979) Dissolution of silicate rocks - application to solute modeling. in E.A. Jenne, ed., *Chemical Modeling in Aqueous Systems*, ACS Symposium Series, **93**: 447-473.
- Wollast, R. (1967) Kinetics of the alteration of K-feldspar in buffered solutions at low temperature. *Geochim. Cosmochim. Acta* **31**: 635-648.



## APPENDIX A

### The Feldspar-Water System

The minerals of the feldspar group are among the most abundant rock-forming minerals in the earth's crust. They are major (> 30%) components of most igneous and metamorphic rocks, and are common in many sedimentary rocks. Most feldspars are formed by crystallization from a melt, but they can also precipitate from hydrothermal solutions. Feldspar crystals consist of networks (as opposed to chains or sheets) of  $\text{SiO}_4$  tetrahedra with  $\text{Al}^{+3}$  substituting for  $\text{Si}^{+4}$  in some of the tetrahedra. Since Al only has a +3 charge, another cation, usually  $\text{Na}^+$ ,  $\text{K}^+$ , or  $\text{Ca}^{+2}$ , is required to maintain electroneutrality. These cations occupy cavities in the network of linked tetrahedra. Chemical formulas of the feldspars are usually written on the basis of 8 oxygens, and almost all natural feldspars fall in the ternary system  $\text{NaAlSi}_3\text{O}_8$ -- $\text{KAlSi}_3\text{O}_8$ -- $\text{CaAl}_2\text{Si}_2\text{O}_8$ .

An abbreviated feldspar nomenclature is presented in Table A.1. Feldspars are classified according to their composition, crystallographic structure and Si-Al ordering. Because these properties vary more or less continuously over broad ranges, feldspar nomenclature is somewhat loose. Compositional boundaries, particularly in the plagioclase series are somewhat arbitrarily chosen to lie at 20% intervals. On the other hand, a change in crystallographic structure is often signified by a different name for the same composition. There are two parts to Table A.1: part a describes the pure component (or end-member) feldspars, while part b covers the intermediate

**Table A.1** Simplified feldspar nomenclature (after Deere, et al., 1971). Pure component (or end-member) feldspar compositions, crystallographic classes and Si-Al ordering are described in part a. Part b describes the intermediate feldspar compositions and structures. For example, a high-temperature andesine has the high-albite structure, but a low-temperature andesine has exsolved at the microscopic level to a Na-rich phase having a low-albite structure and a Ca-rich phase with the low-anorthite structure.

a. Pure component feldspars

<u>End-member Composition</u>	<u>Si-Al Ordering</u>	<u>Crystallographic Class</u>	<u>Mineral</u>
NaAlSi <sub>3</sub> O <sub>8</sub>	random ordered	triclinic triclinic	high-albite low-albite
KAlSi <sub>3</sub> O <sub>8</sub>	random ordered ordered	monoclinic monoclinic triclinic	sanidine orthoclase microcline
CaAl <sub>2</sub> Si <sub>2</sub> O <sub>8</sub>	mostly ordered ordered	triclinic triclinic	anorthite low-anorthite

b. Intermediate composition feldspars

	<u>Composition</u>	<u>Structure</u>	<u>Mineral Name</u>
--	--------------------	------------------	---------------------

Plagioclase Series (NaAlSi<sub>3</sub>O<sub>8</sub> - CaAl<sub>2</sub>Si<sub>2</sub>O<sub>8</sub>)

high temperature series

	An <sub>0-10</sub>	high-albite	albite
complete	An <sub>10-30</sub>	"	oligoclase
solid	An <sub>30-50</sub>	"	andesine
solution	An <sub>50-70</sub>	"	lahradorite
	An <sub>70-90</sub>	"	bytownite
	An <sub>90-100</sub>	low-albite	anorthite

low temperature series

	An <sub>0-3</sub>	low-albite	
microscopic exsolution lamellae	An <sub>3-80</sub>	intermediate	
	An <sub>80-100</sub>	low-anorthite	

Alkali Series (NaAlSi<sub>3</sub>O<sub>8</sub> - KAlSi<sub>3</sub>O<sub>8</sub>)

high temperature series

complete	Ab <sub>0-63</sub>	monoclinic	high-sanidine
solid	Ab <sub>63-90</sub>	triclinic	anorthoclase
solution	Ab <sub>90-100</sub>	triclinic	high-albite
submicroscopic exsolution lamellae	Ab <sub>0-40</sub>	monoclinic	sanidine
	Ab <sub>40-63</sub>	monoclinic	sanidine-cryptoperthite
	Ab <sub>63-75</sub>	triclinic	anorthoclase-cryptoperthite
	Ab <sub>75-90</sub>	triclinic	anorthoclase
	Ab <sub>90-100</sub>	triclinic	high-albite

low temperature series

microscopic exsolution lamellae	Ab <sub>0-15</sub>	monoclinic	orthoclase
	Ab <sub>15-</sub>	monoclinic	orthoclase microperthite
	Ab <sub>90-100</sub>	triclinic	low-albite
microscopic to visible exsolution lamellae	Ab <sub>0-</sub>	triclinic	microcline
	Ab <sub>90-100</sub>	monoclinic	microperthite or perthite low-albite

compositions of the plagioclase solid-solution series ( $\text{NaAlSi}_3\text{O}_8$ -- $\text{CaAl}_2\text{Si}_2\text{O}_8$ ) and the alkali feldspar series ( $\text{NaAlSi}_3\text{O}_8$ -- $\text{KAlSi}_3\text{O}_8$ ). Compositions in the ternary system are usually expressed in terms of the end-member compositions. For example, a plagioclase feldspar containing 80 mol%  $\text{CaAl}_2\text{Si}_2\text{O}_8$ , 15 mol%  $\text{NaAlSi}_3\text{O}_8$  and 5 mol%  $\text{KAlSi}_3\text{O}_8$  would be referred to as  $\text{An}_{80}\text{Ab}_{15}\text{Or}_5$  where the An, Ab and Or refer to the anorthite (Ca), albite (Na) and orthoclase (K) contents, respectively.

At temperatures above about 650°C, the alkali feldspars form a solid solution, but at lower temperatures, these feldspars actually consist of separate Na-rich and K-rich regions. For the higher temperature series (high-albite--sanidine) the scale of unmixing is sub-microscopic (cryptoperthitic), but the exsolution in the lower temperature series (low-albite--orthoclase and low-albite--microcline) is submicroscopic (microperthitic) or even visible to the unaided eye (perthitic). Plagioclase feldspars also form a solid solution series at high temperature, but at lower temperature, plagioclase exsolve into lamellae which alternate between albite and anorthite in composition.

The unmixing of intermediate feldspars in either the plagioclase or the alkali series has important consequences for dissolution studies involving intermediate feldspars. It is probably more realistic to treat intermediate feldspars as mechanical mixtures of two end-members rather than as a single homogeneous phase. Holdren and Berner (1978) show SEM photographs of weathered feldspar grains which suggest that end-member feldspars dissolve more or less uniformly across the exposed surface. On the other hand, alternating lamellae are selectively attacked in intermediate feldspars.

Analysis of experimental results in such a system requires knowledge of the relative surface areas of the two phases in addition to measurements of the bulk surface area.

Another feature of feldspars which may be important in studies of dissolution reactions is the Si-Al ordering. Depending upon the symmetry of the crystal, there are either two or four symmetry equivalent tetrahedral sites in the crystallographic structure. The selectivity of each site towards Al depends upon the feldspar composition as well as on the temperature at which the feldspar solidified and the rate of cooling. High temperature forms are disordered, but lower temperature forms show increasing order. If Al is released in preference to silica in low pH solutions, as is suggested by Chou and Wollast's (1984) experiments, the distribution of Al in the crystal lattice could affect the reaction rate.

The interaction of feldspars with water involves a number of other phases which could saturate and precipitate from solution depending upon the solution composition. The primary alteration phases include clays, micas and zeolites (see Table A2). Helgeson and Murphy (1983) calculated a hypothetical reaction path for the dissolution of microcline in a dilute HCl solution (pH 4) at 25°C. The phases which saturated according to their calculations were gibbsite, kaolinite, quartz and muscovite. Under conditions of higher temperature and silica concentrations approaching or exceeding quartz saturation, zeolites are favored over clays as alteration products of feldspars.

**Table A.2 Secondary minerals (alteration products) in the feldspar-water system.**

Mineral	Composition	Group
gibbsite	$\text{Al}(\text{OH})_3$	
kaolinite	$\text{Al}_2\text{Si}_2\text{O}_5(\text{OH})_4$	clay
montmorillonite	$(1/2\text{Ca}, \text{Na})_{0.7}(\text{Al}, \text{Mg}, \text{Fe})_4[(\text{Si}, \text{Al})_8\text{O}_{20}](\text{OH})_4 \cdot n\text{H}_2\text{O}$	clay
illite	$\text{K}_{1-1.5}\text{Al}_4[\text{Si}_{7-6.5}\text{Al}_{1-1.5}\text{O}_{20}](\text{OH})_4$	clay
muscovite	$(\text{Na}, \text{K})\text{Al}_2[\text{AlSi}_3\text{O}_{10}](\text{OH})_2$	mica
zeolites	$(\text{Na}_2, \text{K}_2, \text{Ca})[(\text{Al}, \text{Si})\text{O}_2]_n \cdot x\text{H}_2\text{O}$	zeolite

## Appendix B

### Analysis of Complex Reaction Systems

A complex reaction system is one in which several reactions are coupled by competition for reactants. Usually in such a system, the individual reactions cannot be isolated from each other by an experimental technique, and experimental determination of rate constants for the component reactions in the complex system requires that many competing effects be sorted out. Whether a reaction system has simple or complex kinetics, certain characteristics are always observed (Wei, 1962):

1. Total mass is conserved ( $\sum_i [A_i] = \text{constant}$ )
2. Concentrations are non-negative (All  $[A_i] \geq 0$ )
3. The rate of change of the mass of each species is a continuous function of all the masses of all the species
4. At equilibrium, the forward and reverse rate for a reaction are equal (in other words, the system is microscopically reversible)
5. There is a potential function which drives the change in composition in the system and whose derivative is negative everywhere in composition space, except at the equilibrium point where the derivative is zero.

Kinetics of single phase systems of monomolecular reactions can, in general, be analyzed by the method of Wei and Prater (1962) who write the network of equations as the product of a rate constant matrix,  $\underline{\mathbf{K}}$ , and a concentration vector,  $\underline{\mathbf{a}}$ :

$$\frac{d\mathbf{a}}{dt} = \mathbf{K} \mathbf{a}, \quad (\text{B.1})$$

where

$$\mathbf{a} = \begin{bmatrix} A_1 \\ \vdots \\ A_n \end{bmatrix} \quad \text{and} \quad k_{ij} = \begin{cases} -\sum_m k_{mi} \quad (m \neq i) & \text{for } j = i \\ k_{ij} & \text{for } j \neq i \end{cases}$$

( $k_{ij}$  corresponds to the reaction  $A_j \rightarrow A_i$  and is an element of the  $\mathbf{K}$  matrix.)

This system of equations is then transformed into an equivalent set of equations which operate in a pseudo-composition space,  $\mathbf{h}$ . The coordinate transformation is made through the eigenvectors of the rate constant matrix,  $\mathbf{K}$ . The eigenvectors of  $\mathbf{K}$  form the basis of the coordinate system,  $\mathbf{h}$ , where the rate equations are uncoupled (Wei and Prater, 1962). The rate constants in the transformed coordinate system are determined experimentally by finding a starting composition such that the reaction path lies along the projection on the reaction simplex of one of the coordinate axes in the transformed coordinate system. Under these conditions, the reaction path follows a straight line from the starting composition to the equilibrium point. Once the rate constants in the transformed coordinate system are determined, the rate constants in the original coordinate system can be calculated. This method is very powerful in determining rate

constants from experimental data, but its application so far has been limited to single phase systems of coupled, monomolecular or pseudomonomolecular reactions.

An alternative method is to solve the system of coupled differential equations numerically. Estimation of rate constants from experimental data generally involves iterative integration of the system of differential equations and an optimization to choose the rate constants which give the best fit to the data (Himmelblau, et. al., 1967; Froment, 1975; Seinfeld, 1970; Glowinski and Stocki, 1981; Watanabe and Himmelblau, 1983). Numerical methods can be used for complex reaction systems involving second and higher order reactions. But, as the number of reactions in a complex system increases, these numerical methods provide less and less insight into the kinetics because more attention is devoted to optimization of solution algorithms.

What is needed is a method that preserves the simple elegance and kinetic insight inherent in the Wei-Prater technique, but which works for large systems involving higher order reactions.

The net rate of an elementary reaction:

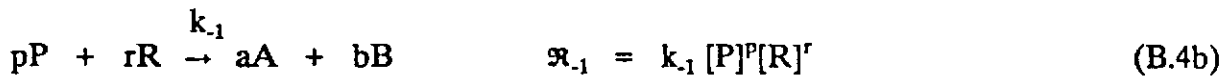
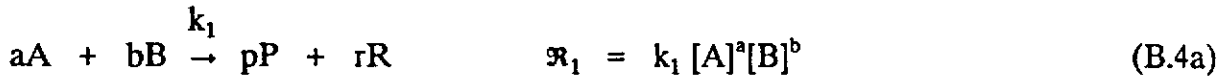


is written as the difference between the forward rate and the reverse rate:

$$r_{net} = k_1 [A]^a [B]^b - k_{-1} [P]^p [R]^r . \quad (B.3)$$



For reasons that will be explained in a moment, we will treat each reversible elementary reaction as a pair of uncoupled, irreversible reactions:



where the  $\mathfrak{R}_i$  are the rates of elementary reactions. The change in concentration with respect to time for component  $A_n$  in a system involving multiple reactions is given by:

$$\frac{d[A_n]}{dt} = \sum_j \nu_n^j (\mathfrak{R}_j) \quad (\text{B.5})$$

where  $\nu_n^j$  is the stoichiometric coefficient of the  $n^{\text{th}}$  component,  $A_n$ , in the  $j^{\text{th}}$  reaction and  $\mathfrak{R}_j$  is the net rate of the  $j^{\text{th}}$  reaction.

The reaction network for a system of reactions is formed by writing equation (B.5) for every component in the system. This system of equations is written in matrix notation as:

$$\frac{dc}{dt} = \underline{\underline{M}} \underline{\underline{k}} \quad (\text{B.6})$$

where  $\underline{c}$  is the vector of component compositions,  $\underline{k}$  is the rate constant vector,

$$\underline{k} = \begin{bmatrix} k_1 \\ \vdots \\ k_n \end{bmatrix}$$

and each element in the variable matrix,  $\underline{M}$ , is given by

$$m_{jn} = \nu_n^j (\mathfrak{R}_j) / k_j \quad (\text{B.7})$$

Because we have written the forward and reverse elementary reactions separately, we can substitute the rate expression for  $\mathfrak{R}_j$  (equation (B.4)) into equation (B.7):

$$m_{jn} = \nu_n^j [A_k]^\alpha [A_l]^\beta \quad (\text{B.8})$$

Given a mechanism (or a trial mechanism) and the corresponding rate laws, equation (A.6) can be solved for the unknown rate constants. Typically, this equation is solved by iterative techniques that minimize an objective function, but there is an alternative: integration of the rate equations and solution of the system by least squares.

The integral of the rate equations is expressed as:

$$\underline{c}(t_2) - \underline{c}(t_1) = \underline{M}^* \underline{k} + \text{constant} \quad (\text{B.9})$$

where

$$m_{jn}^* = \int_{t_1}^{t_2} \nu_n^j [A_k]^\alpha [A_l]^\beta dt$$

where  $\mathfrak{A}_j = k_j [A_k]^\alpha [A_l]^\beta$ . Since the  $[A_k]$  are known from experiments,  $\underline{c}$  and  $\underline{M}^*$  are completely determined.

At this point, there is no guarantee that  $\underline{M}^*$  can be inverted, but each new data point gives a new vector  $\underline{c}$  and a new matrix  $\underline{M}^*$  for the same vector  $\underline{k}$ . By stacking the equations,  $\underline{M}^*$  can be made overdetermined:

$$\begin{bmatrix} \underline{c}(t_2) - \underline{c}(t_1) \\ \underline{c}(t_3) - \underline{c}(t_2) \\ \underline{c}(t_4) - \underline{c}(t_3) \\ \vdots \\ \underline{c}(t_n) - \underline{c}(t_{n-1}) \end{bmatrix} = \begin{bmatrix} \underline{M}_{21}^* \\ \underline{M}_{32}^* \\ \underline{M}_{43}^* \\ \vdots \\ \underline{M}_{n(n-1)}^* \end{bmatrix} \underline{k} \quad (\text{B.10})$$

Equation (B.10) can be solved by constrained least squares, and because the system is overdetermined, a solution does exist. Since the solution technique is direct (as opposed to iterative), there are no problems with convergence, and an initial guess for the values of the rate constants is not required.

## APPENDIX C

### **Bond Additivity Method for Estimating Thermochemical Properties of Aluminosilicate Minerals**

Thermochemical properties of minerals are usually determined from experimental measurements of heat capacities and heat contents. However, thermochemical data are available for only a small fraction of the known minerals due to the difficulty of making the calorimetric measurements. Methods for accurately estimating thermochemical quantities for silicate minerals are highly desirable for a variety of purposes, including defining stability fields for mineralogical phase assemblages in geologic systems as well as for predicting behavior under extreme conditions.

An approach to estimating thermochemical quantities that has been used with great success in a wide variety of applications within organic chemistry is additivity of bond and group properties. In particular, group contributions methods have been used for estimating thermodynamic properties (enthalpy, entropy, heat capacity) of gas-phase hydrocarbon compounds (Franklin, 1949; Souders, et al., 1949a,b; Benson and Buss, 1958; Rihani and Doriaswamy, 1965; Verma and Doriaswamy, 1965; Benson, et al., 1969; Benson, 1976; Thinh, et al., 1971; Eigenmann, et al., 1973), gaseous free radical and ions (Franklin, 1953), and solids (Shaw, 1971). Group contribution methods have also been used for estimating critical properties of a number of organic compounds (Klincewicz and Reid, 1984; Jobak and Reid, 1987).

Estimation of thermochemical properties for minerals has focused on estimating Gibbs energies from the contributions of the oxide components for a very limited group of minerals such as zeolites (La Iglesia and Aznar, 1986), or clays (Nriagu, 1975; Tardy and Garrels, 1974). However, some work has focused on larger groups such as silicates (Chen, 1975). Typically, these methods predict Gibbs energies of formation within about 2%, but the results are only valid for a limited group of minerals at 298 K.

Crystal structures of aluminosilicate minerals are mainly frameworks of Si-O and Al-O tetrahedra, and for many minerals, there are also lattice sites that are occupied by octahedrally coordinated metal atoms. All of the metal atoms are bonded to oxygen atoms. Using published values of enthalpies of formation and entropies of formation of various minerals (Robie, et al., 1979) for which the coordination of the metal atom in the crystal structure is known (Smyth and Bish, 1988), I have calculated individual bond contributions to formation enthalpies and entropies for single metal-oxygen bonds (Si-O, Al-O, Na-O, etc.) by assuming that an overall thermochemical property for a mineral is simply the sum of the individual bond properties which depend on the number, type and coordination of each metal atom in the mineral. The calculated individual bond contributions to the enthalpy and entropy of formation are given in Table C.1. Using these values of individual bond enthalpies and entropies, the enthalpy and entropy of formation can be calculated for most of the aluminosilicates for which both thermodynamic properties and crystal structure data are available (see Table C.2). These results allow reasonably accurate estimation of the thermodynamic properties

of aluminosilicate minerals based solely on knowledge of the composition of the mineral and the coordination of certain species (especially Al, Mg, and Ti).

**Table C.1** Individual bond contributions to the enthalpy and entropy of formation for aluminosilicate minerals at 298 K and 1 bar pressure. These values were calculated by dividing the enthalpy or entropy of formation of each mineral in Table B.2 by the coordination number of each metal atom in the crystal structure. Enthalpies of formation of the minerals are from Robie, et al., (1979).

Bond	Coordination	Individual Bond Contribution	
		Enthalpy (standard error) (kJ/mol)	Entropy (standard error) (J/mol-K)
Si-O	4	-229.91 (0.94)	-46.19 (0.52)
Al-O	4	-205.96 (1.04)	-35.39 (0.58)
Al-O	5	-165.49 (3.76)	-29.91 (2.10)
Al-O	6	-140.08 (0.76)	-26.84 (0.43)
H-O	1	-153.28 (5.03)	-99.43 (2.81)
Na-O	6	- 57.82 (2.73)	- 7.38 (1.52)
Na-O	8	- 43.65 (1.71)	- 7.93 (0.96)
K-O	6	- 62.83 (2.32)	- 8.15 (1.29)
K-O	10	- 38.94 (1.41)	- 4.91 (0.79)
Li-O	6	- 61.07 (1.96)	- 7.41 (1.09)
Ca-O	6	-116.43 (0.74)	-16.31 (0.41)
Ca-O	7	-105.82 (2.87)	-15.01 (1.59)
Ca-O	8	- 91.36 (0.66)	-13.38 (0.37)
Ca-O	10	- 71.85 (2.06)	-10.09 (1.15)
Mg-O	4	-149.05 (3.62)	-21.78 (2.02)
Mg-O	6	-106.78 (0.93)	-18.34 (0.52)
Mg-O	8	- 76.87 (0.88)	-12.73 (0.50)
Fe-O	6	- 47.13 (1.43)	-12.53 (0.80)
Ti-O	6	-157.01 (1.57)	-30.93 (0.88)
Mn-O	6	- 67.36 (1.55)	-12.11 (0.87)

**Table C.2** Comparison of calculated and measured values of the enthalpy of formation from the elements. Measured values are from Robie, et al. (1979).

Mineral	Formula	Measured $\Delta H_f$ (kJ/mol)	Calculated $\Delta H_f$ (kJ/mol)	% Error
Akermanite	$\text{Ca}_2\text{MgSi}_2\text{O}_7$	- 3876.52	- 3827.94	1.25
Albite	$\text{NaAlSi}_3\text{O}_8$	- 3935.12	- 3929.68	0.14
Analbite	$\text{NaAlSi}_3\text{O}_8$	- 3924.24	- 3935.12	-0.28
Anatase	$\text{TiO}_2$	- 938.72	- 942.06	-0.36
Andalusite	$\text{Al}_2\text{SiO}_5$	- 2587.53	- 2587.57	-0.00
Anorthite	$\text{CaAl}_2\text{Si}_2\text{O}_8$	- 4229.10	- 4185.54	1.03
Ca-olivine	$\text{Ca}_2\text{SiO}_4$	- 2316.62	- 2316.80	-0.01
CaAl-pyroxene	$\text{CaAl}_2\text{SiO}_6$	- 3275.68	- 3282.54	-0.21
Chrysotile	$\text{Mg}_3\text{Si}_2\text{O}_5(\text{OH})_4$	- 4361.66	- 4374.44	-0.29
Clinoenstatite	$\text{MgSiO}_3$	- 1547.75	- 1560.32	-0.81
Cordierite	$\text{Mg}_2\text{Al}_3(\text{AlSi}_5\text{O}_{18})$	- 9161.52	- 9174.92	-0.15
Corundum	$\text{Al}_2\text{O}_3$	- 1675.70	- 1680.96	-0.31
Diopside	$\text{CaMgSi}_2\text{O}_6$	- 3210.76	- 3210.84	-0.00
Eucryptite	$\text{LiAlSiO}_4$	- 2123.30	- 2109.90	0.63
Fayalite	$\text{Fe}_2\text{SiO}_4$	- 1479.36	- 1485.20	-0.39
Forsterite	$\text{Mg}_2\text{SiO}_4$	- 2170.37	- 2201.00	-1.41
Gehlenite	$\text{Ca}_2\text{Al}_2\text{SiO}_7$	- 4007.57	- 4029.08	-0.54
Geikelite	$\text{MgTiO}_3$	- 1572.77	- 1582.74	-0.63
Gibbsite	$\text{Al}(\text{OH})_3$	- 1293.13	- 1300.32	-0.56
Grossular	$\text{Ca}_3\text{Al}_2\text{Si}_3\text{O}_{12}$	- 6643.14	- 6632.52	0.16
Ilmenite	$\text{FeTiO}_3$	- 1236.62	- 1224.84	0.95
Jadeite	$\text{NaAlSi}_2\text{O}_6$	- 3029.40	- 3028.96	0.01
Kaliophyllite	$\text{KAlSiO}_4$	- 2121.92	- 2120.46	0.07
Kaolinite	$\text{Al}_2\text{Si}_2\text{O}_5(\text{OH})_4$	- 4120.14	- 4133.36	-0.32
Kyanite	$\text{Al}_2\text{SiO}_5$	- 2591.73	- 2600.60	-0.34
Larnite	$\text{Ca}_2\text{SiO}_4$	- 2305.98	- 2316.80	-0.47
Leucite	$\text{KAlSi}_2\text{O}_6$	- 3038.65	- 3040.10	-0.05
Merwinite	$\text{Ca}_3\text{MgSi}_2\text{O}_8$	- 4566.79	- 4575.70	-0.20
Microcline	$\text{KAlSi}_3\text{O}_8$	- 3967.69	- 3972.16	-0.11
Muscovite	$\text{KAl}_2[\text{AlSi}_3\text{O}_{10}](\text{OH})_2$	- 5976.74	- 5959.68	0.29
Nepheline	$\text{NaAlSiO}_4$	- 2092.11	- 2092.68	-0.03
Perovskite	$\text{CaTiO}_3$	- 1660.63	- 1660.56	0.00
Pseudowollastonite	$\text{CaSiO}_3$	- 1628.65	- 1618.22	0.64
Pyrope	$\text{Mg}_3\text{Al}_2\text{Si}_3\text{O}_{12}$	- 6284.62	- 6284.76	-0.00
Pyrophyllite	$\text{Al}_2\text{Si}_4\text{O}_{10}(\text{OH})_2$	- 5639.80	- 5666.08	-0.47
Quartz	$\text{SiO}_2$	- 910.70	- 919.64	-0.98
Rhodonite	$\text{MnSiO}_3$	- 1319.35	- 1323.80	-0.00
Sanidine	$\text{KAlSi}_3\text{O}_8$	- 3959.56	- 3972.16	-0.32
Sillimanite	$\text{Al}_2\text{SiO}_5$	- 2585.76	- 2583.96	0.07
Sphene	$\text{CaTiSiO}_5$	- 2601.40	- 2602.44	-0.04

**Table C.2 Continued.**

Mineral	Formula	Measured $\Delta H_f$ (kJ/mol)	Calculated $\Delta H_f$ (kJ/mol)	% Error
Spinel	$MgAl_2O_4$	- 2299.32	- 2277.11	0.97
$\alpha$ -Spodumene	$LiAlSi_2O_6$	- 3053.52	- 3046.18	0.24
$\beta$ -Spodumene	$LiAlSi_2O_6$	- 3025.35	- 3046.18	-0.69
Talc	$Mg_3Si_4O_{10}(OH)_2$	- 5915.90	- 5907.16	0.15
Tremolite	$Ca_2Mg_5(Si_8O_{22})(OH)_2$	-12355.08	-12328.84	0.21
Wollastonite	$CaSiO_3$	- 1635.22	- 1632.27	0.18



## **Appendix D**

### **Experimental Quartz Dissolution Rate Data**

The results of the quartz dissolution rate experiments are presented in this appendix. Indicated sample times correspond to the time the sample changer advanced. Since the masses were measured some time after sample collection, a correction for evaporation was applied. Over a several day period, the amount of evaporation loss from a sample tube containing demineralized water was measured. The loss rate was a steady 1.356 ml/day when the samples were not covered by a loose-fitting cover and 0.80 ml/day when the cover was present. These evaporation rates were used to calculate the amount of water loss from each sample over the time from sample collection to sample weighing, and the flow rates,  $\text{HNO}_3$  concentrations and silica concentrations were corrected for water loss. The corrected values along with the measured values are reported in this appendix.

**Table D.1 Results of the quartz dissolution rate experiments. The reported time is the time the sample changer advanced. Measured sample masses were corrected for evaporation applying an average evaporation rate over the time from sample collection to measurement of the sample mass. This correction for evaporation was then used to correct the flow rate and the HNO<sub>3</sub> and silica concentrations.**

S/N	Date	Time	Total Mass (g)	Tare (g)	Sample Mass (g)	Sample Mass (g)	Meas. Flow Rate (ml/hr)	Corr. Flow Rate (ml/hr)	Corr. HNO <sub>3</sub> Conc. (molar)	Calc. pH	Meas. pH	Meas. Silica Conc. (ppb)	Corr. Silica Conc. (ppb)
Deminerlized Water Feed													
1	09/30/88	17:32	23.40	9.29	14.11	15.34					3.92	1	1
2	09/30/88	18:31	33.22	9.12	24.10	25.27	24.43	25.62			5.80	10	9
3	09/30/88	19:30	32.88	9.25	23.63	24.75	23.96	25.09			6.80	11	10
4	09/30/88	20:29	32.29	8.80	23.49	24.55	23.81	24.89			6.60	21	20
5	09/30/88	21:28	32.58	9.18	23.40	24.41	23.72	24.74			5.70	20	19
6	09/30/88	22:27	32.59	9.25	23.34	24.29	23.66	24.63			5.60	24	23
7	09/30/88	23:27	32.49	9.26	23.23	24.12	23.55	24.46			5.40	20	19
8	10/01/88	00:26	32.21	9.08	23.13	23.97	23.45	24.30			5.10	19	18
9	10/01/88	01:25	32.26	9.25	23.01	23.79	23.33	24.12			5.00	22	21
10	10/01/88	02:24	32.20	9.29	22.91	23.64	23.23	23.96			4.70	20	19
11	10/01/88	03:23	32.13	9.29	22.84	23.51	23.16	23.84			4.40	21	20
12	10/01/88	04:23	32.08	9.26	22.82	23.43	23.14	23.76			4.40	21	20
13	10/01/88	05:22	31.80	9.10	22.70	23.26	23.01	23.58			4.50	22	21
14	10/01/88	06:21	31.80	9.16	22.64	23.14	22.95	23.46			4.50	23	22
15	10/01/88	07:20	31.83	9.25	22.58	23.03	22.89	23.35			4.30	20	20
16	10/01/88	08:19	31.67	9.23	22.44	22.83	22.75	23.15			4.40	19	19
17	10/01/88	09:18	31.54	8.99	22.55	22.89	22.86	23.20			4.40	20	20
18	10/01/88	10:18	31.82	9.11	22.71	22.99	23.02	23.31			4.30	19	19
19	10/01/88	11:17	31.05	9.01	22.04	22.26	22.34	22.57			4.30	17	17
20	10/01/88	12:16	31.66	8.96	22.70	22.87	23.01	23.19			4.20	16	16
21	10/01/88	13:15	31.87	9.25	22.62	22.73	22.93	23.05			4.30	19	19
											4.20	18	18

Table D.1 Continued.

S/N	Date	Time	Total Mass (g)	Tare (g)	Sample Mass (g)	Sample Mass (g)	Meas. Flow Rate (ml/hr)	Corr. Flow Rate (ml/hr)	Corr. HNO <sub>3</sub> Conc. (molar)	Calc. pH	Meas. pH	Meas. Silica Conc. (ppb)	Corr. Silica Conc. (ppb)
5.3 M HNO <sub>3</sub> Feed - start at 10:00 3 Oct													
35	10/03/88	10:01	26.77	9.26	17.51	19.24	17.40	19.12	5.075	-0.84		80	
36	10/03/88	11:01	26.00	9.29	16.71	18.41	16.60	18.29	0.018	1.84		150	137
37	10/03/88	12:02	25.27	9.00	16.27	17.93	16.17	17.82	0.022	1.76		90	82
38	10/03/88	13:02	25.33	9.25	16.08	17.71	15.98	17.60	0.020	1.80		80	73
39	10/03/88	14:02	25.25	8.99	16.26	17.86	16.16	17.74	0.030	1.63		220	200
40	10/03/88	15:03	25.24	9.11	16.13	17.69	16.03	17.58	0.405	0.58		290	264
41	10/03/88	16:03	24.53	9.06	15.47	17.00	15.37	16.89	2.900	-0.38		1440	1313
42	10/03/88	17:04	24.53	9.28	15.25	16.75	15.15	16.64	4.575	-0.68		2050	1865
43	10/03/88	18:04	24.00	8.92	15.08	16.55	14.98	16.44	5.085	-0.76		2240	2041
44	10/03/88	19:04	24.54	9.22	15.32	16.75	15.22	16.65	5.235	-0.79		2460	2248
45	10/03/88	20:05	24.12	9.29	14.83	16.23	14.74	16.13	5.040	-0.76			
46	10/03/88	21:05	24.07	9.13	14.94	16.31	14.84	16.20	5.165	-0.78			
47	10/03/88	22:05	23.84	9.26	14.58	15.92	14.49	15.81	5.190	-0.78			
48	10/03/88	23:06	23.92	9.27	14.65	15.95	14.56	15.85	5.180	-0.78			
49	10/04/88	00:06	23.97	9.27	14.70	15.97	14.61	15.87	5.125	-0.78		2470	2274
50	10/04/88	01:07	23.93	9.19	14.74	15.98	14.65	15.88	5.230	-0.80		2260	2085
51	10/04/88	02:07	23.83	9.21	14.62	15.83	14.53	15.72	5.125	-0.78		2480	2291
52	10/04/88	03:07	23.81	9.24	14.57	15.74	14.48	15.64	5.135	-0.78		2510	2323
53	10/04/88	04:08	23.63	9.19	14.44	15.58	14.35	15.48	5.140	-0.79		2510	2326
54	10/04/88	05:08	23.69	9.29	14.40	15.51	14.31	15.41	5.195	-0.80		2630	2442
55	10/04/88	06:09	23.45	9.10	14.35	15.42	14.26	15.33	5.205	-0.80		2470	2298
56	10/04/88	07:09	23.75	9.21	14.54	15.58	14.45	15.48	5.120	-0.79		2420	2258
57	10/04/88	08:09	24.16	9.28	14.88	15.89	14.78	15.79	5.200	-0.80		2340	2191
58	10/04/88	09:10	23.76	9.11	14.65	15.63	14.56	15.53				2280	2138
59	10/04/88	10:10	23.58	9.25	14.33	15.27	14.24	15.18	5.175	-0.80		2070	1942
60	10/04/88	11:11	23.74	9.12	14.62	15.53	14.53	15.43	5.050	-0.78		1720	1619

Table D.1 Continued.

S/N	Date	Time	Total Mass (g)	Tare (g)	Sample Mass (g)	Corr. Sample Mass (g)	Meas. Flow Rate (ml/hr)	Corr. Flow Rate (ml/hr)	Calc. pH	Meas. pH	Meas. Silica Conc. (ppb)	Corr. Silica Conc. (ppb)
61	10/04/88	12:11	23.47	9.23	14.24	15.12	14.15	15.02	-0.80		2550	2402
62	10/04/88	13:11	23.16	9.14	14.02	14.87	13.93	14.77	-0.78		2520	2377
63	10/04/88	14:12	23.30	9.09	14.21	15.02	14.12	14.93	-0.79		2620	2478
64	10/04/88	15:12	23.44	9.21	14.23	15.01	14.14	14.91	-0.81		2640	2503
65	10/04/88	16:12	23.54	9.13	14.41	15.16	14.32	15.06	-0.80		2030	1930
66	10/04/88	17:13	23.72	9.11	14.61	15.32	14.52	15.23	-0.79		1470	1401
67	10/04/88	18:13	24.06	9.22	14.84	15.52	14.75	15.42	-0.81		1840	1759
68	10/04/88	19:14	23.89	9.79	14.10	14.75	14.01	14.65	-0.82		2420	2314
69	10/04/88	20:14	23.77	9.22	14.55	15.17	14.46	15.07	-0.81		3010	2888
70	10/04/88	21:14	23.62	9.27	14.35	14.93	14.26	14.84	-0.83		2490	2393
1.0 N HNO3 Feed - start 23:00 4 Oct												
72	10/04/88	23:15	25.28	9.26	16.02	16.54	15.92	16.43	0.13		80	
73	10/05/88	00:16	25.94	9.09	16.85	17.34	16.74	17.22	-0.76		1450	1405
74	10/05/88	01:16	26.19	9.21	16.98	17.43	16.87	17.32	-0.68		1020	991
75	10/05/88	02:16	26.38	9.26	17.12	17.54	17.01	17.43	-0.62		1120	1091
76	10/05/88	03:17	26.32	9.11	17.21	17.60	17.10	17.48	-0.54		1030	1005
77	10/05/88	04:17	26.56	9.29	17.27	17.62	17.16	17.51	-0.48		1000	978
78	10/05/88	05:17	26.51	9.15	17.36	17.68	17.25	17.57	-0.42		1100	1078
79	10/05/88	06:18	26.41	9.10	17.31	17.60	17.20	17.49	-0.37		1080	1060
80	10/05/88	07:18	26.66	9.10	17.56	17.82	17.45	17.70	-0.31		1210	1190
									-0.27		1100	1084

Table D.1 Continued.

S/N	Date	Time	Total Mass (g)	Tare (g)	Sample Mass (g)	Corr. Sample Mass (g)	Meas. Flow Rate (ml/hr)	Corr. Flow Rate (ml/hr)	Corr. HNO <sub>3</sub> Conc. (molar)	Calc. pH	Meas. pH	Meas. Silica Conc. (ppb)	Corr. Silica Conc. (ppb)
81	10/05/88	08:19	27.22	9.24	17.98	18.20	17.86	18.09	2.060	-0.22		1190	1175
82	10/05/88	09:19	27.69	8.98	18.71	18.90	18.59	18.78	1.940	-0.19		1090	1079
83	10/05/88	10:19	27.54	9.13	18.41	18.57	18.29	18.45	1.790	-0.15		1180	1170
84	10/05/88	15:12	27.11	9.28	17.83	18.45	17.72	18.33	1.675	-0.10		1580	1527
85	10/05/88	16:12	26.28	9.08	17.20	17.79	17.09	17.67	1.580	-0.07		1340	1296
86	10/05/88	17:13	25.84	9.26	16.58	17.14	16.47	17.03	1.505	-0.04		1110	1074
87	10/05/88	18:13	25.92	9.24	16.68	17.20	16.57	17.09	1.445	-0.02		1050	1018
88	10/05/88	19:13	25.80	9.25	16.55	17.04	16.44	16.93	1.395	-0.01		1050	1020
89	10/05/88	20:14	25.63	9.19	16.44	16.90	16.33	16.79	1.330	0.02		1050	1022
90	10/05/88	21:14	25.53	9.11	16.42	16.84	16.31	16.74	1.275	0.04		1060	1033
91	10/05/88	22:14	25.60	9.16	16.44	16.83	16.33	16.72	1.235	0.05		1050	1026
92	10/05/88	23:15	25.75	9.30	16.45	16.81	16.34	16.70	1.200	0.06		1040	1018
93	10/06/88	00:15	25.33	8.92	16.41	16.74	16.30	16.63	1.175	0.07		1020	1000
94	10/06/88	01:16	25.41	9.09	16.32	16.61	16.22	16.51	1.150	0.08		1000	982
95	10/06/88	02:16	25.53	9.29	16.24	16.50	16.14	16.40	1.120	0.10		930	915
96	10/06/88	03:16	25.34	9.11	16.23	16.46	16.13	16.35	1.110	0.10		960	947
97	10/06/88	04:17	25.49	9.25	16.24	16.44	16.14	16.33	1.105	0.10		960	949
98	10/06/88	05:17	24.95	8.81	16.14	16.30	16.04	16.20	1.080	0.11		960	950
99	10/06/88	06:18	25.31	9.18	16.13	16.26	16.03	16.16	1.060	0.12		960	952
100	10/06/88	07:18	25.51	9.25	16.26	16.36	16.16	16.25	1.045	0.12		950	944
101	10/06/88	08:18	25.26	9.26	16.00	16.07	15.90	15.96	1.055	0.12		960	956
102	10/06/88	09:19	25.25	9.08	16.17	16.20	16.07	16.10	1.035	0.13		960	958

Table D.1 Continued.

S/N	Date	Time	Total Mass (g)	Tare (g)	Sample Mass (g)	Corr. Sample Mass (g)	Meas. Flow Rate (ml/hr)	Corr. Flow Rate (ml/hr)	Corr. HNO <sub>3</sub> Conc. (molar)	Calc. pH	Meas. pH	Meas. Silica Conc. (ppb)	Corr. Silica Conc. (ppb)
0.31 N HNO <sub>3</sub> Feed - start 10:00 6 Oct													
105	10/06/88	10:18	26.98	9.30	17.68	18.49	17.58	18.38	0.314	0.65		0	
106	10/06/88	11:19	26.83	9.29	17.54	18.32	17.44	18.21	1.000	0.16		880	841
107	10/06/88	12:19	26.63	9.28	17.35	18.09	17.25	17.99	0.850	0.24		770	737
108	10/06/88	13:19	25.88	9.10	16.78	17.49	16.68	17.39	0.740	0.30		720	690
109	10/06/88	14:20	27.29	9.15	18.14	18.82	18.03	18.71	0.680	0.34		710	681
110	10/06/88	15:20	27.49	9.25	18.24	18.89	18.13	18.77	0.620	0.37		630	607
111	10/06/88	16:21	27.04	9.24	17.80	18.41	17.69	18.43	0.565	0.41		640	618
112	10/06/88	17:21	26.03	9.00	17.03	17.61	17.17	17.75	0.520	0.45		630	609
113	10/06/88	18:20	26.02	9.12	16.90	17.45	17.04	17.75	0.495	0.47		620	600
114	10/06/88	19:20	25.87	9.00	16.87	17.39	17.01	17.59	0.455	0.50		620	601
115	10/06/88	20:19	25.73	8.95	16.78	17.26	16.91	17.53	0.430	0.53		620	602
116	10/06/88	21:19	25.99	9.25	16.74	17.19	16.87	17.40	0.415	0.54		590	573
117	10/06/88	22:19	26.06	9.22	16.84	17.26	16.97	17.33	0.395	0.56		600	584
118	10/06/88	23:18	21.66	9.11	12.55	12.94	12.65	17.40	0.365	0.59		560	546
119	10/07/88	00:18	25.95	9.21	16.74	17.09	16.87	13.04	0.365	0.60		580	563
120	10/07/88	01:17	25.80	9.11	16.69	17.01	16.82	17.23	0.355	0.60		590	578
121	10/07/88	02:17	26.05	9.28	16.77	17.06	16.90	17.15	0.350	0.61		590	579
122	10/07/88	03:16	25.92	9.25	16.67	16.93	16.80	17.20	0.330	0.63		590	580
123	10/07/88	04:16	25.84	9.14	16.70	16.93	16.83	17.06	0.330	0.63		590	581
124	10/07/88	05:15	25.71	9.13	16.58	16.77	16.71	17.06	0.325	0.64		570	562
125	10/07/88	06:15	25.89	9.21	16.68	16.84	16.81	16.91	0.310	0.66		580	573
126	10/07/88	07:14	25.92	9.18	16.74	16.87	16.87	16.98	0.315	0.65		580	574
127	10/07/88	08:14	26.65	9.23	17.42	17.52	17.56	17.00	0.310	0.65		590	585
128	10/07/88	09:13	27.15	9.09	18.06	18.12	18.20	17.66	0.300	0.67		600	597
								18.27	0.305	0.66		590	588

Table D.1 Continued.

S/N	Date	Time	Total Mass (g)	Tare (g)	Sample Mass (g)	Corr. Sample Mass (g)	Meas. Flow Rate (ml/hr)	Corr. Flow Rate (ml/hr)	Calc. pH	Meas. pH	Meas. Silica Conc. (ppb)	Corr. Silica Conc. (ppb)
Demineralized Water Feed												
140	10/17/88	11:53	25.20	9.10	16.10	18.51	16.04	18.45		3.40	15	15
141	10/17/88	12:53	25.05	9.13	15.92	18.30	15.86	18.23		4.05	169	147
142	10/17/88	13:53	24.90	9.25	15.65	18.00	15.59	17.93		3.80	165	144
143	10/17/88	14:54	25.06	9.28	15.78	18.10	15.72	18.03		3.95	151	131
144	10/17/88	15:54	24.70	9.09	15.61	17.89	15.55	17.83		3.75	161	140
145	10/17/88	16:54	24.55	9.15	15.40	17.65	15.34	17.59		3.50	199	174
146	10/17/88	17:54	24.53	9.23	15.30	17.52	15.24	17.45		3.10	154	134
147	10/17/88	18:54	24.32	9.14	15.18	17.37	15.12	17.30		3.05	134	117
148	10/17/88	19:55	24.48	9.18	15.30	17.45	15.24	17.39		3.03	150	131
149	10/17/88	20:55	24.10	9.12	14.98	17.10	14.92	17.04		3.13	138	121
150	10/17/88	21:55	24.04	9.26	14.78	16.87	14.73	16.81		3.05	153	134
151	10/17/88	22:55	24.32	9.12	15.20	17.26	15.14	17.19		2.95	157	138
152	10/17/88	23:56	24.58	9.24	15.34	17.36	15.28	17.30		2.98	153	135
153	10/18/88	00:56	24.55	9.27	15.28	17.27	15.22	17.21		3.16	152	134
154	10/18/88	01:56	24.35	9.24	15.11	17.07	15.05	17.00		3.22	141	125
155	10/18/88	02:56	24.09	8.96	15.13	17.05	15.07	16.99		3.25	153	135
156	10/18/88	03:56	24.00	9.16	14.84	16.73	14.79	16.67		3.32	141	125
157	10/18/88	04:57	24.14	9.26	14.88	16.74	14.83	16.68		3.25	140	124
158	10/18/88	05:57	24.22	9.30	14.92	16.75	14.87	16.69		3.25	139	124
159	10/18/88	06:57	24.20	9.29	14.91	16.70	14.86	16.64		3.34	126	112
160	10/18/88	07:57	24.04	9.26	14.78	16.54	14.73	16.48		3.43	127	113
161	10/18/88	08:58	23.69	9.10	14.59	16.32	14.54	16.26		3.40	120	107
										3.42	132	118

Table D.1 Continued.

S/N	Date	Time	Total Mass (g)	Tare (g)	Sample Mass (g)	Corr. Sample Mass (g)	Meas. Flow Rate (ml/hr)	Corr. Flow Rate (ml/hr)	Corr. HNO <sub>3</sub> Conc. (molar)	Calc. pH	Meas. pH	Meas. Silica Conc. (ppb)	Corr. Silica Conc. (ppb)
0.1 N HNO <sub>3</sub> Feed - start 09:10 18 Oct													
162	10/18/88	09:58	23.86	9.00	14.86	16.56	14.81	16.50	0		1.22	0	
163	10/18/88	10:58	24.01	9.23	14.78	16.44	14.73	16.38			3.51	119	107
164	10/18/88	11:58	23.72	9.20	14.52	16.15	14.47	16.09	0		3.54	112	101
165	10/18/88	12:58	23.60	9.00	14.60	16.20	14.55	16.14				136	122
166	10/18/88	13:59	23.68	9.23	14.45	16.02	14.40	15.96	1.59E-17	16.84	3.06	142	128
167	10/18/88	14:59	23.82	9.11	14.71	16.24	14.66	16.18				201	181
168	10/18/88	15:59	24.29	9.26	15.03	16.53	14.97	16.47	0.144	1.00	1.22	265	240
169	10/18/88	16:59	24.67	9.24	15.43	16.90	15.37	16.84				287	261
170	10/18/88	17:59	24.19	9.24	14.95	16.39	14.89	16.32	0.234	0.80	1.08	291	266
171	10/18/88	19:00	24.04	8.97	15.07	16.47	15.01	16.41				297	271
172	10/18/88	20:00	24.61	9.20	15.41	16.78	15.35	16.72	0.24	0.79	1.09	296	271
173	10/18/88	21:00	23.88	9.15	14.73	16.07	14.68	16.01				335	308
174	10/18/88	22:00	23.97	9.29	14.68	15.98	14.63	15.93	0.242	0.79	1.08	258	237
175	10/18/88	23:01	23.97	9.09	14.88	16.15	14.83	16.09				300	276
176	10/19/88	00:01	24.34	9.11	15.23	16.47	15.17	16.41	0.242	0.78	1.07	321	296
177	10/19/88	01:01	24.33	9.26	15.07	16.28	15.01	16.22				349	323
178	10/19/88	02:01	24.18	9.27	14.91	16.08	14.86	16.03	0.241	0.78	1.07	366	339
179	10/19/88	03:01	24.19	9.24	14.95	16.09	14.89	16.03				372	345
180	10/19/88	04:02	24.02	9.10	14.92	16.03	14.87	15.97	0.239	0.79	1.05	379	352
181	10/19/88	05:02	23.76	9.13	14.63	15.71	14.58	15.65				326	303
182	10/19/88	06:02	24.44	9.11	15.33	16.37	15.27	16.31	0.239	0.78	1.07	364	339
183	10/19/88	07:02	24.98	9.11	15.87	16.88	15.81	16.82				356	333
184	10/19/88	08:03	24.92	9.14	15.78	16.76	15.72	16.70	0.245	0.77	1.12	369	347
185	10/19/88	09:03	24.76	9.22	15.54	16.49	15.48	16.43				365	344
186	10/19/88	10:03	27.31	9.25	18.06	18.97	17.99	18.90	0.242	0.77		348	328
												354	337



## **Acknowledgements**

The list of people who have contributed to this thesis is longer than the thesis itself. At the Los Alamos National Laboratory, Robert Brownlee, John Whetten, Wayne Morris, Hugh Murphy and Doyle Evans approved a leave of absence so I could pursue graduate studies. I have had many useful discussions on various aspects of this work with Bob Potter, Dave Bish, Fraser Goff, Jamie Gardiner, Grant Heiken, Dave Vaniman, Lee Brown and Cheryl Rofer. Dale Counce and Pat Trujillo allowed me to use laboratory space, equipment and supplies, and performed some of the analyses. Their words of support and interest helped immensely in the experiments. Roland Hagen and Gary Luedemann helped with the SEM work and Dave Mann provided assistance with sample preparation. John Paskiewicz helped mount and re-photograph the SEM photos, and Anthony Garcia helped with some of the graphics.

At MIT, I have received assistance, encouragement and friendship from a number of fellow students, especially Kevin and Linda Sparks, Paul Webley, Mark Wilkinson, Rick Rauenzahn, Carl Graham, Jim and Holly Ferguson, and Bruce Robinson. Even a few faculty members deserve mention - Jeff Tester, Pretinder Virk, Robert Reid, Mike Manning, James Wei, George Stephanopoulous, Ueli Suter and Mike Mohr - for their excellent teaching, advice and encouragement. I also wish to thank Ms. Jean Beuche of the graduate office for her help in dealing with the various requirements, forms, questions, copies, and general all around problems encountered on the journey through the Chemical Engineering Department.

I also wish to thank E. James Davis, formerly head of the Department of Chemical Engineering at the University of New Mexico, Alfred Truesdell of the USGS-Menlo Park, Joseph Smyth of the University of Colorado at Boulder, Rich Holdren formerly of the University of Rochester, and Kevin Knauss at the Lawrence Livermore National Laboratory for discussions, preprints of papers, and for access to unpublished data.

Not the least of the contributors to this thesis have been members of my family. My aunts, uncles and cousins in Oklahoma, Texas and Illinois have provided interesting discussions, words of encouragement, meals and a place to sleep on my travels back and forth to Boston. In addition to the above, my brother, Mark, has helped with the purchase of the HP Vectra that I have used (with much appreciation) for calculations, graphics and word processing.

It is hard to explain to young children why Dad has to work all the time or why Dad is so far away in Boston. When my son, David, was two years old, I went to Boston for the first time. His ninth birthday is only a few months from the time I am writing this. David's life and that of his sister, Danika, who is four, have been dominated by this thesis and by the fallout from it. I sincerely hope that someday they might appreciate what I have written here and why, and that they might know that being away from them was the hardest part of all.

From the beginning, I have had the strongest support from my parents, Earl and Betty Grigsby. I suspect that by now, my father has gotten far more than he bargained for in his exhortations for me to get an education. If I do half as well with a PhD as he has done with his seventh grade education, I will be satisfied. There is no better model for a man than he. Words like encouragement and support are not enough to describe the contributions of my mother. She has always been beside me in whatever I have attempted. For her, I have only the deepest love.

Two people have been "in the trenches" with me. The first is my long-time friend, boss, teacher and thesis adviser, Jefferson Tester. Jeff is the first chemical engineer I ever saw. When I started working for him at the Los Alamos National Laboratory in October, 1976, I found that he could figure out an answer or an approach to an answer for every question I had about my work. We've done a number of interesting things related to geothermal chemistry, but I'm sure that he is as happy as I am that this phase of our working relationship is ended. My appreciation for Jeff's help also extends to his wife, Sue. They can rest secure in the knowledge that I don't need to store my worldly goods in their attic again.

The second person in the trenches with me is Lois Toevs, MD, PhD (even if it's from CalTech), my friend, cooking, hiking, gardening, card-playing and just all around companion, lover and future wife. I thank her for taking me into her house and heart so that I could fulfill my dreams (more than just finish my PhD) out of the rain. I'll be repaying her for the rest of my life.

## **Biographical Sketch**

Charles Owen Grigsby was born on November 8, 1951 in Hutchinson, Kansas. He was raised in Artesia, New Mexico and received his BS in geology (1973) at the New Mexico Institute of Mining and Technology in Socorro, New Mexico. After working at the New Mexico Bureau of Mines and Mineral Resources in Socorro, he joined the staff of the Los Alamos National Laboratory. While working on the Hot Dry Rock Geothermal Program, he came under the gentle influence of Jefferson Tester who interested him in the art of chemical engineering. In 1976, he started graduate work in chemical engineering at the Los Alamos branch of the University of New Mexico, but transferred to MIT to complete his master's degree (1983) and his doctorate. He is the author or coauthor of 32 technical publications in refereed journals or Los Alamos reports.

On receiving his PhD, he will return to the Los Alamos National Laboratory where he hopes to develop or resume new and less expensive hobbies such as gardening, skiing, and camping with his wife-to-be and with his children.

**This page intentionally left blank.**